UNIVERSITY OF SOUTHAMPTON

FACULTY OF ENVIRONMENTAL AND LIFE SCIENCES

Ocean and Earth Science

Tidal-range and tidal-stream energy characterisation in the Gulf of California, Mexico

By

Carlos Joel Mejia Olivares

Thesis for the degree of Doctor of Philosophy

April 2019

UNIVERSITY OF SOUTHAMPTON

ABSTRACT

FACULTY OF ENVIRONMENTAL AND LIFE SCIENCE

Ocean and Earth Science

Doctor of Philosophy

TIDAL-RANGE AND TIDAL-STREAM ENERGY CHARACTERISATION IN THE GULF OF CALIFORNIA, MEXICO.

Carlos Joel Mejia Olivares

In the last two decades, there has been a growing interest in tidal energy, which is a predictable source of renewable energy driven by astronomical forces. To date, no dedicated assessments of the available tidal-stream energy resource have been carried out for the Gulf of California, México (hereafter GC) and only two limited studies of tidal-range have been undertaken in this region. The northern part of the GC has a relatively large mean tidal-range (up to 5 m). Furthermore, tidal flows of over 1.5 m/s have been recorded on spring tides in between the Midriff Islands in the central part of the GC. Hence, this region has the potential for tidal energy exploitation. However, locations like the GC, with a strong diurnal tidal influence and less energetic tidal currents, but in deeper waters, have often been overlooked. The aim of this thesis is therefore to quantify the theoretical tidal-range and tidal-stream energy characterisation within the GC.

The first objective is to quantify the theoretical tidal-range energy resource. This was done using tidal level predictions from a depth-averaged barotropic hydrodynamic model, extensively validated against tide gauge and current observations. A 0-D modelling approach was then used to determine the power that can be technically exploited at four key sites in the northern regions of the GC. The results indicate that the annual energy yield ranges from 20 to 50 kWh/m^2 while the maximum values are between 45 and 50 kWh/m^2 in the vicinity of the Gulf of Santa Clara. This site was the best performing in regard to tidal-range energy potential, delivering a technical annual energy output of 125 GWh (ebb-only), 159 GWh (two-way) and 174 GWh (two-way with pumping), assuming an impound area of 10 km^2.

The second objective is to determine the present day theoretical tidal-stream energy resource available in the GC. This was done by utilising tidal current predictions from the hydrodynamic model. The highest current speeds of 2.4 m/s were found to occur in the channel between San Lorenzo and San Esteban Island (hereafter San Lorenzo Passage), and three lower-velocity potential sites were identified in the channels between: (1) Baja California Peninsula and San Lorenzo Island; (2) San Esteban and Tiburon Islands and (3) Baja California Peninsula and Angel de la Guarda Island. Although peak kinetic power density (hereafter KPD) in these regions is found to be relatively low (~ 3 to 6 kW/m^2), the large water depth (100 to 500 m) results in an undisturbed theoretical annual mean power of between 100 to 200 MW. Technical power was estimated for four device types, first assuming just an array of devices near the surface, and second an array of devices down through the water depth. The estimated total annual mean technical power varied between 251 and 460 MW, considering just a near surface area, and between 304 and 1030 MW if the full water column was utilised. Results of the hydrodynamic model, based on localised refined bathymetry datasets, highlighted that global and freely available bathymetry data products under-resolve the energy resource by up to 75%. Findings also suggesting that diurnal and higher order harmonic constituents are important for accurate resource assessments in this region.

A detailed analysis of the 3D characteristics of tidal currents in the central Gulf was undertaken, using predictions from a HAMSOM model, developed previously. This analysis has shown that current velocities varying considerably with depth, and the vertical profile varies depending on site. At the four sites, considered here, the current speeds are fastest in the upper water column. A novel analysis was also undertaken assessing whether knowledge of the phase relationship between tidal energy sites be exploited by aggregating the electricity generated by a number of geographically distributed sites. The results highlight that if one considers tidal-range and tidal-stream schemes separately, it is not possible to generate a form power supply through a day from the four tidal-range and four tidal-stream sites identified. However, if one considers tidal-range and tidal-stream sites together, it is possible to generate a more consistent supply, with short periods of zero electricity generation.

In conclusion, the northern part of the GC contains several promising locations for a tidal-range energy extraction, with a two-way and pumping scheme option appearing viable for these sites. The tidal-stream resource was found to be large at four main areas in the central region of the GC, but new turbine technologies would be required to exploit these ‘next generation’ resource regions. This study highlights that regions like the GC, with a strong diurnal tidal influence and less energetic tidal-ranges and currents, but in deeper waters, should not be overlooked when considering sites around the world suitable for tidal energy exploitation.

List of Contents

List of Figures

List of Tables

Academic thesis: Declaration of authorship

I, Carlos Joel Mejia Olivares, declare that this thesis "Tidal-range and tidal-stream energy characterisation in the Gulf of California, Mexico" and the work presented in it are my own and has been generated by me as the result of my own original research.

I confirm that:

1. This work was done wholly or mainly while in candidature for a research degree at this University;
2. Where any part of this thesis has previously been submitted for a degree or any other qualification at this University or any other institution, this has been clearly stated;
3. Where I have consulted the published work of others, this is always clearly attributed;
4. Where I have quoted from the work of others, the source is always given. With the exception of such quotations, this thesis is entirely my own work;
5. I have acknowledged all main sources of help;
6. Where the thesis is based on work done by myself jointly with others, I have made clear exactly what was done by others and what I have contributed myself;
7. Parts of this work have been published as:

Mejia-Olivares, C.J., Haigh. I.D., Wells, N.C, Coles, D.S., Lewis, M. and Neill, S.P, 2018. Tidal-stream energy resource characterisation for the Gulf of California, México. Energy, 156, 481-491. https://doi.org/10.1016/j.energy.2018.04.074

Mejia-Olivares, C.J., Haigh. I.D., Angeloudis A., Lewis, M. and Neill, S.P, 2018. Tidal range energy resource assessment of the Gulf of California, Mexico. In review with Renewable Energy.

Mejia-Olivares, C.J., Haigh. I.D., Lewis, M. and Neill, S.P, 2019. Sensitivity assessment of bathymetry and choice of tidal constituents on tidal-stream energy resource characterisation in the Gulf of California, Mexico. In review with Applied Ocean Energy.

Mejia-Olivares, C.J., Haigh. I.D., Lewis, M. and Neill, S.P, 2019. Sensitivity of bathymetry and choice of tidal constituents on tidal-stream energy resource characterization in the Gulf of California, Mexico, in: EWTEC 2019. Naples, pp. 1–6. Accepted and published with EWTEC 2019.

Signed:

Carlos Joel Mejia Olivares

Date: 2/04/2019

Acknowledgements

First and foremost, thanks to God for giving me this opportunity for continuing my studies. All praise, honour and glory to my Lord Jesus Christ for his richest grace and mercy for the accomplishment of this project and thesis.

I would like to thank my two sponsors CONACyT (the National Council of Science and Technology) through the grant “Becas en el extranjero 2014-1” grant reference CVU 536867 and the University of Southampton. I acknowledge the receipt of a studentship from both institutions, enabling the project to take place. Thank you to Dr. Rodolfo Casarin Silva from the National Autonomous University of Mexico (UNAM) for providing the initial data for making my research proposal enabling me to apply for a PhD position at the University of Southampton. Dr. Silvio Marinone and Dr. Manuel Lopez from CICESE for proving the higher bathymetry data in the Gulf of California and the ADCP data respectively.

I wish to express my deep gratitude to Dr. Ivan Haigh who unconditionally took my project in the second year of my PhD. Ivan Haigh transformed this initial project into an excellent peace of work. He provided me with an excellent example of working as a researcher, his ability to motivate and his technical and coding skills in Matlab which are exceptional. Thank you very much to the co-authors of my publications for their support through positive and constructive comments and enriched feedback regarding my work: Dr. Simon Neil and Dr. Matt Lewis from the University of Bangor, Dr. Daniel Coles from the University of Southampton and Dr. Athanasios Angeloudis from the University of Edinburgh.

My family have been most supportive through the PhD, offering motivation, perspective and a genuine interest in my work. Thanks a lot to my Mum (Elba Olivares Chavez), my brother (Jose Gabriel Mejia Olivares), and the best Dad on Earth Gabriel Mejia Hernandez who sadly passed away in 2013 but he is still blessing me every day from heaven. My Dad always kept my family together and he loved all of us massively. Thanks Mum and Dad for making me the man I am, full of values, respectful, passionate for everything I love, hard worker, tenacious and a man of full dreams and hopes. Thanks Aunty Gloria Olivares for your support along all my life, thanks my cousin Ariadna Martinez Olivares for all your support, you have been the sister I always wished for. Also, thanks to all the members of my family for believing on me: Aunty Yolanda, Uncle Antonio, my sister in law Emma Nikte, my niece Naomi Gabriela and all my family overall. I also owe an enormous debt of gratitude to my wife Rachael who has picked me up from the deepest lows, offered unconditional support, loving me massively and take care of me by the bucket load, and kept my work-life balance on track in the last year of my studies.

Thank you very much to my best friend Hector Salcedo Roman who has taken care of my beautiful and precious house in Mexico and giving me unconditional support to continue my studies. Thanks Hector for all your help, your support, you have been a very important person in my life in the last 8 years of our friendship. Thanks to all my international friends in the UK, especially to my best international friend and like my brother the recently graduated Dr. Luis Vicente Wilches from Medellin Colombia, Thanks Luisito for all your support, understanding and lovely moments we had have shared together. Thank you for your unconditional friendship and support throughout my PhD journey to Yurani Moreno, Diana Jazmin, Luis Jairo, Juliana Negrete, Erick Montes de Oca, Andres Felipe Osorio Muriel, Diego Ojeda, Giuseppe Provenzano, Edward Wort, Lina Zapata, and all of the innumerable friends I have.

Abbreviations

ADCP	Acoustic Doppler current profilers
BC	Ballenas Channel
CICESE	The Centre for Scientific Research and Higher Education at Ensenada
C_D	Discharge coefficient (dimensionless)
CF	Capacity factor
C_p	Power coefficient
DEL	Delfin Basin
DECC	Department of Energy and Climate Change in the UK
E	Kinetic energy
ETOPO	Global relief model of Earth's surface that integrates land topography and ocean bathymetry
E_{annual}	Annual energy yield
F_c	Centrifugal force
GWh/year	Giga Watts hour per year
GC	Gulf of California
GEBCO	General Bathymetric Chart of the Oceans
IPCC	The Intergovernmental Panel on Climate Change
IEA	International energy agency
kW/m^2	Kilowatts hour per meter square
KPD	Kinetic power density
K_1	Lunar diurnal constituent
MW	Mega watts
M_2	Principal lunar semi-diurnal tidal constituent
N_2	Larger lunar elliptic semidiurnal constituent

OTIS	OSU Tidal Inversion Software
O_1	Lunar diurnal constituent
P	Power in Watts
P_t	Power of the turbine using a discharge factor
P_{KPD}	Instantaneous undisturbed theoretical power kinetic density
$P_{density}$	Power density
PSU	Practical Salinity Unit
P_1	Solar diurnal constituent
Q_t	Discharge flow through a turbine
Q_1	Larger lunar elliptic diurnal constituent
RMSE	Root means square error
SL	San Lorenzo Island
SE	San Esteban Island
SENER	Mexican ministry of energy
S_2	Principal solar semi-diurnal tidal constituent
“TPXO	It is a series of fully-global models of ocean tides” derives from OTIS (Oregon State University Tidal Inversion Software)
T_TIDE	Matlab coding subroutine to predict tidal level constituents
TWh/year	Tera watts hour per year
TELEMAC	system which is a powerful integrated modelling tool for use in the field of free-surface flows.
UK	United Kingdom
u	Component u of the velocity (eastward)
v	Component v of the velocity (northward)
V	Depth-averaged current velocity

USA	United Stated of America
W	Watts
W	Work

Chapter 1: Introduction

1.1 Motivation

In the last two decades the demand for, and production of electricity has massively increased (Figure 1.1a) (Neill and Meza, 2018). This has been driven by the enormous growth in human populations (Figure 1.1b). From 1975 to present, global populations have grown by almost 2.5 billion and the demand of electricity has more than doubled as a result (International Energy Agency, 2016). Around the world, electricity generation is still heavily dependent on fossil fuels. However, fossil fuels are dwindling and furthermore, there are increasing pressures relating to climate change. Climate change has resulted in an increase in global temperatures, with many associated negative social, economic and environmental consequences (IPCC, 2014). These two important issues are driving the move towards low carbon renewable sources of energy. There is a growing emphasis on finding alternative and efficient methods to generate electricity which is essential for continued economic development and well-being of the world’s population. Moreover, clean energies would significantly contribute to reducing greenhouse gases emissions in line with the Paris Climate Change Agreement (Tiwari et al., 2011).

Over the last two decades there has been increased interest in marine renewable energy exploitation (Neill and Meza, 2018). The oceans cover around 70 % of the planet and are considered to be one of the greatest sources of renewable energy. There are four main forms of marine energy generation (illustrated in Figure 1.2), namely: (1) wave power; (2) Ocean thermal energy; (3) osmotic energy; and (4) tidal power (Marine energy, 2016). Wave power is the capture of the kinetic energy of waves, which are generated by wind as it blows across the ocean. Wave energy is more predictable than wind and solar energy and has the potential to generate up to 80,000 TWh of electricity per year (IEA, 2015). Thermal power utilizes the differences in temperatures between cold deep and warmer shallow waters to run a heat engine to generate electricity. It has been estimated that thermal energy could produce >800 TWh of electricity per year (IEA, 2015). Osmotic power, also called salinity gradient power or blue energy, is the energy available from the difference in salt concentrations between fresh river water and sea water. At the mouth of rivers, where fresh and sea water mixes, energy associated with the salinity gradient can be harnessed using pressure-retarded reverse osmosis process and associated conversion technologies (OES, 2016). It has been estimated that Osmotic energy could produce >2,000 TWh of electricity per year (IEA, 2015). Tidal power, which is the focus of this thesis, uses the twice (and in some locations once) daily movement of water generated by astronomical forcing of the Moon and Sun. Tidal energy offers many benefits compared to other sources of marine renewable energy, because of the regular and predictable nature of ocean tides.

There are two main forms of tidal energy (illustrated in Figure 1.3), namely: (1) tidal-range energy, which utilizes potential energy from the water-level differences between two bodies of water, within the rise and fall of the tide, through the construction of a tidal barrage or lagoon (Prandle, 1984; Baker, 2006, World Energy Council, 2007) (Figure 1.3a); and (2) tidal-stream energy, which exploits the kinetic energy of tidal currents, through the use of a variety of devices that are able to convert the linear velocity of the ocean’s currents into a rotational torque (Bahaj, 2011) (Figure 1.3b). The theoretical tidal-range and tidal-stream energy resource worldwide, has been estimated to be in the order of 1,200 TWh/year (World Energy Council, 2007). However, in practice only a limited percentage of that energy can be extracted (Garret and Cummins, 2008).

Tidal-range energy has a long history. Mills in villages and towns have utilised tidal energy for at least the last 800 to 900 years (Rosario et al., 2006). More recently, tidal-range energy has been utilized in a few large-scale projects. This includes the first commercial project, the Rance Tidal Power Station in France built in 1967 and subsequent schemes in Kislaya, Gubska in Russia, Lake Shiwa in South Korea, and Jiangxia in China and Nova Scotia in Canada. These schemes involved the construction of large tidal barrages in tidal inlets or Bays (Charlier, 2007). Many other potential locations have been identified as being suitable for tidal-range energy extraction. These include, for example: the Severn Estuary and the Bristol Channel, UK (SBC, 1981; Neill et al., 2017); the coast of New Jersey, USA (Tang et al., 2014); the Atlantic east coast and Pacific west coast of Canada (Nova Scotia Power, 2018) and the Sihwa Lake Tidal Power Station in South Korea (Waters and Aggidis, 2016; Bae, et al., 2010; Park, 2017). More recently, there is increasing interest in utilising small bays and lagoons for tidal energy extraction, such as the well-publicized Swansea Lagoon project (Waters and Aggidis, 2016), as opposed to the very large barrage schemes which normally include a barrage construction along the coast, across bays and in estuaries.

To date, there has been only one commercial-scale scheme exploiting tidal-stream energy. This is the Strangford Lough scheme in North Ireland which started development in 2008 (Marine energy, 2016 and 2017). In addition, there are currently three pre-commercial array projects prototypes under construction. These are located Northern of Caithness at Pentland Firth and Orkney Waters , Scotland, the Bay of Fundy in Canada and in Brittany, France (Marine Energy, 2016). Many other locations around the world have been identified as having the potential for tidal-stream energy. These include, for example: Portland Bill (Blunden and Bahaj, 2006), Pentland Firth (Adcock et al., 2013; Draper et al., 2014; Fairley et al., 2015) and Anglesey Skerries in the UK (Serhadlıoğlu et al., 2013; Lewis et al., 2015); Johnstone Strait, Vancouver Island, Minas Passage, and the Bay of Fundy in Canada (Sutherland et al., 2007; Karsten et al., 2008; Walters et al., 2013); and Kinmen Island in Taiwan (Chen et al., 2013) and Hulu Island in China (Gao et al., 2015).

Recently, there has been growing interest in exploiting tidal energy extraction for countries within Latin America. In the developing countries in Latin America, in particularly, the demand for electricity has increased considerably in recent decades due to substantial economic development and population growth (Aleman-Nava et al., 2017). There are currently no tidal-range or tidal-stream energy schemes in operation (or even planned) in Latin America. However, several studies in recent years have identified locations that would potentially be suitable for tidal energy extraction. With the exception of sites in Mexico (see paragraph below), locations suitable for tidal-range energy have not yet been identified or assessed in Latin American. However, several studies have carried out resource assessments for tidal-stream energy in Latin America which include the southern part of Chile (Herrera et al., 2010), Buenaventura Bay on the Pacific coast in Colombia (Osorio et al., 2016), Baiá de Todos os Santos Bay in Brazil (Marta-Almeida et al., 2017) and Cabo Polonio in Uruguay (Alonso et al., 2017).

This thesis focuses on Mexico which is the second largest country in Latin America (after Brazil). Mexico’s crude oil reserves rank within the top 10 in the world (Alemán-Nava et al., 2014) and its electric power consumption per capita is approximately 2,090 kWh (World Bank, 2018). In 2012 and 2013 Mexico supplied electricity at roughly 260 TWh and 220 TWh, respectively. 80 % of the electricity produced in the country is from thermal power plants and as a result, the country is highly dependent on the use of fossil fuels (SENER, 2015). In 2013, total carbon dioxide (CO_2) emissions from electricity production in Mexico was approximately 133 million metric tons (SENER, 2013). However, Mexico has set an ambitious target of generating 35% of its total energy from renewable sources by 2027 and thus lowering his carbon emissions (SENER, 2013). Currently 19 % of Mexico's electricity is produced through renewable sources, which mainly consist of solar, wind turbines, biomass, geothermal and hydropower energy (Alemán-Nava et al., 2014, SENER, 2015). Currently, no electricity is generated via tidal energy in Mexico.

However, a few recent studies have identified sites in Mexico with potential for tidal-range power. For example, Hiriart-Le Bert et al. (2009) assessed the feasibility and potential tidal-range power resources for a tidal barrage situated in the northern most reaches of the GC, which has a relatively large tidal-range (over 5 m). Tapia et al. (2013) highlighted three potential suitable sites for tidal-range energy extraction in the GC, including: (1) San Rafael Bay; (2) Bay of Soldado; and (3) the Bay of Santa Maria. They concluded the Bay of Santa Maria would be viable for tidal-range energy generation for the reason that the nearest available grid connectivity is in the vicinity at San Felipe Port, whereas at the other sites the nearest grid connectivity is much further away. To date, no tidal-stream energy resource assessments have been carried out for sites in Mexico. However, tidal flows of over 1.5 m/s have been recorded during spring tides in between the Midriff Islands in the GC (Badan-Dagon et al., 1991; Lopez et al., 2008). Therefore, this region holds promise for tidal-stream energy extraction.

Tidal range power plants in selected sites require some characteristics to be taken into account which are relatively limited around the world such as: (1) minimum tidal range; (2) water depth; (3), grid connectivity; and (4) intermittent energy generation. In regards to tidal range the minimum requirement is 5 m which would be sufficient to economically deploy turbines to generate electricity (more recently study by Neill et al. 2018). Water depth is a relevant parameter that provides the ideal seabed conditions and geomorphology of the study area for the construction of a barrage or tidal lagoon (maximum water depth of 30 m). Grid connectivity is a key constraint for tidal range power plants as the proximity of the closest power station can result in a significant challenge. Previous timing generation studies indicate that there is an intermittent period of time, along the tidal cycle, when the power generation is interrupted (Burrows et al., 2009c; Xia et al., 2010; Aggidis and Benzon, 2013; Angeloudis and Falconer, 2017). Also, operational modes and maximisation of power output play an important role in obtaining optimum power levels to meet with the electricity demand (Bray et al., 2016;

Angeloudis and Falconer, 2017; Angeloudis et al., 2016b; Angeloudis et al., 2018; Lisboa et al., 2017). Moreover, there are a few more complex factors that need to be considered for assessing tidal range power plant feasibility. The initial investment required for the development of tidal power plants, at this stage, is exceptionally expensive as previously found during the Swansea Lagoon project (Atkins, 2004; Baker, 2006; Waters and Aggidis, 2016, 2016b). The design of an operational tidal power plant needs to be carefully assessed to minimise the potential environmental impact (Hooper and Austen, 2013; Angeloudis et al., 2016a). Hydrodynamic effects need to be determined to analyse the tidal amplitude changes as a result of tidal power scheme construction (Howards et al., 2007; Watson and Shaw, 2007; Falconer et al., 2009; Burrows et al., 2009a and 2009b; Xia et al., 2010 and 2012; Fairley et al., 2014). Furthermore, tidal current variations represent an important challenge to address for this type of renewable energy (Falconer et al., 2009; Burrows et al., 2009b; Angeloudis et al., 2017).

When it comes to identifying the suitability of a tidal energy site, the main characteristics usually considered are: (1) energetic resource; (2) water depth; (3) proximity to the grid connection and power variability. In regard to energetic resource, the present tidal-stream devices available require current speeds of >2.5 m/s. In regards to water depth, these current devices are normally bottom mounted, in water depths <80 m. Grid connectivity plays an important role in getting the electricity generated by the turbine to where it is needed (Lewis et al., 2015) and (4) power variability represents an important challenge for the grid network as a result of an intermittent electricity generation (Robins et al., 2015; Goward-Brown et al., 2017; Lewis et al., 2019). Furthermore, tidal phasing and asymmetry is relevant to determine the availability of the resource generation along the tidal cycle as well as the occasions when electricity generation is fluctuating (Iyer et al., 2013; Neill et al., 2014 and 2016; Ward et al., 2018). While these factors are the main elements to be considered for feasibility, other aspects would be taken into account, such as : environmental impacts (Robins et al., 2014); noise generated by the devices (Robinson and Lepper, 2013; Lloyd et al., 2014; Robinson, 2016;), potential risk for collision of the moving components of the turbine and the impact on marine life when passing nearby the devices (Hastie et al., 2018), flow reduction (Ahmadian and Falconer, 2012; Martin-Short et al., 2015; Coles et al., 2017; De Dominicis et al., 2018), birds migration (Friend of the Earth Cymru, 2004) and marine mammal surveys (Inger et al., 2009). In addition, the turbine array configuration and interaction between and within a row of devices

(Harrison et al., 2008; Myers and Bahaj, 2009; Harrison et al., 2011; Mcintosh et al., 2012; Fallon et al., 2014; Abolghasemi et al., 2016; Lo Brutto et al., 2016, Coles et al., 2017,); also the social impacts such as the cost of electricity (Boyle, 2004; ORE Catapult, 2018; UK Marine energy, 2019); and the impact on commercial ships, and navigation routes (O'Rourke et al., 2014).

In summary, it is evident that the GC in Mexico has promising potential sites for both tidal-range and tidal-stream energy extraction. Furthermore, the Mexican government is keen to exploit this available resource and carry out detailed studies to more accurately identify suitable and viable sites. To date there have only been two previously mentioned studies (e.g., Hiriart-Le Bert et al., 2009; Tapia et al., 2013) that have been carried out an assessment of the potential tidal-range energy resources in the GC. However, these have used only limited data sets, basic methodologies and narrow scientific support for evaluating the resource. Furthermore, no study has yet assessed the tidal-stream energy resource potentially available in the region, despite the fact high current speeds have been record in the Midriff area (Badan-Dagon et al., 1991; Lopez et al., 2008). Moreover, in contrast to other regions in which the tidal energy resource has been explored, the GC is relatively deep, and diurnal tidal constituents are typically larger; hence the resource characterisation is expected to contrast considerably from previously identified tidal-stream sites. Therefore, there is a timely need to carry out a comprehensive assessment of the potential tidal-range and tidal-stream energy resource available in the GC and to consider the viability of utilising this.

1.2 Aims and objectives

Therefore, the overall aim of this thesis is to evaluate the theoretical tidal-range and tidal-stream energy resource available in the GC, Mexico. To address this aim there are two objectives, as follows:

1. To quantify the present day potential theoretical tidal-range energy resource available in the GC, Mexico;
2. To determine the present day potential theoretical tidal-stream energy resource available in the GC; and

To achieve objectives 1 and 2 a depth (average) barotropic model has been configured and extensively validated against measured data. Predicted tidal levels and tidal currents have then been used to estimate the energy available energy resource in the GC. Comprehensive sensitivities tests have been undertaken to determine how the predicted energy resource varies depending on which bathymetric data is used to configure the model grid and the choice of tidal constituents.

The GC, also known as the Sea of Cortez, is a semi-enclosed sea (Figure 1.4). Its length is about 1,100 km and its width dimensions are between 48 and 240 km and it covers an area of 177,000 km^2. The GC is divided into three main regions: (1) the northern region (Figure 1.4b); the central or Midriff region (Figure 1.4c); and the southern region. The GC has a complex bathymetry with a depth varying from around 200 m in the upper Gulf to 3,600 m at its entrance with the Pacific Ocean. The areas of most interest to this study are the northern GC, which has tidal-range of over 5 m (Marinone et al., 2009), and the area around the Archipelago (or Midriff Islands) in the central area of the GC, which has high current speeds (Badan-Dagon et al., 1991). Therefore, these areas represent promising sites for tidal-range and tidal-stream energy extraction.

1.3 Structure of thesis

The structure of this thesis is as follows. **Chapter 2** outlines tide generation principles, provides the background on tidal-range and tidal-stream energy and gives an overview of the relevant literature in this regard. It then discusses the main oceanographic and meteorological characteristics of the study area and summaries the main knowledge gaps. **Chapter 3** describes the configuration and validation of the hydrodynamic numerical model used in **Chapters 4** and **5**. The two objectives are then addressed in turn in **Chapters 4 and 5**, respectively. Each of **Chapters 3, 4 and 5** starts with a short introduction providing the motivation and objective for that chapter, followed by a description of the methods, results, discussion and conclusions, for that chapters. **Chapter 6** provides a synthesis and discussion of the main findings from Chapters 4 and 5, in light of important considerations when identifying a tidal energy site, and furthermore, additional analysis of the 3D structure of tidal currents and phasing of the tide is undertaken to provide further insight. Finally, conclusions, are given in **Chapter 7.**

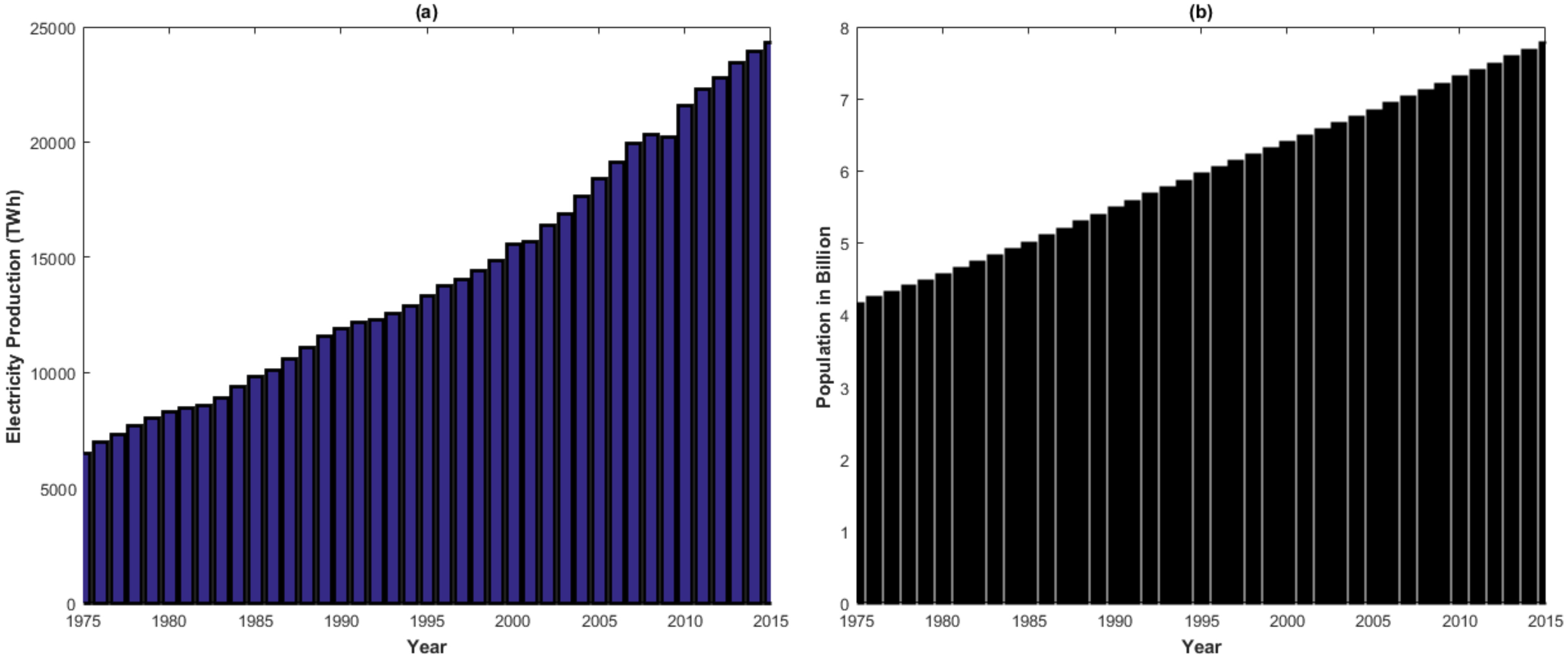

Figure 1.1. Global (a) Electricity production (source of data https://tinyurl.com/yb5ct288); and (b) population growth (source of data: https://tinyurl.com/y7w8qdkt from 1975 to 2015).

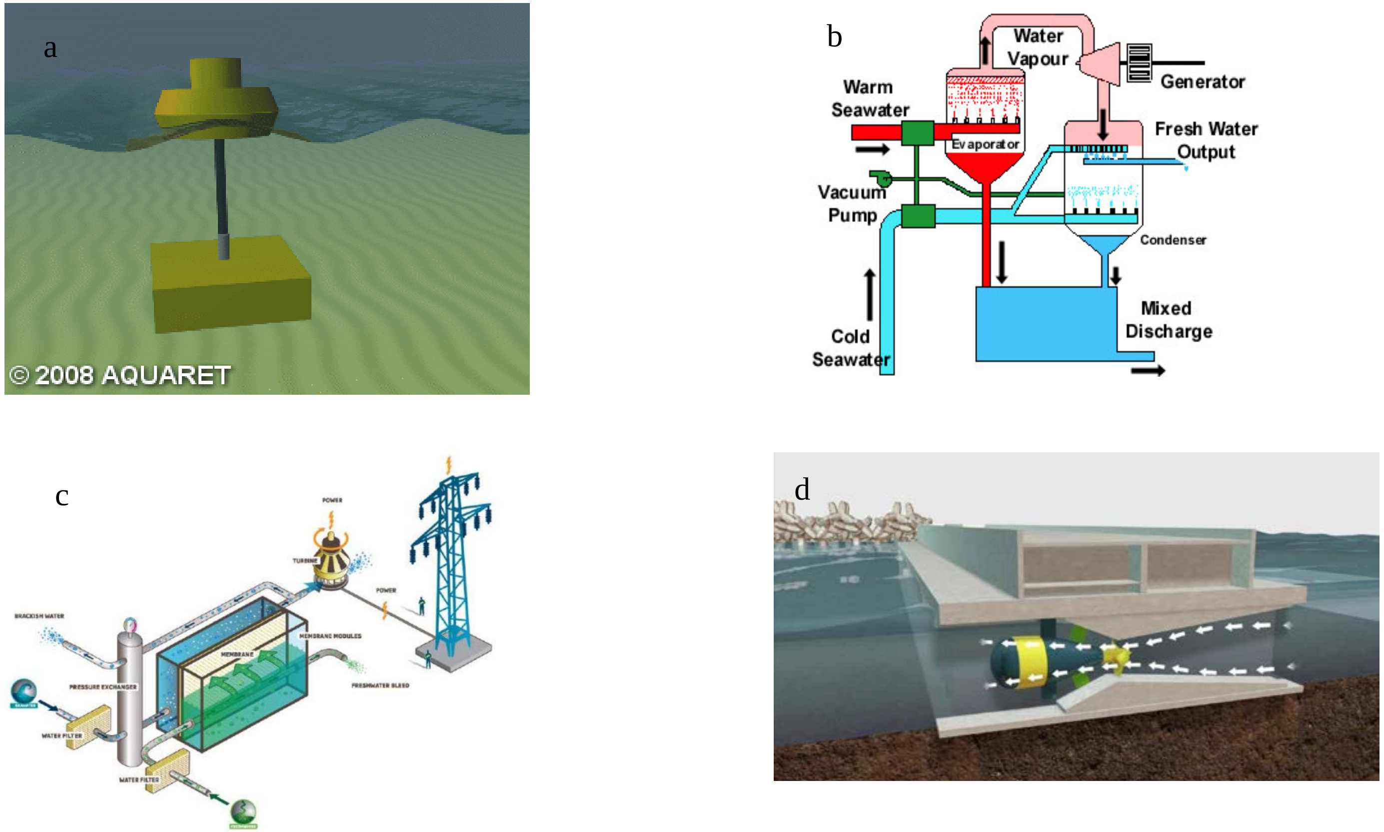

Figure 1.2. Illustrations of the four main marine energy types, namely: (a) wave power; (b) thermal power; (c) osmotic power; and (d) tidal power. Sources: (a) https://tinyurl.com/y8e5aolp (b) https://tinyurl.com/y8yksay7 (c) https://tinyurl.com/yb5ud5ay, https://tinyurl.com/yc5amocz (d) https://tinyurl.com/ydxbmhft.

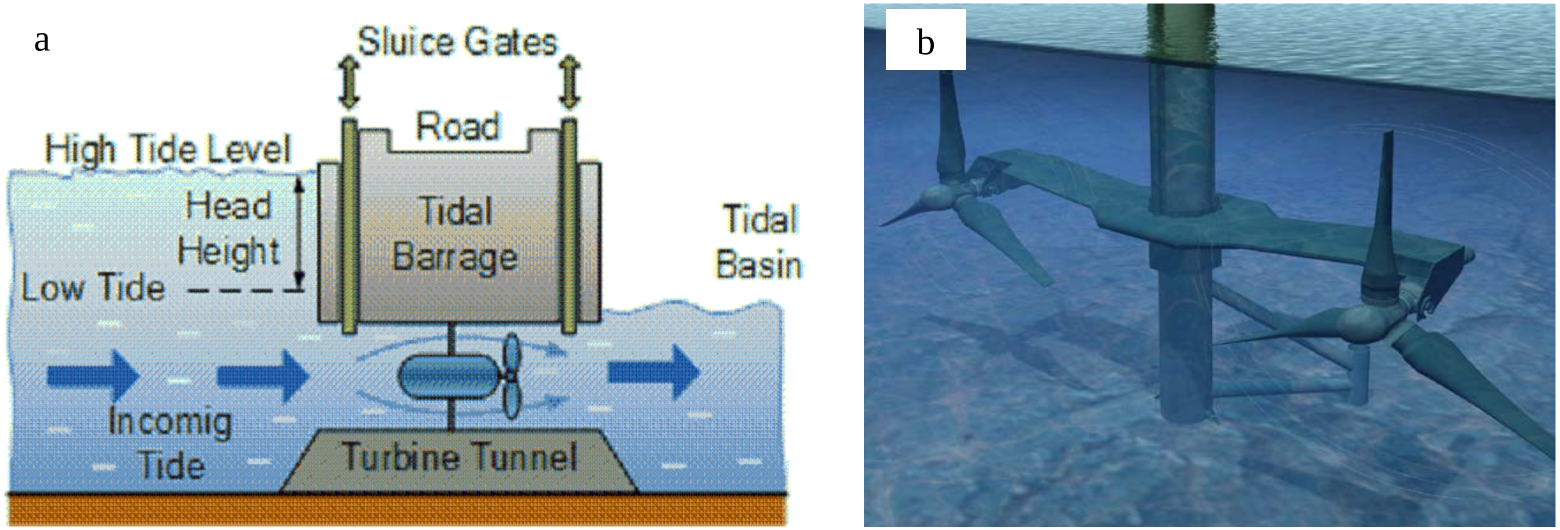

Figure 1.3. Illustrations showing the two types of tidal power, namely: (a) tidal-range power; and (b) tidal-stream power. Source: (a) https://tinyurl.com/y9eu9jo2; (b) https://tinyurl.com/yc5amocz.

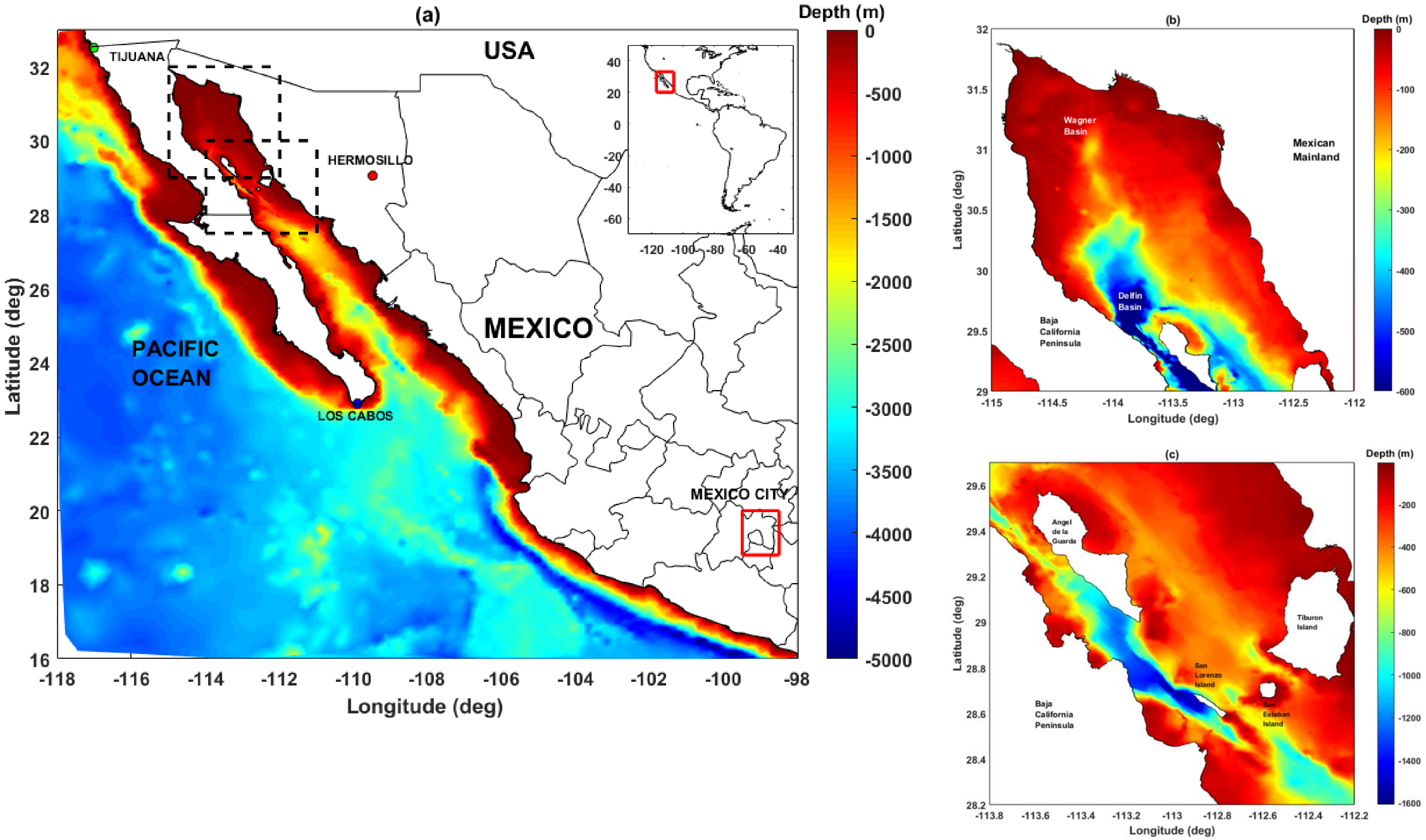

Figure 1.4. Maps showing the: (a) GC; (b) Northern GC; and (c) Midriff area of the GC.

Chapter 2: Background: Literature review

This chapter outlines tide generation principles, provides the background on tidal-range and tidal-stream energy and gives an overview of the relevant literature in this regard. The chapter has four main sub-section, as follows. Section 2.1 provides a background to astronomical tides. An overview of tidal-range and tidal-stream energy is given in Section 2.2. Section 2.3 discussed the characteristics of the study area. A summary is given in Section 2.4, highlighting key knowledge gaps in relation to the thesis objectives.

2.1 Astronomical tides

Tides are the regular rise and fall of the sea caused by astronomical forces associated with the gravitation attraction and rotation of the Earth, Moon and Sun system (Haigh, 2017). The term tides is often use to describe the vertical variation in the sea level, whereas the term tidal currents is often used for the horizontal movement of water. This section describes how tides are generated (Section 2.1.1), key characteristics of tides using the equilibrium theory (Section 2.1.2), the dynamic theory of tides (Section 2.1.3), spatial variations in tidal levels and currents (Section 2.1.4), tidal analysis and prediction (Section 2.1.5) and tidal modelling (Section 2.1.6).

2.1.1 Tide generating force

The study of tides has a long history and is the oldest branch of physical oceanography (Cartwright, 1999, Bishop, 2008). The basic understanding of how tides are generated lies in Isaac Newton's Laws of Gravitation Attraction and Motion. Newton's Law of Gravitation states that the force of attraction (F) of two particles of mass M_1 and M_2 separated by distance r, is given by:

$$F = G\frac{M_1 M_2}{r^2} \tag{EQ. 2.1}$$

Where G is the universal gravitation constant, which is 6.6 $\times 10^{-11}$ N·m^2/ (kg^2). This equation shows that the gravitation force increases if the mass of the two bodies increases and the distance between the two bodies reduces.

To understand the importance of the Moon's role in generating tides, consider that the Earth and Moon form a single system. They mutually revolving around a common center of mass. The Earth is 81 times larger than the Moon, and as a result the center of mass of the system lies within the Earth. The Earth and Moon circle this central point, without any rotation in absolute space. As a result, each point on the Earth travels in circles with the same radius. They therefore experience an equal centrifugal force (F_c), directed parallel to a line joining the centers of the Earth and Moon. The centrifugal force is the same everywhere on Earth.

For the Earth-Moon system to remain in equilibrium, the total centrifugal force must balance the force of gravitation attraction. If it didn't, the Earth and Moon would accelerate away or towards each other. At the center of the Earth the two forces balance. However, at locations nearer to the Moon the gravitation force is larger than the centrifugal force. For locations further away, the centrifugal force is larger than the gravitation force. This difference is the lunar tide-generating force (F_{dm}), which at a point on Earth is (Pugh, 1996):

$$F_{dm} = \frac{GM_m R_e}{dm^3} \qquad \text{(EQ. 2.2)}$$

Where M_m is the Mass of the Moon, R_e is the radius of the Earth, d_m is the distance from the Earth's centre to the centre of the Moon. The solar tidal force, associated with the Sun, can be considered similarly. However, the greater distance between the Earth and Sun offsets the fact that the mass of the Sun is much greater than the mass of the Moon. Hence, the solar tide generating forces are about half those of the lunar forces.

2.1.2 Equilibrium tidal theory

The Equilibrium theory, established by Newton, is useful for describing several key features of observed tides. This theory assumes: (1) the Earth has no land and is covered by water of a uniform depth; (2) the ocean responds immediately to the tide generating force; and (3) the effects of the Earth's rotation and friction can be ignored. Assume a stationary Moon, aligned with Earth's equator. In this case the lunar tide-generating force would cause two bulges on opposite sides of Earth. The Earth rotates, beneath these bulges, taking 24 hours to complete one rotation. Therefore, on the Earth's surface you would experience two high tides each day, the height of which would decrease as you moved north or south of the equator. By the time Earth has completed one rotation, the Moon has moved on in its rotation. This is why high semidiurnal tides occur every 12 hours and 25 minutes, not every 12 hours. If you ignore now the Moon and just consider the Sun, then the same features would be observed, except the time between high waters would be exactly 12 hours. However, the maximum height of high water would be just less than half of that observed for the Moon because the tidal-generating force associated with the Sun is half that of the Moon, as discussed in Section 2.1.1.

Now consider the effect of the Moon and Sun combined. During full or new moon, when the Earth, Moon and Sun are aligned, the equilibrium tidal bulges associated with the Moon and Sun are in phase and combine (Figure 2.1). This leads to so called ‘spring tides’ (Figure 2.1a and Figure 2.2a), with larger than average tidal-ranges. When the Moon is positioned half way between the new and full phases, the two tidal budges are out of phase. This combines to produce so called ‘neap tides’ with smaller than average tidal-ranges (Figure 2.1b and Figure 2.2a).

Tidal patterns are complicated by two important factors. First, the Moon’s orbital plane around the Earth and the Earth’s rotational plane around the Sun are not always over the equator. Second, and the Moon’s orbit around the Earth, and the Earth’s orbit around the Sun, are not circular, they are elliptical. As a result of these two factors we observe diurnal inequality (one tide on each day is larger than the other in semi-diurnal regions), different forms of types (i.e. semi-diurnal, diurnal and mixed) and variations in tidal-range over monthly, annual and longer time-scales (Haigh et al., 2011). These influence the height of tidal levels and strength of tidal currents on daily, fortnightly, monthly, seasonal and inter-annual time-scales and are thus important to understand in relation to tidal energy.

2.1.3 Dynamic theory of tides

The equilibrium theory, discussed in Section 2.1.2, helps to describe several key features of tides (e.g., spring-neap tidal cycles) and serves as a reference system for tidal prediction, via harmonic analysis (see Section 2.1.5). However, tides in reality bear no resemblance to those predicted by equilibrium tidal theory, because none of the three principle assumptions Isaac Newton made in the theory are valid (Pugh and Woodworth, 2014). Thus, this sub-section describes the dynamic theory of tides, including a description of amphidromic systems, tidal resonance, shallow water effects, and the effect of topography on tides. Accounting for these factors contributes significantly to understand the tidal patterns observed around the globe.

In the equilibrium theory, Isaac Newton assumed that: (1) the earth is covered by an ocean of uniform depth with no land masses; (2) the ocean responds immediately to the tide-generating force; and (3) the effects of rotation and friction can be ignored. If these assumptions were valid, the largest tides would be located near to the equator and tidal-range would be smallest at the poles. The theory also suggests that semidiurnal tides would occur near to the equator and diurnal tides near to the poles. This bears no reasonable to real tides. This is because none of the principle assumptions of the equilibrium theory are valid, due to the fact that: (1) landmass on earth prevent the tidal bulges from directly circumnavigating the globe; (2) the rotation of the earth on its polar axis is too rapid for the inertia of the water masses to be overcome in sufficient time to establish an immediate equilibrium tide; and (3) water movements are subject to friction and the effect of the Coriolis force (as a result of the spin of the earth surface) which acts to divert water to the right in northern hemisphere and to the left in the southern hemisphere.

The combination of these three factors causes amphidromic systems to develop. Amphidromic systems are set up in the main ocean basins and on continental shelves and large bays. In the Northern Hemisphere, the tidal crest travels in an anti-clockwise direction around the basin and in the southern hemisphere the wave tracks in a clockwise direction. At the centre of the system, the tidal-range is minimum and increases as you move away from this point. The GC is situated at the interface of two amphidromic systems. In the northeast Pacific, the tidal travels anti-clockwise around an amphidromic point located to the west of the GC. The tidal wave thus travels in northwards up the west coast of the Mexican Coastline. Another amphidromic point is located to the south of the GC, and the tidal wave rotates clockwise around this. Hence the tidal wave propagates southward along the southwest coast of Mexico.

Tidal waves propagate as shallow water waves, because their wave lengths are long. Hence their speed depends on water depth. Tidal waves are reflected at coastal boundaries and where there is a sudden change in water depth. Standing waves can therefore develop when two progressive tidal waves interact. Tidal resonance is also an important factor in many regions. Each ocean basin, or Shelf Sea, or large bay has a natural period of oscillation. Resonance, occurs when the natural period of oscillation is close the main tidal frequencies (e.g., the M_2 tidal constituent has a period of 12.42 hours) which results in higher tidal-ranges. Tidal resonance is most pronounced in regions where a continental shelf is about a quarter wavelength wide. Here the incident tidal wave can be reinforced by reflections between the coast and the shelf edge, producing a much higher tidal-range at the coast. Examples of this effect are found in the Bay of Fundy (Garrett, 1972; Greenberg, 1979; Godin, 1998; McMillian, 2008), the Bristol Channel (Fong and Heaps, 1978; Serhadlıoğluet et al., 2013; Liang et al., 2014; Adcock et al., 2015; Gao and Adcock, 2016), the Patagonian Shelf (Webb, 1976; Clarke and Battisti, 1981; Genco et al., 1994; Glorioso and Flather, 1997) and on the continental shelf of northwest Australia (Chapman, 1938). Tidal resonance is also an important factor within the ocean circulation in the GC. The length of the Gulf makes it almost resonant to the semidiurnal tidal harmonics (Filloux, 1973; Filloux and Lavin, 2003).

Tidal wave lengths are long in the open ocean and their amplitudes are typically small. As tides approach and cross onto the continental shelf, their wave lengths reduce and as a result their amplitudes increase, because the wave energy becomes concentrated in a smaller area. The speed of the tidal wave reduces in shallow water because of the reduction in water depth and the increase in friction between the wave and the seabed. As the tidal wave approaches even shallower water near the coast, it encounters irregular topography of the coastline and moves into estuaries and bays and undergoes larger distortions. This can result in the length of the flood tide being longer than the ebb tide, which can significantly influence tidal currents. Eventually the tidal amplitude will be reduced by bottom friction in very shallow water. The natural period of the GC was reported by Godin (1993) as 14.4, 12.6 and 11.7 hours when using three different methods and bathymetries along the GC.

2.1.4 Spatial variations in tidal levels and currents

As seen from the dynamic tidal theory, described above in Section 2.1.3, tides behave very differently in different regions and hence observed tidal levels and associated tidal currents vary considerably around the world. Understanding this spatial distribution, and identifying where tidal levels and currents are largest, is crucial for tidal energy resource assessments and the planning and design of new schemes. A brief description of how tidal levels and tidal currents vary around the world, and their characteristics, is given here.

Tidal levels are the vertical movement of water caused by the rise and fall of the tide. Tidal levels (Figure 2.2a) include the height of low and high water, and the difference between them, namely tidal-range. The global variation in tidal-range is shown on Figure 2.3. Tidal-ranges are typically smallest in the open ocean, along open ocean coastlines and in almost fully enclosed seas (e.g. Mediterranean). Tidal-ranges are usually largest in semi-enclosed seas and funnel-shaped entrances of bays and estuaries (e.g. the GC, Bristol Channel in the UK, and the Bay of Fundy in Canada). Tidal-ranges are also large in regions where a continental shelf has the right combination of depth and width for tidal resonance to occur (e.g., northwest Australian and Patagonian shelves).

Tidal currents (also known as tidal-stream) are the horizontal movement of water caused by the rise and fall of the tide (Figure 2.2b). Tidal currents are normally expressed in terms of three components, u, v and w, reflecting the eastward, northward and vertical component. Tidal currents can also be quantified in terms of flow speed and direction. Flood tide is the interval period when the water level is rising from low to high tide, whereas ebb tide is the period the tidal level is falling from high to low water. Generally, the larger the tidal-range the larger tidal currents are, so the spatial distribution of tidal currents closely follows that of tidal-range (shown in Figure 2.3). However, tidal currents are strongly influenced by local bathymetry and topography, such as the shape of bays and coastal embayment or headlines. Consequently, tidal currents are often large in straits (e.g., Pentland Firth, Scotland), between islands and at the entrance to estuaries and inlets (Ross, 1995) or around headlines (e.g. Portland Bill, UK). Tidal currents regularly travel parallel to coastline. However, this is often not the case at the mouth of estuaries and bays (Knauss, 1979).

2.1.5 Tidal analysis and prediction

Tidal levels, and therefore tidal currents, are entirely predictable as they are associated with the regular, deterministic, astronomical forces, described in Section 2.1.1. Methods for predicting tidal levels (or currents) have gone from simple approaches that relate high water timing to the phases of the Moon (Pugh and Woodworth, 2014) to more innovative harmonic (Doodson, 1921; Godwin, 1972; Foreman, 1977) and response (Munk and Cartwright, 1966) analysis methods. The most widely used approach is the harmonic analysis method. This is based on the equilibrium tidal theory previously describe in Section 2.1.2. The basis of this approach is that however complex time-series of tidal levels or currents appear, variations at any particular location can by represented by the addition of simple harmonic terms, known as tidal constituents. Therefore, tidal harmonic analysis defines the tidal elevation, z, at a point as:

$$z = \sum_{i-1}^{n} A_i\, f_{i\,\cos(w_i t + V_i - G_i + U_i)} \qquad \text{(EQ. 2.3)}$$

Where n represents the number of constituents, A_i and G_i the amplitude and the phase of the constituent respectively, f_i is the nodal amplitude correction factor and u_i is the nodal phase correction factor, w_i is the angular velocity of the constituent (expressed in ° for tidal notation) , t is the time in fractional hours and V_i represents the equilibrium phase. Each tidal constituent has a fixed frequency which corresponds to the frequency of the astronomic tidal constituent that gives rise to it, and also an amplitude and phase which is unique to a given location. There are at least 400 tidal constituents (Doodson, 1921; Cartwright and Tayler, 1971), but the tidal can often be predicted accuracy using a small subset of these. An example of the main semidiurnal (approximately twice a day) and diurnal (once a day) tidal constituents, are listed in Table 2.1.

2.1.6 Tidal modelling

Finally, tidal hydrodynamic modelling is briefly described here. Tidal models have increasingly been used over the last 50 years, for a variety of applications to improve understanding of tidal characteristics at different locations (Pugh and Woodworth, 2014). Tidal models are particularly useful for mapping tidal energy resources as they can be used to predict tidal levels and tidal currents spatially at every model grid point across a model domain, unlike measurements which record tides at only discrete locations.

In 1969, the first successful attempts at modelling ocean tides globally used hydrodynamic interpolation techniques. These focused on the main semidiurnal M_2 tidal constituent and had horizontally resolutions of 1° (Pekeris and Accad, 1969; Parke and Hendershott, 1980). Schwiderski (1980) set up the first more realistic global ocean tide model which assimilated data from more than 1,700 tide gauges records for the two tidal constituents M_2 and K_1. This had an accuracy of 5 cm in the open ocean. In the late 1980's, the first altimetry datasets from GeoSat were used to establish global tidal datasets which improve the accuracy of the model developed by Schwiderski (1980). Since then, global tidal modelling has continued to improve rapidly with better measurements of tides from TOPEX/Poseidon from 1992 onwards, and follow on missions, and significant advances in computational facilities (Shum et al., 1997).

To date three main types of tidal models have been developed (Wilmes, 2016). The first are empirical models that include analysis of satellite datasets, without the use of hydrodynamic models. Examples of this include the EOT11 (Savcenko and Bosch, 2012) and OSU12 (Fok, 2012) models. The second are hydrodynamic tidal models that assimilate data from tide gauges and/or satellite altimetry datasets. Assimilated tidal models include TPXO (Egbert and Erofeeva, 2002), FES2012 (Carrère et al., 2012) and HAMTIDE (Taguchi et al., 2014). The third type are forward tidal models which compute the tides purely from the hydrodynamic equations. Such unconstrained tidal models include OTIS (Egbert et al., 2004), HIM (Hallberg and Rhines, 1996) and STM-1B (Griffiths and Peltier, 2009). There are now numerous open source and commercial numerical modelling packages capable of simulation tides (Some of which are listed in Table 2.2), including the TELEMAC suite of tools which is utilised in this thesis (see Chapter 3).

2.2 Tidal energy

Having provided a background to tides in Section 2.1, this chapter now moves to tidal energy specifically. This section starts with a basic description of energy and power definitions (Section 2.2.1), and then an overview of tidal-range (Section 2.2.2) and tidal-stream energy (Section 2.2.3) is given. For both types of tidal energy, the different schemes currently being utilised are discussed, then past studies that have carried out energy resources assessments are briefly reviewed and finally the different methods for estimating the available resources are described.

2.2.1 Energy and power definitions

As Neill and Meza (2018) point out, it is important, in the context of renewable energy, that the terms energy and power are used in the correct way. Energy is a complex concept to explain, but essentially it is the ability of a system to perform work. Work is defined as being the energy transferred to or from a body and requires an applied force to move an object a certain distance (Figure 2.4a). Energy, according to the first law of thermodynamics, cannot be destroyed or created, it can only be transformed from one form to another. Power is defined as the rate at which energy is converted from one form to another or transferred from one place to another place. The unit of energy is the Joule (J). A Joule is the work done when a force of 1 Newton (N) is applied over a distance of 1 m. In contrast, power is measured in Watts (W). 1 W is equal to 1 Joule per second (J/s).

For tidal energy we are interested in potential and kinetic energy. Potential energy is the energy stored in an object or fluid as a result of its vertical position (Figure 2.4b). In the case of a fluid, potential energy is determined by the hydrostatic equation given by:

$$P_z = P_A - \rho g(z - \zeta) \text{ (Units Pascal)} \quad \text{(EQ. 2.4)}$$

Where P_z is the hydrostatic pressure at any given point, z is the water depth (m), P_A refers to the atmospheric pressure that is acting on the water column below surface, ρ is water density (kg/m^3) and ζ is the displacement of the water level from the mean reference water level. The negative sign indicates that water depth (z) increases upwards, thus water depth is negative below the mean water surface. Therefore, it can be concluded that pressure increases with depth (Figure 2.5b).

Kinetic energy is the energy that an object or fluid possesses due to its motion and it is dependent on the mass and the change of the velocity of the body (Figure 2.5a). Thus, this energy can be transferable into work once the object or fluid particle has been moved from one point to another (Beer et al., 2018). Therefore, kinetic energy is given by:

$$E = \frac{1}{2}\, m\, V^2 \qquad \text{(Units J)} \qquad \text{(EQ.2.5)}$$

Where m is the mass of the object or fluid particle and V is the velocity. Considering a constant acceleration, the kinetic energy is equal to the work done as $E = W$. The kinetic energy in a fluid in motion is often referred to as mass flow (Mott, 2006) which is defined as the quantity of flow that pass through any given area from one point to another (Figure 2.5a). Mass flow can be expressed by the following equation:

$$m = \rho\, V\, A \qquad \text{(Units Kg/m}^3\text{)} \qquad \text{(EQ. 2.6)}$$

Where ρ is density (kg/m^3), V is the flow velocity (m/s) and A is the area (m^2) where the flow pass from an initial to a final point. By including the mass flow equation into Equation 2.7, energy can be re-written as follow:

$$E = \frac{1}{2}(\,\rho\, V\, A)\, V^2 \qquad \text{(Units J)} \qquad \text{(EQ. 2.7)}$$

2.2.2 Tidal-range energy

Tidal-range power utilizes potential energy from the water-level differences between two bodies of water, within the rise and fall of the tide, through the construction of a tidal barrage or lagoon (Prandle, 1984; Baker, 2006). This section outlines the main operational schemes and devices that are currently utilized, or planned, for tidal-range energy exploitation (Section 2.2.2.1). Then a brief review is given of the most relevant past studies that have undertaken tidal-range resource assessments to date (Section 2.2.2.2). Finally, the main methods for estimating the available tidal-range resources are described (Section 2.2.2.3).

2.2.2.1 Operational schemes and devices

Tidal-range energy has a long history, having been used in local tidal mills for at least the last 800 to 900 years (Rosario et al., 2006). An example of such a mill, is the Eling Tidal Mill in

Totton, Hampshire, UK, which is still operational today. Over the last 60 years, tidal-range power has been utilized in commercial projects in five large-scale schemes. The first commercial tidal-range power plant was the La Rance estuary barrage in France (Figure 2.6a). This became operational in 1966 and generates a maximum power output of 240 MW (approximately 0.480 TWh/year; Aggidis, 2010). Other subsequently installed tidal-range power stations include: (1) the Kislaya Guba Tidal Power Station in Russia (Figure 2.6b) which currently produces 1.5 MW of power (approximately 277 TWh/year; Waters and Aggidis, 2016); (2) the Sihwa Lake Tidal Power Station in South Korea (Figure 2.6c), the world's largest tidal power installation which produces around 254 MW of power (approximately 0.550 TWh/year; Waters and Aggidis, 2016; Bae et al., 2010, Park, 2017); (3) the Jiangxia Tidal Power Station in China (Figure 2.6d), which produces 4.1 MW of power (approximately 7.3 GWh/year; Waters and Aggidis, 2016); and (4) the Annapolis Royal Generating Station in Canada (Figure 2.6e), which produces 20 MW (between 29,200 MWh/year and 36,500 MWh/year; Nova Scotia Power, 2018). These tidal-range power stations became operational in 1966, 1968, 1994, 1985 and 1984, respectively. In the last decade, there has been growing interest in utilising tidal-range power on a much small scale. This includes the well-publicised proposed Swansea Bay scheme (Waters and Aggidis, 2016b). Swansea Bay is discussed in more detail in Section 2.2.2.2.

Within tidal-range schemes, three main types of devices have been developed for harnessing the potential energy arising from the water level differences. These include: (1) one-way turbines which generate energy only on the incoming (flood) or outgoing flow (ebb) tide; (2) two-way turbines which generate energy during both ebb and flood periods (Prandle, 1984); and (3) two-way turbines with pumping (Waters and Aggidis, 2016) (Figure 2.7).

Most tidal-power stations use Kaplan turbines to generate electricity (Figure 2.8). The basis of these were developed more than a hundred years by Austrian engineer Victor Kaplan (Hansson, 1977). Since then, they have only undergone small variations in regards to the original design. There are two main types, unidirectional and bidirectional flow turbines. The unidirectional turbine originally evolved from vertical axis turbine design to become of one of the most used turbines in hydro-electrical power plants. Kaplan turbines are highly compatible with low head tidal-ranges and contain deflected vanes and adjustable blades to direct the flow and optimize the efficiency of the incoming flow. Bulb Kaplan bi-directional flow turbines can work during the full tidal cycle (e.g., twice a day during both flood and ebb periods). These types of turbines can be designed to pump water into the basin. The significantly time reduction during the filling of the basin is attractive as it reduces the holding time where the turbines is not able to generate power due to the low head in the basin.

2.2.2.2 Past studies of tidal-range energy resource assessment

Numerous past studies have assessed tidal-range power, for different locations around the world, and these are briefly reviewed here. A comprehensive list of these studies is given in Table 2.3, along with information on the location, tidal-range, methodology utilized to assess the site and available power estimates. From Table 2.3 it can be seen that numerous studies have been undertaken in the last 40 years for 12 countries: UK, Spain, France, Australia, Mexico, Iran, Taiwan, Brazil, China, Bangladesh, India and Korea. The locations identified are mostly situated within bays (i.e., Bay of Fundy in Canada, Bay of Cadiz in Spain), estuaries (i.e., Severn Estuary, Mersey Estuary in the UK, Bacanga Estuary in Brazil), archipelagos (i.e., Matsu archipelago in Taiwan), semi-enclosed seas (i.e., GC, Mexico; Persian Gulf, Iran) and in channels or large tidal rivers (i.e., the Rance River in France, Bristol Channel in the UK). Typically, the tidal-range at these locations exceeds 4 m while the available power that potentially could be utilized varies from 2.3 TWh/year up 16.8 TWh/year. These assessments also highlighted the potential for tidal-range energy that could be harnessed using a variety of methodologies. They were carried out utilizing a range of theoretical, technical and practical methodologies using global and regional numerical models to estimate the available power in those regions. Ocean circulation and the hydrodynamics of the study area played an important role in assessing the site and observations were used to validate the models to ensure they accurately reproduced tidal levels across the study area. A key characteristic at many of the sites is tidal resonance. Detailed studies of resonant behaviour were carried for the Bay of the Bay Fundy in Canada (Garret, 1972; Greenberg 1979; Godin, 1998; McMillian, 2008), the GC in Mexico (Filloux, 1973; Lavin and Marinone, 2003) and the Bristol Channel in the UK (Fong and Heaps, 1978; Serhadlıoğlu et al., 2013; Liang et al., 2014; Adcock et al., 2015; Gao and Adcock, 2016).

An important consideration is how much tidal amplitudes might change in the direct area and vicinity as a result of a tidal power scheme construction. Several studies have reported tidal amplitude changes for many counties, such as Canada (Bay of Fundy Tidal Power Review Board, 1977; Greenberg, et al., 1979; Sucsy et al., 1993) and the UK (Howards et al., 2007; Watson and Shaw, 2007; Falconer et al., 2009; Burrows et al., 2009a 2009b; Xia et al., 2010, 2012; Fairley et al., 2014). In the Minas passage in the upper Bay of Fundy in Canada, a study by McMillan et al. (2008) states that power extraction projects would increase the amplitude of the tide by 15 % along the coast of Maine and Massachusetts while the tidal amplitudes would decrease 30 % within the Minas Basin. Cornett et al. (2011) reported a variety of tidal-range changes within the Gulf of Maine which can have significant impacts as a result of building a tidal lagoon scheme. Following this, Cornett el al. (2013) found a potential tide increase of 1.4 cm in the Boston Bay and increasing the embankment area of the lagoon tide would increase the tide by 7.2 cm. Similarly, a study conducted by Sucsy et al. (1993) analyses the tidal-range changes causes for the M_2 tidal constituents assuming a large barrier in the Gulf of Maine. This study concluded that tidal amplitudes in the Gulf of Maine would change by up to 50 cm by the presence of a tidal barrage, similar to findings from a previous study undertaken by Greenberg et al. (1979). The Severn Estuary within Bristol Channel in the UK has also been the focus of previous studies. Hydrodynamic changes in tidal currents, tidal levels and discharges were investigated by Falconer et al. (2009). They identified reductions in tidal currents of up to 0.6 m/s while the water levels were predicted to slightly decrease by around 0.2 to 0.5 m as a result of the construction of a barrage within the outer Bristol Channel. Another assessment of the Bristol Channel by Burrows et al. (2009b) found significant reductions in the M_2 tidal constituents of up to 80 cm in the Severn estuary and the S_2 changed by up to 21 cm in the Dee Estuary. Therefore, all these studies make a major contribution to research on tidal-range energy hydrodynamic changes by demonstrating significant impacts of tidal-range variations as a results of tidal barrage projects.

Having accurate bathymetries is crucial when using numerical models for assessing tidal energy. A few studies have undertaken sensitivity tests using different bathymetry products. For instance, Burrows et al. (2009c) used two different bathymetry data sets. As a result, the annual energy estimated in Morecambe Bay increased from 5.83 TWh when the model utilized DoEn bathymetric sources to 6.45 TWh when data from the BODC was used.

One of the countries which host a number of promising locations for tidal-range energy power is the UK. This is because several stretches of coastline around the UK have high tidal-ranges. The region for which most investigations have been undertaken is the Bristol Channel. Initial estimates of the potential tidal-range energy resource in the Bristol Channel were carried out in 1974 and 1988 by the Severn Barrage Committee (1981) and Severn Tidal power group (1989). Later, Binnie and Partners (1989) estimated an installed capacity of around 331 to 342 MW with an annual energy of 629 to 625 GWh utilizing a high number of turbines (92 and 98 deployed turbines respectively). In 2007, the Severn Barrage group estimated a maximum output generation around 17 TWh/year. This assessment originally proposed a partial block of the estuary through a 10 miles long barrage constructed at Lavernock Point west of Cardiff to near Brean Down (known as Cardiff-Weston). Following this study, the Sustainable development commission in 2007 reported similar power generation of 17 TWh/year utilizing a barrage length of 16.1 km at Cardiff-Weston. Alternatively, the construction of a second barrage was suggested for a power plant with an additional 4.1 km of embankment area using a shoots barrage at the upper Bristol Channel which could produce 2.75 TWh/year. In 2010, the Department of Energy and Climate Change (DECC, 2010b) highlighted several sites within the Severn Estuary with a total resource around 28.3 TWh/year. The main differences between Severn Group and DECC studies is the use of a variety of schemes utilized by DECC which pre-selected potential embankment areas of different locations such as Cardiff Weston Barrage, Shoot Barrage, Beachley Barrage, Welsh grounds Lagoon and Bridgwater Bay Lagoon, resulting in higher annual energy yield estimates within the Severn Estuary and Bristol Channel.

An important location in the UK with large tidal-ranges (10.5 m) is Swansea Bay located in south Wales (Parsons Brinckerhoff Ltd, 2010). As a result of the environmental impacts with the construction of the Cardiff-Weston barrage, an alternatively way of power plant construction was suggested by Friends of Earth Cymru (2004). This proposal consisted of the construction of 5 km^2 lagoon in Swansea Bay that can produce around 0.187 TWh/year. More recently however, a study by Petley and Aggidis (2016) presented four different operational modes where the annual energy was estimated at approximately 479, 596, 726, and 731 GWh/year. Furthermore, Waters and Aggidis (2016b) calculate the rated output for the Swansea lagoon project as 320 MW using a theoretical methodology describe in Section 2.2.2.3. Also, the authors highlighted four potential sites at Cardiff which could generate an output rate between 1800 to 2000 MW (Tidal Lagoon Cardiff, 2014).

In the early 1970’s, several studies quantified the tidal-range energy resource for the Bay of Fundy, Canada, which hosts the largest tidal-range on earth (Bay of Fundy Tidal Power Review Board, 1977). Subsequently, several energy resource assessments have been undertaken in the last 4 decades. McMillian et al. (2006) and Delta Marine consultants (2007) conducted an initial practical estimation by adding turbines into a numerical model where the resource indicated that the extractable feasible power exceed 16 MW. A more recent assessment by Cornett et al. (2013), indicate that the annual energy extraction would be 220 MW to 480 MW.

In Asia, recently investigations have been conducted in several countries to assess the feasibility of tidal-range energy. In Bangladesh, a theoretical monthly resource of tidal-range energy in the Bay of Bengal in Bangladesh was undertaken by Sikder et al. (2014). Their initial assessment suggested five potential sites for tidal-range energy extraction. The most suitable site was located in the Satalkhal River where the power was estimated to be up to 14.74 MW using a two way generation operational scheme (ebb-flood) and a maximum tidal-range of over 7 m. Hashemi et al. (2017) estimated the available extractable tidal-range energy in the Persian Gulf in the Khowr-e Musa Estuary where the tidal-range during spring tide is around 5 m. The maximum power was estimated during a mean spring tidal cycle to range from 150 MWh with a barrage of 870 m to 535.98 MWh when utilizing a longer barrage of 1100 m length. A study by Jia-Shiuan and Chen (2014) from the northwest of Taiwan indicated a potential estimated annual power of 38.6 GW/h a year utilizing a vertical axis turbine. Following by the construction of a tidal power plant in 1997, there has been more recently 2 studies related to tidal-range energy within this region in Korea at the Yellow Sea. Shi et al. (2011) estimated that the theoretical power for tidal-range energy scheme on the Chinese coast could equate to 21.8 GW and an annual energy of 0.624 GW/h a year. Furthermore, Park (2017) quantified the theoretical maximum tidal power in the Yellow Sea utilizing a non-free flow computational barrage. The maximum power estimation for this new technology (DTP, Dynamic Tidal Power) was 23,383 MW and 61 TWh/year equivalent to 12 % of the electricity demand in Korea in 2014.

Several energy resource assessments have been undertaken recently for Latin America. An initial assessment of marine energy in Colombia was undertaken by Osorio et al. (2016). Tidal-range energy at the Colombian Pacific coast at Buenaventura Bay was initially estimated to be between 100 W/m^2 and 250 W/m^2 on the ebb and flood tide, respectively, with a maximum power supply of 8.1 MW. However, significant challenges and constraints were identified with regards to the grid connectivity and the initial cost of the project, therefore this initial proposed project was dismissed. Another country interested in utilizing tidal energy is Brazil. Although 80 % of electricity demand of Brazil is supplied via renewable sources, there is interest in utilizing marine energy along the Atlantic coast. A theoretical tidal-range power assessment was undertaken by Ferreira et al. (2009). Results indicated that the power output at the Bacanga Estuary in Brazil ranges from 27 to 34 MW. However, the maximum power output in an intermittent 4 hour tidal cycle generation is roughly 3.14 MW. Aisiks and Zyngierman (1984) estimated that tidal-range power could generated around 37 TWh at five potential sites along the Argentina’s Atlantic coast, where the tidal-range is 6 to 7.5 m approximately (Aisiks, 1993). Despite these assessments, no tidal-range energy power plants have been developed in Latin America to date.

Two past studies have undertaken initial tidal-range energy resources assessments for Mexico. Hiriart-Le Bert et al. (2009) assessed the feasibility and potential tidal-range power resources for a tidal barrage situated in the northern most reaches of the GC, which has a large tidal-range. They estimated the annual electricity production to be in the range of 872 to 17,325 GWh/year. Similarly, in the article by Tapia et al. (2013) it is reported that the initial power mainly is at three potential sites in the GC. The maximum available power estimated in San Rafael Bay was 14 MW while the minimum power of 1.3 MW was estimated within the Bay of Soldado. Finally, for the Bay of Santa Maria, the maximum tidal power was estimated to be approximately 2.5 MW. Therefore, this site was considered viable for tidal-range energy generation as it is located nearest to the available grid connector at San Felipe Port. These two studies identified sites suitable for tidal-range energy in the GC, but were very limited in scope. Therefore, it is pertinent to quantify the theoretically available extractable tidal-range energy in the northern part of the GC where the tidal-range is over 5 m (Marinone, 1997).

2.2.2.3 Methodologies to assess tidal-range energy

The past studies that have assessed the potential tidal-range energy resources for different parts of the world (summarised in Table 2.3) have utilized two main approaches. They have either tended to estimate the: (1) theoretical potential energy density (Neill et al., 2018); or (2) the technical power (Xia et al., 2012). These approaches are summarised below.

Theoretical assessment method: In the first method, the theoretical potential energy is estimated from tidal predictions from a numerical model, assuming no disturbance of the flow. Vertical tidal movements contain potential energy that can be transferable into a power. When the incoming flow of the tide is blocked, via the construction of a barrage construction, the potential energy of the basin can be harnessed to generate electricity. The theoretical power density ($P_{density}$ per m^2) utilising the potential energy of the tidal amplitudes is given by:

$$P_{density} = \frac{1}{2} \ Ag\rho h^2 \qquad \text{(Units J)} \qquad \text{(EQ. 2.8)}$$

Where A is the area of the impounded basin (in this case we considered 1 m^2), ρ is the density of sea water (1025 kg/m^3), g is the acceleration due to gravity (9.81 m/s^2), and h (in m) is the head, normally defined as the water level differences between HW (high water) and LW (low water) peaks of a tidal elevation time series. The annual energy yield resource (E_{annual}) can then calculated as follows:

$$E_{annual} = \sum_{i=1}^{n} \left(\frac{1}{2}\rho g A {h_i}^2\right) \quad \text{(Units J)} \qquad \text{(EQ. 2.9)}$$

Where n is the accumulated water transitions from HW to LW, or LW to HW. Moreover, at that specific moment, in theory there is no rotation of the turbines. Therefore, the maximum head or level for full turbine-generation is available when the water achieve its maximum level in the basin.

Following the construction of the tidal-range power plant in La Rance, France many other countries with high tidal-ranges started to assess their potential for tidal-range energy. Early studies by one of the most important countries which holds the second largest tides in the world is the UK. Since the 1970's there have been numerous studies to identify suitable and feasible potential locations to build tidal-range power stations around the UK. The region for which most investigations have been undertaken is the Bristol Channel in the southwest of England/South Wales. In the late 1970's and early 1980's the Severn Barrage committee (1981) published the first tidal-range power which assess several regions with the Bristol Channel Moreover, this report includes the initial theoretical tidal-range power for other UK estuaries such as Mersey Estuary, Morecambe Bay, etc. Furthermore, following these studies, in 1980 eight estuaries in north-west England were identified as a potential for tidal power energy (Baker, 1991). Binnie and Partners (1987) estimated the potential power generation in the Solway Fifth which forms part of the border between England and Scotland. That study included a large number of turbines (180, 92 and 98) with a massive reservoir area of 860 and 44.70 km^2. As a result, the annual energy was theoretically estimated to be as large as 10,050 GWh/year. Nevertheless, as a comparison with similar authors recommendations, there is a highly risk of environmental impacts that need to be taken into account as part of a tidal power extraction project. Friend of the Earth Cymru (2004) presented one of the first studies that highlighted likely potential negative environmental consequences which could affect, for example the migration of birds.

The past decade has seen a rapid development of theoretical studies in the UK. An excellent recent review of the theoretical energy yield assessment that have been undertaken worldwide is provided by Neill et al. (2018). This work evaluates the theoretical annual energy yield worldwide to be approximately 25,880 TWh, mostly distributed in 11 countries in 4 continents.

Furthermore, the authors assumed a minimum acceptable power density of 50 kWh/m^2 from a constant mean tidal-range of 5 m and another consideration is water depths (less than 30 m). Based on a variety of scenarios of maximum threshold of 60 and 84 kWh/m^2 the majority of the resource in the world (54 %) is located in the UK specifically in the northwest within Liverpool Bay, Severn Estuary, Bristol Channel, the Wash and the southeast of England. However, many places around the world were dismissed such as: Spain (Rosario et al., 2006), Bangladesh (Sikder et al., 2014), Taiwan (JIA, et al., 2014); New Zealand (Moore et al., 2014); Persian Gulf (Hashemi et al., 2017); and Mexico (Hiriart-Le Bert et al., 2009). Furthermore, important considerations were suggested by assessing theoretical tidal resources as the non-astronomical effects can contribute negatively to tidal-range.

Technical assessment method: This methodology consists of integrating mathematically, the discharges across the turbines and sluices within a 1D or 2D hydrodynamic model. The commercial turbine technical specifications are taken into account. The discharge of the sluices can be calculated as (Baker, 2006) follows:

$$Q_s = C_d A_s \sqrt{2gH} \qquad \text{(Units m}^3\text{/s)} \qquad \text{(EQ. 2.10)}$$

Where Q_s is the flow discharge in m^3/s which can be obtain by the pre-selected hill turbine chart Q_t, C_d is the sluice discharge coefficient, A_s represent the flow area through a built hydraulic structure, g is the acceleration of the gravity and H is the difference of levels upstream Z_u and downstream Z_d respectively. The discharge coefficient depends upon the kind of structure within the tidal-range power station. Sensitivity tests of several C_d factors where conducted by Xia et al. (2010). Therefore, the discharge factor can be included within the power output as:

$$P_t = \rho g Q_t H \eta_t \qquad \text{(Units W)} \qquad \text{(EQ. 2.11)}$$

Where Q_t is the flow discharge of the turbine in m^3/s and η_t represent the efficiency of the turbine. The relationship between water head, discharge and power output can be seen in Xia et al. (2012) where the authors conclude that instead of using Equation 2.11 to calculate the power output, the power would be calculated once the water level is known. Also, the power is directly proportional to the amplitude magnitude whereas the magnitude of the flow discharge reaches its maximum value where the water level head up, water density, the acceleration of the gravity, flow discharge and the efficiency of the turbine.

The first technical assessment for Europe was carried out by Hammons (1993). The resource was calculated by varying the power over a spring and neap cycle and utilizing a parametric model. The technical available tidal energy resource for Western Europe was estimated to be 105.4 TWh/year. Several studies in 2009 and 2010 assessed the technical resource available around the UK (Burrows et al., 2009a; 2009b; Yates et al., 2010) and the Irish Sea (Burrows et al., 2009c). These studies had differences in the way all the authors approach the resources using a variety of operational schemes, showing some similarities while the applied two different model approach (0D and 2D) and also the scheme operation (ebb, flood, ebb-flood and pumping, previously described in Section 2.2.3.1).

A study was conducted by Falconer et al. (2009) for tidal energy in Severn Estuary with the Severn Barrage and Fleming Lagoon. The methodology suggested inclusion of 216 turbines in the barrage or lagoon project (with sluices) into the domain area with a refined mesh of 40 m. The most important technically relevant finding was the predicted water levels and the power curve during a tidal cycle. These results were schematically well explained in three main stages: (1) filling the basin during 4.5 h; (2) holding the water lever for 2.5 h and; finally, (3) the generation time within the next 5.4 h. The scheme presented in this study predicted an energy output of 24.2 GWh/year during mean spring cycle.

Aggidis et al. (2012) estimated the technical power for the Solway Fifth over a year. This study consist of including a turbine chart specifications developed by turbine manufacturers Andritz Hydro. The results indicated a total energy generation of 9.44 TWh/year utilising 180 turbines of 7 m diameter with a starting head of 2.5 m and a maximum generation per turbine as 25 MW. As a comparison with the figures showed by HM Government (2010) for the Solway where there is a potential annual power of 10.2 TWh/year (no-methodology was in detail reported) there are small differences compared to the study by Aggidis et al (2012). One of the differences between these studies is the flow rate input into the turbine and the barrage modelling conditions.

2.2.3 Tidal-stream energy

Tidal-stream energy exploits the kinetic energy of tidal currents, through the use of a variety of devices that are able to convert the linear velocity of the ocean's currents into a rotational torque (Bahaj, 2011). This section outlines the main types of operational schemes and devices that are currently utilized, or planned, for tidal-stream energy exploitation (Section 2.2.3.1).

Then a brief review is given of the most relevant past studies that have undertaken tidal-stream resource assessments (Section 2.2.3.2). Finally, the main methods that have been used for estimating the available tidal-stream resources at different locations are described (Section 2.2.3.3).

2.2.3.1 Operational schemes and devices

To date, there is only one commercial-scale scheme exploiting tidal-stream energy. This is the Strangford Lough scheme in North Ireland which started being developed in 2008 (Marine energy, 2016). In addition, there are currently three pre-commercial array projects prototype under construction. These are located Northern of Caithness at Pentland Firth and Orkney Waters, Scotland, the Bay of Fundy in Canada and in Brittany, France (Marine Energy 2016; Ocean Energy systems, 2016; Tidal stream projects MeyGen, 2019).

Over the last two decades a wide range of different marine energy devices have been proposed or proto-types developed. Many of the technologies are at different levels of development. Two main categories of marine tidal-stream energy extraction devices have been developed (shown in Figure 2.9): (1) rotating devices or marine current devices; and (2) reciprocating devices (Rourke et al., 2010). Rotational devices use propellers (similar to wind turbines) to extract the kinetic energy of moving water to power turbines (Figure 2.9a). The main differences, from wind turbines, are the flow density and the thrust that each device is capable of tolerating in regular operational conditions. Marine turbine devices could have two or three-blade turbines (with vertical or horizontal axis) regularly installed within a support hub (call it rotor). A gearbox at the back is attached to convert the relatively low flow velocities to high rotation speed. Currently developments require tidal-stream flows >2 m/s (Myers, 2003) and a maximum depth of <80 m (Iyer et al., 2013; Lewis et al., 2015) obtaining a maximum efficiency in ideal conditions of around 48 % (Burton et al., 2001). Currently, gravity, monopile and tripod structures are commonly deployed on the sea bed. These devices are known as ‘first generation turbines’. 'Second-generation structures’ may include floating devices that are normally installed on a mounting platform.

Reciprocal oscillation hydrofoil devices are significantly different. They use the forces generated by pressure gradients as a result of the relative movement of the tidal current around the foil and capture the resultant tangential force that acts on the blade (Figure 2.9b). As a result, the blades of the device creates vertical movements of the blade resulting in pressure on a detached hydraulic reciprocating ram pump. The attached hydraulic piston transfers the potential energy into hydraulic-pressure energy by a hydraulic cylinder in an electrical generator. The hydrofoil can increase or decrease its elevation depending on the attack angle of the device and the tidal stream inflow. The foil design is one of the more promising devices to efficiently utilize tidal stream flow (University of Strathclyde in Glasgow, 2016). They depend upon parameters, such as turbines blades size, attach angle, tidal-stream velocity and the capacity of the hydraulic reciprocating pump.

An important consideration is the design of a scheme array. A number of studies have assessed sites utilizing primarily, a single turbine characterisation with power rates between 1 and 1.2 MW (Bahaj et al., 2007; O'Rourke et al., 2009; Lo Brutto et al., 2016) (see also, www.marineturbines.com, 2018). However, in order to fully utilise the energy at a site, it would be necessary to include multiple turbines in an array (Bahaj 2011; Vennell et al. 2015; Adcock and Draper, 2015). Within an array, a group of turbines the disturb flow dynamics and interact. The array density (number of turbines into the array) depends on the number of deployed turbines in each row lateral and longitudinal along the study area (Bahaj and Myers, 2004; Coles et al., 2017). It is also important to take into account technical constrains, such as, wake interaction between the turbines and the effect of the wakes (Harrison et al., 2008; Myers and Bahaj, 2009; Harrison et al., 2011; Mcintosh et al., 2012; Fallon et al., 2014; Abolghasemi et al., 2016; Lo Brutto et al., 2016), turbulence behind the turbine (Mycek et al., 2014; Blackmore et al., 2011; Blackmore et al., 2013 and 2014a, 2014b), flow reduction along array (Coles et al., 2017; De Dominicis et al., 2018), suitable longitudinal and lateral space and turbine performance (Bahaj 2011; Vennell et al. 2015; Adcock and Draper, 2015; De Dominicis et al., 2017).

2.2.3.2 Review of past studies assessing tidal-stream energy

Numerous past studies have assessed tidal-stream energy, for different locations around the world, and these are briefly reviewed here. A comprehensive list of these studies is given in Table 2.4 along with information regarding the modelling approach taken, the boundary conditions used, and the methodology to assess the available energy resource and the estimates of the available resource. Although there have been many tidal-stream energy assessments worldwide, only a select number of countries have sites that are considered feasible for tidal stream energy extraction. The main reason for this is that the source is highly dependent on current speed (rated power at around 2.3 m/s and cut in speed of 0.7 m/s) (Frankel, 2007), shallow waters (less than 50 m depth) and the accessibility of the grid connector. First generation turbine criteria require peak flow velocities of around 2.5 m/s (Lewis et al., 2015). Current speeds of this magnitude have only been identified for 16 countries around the world (Lewis et al., 2015). Some locations worldwide with current speeds >2.5 m/s are Pentland Firth (Adcock et al., 2013; Draper et al., 2014) and the Channel Islands in the UK (Coles, et al., 2017; Guillou et al., 2018), western Brittany coast of France (Thiebaut and Sentchev, 2017), the Race of Alderney, France (Myers and Bahaj, 2005), Minas Passage (Karsten et al., 2008; Walters et al., 2013) and Johnstone Strait (Sutherland et al., 2007) in Canada.

Since the construction of the first pre-commercial project in 2006 in Northern Ireland at the Strangford Lough, there has been more interest in assessing and exploring potential candidate sites around Northwest Europe (Serhadlıoğlu et al., 2013). Locations around the UK close to coastal headlands have been assessed including for instance: Pentland Firth in Scotland (Easton et al., 2012; Adcock et al., 2013; Martin-Short et al., 2015; Neill et al., 2017). Here tidal current speeds exceed 5 m/s. In 2010, the Crown Estate assigned a leasing project to MeyGen Limited to develop a 398 MW tidal stream project at Pentland Firth and Orkney Waters. Currently this project is the largest planned tidal stream project worldwide and the plan is to install 49 turbines (1.5 MW turbines) with a total energy production of 73.5 MW (Tidal Stream Projects MeyGen, 2019). Another important location in the Northwest of the UK is the Skerries in the Irish Sea (Robins et al., 2014; Serhadlıoğlu et al., 2013). At this location tidal currents reach 4 m/s in shallow water where the depth is between 45 and 55 m. Portland Bill in the Southeast of England also represents a potential site due to its flow velocities which are around 3.2 to 3.6 m/s (Blunden and Bahaj, 2006). Information related to the marine renewable energy in the UK was mapped in the Marine Renewable Atlas in 2008 (www.renewables-atlas.info).

In the Americas a few studies have assessed the most suitable sites for tidal-stream energy extraction. One of the most potentially viable places for tidal-stream extraction is the Bay of Fundy in the Gulf of Maine, because the current-speed velocities here exceed 5 m/s (Karsten et al., 2013). There is an innovative marine energy project management by Offshore Energy Research Association that consist of testing Tidal In-Stream Energy Conversion (TISEC) devices in the Minas Passage in the Bay of Fundy where current estimates from the electrical power research Institute (EPRI) indicate a potential energy resource between 300 KW up to 8000 MW.(OERA, 2018). Additionally, the resource in this area has also been assessed by Karsten et al. (2013) and Cornett et al. (2010) where the theoretical KPD is between 50 and 80 kW/m^2 while the maximum power output by turbine is currently 2000 MW.

In Latin America, Osorio et al. (2016) undertook a tidal-stream energy assessment for Buenaventura Bay in Colombia, and estimated that the KPD for that region was relatively small, in the order of 40 W/m^2, with the maximum current speed 0.7 m/s. Herrera et al. (2010) suggested that there might be locations in Strait of Magellan in southern Chile that may be feasibility for tidal-stream energy extraction, with an estimated KPD exceeding 10 kW/m^2. González-Gorbeña et al. (2015) carried out a tidal-stream energy assessment for San Marcos Bay in Brazil and estimate the resource to be between 9.2 and 11.2 MWh/m^2. Another assessment undertaken in the same country by Marta-Almeida et al. (2017) indicated that the potential KPD available at Baiá de Todos os Santos is between 1.3 and 2.5 kW/m^2, with maximum peak tidal flow velocities of 1 m/s. Alonso et al. (2017) assessed the potential tidal-stream energy resource between La Paloma and Cabo Polonio on the Atlantic coast of Uruguay, and estimated a KPD of 0.06 kW/m^2.

No assessment of tidal-stream energy has been undertaken for Mexico, despite the fact that peak spring tidal flows of over 1.5 m/s have been measured between the Midriff Islands in the GC (Badan-Dangon et al., 1991; Lopez et al., 2008) (Figure. 1.1a). Therefore, this region holds some promise for tidal-stream energy extraction, and hence is the focus of this study. In contrast to other regions in which the tidal stream energy resource has been explored, the GC is relatively deep, and diurnal tidal constituents are typically larger; hence the resource characterisation is expected to contrast considerably from previously identified tidal stream sites.

2.2.3.3 Methodologies to assess tidal-stream energy

In the last few decades, five main methods have been used to estimate the tidal stream-energy resource, at different locations (Hagerman et al., 2006). These methods are: (1) the theoretical undisturbed kinetic energy method; (2) the 1D theoretical model for an open channel; (3) the technical energy method which includes the power coefficient of the turbines efficiency within the power equation; (4) the practical method that include the disturbed drag coefficient within the computational simulations; and (5) the experimental farm method which involves testing turbines in a tank or flume. These methods are described below.

The theoretical undisturbed kinetic energy method: The theoretical kinetic energy method has been applied in several studies (i.e. Myers and Bahaj, 2005; Hagerman et al., 2006; Blunden and Bahaj, 2007; O'Rourke et al., 2010) and is based on estimating the undisturbed kinetic energy flow. It assumes there are no interactions of the devices with the flow. This method was originally developed to estimate the energy resource for horizontal-axis wind turbines (Burton et al., 2001). The theoretical kinetic energy method depends on the cube of the current speed. Thus, the theoretical power (P) can be obtained by:

$$P = \frac{1}{2}\rho \int (U^3 dA) \qquad \text{(Units W/m}^2\text{)} \qquad \text{(EQ. 2.12)}$$

Where ρ is the water density (kg/m^3), A is the cross-sectional area (m^2) of the flow passing for the rotor (m^2) and U is the flow velocity (m/s). The flow velocity is normally estimated from a numerical model.

The first theoretical approaches were conducted in the UK by Fraenkel (1979), utilizing a simple form of the kinetic energy flux equation (EQ. 2.12) while Wyman and Peachey (1979) used Admiralty navigation data to obtain the initial figures of the tidal-stream energy resource within UK waters (Blunden and Bahaj, 2007). An important review utilizing navigational charts was conducted by the Energy Technology Support Unit (1989). This consisted of identifying places with mean spring current speed greater than 2 m/s in the UK and water depths >20 m (ETSU, 1993; European commission, 1996). These studies were purely theoretical and they were limited by the lack of information and appropriate techniques to analyse more realistic flow conditions. More recent studies of theoretical assessment in the UK were conducted by Black and Veatch (2004, 2005). The main contribution from these works was to include a “Significant Factor Impact” which is an estimate of the proportion of the energy flow that can be viably extractable without any environmental impact, considering the array configuration previously proposed by ETSU (1993) and the European Commission (1996). Bahaj and Myers (2004) utilized Admiralty chart data and the array configuration method. An understanding about the theoretical methodology was reported by Hagerman et al. (2006). This paper begins with a brief explanation about the main concepts of tidal-stream theoretical assessments such as power density as a function of current speed, cut-in velocity and rated speed to name a few. The aim of this paper was to assess the west and east coast of USA by collecting observations data for tidal levels and currents within channels, rivers and bays. Also, the paper highlighted the use of programs to predict the current (i.e. WXTide32). Tarbotton and Larson (2006) and Cornett (2006) investigate the KPD on the west and east coasts of Canada. Due to the complexity of the western coast of Canada, in the British Columbia Province, an innovative new analytical method was proposed to assess the theoretical power across a narrow channel (see below). More recently, numerous studies have carried out theoretical energy assessments (e.g. González-Caballin et al., 2016; Wang and Yang, 2017;

Alonso et al., 2017; Marta-Almeida et al., 2017; Thiebaut and Sentchev, 2017; Campbell et al., 2017; Guillou et al., 2018; Mejia-Olivares et al., 2018; Hazim et al., 2019). In these studies, a variety of new methods have been proposed to assess the tidal-stream resource. For example, Blunden and Bahaj (2006) developed a method that combined the theoretical assessment with a drag coefficient approach, as discussed later.

One-dimensional theoretical model for an open channel: This method takes into account the cross sectional area of the channel as well as the number of turbines that can be deployed and the amplitude of the tide within the channel. A one dimensional analytical model was proposed by Triton Consultants (2002) and Bryden et al. (2004) to estimate the potential tidal-stream energy resource in channels in Canada. The Canadian southwestern coast, hosts several channels and straits (i.e. Strait of Georgia, Juan de Fuca strait, Johnstone strait) between Vancouver Islands, Queen Charlotte Islands and the mainland of the British Columbia province. Triton Consultants (2002) estimated the maximum power in a natural channel using the following equation:

$$P_{average} = \gamma \rho g a Q_{max} \qquad \text{(Units W)} \qquad \text{(EQ. 2.13)}$$

Where γ is the coefficient depending upon the balance of force by friction or acceleration in the natural regime apart from including turbine drag, ρ is the sea water density, a is the sinusoidal height amplitude difference to the ends of the channel (within 10 %), which varies from 0.20 and 0.24, g is the gravitational acceleration and $Q_{\max}$ is the maximum peak flood volume in natural tidal regime (Figure 2.10). This expression is derived from an initial momentum equation. An initial estimation stated that only 10 % of the maximum power can be harnessed. However, many considerations have to be taken into account for different sites around the world. For instance, if a tidal fence occupied all of the cross-sectional area, each turbine would have its own frictional effects. Another assumption is that the channel is constricted (narrow) and there is no flow modifications along both sides of the channel (entrance and at the end). In addition, it was assumed that the current is fully independent of the cross-sectional position, for example, when there is vertical shear though the channel. Consequently, it would be necessary to amend the average current speed

The results from Triton Consultants (2002, 2006) indicated a potential power extraction of 600 MW at Discovery Passage and Johnstone Strait. However, there is a potential tidal regime reduction of 10 % within Discovery Passage. Bryden et al. (2007) investigated the flow alterations using a theoretical model of a simple channel and applied this to the Pentland Firth and Yell Sound. This model took into account the hypothetical scenarios of channel dimensions. Subsequently, they combined the conservation of momentum and conservation of mass equations to obtain an alternative power equation which utilized as input parameters the volumetric flow rate, wetted perimeter of the turbine (percentage volume that cover the turbine), channel dimensions and flow depth. As a result of applying this equation, which estimates the available power in a channel, extracting only 10 % of the available kinetic energy flux, the undisturbed flow reduces by 3 % while 20 % of power extraction results in 6 % flow speed reduction. The authors conclude that the simple model had certain limitation as a result of the hydrodynamic interaction of the flow in 2D and 3D flows. Bryden and Couch (2006) carried out further analysis between the ambient flow and the energy extraction where the head heights and flow speed were compared against the flow rate. They found that the amplitude of the tide decreases across the channel as well as the flow speed of around 5.8 % as a result of the energy extraction.

Garrett and Cummins (2004 and 2005) proposed a one dimensional analytical model that would applicable within a channel. This method is regularly used to determine the maximum average power that would be potentially extractable varying the cross-sectional area of the channel, number of turbines, amplitude of the tide and frequency. As a result of this model a power equation is derived (EQ. 2.13). This equation was proposed under the consideration of neglecting the natural friction factor of the channel. Moreover, this equation takes into account the drag coefficient of the turbine which is linearly proportional to the volumetric flow rate.

This methodology was utilized by Tarbotton and Larson (2006) assess the potential energy between Strait of Georgia and Johnstone Strait in Canada where the tidal currents exceed 5 m/s. The mean power within the British Columbia province where these channels are located was estimated up to 4 GW. Following this study, a theoretical approach was carried out at the same region by Sutherland et al. (2007) utilizing a 2D model and increasing the drag coefficient γ given in EQ. 2.13. The authors compared the power potential using two method applied in different regions as Discovery Passage, Cordero Channels, and northwest Johnstone strait. The power potential was estimated though the hydrodynamic model as 886 MW while there is a slightly reduction in the power rate as 826 MW using an analytical one dimensional model. One important key finding of this work was that the currents reduce significantly in all study cases as a result of the drag coefficient. While increasing the drag coefficient within the power equation, the currents speed reduce significantly as 57 % to 59 %.

Subsequently to the work of Garret and Cummins (2008) the model was extended based on utilizing different shapes and physical characteristics of the channels and also including partial fences within the channel in order to obtain more realistic scenarios due to the presence of a turbine in the undisturbed flow. The main contribution for this work was related to the drag factor exerted on the turbines which can be affected by the power extraction and reduce the flow in the channel. Furthermore, there is not currently a method which determines hydrodynamic changes of the channel.

Technical energy method: This method consists of including the efficiency of the turbine characteristics, through the power coefficient, into the power equation theoretical power (EQ. 2.12). The power coefficient factor includes mechanical loses with regards to the turbine design for example the loss because of the gearbox and bearing generator efficiency. Furthermore, this value depends upon the turbine type and no turbine can operate at the maximum power coefficient usually provided by the designers of the turbines. Thus, the German physicist Albert Betz established that the maximum kinetic energy that a wind turbine can convert to work is 16/27 (59.3 %) and therefore the maximum power coefficient is $C_{P\max} = 0.59$ (dimensionless). A list of power coefficients used by previous studies is given in Table 2.5 and ranges between 0.35 and 0.45. Therefore, including this factor into EQ. 2.12 the technical power can be defined as:

$$P = \frac{1}{2}\rho A\, V^3\, Cp \qquad \text{(Units W)} \qquad \text{(EQ. 2.14)}$$

An example of the technical resource approach was carried out by EPRI (2006) for the west and east coasts of USA. They estimated the annual energy output considering turbine arrays in different regions, utilizing existing prototype designs which include turbine efficient factors (power coefficient Cp) to determine the optimal lateral and longitudinal space within the array. They also included electricity cost analysis including the total investment for a tidal-stream power plant project. They therefore identified only two potential sites in the western USA (Knik Arm in Alaska and Golden Gate in California) and one likely site in eastern USA (Western Passage on Maine).

Practical method: This method consists of incorporating certain practical constraints relating to features of the study area, such as: water depth, flow speed limitations, shipping routes, current commercial designs, flow reduction along the array configuration and grid connectivity. Furthermore, the practical method consists of the use of a variety of parameters based on a real turbine design, for instance a turbine power curve from a commercial device, cut-in speed (which is the minimum velocity that the turbine needs to start rotating), power rate and maximum available power (Lewis et al., 2015; Thiébaut and Sentchev, 2017; Campbell, et al., 2017). Another parameter is the flow reduction along the array configuration that needs to be considered due to potential hydrodynamic changes in the study area. Finally, this methodology considers the estimation of the cost of electricity production and reliability of the project as well as the technical feasibility, maintenance, proximity to the grid connection and operational constraints (Boyle, 2004).

O'Rourke et al. (2010) estimated and compared the tidal energy resource in Ireland using the three approaches above (theoretical, technical and practical) using results from a 2D barotropic model. The theoretical resource was estimated to be 230 TWh/year under the assumption of a 10-20m turbine diameter while the technical and practical resource were calculated as 10.46 TWh/year and 2.633 TWh/year, respectively. The main differences with these methods is that the theoretical method takes into account all the study area where velocities may vary below 1.5 m/s, while the technical and practical method consider the power coefficient of 0.5 and constraints related to water depths (depth areas between 20m and 40m) and peak flow velocities greater than 2.0 m/s, respectively.

Disturbed drag coefficient method: This method aims to characterise the turbine array setting within the hydrodynamic model by increasing the natural bottom coefficient factor. The thrust coefficient (drag) produced by the turbine within the power equation be given by:

$$P_e = \frac{1}{2}\, C_d\, \rho \eta A\, V^3 \qquad \text{(Units W)} \qquad \text{(EQ. 2.15)}$$

Where $C_d = K_0 + K_t$ (dimensionless) is the quadratic bottom coefficient, K_0 is the natural bottom coefficient, while K_t is the thrust coefficient associated with the included turbine. K_t (thrust coefficient) is obtained as a result of the measurements of axial force and torque in a turbine hub. For marine current turbines the thrust coefficient were initially measured in a towing tank by Bahaj et al. (2007) and used into hydrodynamic simulations by Sutherland et al. (2007). K_t can be written as a function of wake velocity coefficient, FR (Froude number) and B (blockage ratio) as defined by Adcock et al. (2013). The bottom coefficient is distributed and apply uniformly along the area covered by the turbine at the bottom of the seabed over the region with the highest flow speed. The drag coefficient is set up within the momentum equation, similar to the natural bottom friction coefficient. The natural drag coefficient can be expressed within the governed equations as:

$$\tau_x = \rho\, C_d u \sqrt{u^2 + v^2} \qquad \text{(Units N/m}^2\text{)} \qquad \text{(EQ. 2.16)}$$

$$\tau_y = \quad \rho \, C_d v \sqrt{u^2 + v^2} \qquad \text{(Units N/m}^2\text{)} \quad \text{(EQ. 2.17)}$$

Where τ_x and τ_y are the bed stress in both Cartesian components, ρ water density in kg/m^3, u and v are the horizontal components m/s (eastward and northward respectively) and C_d is the natural drag coefficient.

The first study of this nature was by Blunden and Bahaj (2006), and this was followed by the study of Sutherland et al. (2007). Later, Serhadlıoğlu et al. (2013) and Adcock et al. (2013) included turbines arrays into their computational simulations and estimated the available power in the Pentland Firth in Scotland. A clear example of to how apply the drag coefficient factor within a 2D hydrodynamic computational model (RICOM) is fully explained by Plew and Stevens (2013) and Coles et al. (2017). These method can be utilized with a 2D (in shallow waters) or 3D hydrodynamic model. Goward-Brown et al. (2017) indicated, for the Pentland Firth, that the drag coefficient in a 3D model can be also applied at the sea bed similarly to a 2D hydrodynamic model. The authors configure the array and applied a drag coefficient value of 0.0025 (dimensionless) within an idealized channel area of 30 length and 20 km width where the flow exceeded 2 m/s. In the case of the 3D model, the turbine size was applied in the middle of the top third of the channel in order to allow the turbine free clearance from top and bottom; while in the case of a 2D model the diameter of the turbine is selected based on the water depth, thus, the diameter is as big as the water column, this consideration can be utilized using a 2D model within shallow waters regions (<60 m depth). In addition, this method was validated through an experimental validation of the drag method and the characterisation of the array density (number of turbines set up in a cover region) in a regional scale models have been recently undertaken by Coles et al. (2016). Finally, as a result of the use of this methodology, several authors have pointed out that increasing the drag coefficient (see Table 2.6 for references) would have significant impacts within the study area such as flow reduction, hydrodynamic changes in tides and currents (McMillan et al., 2008; Plew and Stevens, 2013; Adcock et al., 2013; Karsten et al., 2013; Coles et al., 2017; Goward-Brown et al., 2017).

Experimental farm method: This method involves the testing of small scale-turbines in a water tank or flume. Bahaj and Myers (2004) assessed marine turbine small-prototypes under control conditions. The results of that study suggested that the turbines in an array configuration should be separated by 10 to 15 times the diameter of the turbine (Figure 2.11). Moreover, the swept area of the turbine allocated in an array depends upon three parameters: (1) the depth of the site, which should be 0.25 H (Figure 2.12), where H is the total height above the sea bed ;

(2) the lateral spacing which need to be 12 % of the blockage ratio used in CWC trials; and (3) minimum lateral space between turbines that would to be at less 200 m, while the longitudinal spacing between rows of turbines would be 500 m (Myers and Bahaj, 2005).

Since the first “farm method” was proposed by Myers and Bahaj (2005), this methodology was transferable to hydrodynamic modelling approaches (Walkington and Burrows 2009). As a result, there have been numerous studies utilising the farm method when setting up turbine arrays in hydrodynamic modelling (Bai et al., 2009; Ahmadian et al., 2012; Ahmadian and Falconer, 2012; Neill et al., 2012; Fallon et al., 2014; Adcock and Draper, 2015; Coles et al., 2017; De Dominicis et al., 2017; Coles et al., 2018; De Dominicis et al., 2018). Furthermore, this method has been used to simulate the turbine arrays within Computational Fluid Dynamic (CFD) software (Harrison, et al., 2009) to represent the interaction between the turbine arrays setting up the array density within an undisturbed flow. Alternatively the farm method was utilised through the linear momentum actuator disc theory (LMTD) where the turbine is characterised using a rotor disc within the cross sectional area flow (Houlsby et al., 2008). This representation of the turbine through the actuator disc has been used to measure a variety of parameters related to the turbine performance (Bahaj et al., 2007; Houlsby et al., 2008; Batten et al., 2008; Harrison et al., 2011; Mcintosh et al., 2012; Batten et al., 2013; Blackmore et al., 2014b); thrust coefficient, velocity profile downstream, turbulence (Mycek et al., 2014; Blackmore et al., 2011; Blackmore et al., 2013 and 2014) and wakes turbine effects (Harrison et al., 2008; Myers and Bahaj, 2009; Maganga et al., 2010; Harrison et al., 2011; Mcintosh et al., 2012; Fallon et al., 2014).

To understand more realistically the main parameters that would affected the downstream flow interaction around the horizontal marine current turbine, an experimental method was characterized utilising a rotor disk tested within a flow rate control flume. This method involved submerging a small scale rotor disk within a flume. The porosity of the disk could be varied to replicate the thrust force (ratio of open to closed area) as well as the distance device along the flume. The actuator disk theory was proposed by Burton et al. (2001) for wind turbines. Later, experimental testing for marine energy turbine applications was conducted by Myers et al. (2008a, 2008b). They examined the lateral and longitudinal space between devices in a turbine array configuration. Furthermore, Myers et al. (2010) carried out more detailed laboratory tests utilising the rotor disk method. The aim was to analyse the turbulence ambient flow, velocity profiles close to the seabed, wake interaction along an array, flow reduction (that passed around the rotor) and performance of the turbine. One of the advantages of this method is the more realistically representation of the ambient flow (in controlled flow conditions) as well as the contribution of wake interaction along the array, thrust coefficient of the turbine and the application of the artificial bed roughness which determine the flow reduction along the array.

2.3 Overview of study site

This section provides a background to the study site, the GC. First a general overview of the site is given (Section 2.3.1) and then the tidal conditions are described (Section 2.3.2). A discussion of the oceanography characteristics and meteorological aspects of the region follows (Section 2.3.3). A brief summary is given in Section 2.4, highlighting key knowledge gaps in relation to the thesis objectives.

2.3.1 General characteristics

The GC is a semi-enclosed basin located to the northwest of Mexico City (Figure 1.4a). It is approximately 1,100 km long and around 45 to 240 km wide and encompasses more than 800 islands. The GC is divided into three main parts: (1) the southern part (the entrance of the Gulf); the central part (normally known as Midriff area or Archipelago); and (3) the northern upper region of the Gulf. Its average depth varies from around 200 m in the upper Gulf to 3,600 m at its entrance with the Pacific Ocean (Figure 1.4a). It also contains several deep basins, such as Tiburon, Delfin and Wagner basin (Figure 1.4b) which are on average approximately 400, 800 and 200 m deep, respectively. The Midriff region contains some important islands, such as Smith, Salsipuedes, San Lorenzo, and San Esteban Islands. The biggest of the Gulf islands is Angel de la Guarda and Tiburon. These islands form channels between them, such as Ballenas channel which is located between the Baja California peninsula and Angel de la Garda Island and is about 14 km wide and ~800 m deep. There is also a channel between the San Lorenzo and San Esteban Islands which is approximately 18 km wide and ~500 m deep. Tidal currents are faster in these channels. The northern GC has relatively shallow waters with depths ranging from 20 to 200 m depth (Figure 1.4b) within the norther GC. The tidal-range is large in this area at around 5 m (Marinone, 2003). The areas of most interest to this study are: (1) the northern GC as this is the area with the biggest potential for tidal-range energy exploitation given the tidal-range here is over 5 m; and (2) the region around the Midriff Islands in the central region, as a previous study indicates that currents in this region exceed 1.5 m/s (Badan-Dagon et al., 1991) and hence there is potential for tidal-stream energy exploitation.

2.3.2 Tidal conditions

Understanding and mapping of tides in the GC is fundamental in this study. This section therefore briefly describes the characteristic of tides in the GC. The Pacific Ocean plays an important role in the generation of tides in the GC which are mainly generated by co-oscillation with low frequencies of tides (Beier, 1997; Ripa, 1997). The dominant tidal constituent in the GC are the M_2, S_2, K_1 and O_1 constituents (Argote et al., 1995; Marinone 2003; Lavin and Marinone 2003). Figure 2.13 shows the 3 main semidiurnal and main diurnal tidal constituents. The M_2 constituent is around 0.5 m at the entrance of the GC and increases to 2.3 m in the northern regions (Figure 2.13a), while the S_2 constituent increases from south to north from 0.2 m to 0.8 m (Figure 2.13b). The diurnal tidal constituents have lower amplitudes (Figure 2.13 d, e and f) and range from 0.05 m to 0.6 m. The amplification of the semidiurnal components occurs as the GC is nearly resonant within the principal semidiurnal component, similar to the Bristol Channel in the UK (Fong and Heaps, 1978; Serhadlıoğlu et al., 2013; Liang et al., 2014; Adcock et al., 2015; Gao and Adcock, 2016). The tides in the GC are mixed mainly semidiurnal in the southern and northern GC and are mixed mainly diurnal in the Central GC (Figure 2.14b).

2.3.3 Meteorological and oceanographic characteristics

Tidal levels and tidal currents in the GC are influenced by other meteorological and oceanography processes such as wind forcing, stratification, water mass exchange, heat exchange and internal waves. Each of these processes is briefly described below.

Wind plays an important role in influencing stratification and currents within the GC. Wind patterns over the GC are strongly influenced by the mountain ranges either side of the Gulf. In winter, autumn and spring the dominant wind directions are from the northwest and wind speeds range from 8 to 12 m/s. In summer the dominant wind direction is from the south and wind speed is $\leq$5 m/s (Roden, 1964; Merrifield and Winant, 1989). Pares et al. (2003) suggested that wind has a limited influence in summer on the northern GC. In contrast, summer reversals may occur for short periods, or even a few days, over the southern GC.

Stratification can strongly influence tidal currents in the GC. The strongest stratification is located near to the bottom of the northern sills of the GC, in the vicinity of the San Lorenzo, San Esteban and Ballenas channel due to the high sea surface temperatures and warm upper layer (Lopez et al., 2006, 2008). The northern GC's circulation is similar to an estuary and therefore depends on two main flows: (1) the incoming flow of cold and salty water from the bottom (2) the outgoing fresh water at the surface. Furthermore, large tidal currents in San Esteban Basin reach more than 1.0 m/s, contributing significantly to tidal mixing that pumps nutrients to euphotic zones (where sufficient sunlight is present for photosynthesis), especially in the GC which has high levels of nutrient productivity (Lavin and Organista, 1988; Alvarez-Borrego and Lara-Lara, 1991).

Sea surface temperature is one of the most important factors that determine heat exchange between the ocean and atmosphere. In addition, sea surface temperature conditions in the GC are unique due to the combinations of high temperatures and nutrients. Consequently, there is a hugely variety of sea life and local biodiversity as a result of the stratification. Therefore, sea surface temperatures are very attractive to several species that normally reproduce in the GC (Lavin and Organista, 1988; Alvarez-Borrego and Lara-Lara, 1991).

Water masses play an important in the GC as it is connected to the Pacific Ocean. As a result, the differences in water mixing modifies the salinity and consequently the thermohaline structure which in turn influences the vertical mixing and the tidal currents. The water of the Eastern Tropical Pacific Ocean passes through the mouth of the GC in a line between Cabo San Lucas and Cabo Corrientes. The surface salinity of the GC is greater than 35 PSU (Practical Salinity Unit) as a result of high temperatures in the upper layers (Lavin and Marinone, 2003). Furthermore, the salinity of the deep waters at the entrance of the GC increases towards the upper layers, reaching 34.50 PSU in the central region of the Gulf (Midriff area) where the average depth is between 600 and 900 m. On the other hand, the Subtropical Subsurface Water is located between 150 to 500 m water depth and it is mainly created from the Subtropical Subsurface water as a result of the main influence of the Eastern Tropical Pacific Ocean where the salinity reaches the lowest value of 33 PSU and causing evaporation at the upper layers (Wyrtki, 1966, 1967). Another important water mass is the California Current waters that are situated near to the mouth of the GC. The salinity here is less than 34.5 PSU with a relatively stable temperature between 12 °C and 18 °C. Bray (1988a), Torres Orozco (1993) and Lavin et al. (1995) found that one of the most significant processes is the water mass formation, is interaction with the Subtropical Subsurface water and the effect of evaporation. Water mass formation mainly appears in the northern part of the GC, and leads to additional vertical mixing due to tidal currents, wind and winter convection conditions. The Eastern Tropical Pacific

Ocean system exerts a significant influence on the movements of water masses at the entrance of the GC (Wyrtki, 1967; Baumgartner and Christensen 1985; Fiedler 1992; Strub and James. 2002a). The currents in the mouth of the GC experience considerable variability. For instance, the seasonal variability of the Inter-Tropical Converge Zone (ITCZ) influences how far south the currents off the coast of California move and how far north the Costa Rica current moves (Wyrtki, 1967; Fiedler, 1992).

The GC absorb heat from the atmosphere through its surface and as a result there is a seasonal circulation in the thermohaline zone resulting in important differences in sea surface temperature, salinity variations and tidal mixing and stratification. Also, the evaporation processes are mainly responsible for high salinity in the GC. The mean heat flux in Guaymas Basin in the northern GC was estimated monthly by Castro et al. (1994). Their results indicated considerable seasonality due to the effect of meteorological and astronomical variables such as solar heating which results in a large amount of heat loss due to evaporation. Moreover, the seasonal cycle has two important characteristics (Bray, 1988a; Lavin and Organista, 1988; Ripa and Marinone, 1989; Paden et al., 1993). First, air temperature at the surface on average provides heat to the GC. Second, the northern GC loses heat in the last two months of every year.

Tidal mixing in the region is associated with internal waves (Badan-Dangon, 1989; Paden et al., 1993). As a result, tidal mixing is making responsible for the cooler surface temperatures in the Midriff area in the central GC. Tidal mixing is also important for pumping nutrients to the surface productivity zone and has a significant influence on the thermohaline circulation. Internal tides or baroclinic tides are generated by the interaction between the tidal current and the topography features of the local site. Normally the internal waves appear more frequent in summer when they are captured within the density gradient zone (thermohaline layer) (Holbrook et al. 1980). The internal waves have certain conditions for instance their period are short, only about 10 minutes, whereas the wavelength can vary from 100 m up to 2 km (Holbrook et al. 1980). Since the 1970’s only a few studies of internal waves in the GC have been carried out. Internal wave observations were undertaken by Fu and Holt (1984) using satellite radar images and revelled that the internal waves propagate to the northern Gulf from the narrow part of San Lorenzo and San Esteban Island (hereafter San Lorenzo Passage). Furthermore, a more recent study on internal wave analysis through Eulerian currents and CTD profiles can be found in Filonov and Lavín (2003). However, this study did not include the influence of the internal waves and their effects on kinetic energy extraction evaluations.

2.4 Summary

This literature review has shown that numerous tidal-range and tidal-stream energy resource assessments have been carried out worldwide. However, even though the Latin-America region is committed to increasing its use of renewable energy sources, only a limited number of studies of tidal energy have been undertaken for Latin American countries. Only a few select studies have considered tidal renewable energy for Mexico. Furthermore, the Mexican Government is keen to explore and evaluate all the alternatives of renewables available through the country. Therefore, the aim of thesis is to identify potential sites for tidal energy in the GC.

Tidal-range in the northern part of the GC is large and this region therefore holds promise for tidal-range energy exploitation, particularly as the region has shallow water depths (<50 m). However, to date only two studies (Hiriart et al., 2009; Tapia et al., 2013) have assessed the tidal energy resource in this region. Furthermore, these two studies have only used very basic approaches to estimate the available tidal-range energy resource potentially available. Although the region has potential for tidal energy extraction, the electricity grid network connectivity currently poses a major limitations and links to the grid need to be carefully considered for any future tidal barrage power plant or tidal lagoon. Therefore, the first objective of this thesis is to quantify the present day potential theoretical tidal-range energy resource available in the GC, Mexico.

Several oceanographic focused studies (e.g. Badan-Dangon, 1991; Marinone, 2000, 2003, 2006, 2007, 2008; Lopez et al., 2006, 2008; Marinone et al., 2009) have identified that there are fast tidal current speeds in the Midriff region of the GC. However, to date no studies have assessed the potential tidal-stream energy resources in this region. Worldwide, most tidal-stream focused past studies have assessed the potential resource of sites with fast tidal currents in relatively shallow water. Currently, commercial tidal-stream turbines require high current speed greater than 2.5 m/s and water depths less than 100 m depth. Thus, regions with less energetic tidal currents, but in deeper waters, like the GC, have been overlooked and therefore, provide an interesting case study. Therefore, the second objective of this thesis is to quantify the theoretical tidal-stream energy resource in this region.

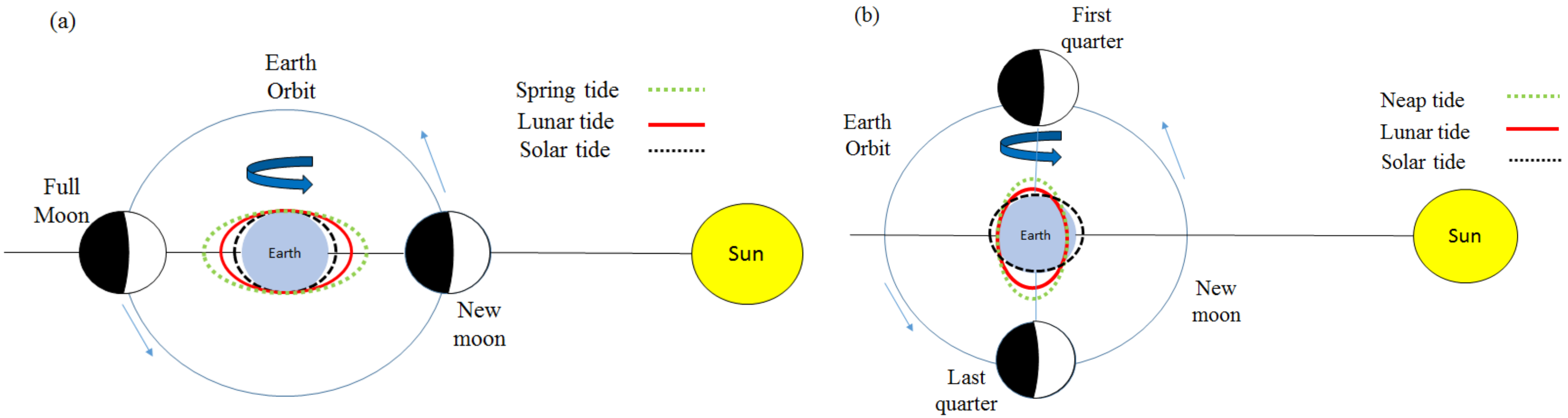

Figure 2.1. View of the earth, moon and sun from above for: (a) spring tidal conditions; and (b) neap tidal conditions. Source: Adapted from Haigh (2017).

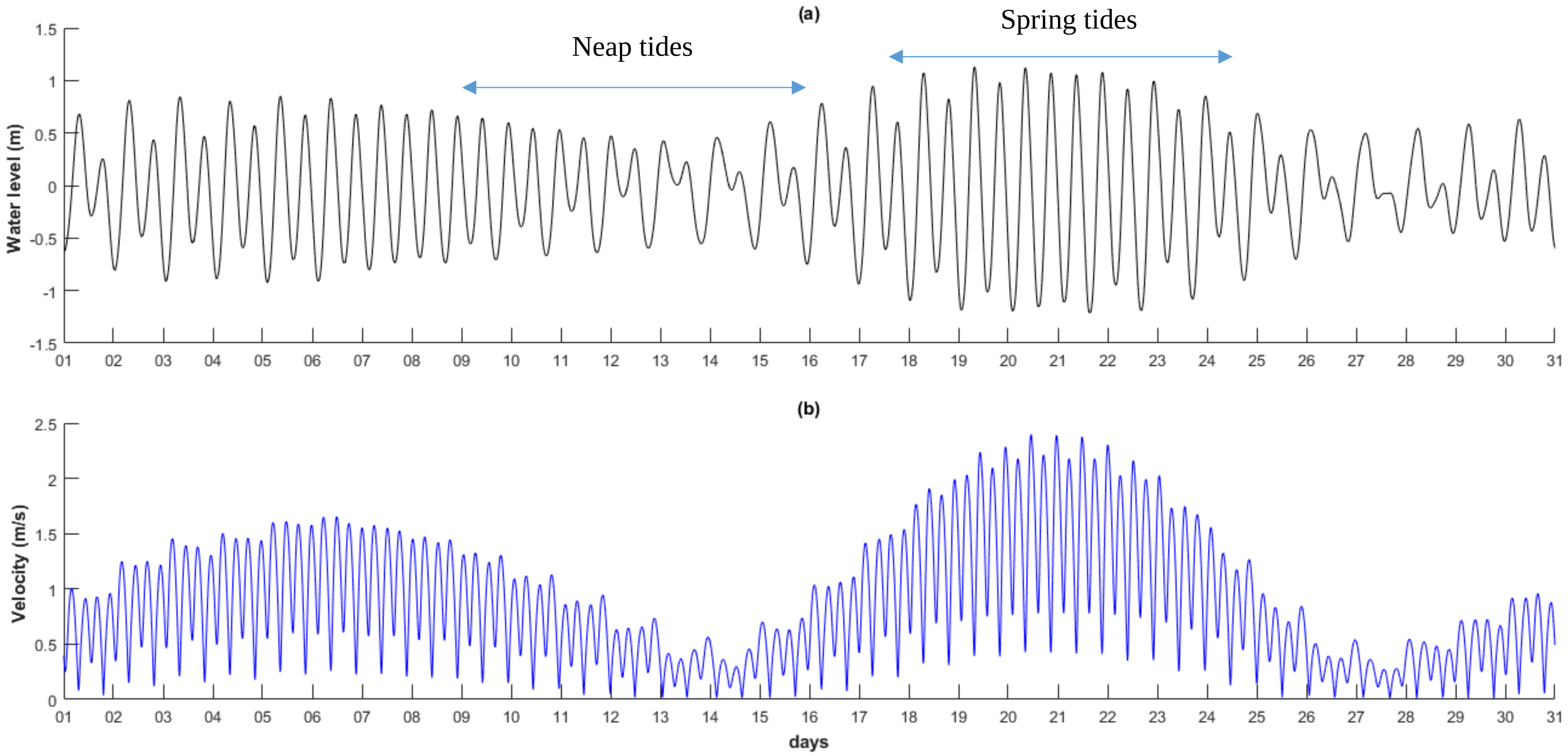

Figure 2.2. An example time series of a month of predicted: (a) water level; and (b) current speeds, in the GC, illustrating neap and spring tidal periods.

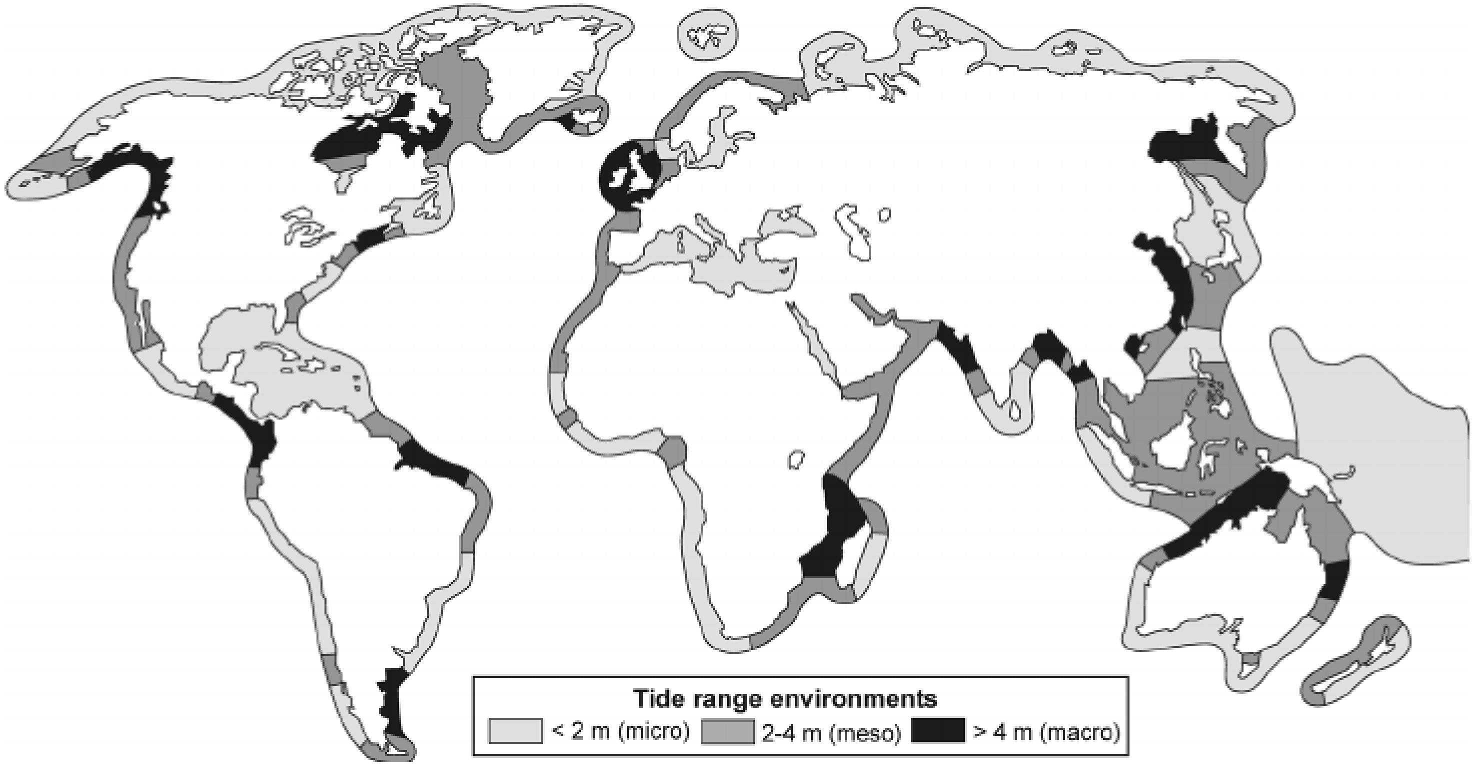

Figure 2.3. Map over global variation in tidal range (Davies 1980, modified by Masselink and Hughes 2003, Source from the last published paper, Rosendahl Appelquist and Halsenaes, 2015).

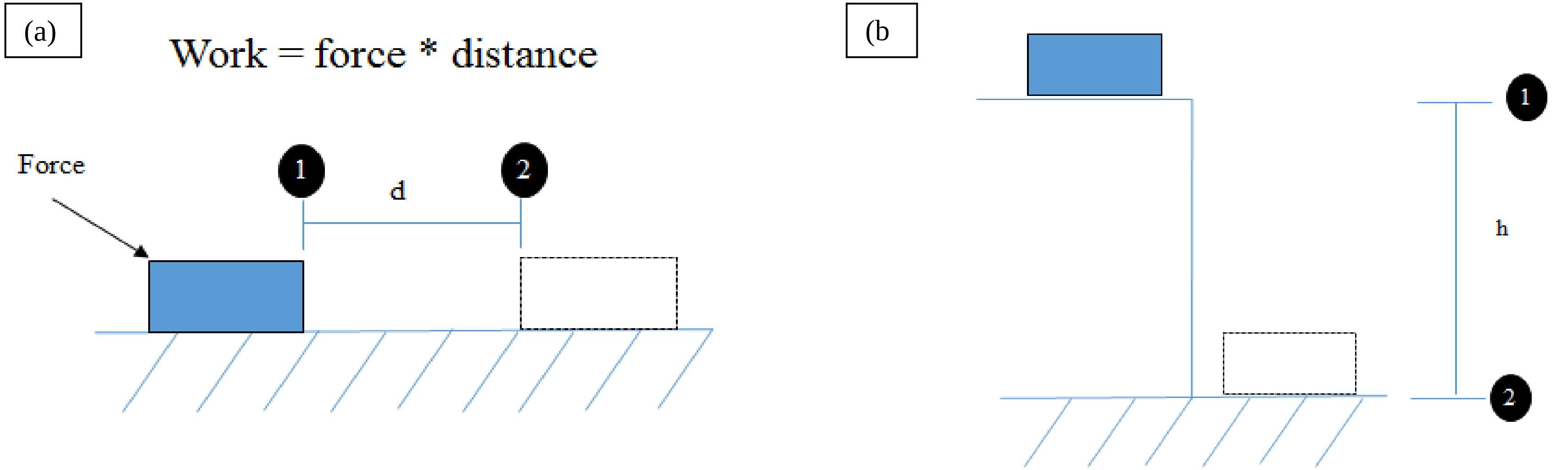

Figure 2.4. Schematic definitions of (a) work and (b) potential energy.

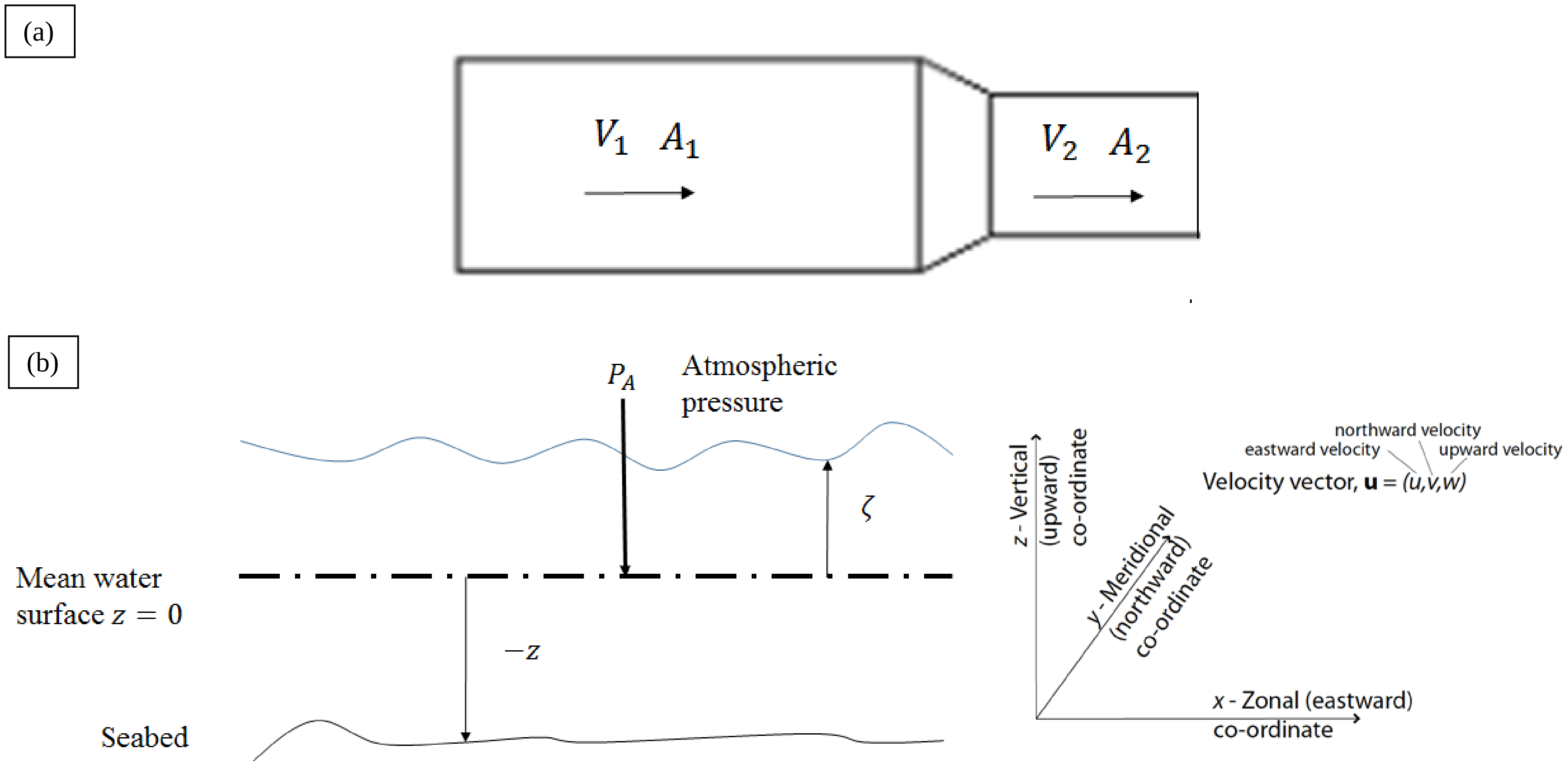

Figure 2.5. (a) Kinetic energy in a fluid and (b) potential energy of the fluid based on the hydrostatic equation (adapted from Pugh and Woodworth, 2014).

Figure 2.6. (a) Power energy station at the Rance river, France. (b) Power energy station at Kislaya Guba, Russia. (c) Power energy station at the The Sihwa Lake in South Korea. (d) Jiangxia power plant. (e) Annapolis tidal power station, Nova Scotia Canada. Source

(a) https://tidalenergytoday.com/2017/07/24/iea-france-top-tidal-energy-generator-in-2016/
(b) http://www.greenenergyjubilation.com/facts-about-tidal-power-plants-that-are-in-operation-today/
(c) https://tidalenergytoday.com/2014/12/17/video-aerial-footage-of-sihwa-lake-tidal-power-station/
(d) https://tidalenergytoday.com/2015/01/30/introducing-the-largest-chinese-tidal-power-plant/
(e) https://tidalenergytoday.com/2015/01/20/video-annapolis-tidal-power-station/

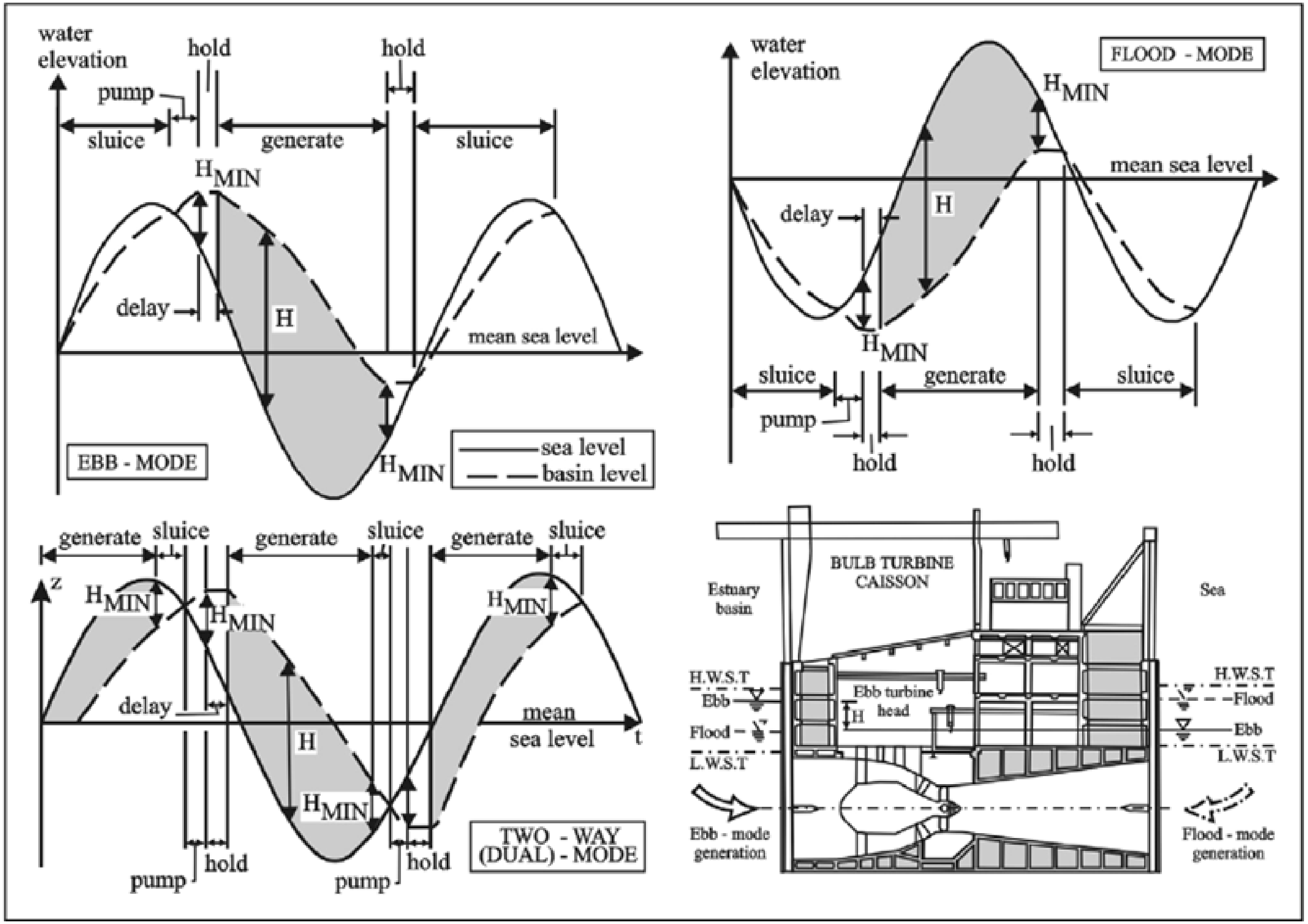

Figure 2.7. Operational schemes of tidal power plants. Source: (Burrows et al., 2009b)

Figure 2.8. Kaplan turbine. Source: http://voith.com/corp-en/news-room/press-releases_49042.html.

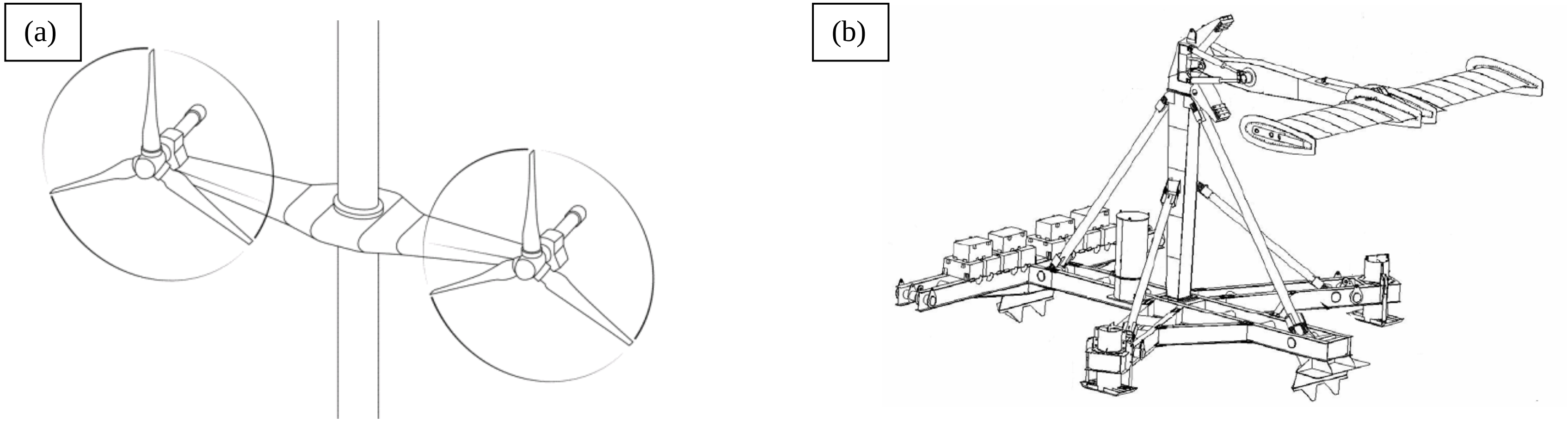

Figure 2.9. Marine current device classification: (a) Rotational device, (b) oscillating hydrofoil design.

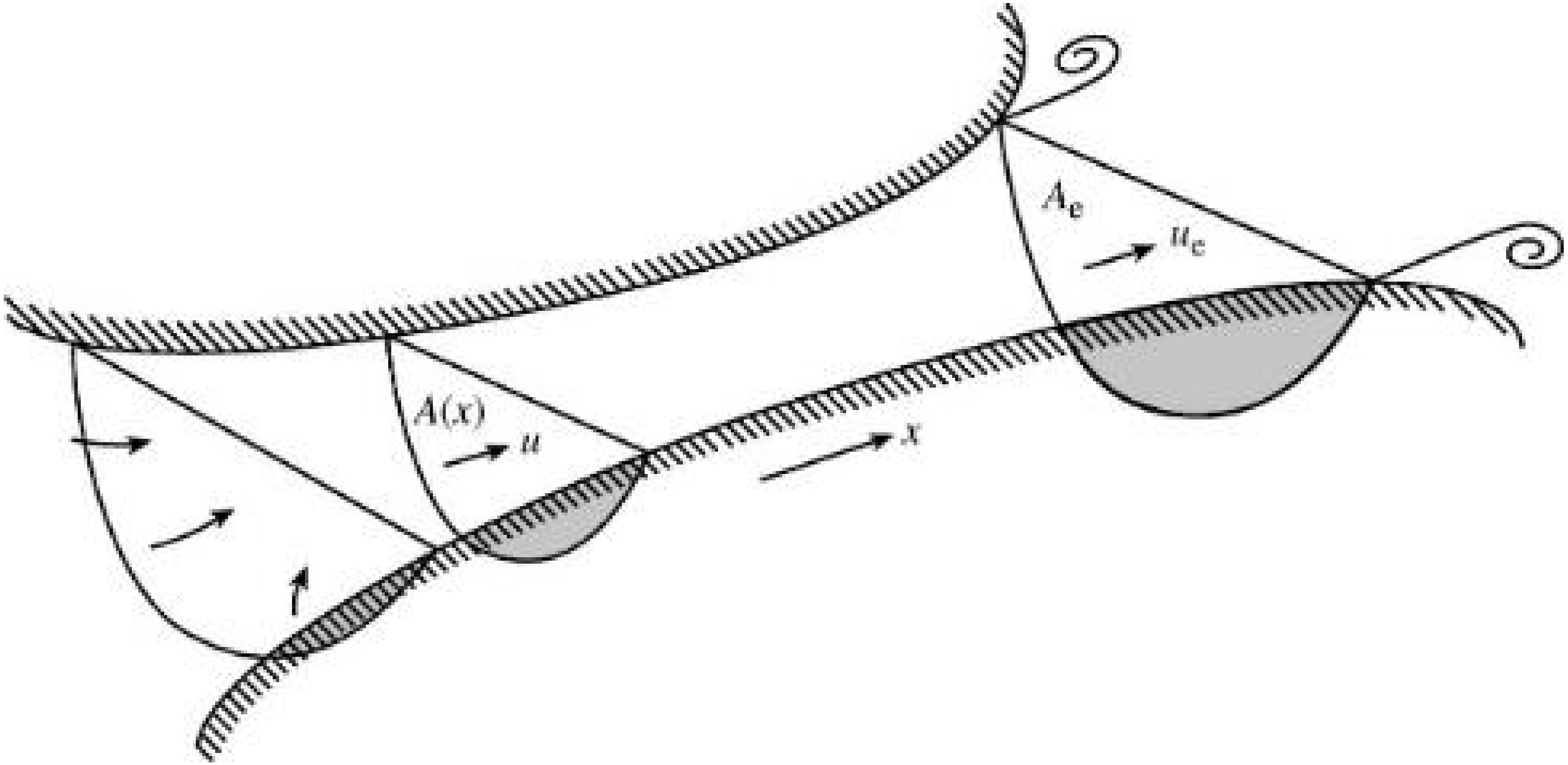

Figure 2.10. Basins connected with unequal tidal elevations. The current with u speed and *A (x)* cross-sectional area. Image from Garrett & Cummins, 2008.

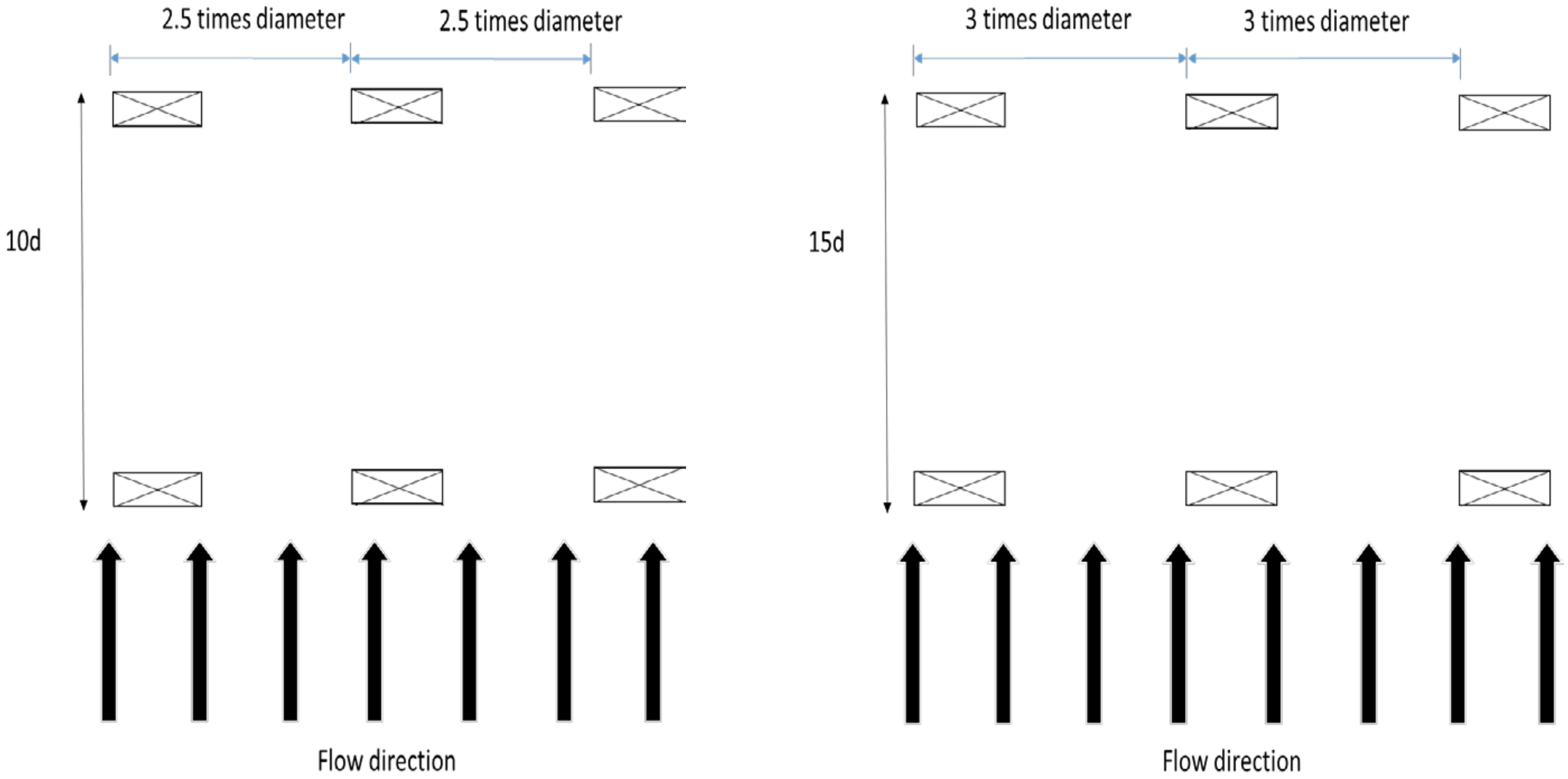

Figure 2.11. Lateral and longitudinal spacing proposed by Bahaj and Myers (2004).

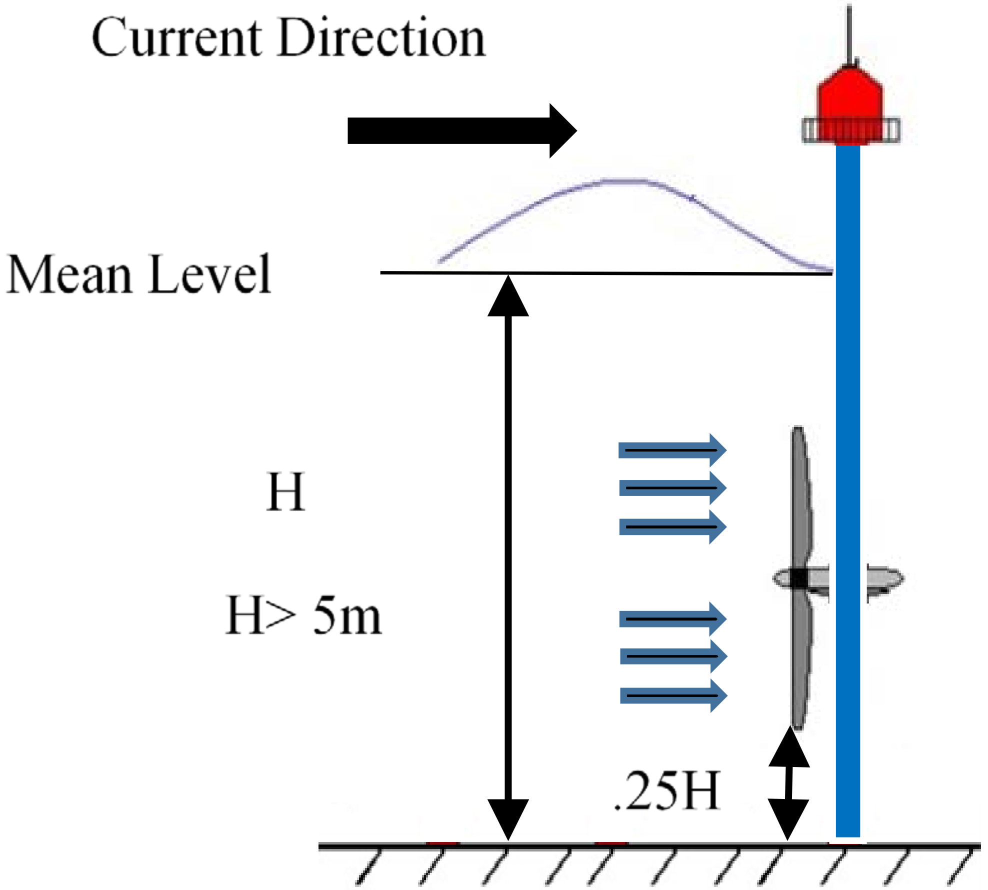

Figure 2.12. Minimum distance between the seabed and the blade of the turbine proposed by Bahaj and Myers (2004).

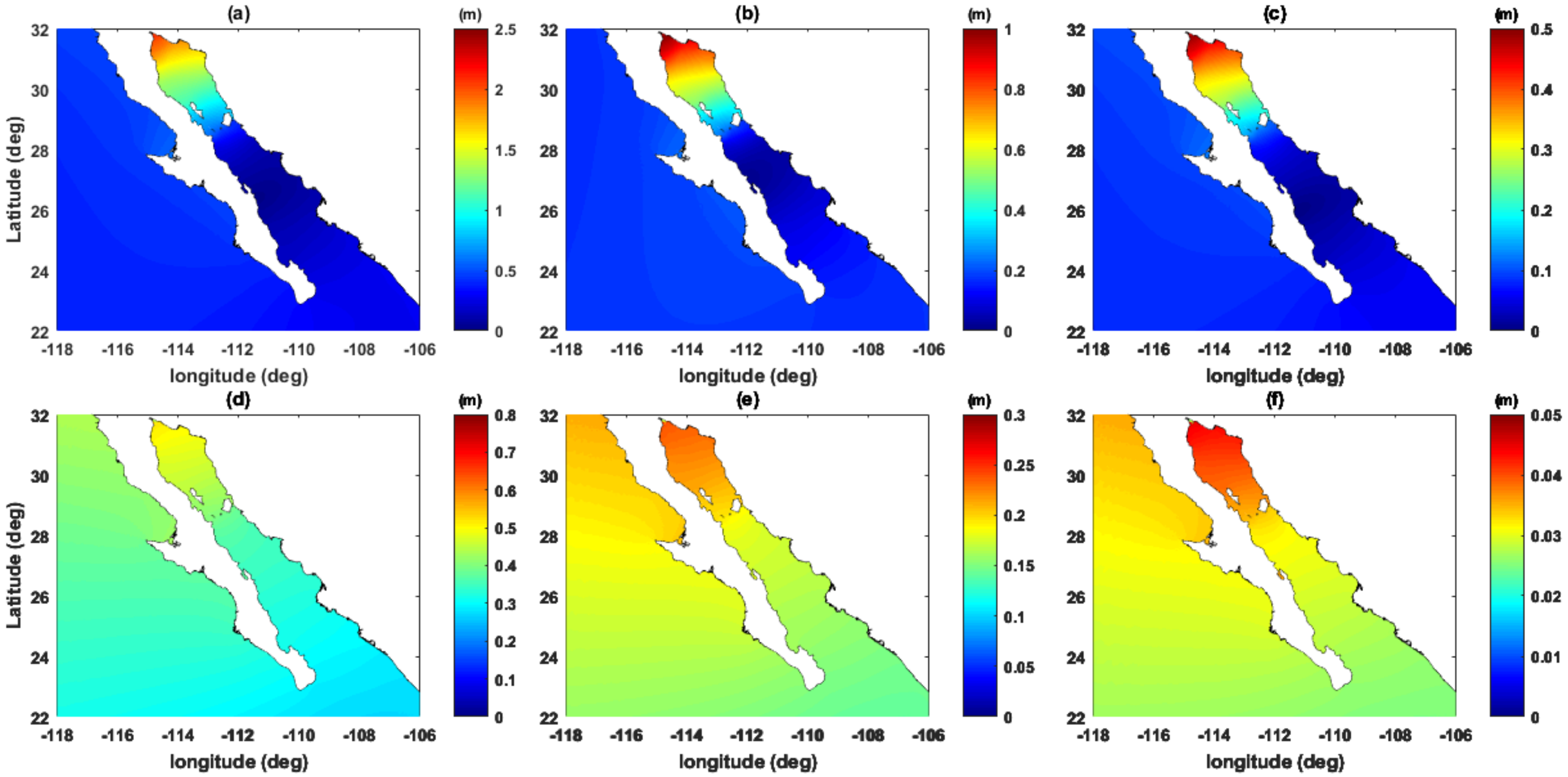

Figure 2.13. Amplitude of the main semidiurnal and diurnal tidal constituents: (a) M_2, (b) S_2, (c) N_2, (d) K_1, (e) O_1 and (f) Q_1. Source TELEMAC model describe in Chapter 3.

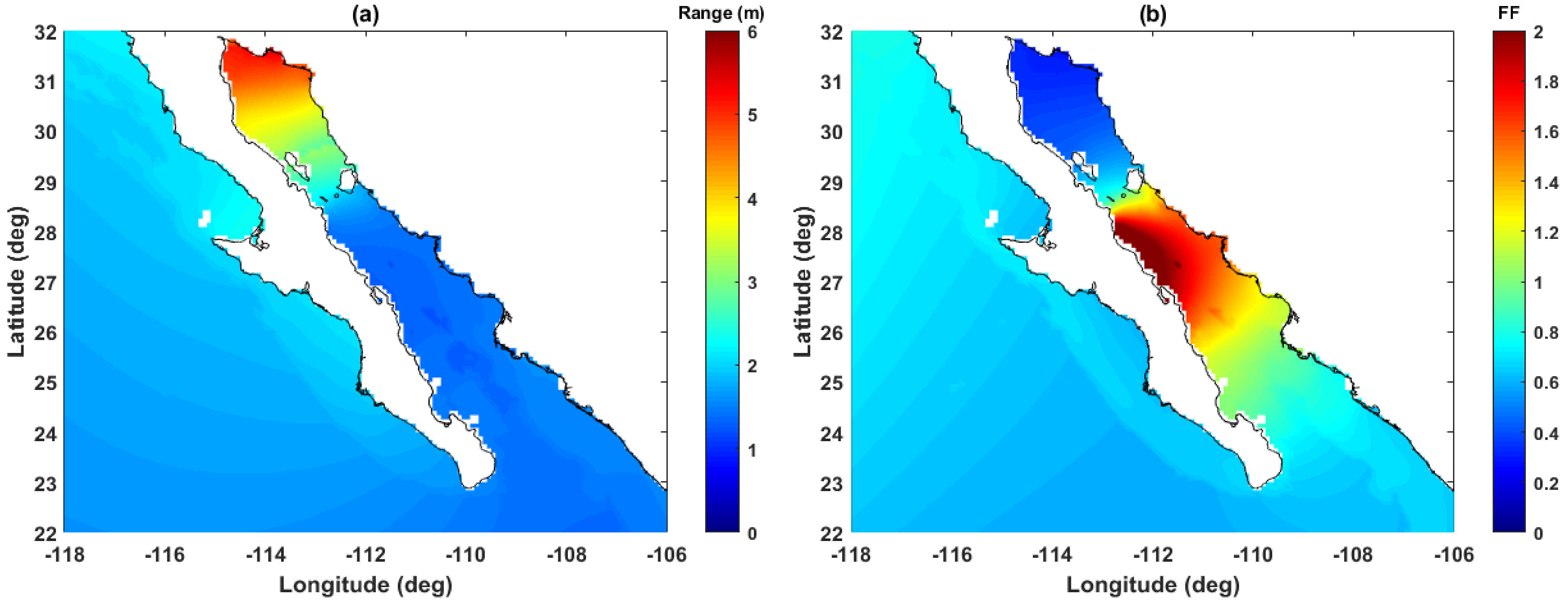

Figure 2.14. (a) Tidal-range of the GC (b) Tidal form factor, both using the OTIS (Regional Pacific Ocean dataset). (http://volkov.oce.orst.edu/tides/global.html).

Table 2.1. Main tidal constituent for Los Angeles. Source, https://tidesandcurrents.noaa.gov/harcon.html?id=9410660.

Type of Tidal	Tidal Name component	Period (in hours)	Amplitude (m)	Phase (°)	Brief Description
Semidiurnal	M_2	12.42	1.69	273.6	Main Lunar Constituent
Semidiurnal	S_2	12.00	0.66	266.1	Main Solar Constituent
Semidiurnal	N_2	12.66	0.39	256.1	Larger Lunar constituent
Semidiurnal	K_2	11.97	0.19	254.8	Soli-lunar constituent
Diurnal	K_1	23.93	1.12	87.3	Luni-solar Declinational constituent
Diurnal	O_1	25.82	0.71	80.7	Main Lunar Declinational constituent
Diurnal	P_1	24.07	0.35	84.9	Main solar constituent
Longer	Mf	327.86	0.00	0.0	Lunar every two weeks constituent

Table 2.2. Hydrodynamic models previously used for marine energy assessments.

Model name	Spatial dimensions	Model Description	Reference
Delft	2D and 3D	Interaction between wave and currents, 2D and 3D no-hydrostatic flow features, Sediment transport, multi domain grid within Cartesian and spherical coordinates system	https://csdms.colorado.edu/wiki/Coastal_models
FVCOM	3D	Free surface 3 dimensional model including unstructured grid. Model adapted from (GOTM) The ocean turbulent model.	http://eco37.mbl.edu/FVCOM/PIE-FVCOM.html
FUNDY	3D	Ideal for continental shelfs studies including wave and density variation.	https://csdms.colorado.edu/wiki/Coastal_models
MIKE 21	2D and 3D	Simulate a variety of process along the coastal and offshore structures for instance, physical, chemical process and environmental processes.	http://releasenotes.dhigroup.com/2012/MIKE21relinf.htm
FLUIDITY	2D and 3D	Also mainly used for geophysical fluid dynamics, ocean modelling and computational fluid dynamic CFD.	http://fluidityproject.github.io/#main
HYCOM	2D	Hybrid Coordinate Ocean Model, Ideally used for stratification studies. This model utilized the isopycnic coordinate circulation models in order to extend the study region towards shallow waters and or stratified oceans. Another special feature is the use of the sigma coordinates system to characterize the flow behaviour at the surface	https://hycom.org/hycom
MITgim	2D	MIT General Circulation Model enable atmospheric, ocean and climate studies. One of the model's features is a non-hydrostatic that allow to simulate the hydrodynamic fluid phenomena in a variety of scales.	http://mitgcm.org/
RICOM	2D and 3D	RICOM is an unstructured-grid finite-element coastal ocean model usually used for tidal current simulations, storm surge forecast, tsunami analysis and sea level rise.	https://csdms.colorado.edu/wiki/Coastal_models
ROMS	3D	Regional ocean modelling systems extended their capability to global studies using the Navier-Stokes primitive equations to solve for physical riables as temperature, salinity, and additionally kinetic energy assessments.	http://www.myroms.org/
DIVAST	2D	Depth Integrated Velocity And Solute Transport, depth integrated model that solves the Navier-stoke equations and also designed especially for shore modelling and estuarine. Not suitable where the flows are vertically unsteady (Turbulent) and vertical stratified flow	http://www.designed4style.com/clients/websites/marcon/website/services/nm_divast.htm
ADCIRC	2D and 3D	This software model tides, wind driven, analysis of storm surge and flooding. The finite element in space and flexible unstructured grid is utilized.	https://csdms.colorado.edu/wiki/Coastal_models
TELEMAC	2D and 3D	TELEMAC Modelling software suite of tools was chosen to predict tidal levels and currents. Compatible with few pre-processor as Funda, Blue Kenue, Matisse and Janet	http://www.opentelemac.org/

Table 2.3. Tidal-range energy assessments worldwide at the time of writing.

Location	Tidal-range (m)	Methodology used	Power	Reference
Solway fifth, UK	7 m,10 m, 5.64 m	Theoretical assessment method	625,629 and 10,050 GWh	Binnie and Partners (1989)
Bay of Cadiz, Spain	2 m	Theoretical assessment method	12GW	Rosario et al. (2006)
Bay of Fundy, Canada	16 m during spring tides	Theoretical assessment method	220 MW to 280 MW	Delta Marine Consultants, (2007)
Solway fifth, UK	5.5 m	Non information provided	300 MW	Howard et al. (2007).
Swansea Lagoon, UK	7 m	Non information provided	0.187 TWh/year.	Friend of the Earth Cymru (2004)
North west England		Technical assessment method	Dual mode energy 2D model	Yates et al. (2010)
Solway fifth,	Mean tidal-range 2.7 m,		6.82 TWh/year	
Morecambe bay,	Mean tidal-range 3.0 m,		3.99 TWh/year	
Mersey,	Mean tidal-range 3.2 m,		0.74 TWh/year	
Dee estuary	Mean tidal-range 2.9 m		0.8 TWh/year	
Dee, UK	3.2 m approx.	Technical assessment method	1.35 TWh/year	Burrows et al. (2009a).
West coast of England, UK		Technical assessment method		Burrows et al. (2009b)
Solway Firth	Mean tidal-range 2.7 m,		9.6 TWh/year	
Morecambe Bay	Mean tidal-range 3.0 m,		5.9 TWh/year	
Mersey	Mean tidal-range 3.2 m,		0.57 TWh/year	
Dee	Mean tidal-range 2.9 m		0.89 TWh/year	
Severn	Mean tidal-range 3.5 m		15.81 TWh/year	
Irish sea			Dual mode energy 2D model	Burrows et al. (2009c).
Solway fifth,	Mean tidal-range 2.7 m,	Technical assessment method	10.8 TWh/year	
Morecambe bay,	Mean tidal-range 3.0 m,		7.13 TWh/year	
Mersey,	Mean tidal-range 3.2 m,		0.9 TWh/year	
Dee	Mean tidal-range 2.9 m		1.3 TWh/year	
Severn.	Mean tidal-range 3.5 m		20 TWh/year	
Northwest UK			20.2 TWh/year	
Severn estuary	5.3 m	Technical assessment method	24.2 GWh/year	Falconer et al. (2009)
Severn estuary, UK	Mean tidal-range of 8.2 m	Non information provided	17 TWh/year	Sustainable Development commission (2007)
Mersey Estuary	Mean spring tidal-range of 8 m		1.4 TWh/year	
Loughor Estuary	Mean spring tide of 3.9 m		15.1 GWh/year	
Duddon Estuary	Mean tidal-range of 5.8 m		212 GWh/year.	
Wyre Estuary	Mean tidal-range of 6.6 m		123-133 GWh/year	
Severn estuary, UK	6 to 12 m over the neap–spring cycle.	Technical assessment method	17 TWh/year	Watson and Shaw (2007)
Gulf of California, Mexico	Over 5 m	Theoretical assessment method Theoretical assessment method	26 GW 14 MW	Hiriart et al. (2009) Tapia et al. (2013)

Location	Tidal-range (m)	Methodology used	Power	Reference
Bacanga estuary, Brazil	6.5 m	Theoretical assessment	14,000 MWh/year	Ferreira et al. (2009) Leite et al. (2015)
Severn estuary, UK	14 m during spring tide	Technical assessment method using turbines into the model simulations	12.7 TWh/year	Xia et al. (2010)
Bristol Channel, UK				HM Government, (2010).
Severn	Mean tidal-range 14 m	Non information provided	19.7 TWh/year	
Solway Firth	Mean tidal-range 5.5 m		10.2 TWh/year	
Morecambe Bay	Mean tidal-range 6.3 m		4.6 TWh/year	
Wash	Mean tidal-range 4.4 m		3.7 TWh/year	
Humber	Mean tidal-range 4.1 m		1.6 TWh/year	
Thames	Mean tidal-range 4.2 m		1.3 TWh/year	
Mersey	Mean tidal-range 6.4 m		1.3 TWh/year	
Dee	Mean tidal-range 5.9 m		1.1 TWh/year	
Cardiff Bay-Weston Barrage	Non information provided		16.8 TWh/year	
Shoots Barrage	Non information provided		2.7 TWh/year	
Beachley Barrage	Non information provided		1.2 TWh/year	
Welsh Grounds Lagoon	Non information provided		2.6 TWh/year	
Bridgewater BAY	Non information provided		6.2 TWh/year	
Cardiff Weston Barrage, UK	Non information provided	Non information provided	15.6 TWh/year	House of Commons (2013)
The Rance river, France	8.5 m	Theoretical and practical estimation.	240 MW	Andre, (1976) O Rourke, (2010)
Severn estuary, UK	14 m	Technical assessment method using turbines into the model simulations	13 to 16 TWh/year	Xia et al. (2012)
Bay of Fundy, Canada	16 m during spring tides	Technical methodology	264 MW	Cornett et al. (2013)
Solway fifth, UK	14 m	Theoretical assessment method	8 to 9 TWh/year	Aggidis et al. (2012)
Bristol Channel, UK		Technical methodology		Yates et al (2013)
Solway fifth,	Mean tidal-range 2.7 m,		Max 8.82 TWh/year	
Morecambe bay,	Mean tidal-range 3.0 m,		Max 5.37 TWh/year	
Mersey,	Mean tidal-range 3.2 m,		Max 0.82 TWh/year	
Dee	Mean tidal-range 2.9 m		Max 0.83 TWh/year	
Severn.			Max 13.07 TWh/year	
Mersey estuary, UK	14 m during spring tides	Technical assessment method using turbines into the model simulations	13.10 and 11.73 TWh respectively	Aggidis and Benzon (2013)
Matsu archipelago, Taiwan,	4.9 m	Technical assessment method	8.85 MW	Jia-Shiuan et al. (2014)

Location	**Tidal-range (m)**	**Methodology used**	**Power**	**Reference**
Jiangxia , China	8.39 m	Technical assessment method	7 MWh/year	Zhang et al. (2014)
Sandwip Island of Bangladesh	7.03 m	Theoretical assessment method	2668 MW/year	Sikder et al. (2014)
The Gulf of Cambay and Gulf of Kutch, India	11 and 8 m respectively	Theoretical assessment method	8000 MW	Sen et al. (2015)
Swansea Lagoon. UK	10 m	Theoretical assessment method and Technical method	160MW	Petley and Aggidis (2016)
Swansea Lagoon. UK	10.5 m	Theoretical assessment method	320 MW	Waters and Aggidis (2016)
Lake Sihwa, Korea	7.8 m during spring tide. Max tidal range 9 m	Technical assessment method	552.7 GWh/year	Bae, (2010) Park, (2017)
Persian Gulf, Iran	5 m during spring tide	Theoretical assessment method	150 MWh	Aslani et al. (2017)
Kimberley region of Western Australia.	10 m	Theoretical assessment method	3,000 MW	Tidal power in Australia (2017)
Global resource assessment	Please see reference for tidal-range details at sites	Theoretical assessment method	25,880 TWh	Neill et al. (2018)

Table 2.4. Tidal-stream energy assessments worldwide at the time of writing.

Location	Current speed	Modelling approach	Boundary Forcing	Methodology used	Power or Power density	Reference
UK, Alderney Race	spring rate ~5 m/s	Data from Admiralty Charts	Non information provided	Undisturbed theoretical kinetic energy flux method and experimental farm method.	7.4 TWh/year	Bahaj and Myers (2004)
France, Alderney Race	spring rate ~5 m/s	2D Aerofoil	Tidal current data from Atlas NP 264	Experimental farm method	Annual energy output 1340 GWh	Myers and Bahaj (2005)
USA, East and west coast.	From 1.5 up to 6.67 m/s	WXTide32		Undisturbed theoretical kinetic energy flux method		Hagerman et al. (2006)
Canada, East and west coast.	average flow speed of 2.11 m/s	WebTide Tidal Prediction Model (v0.7.1)	M$_2$ tidal constituent	Undisturbed theoretical kinetic energy flux method	Mean annual power 42,000 MW	Cornett (2006)
Bay of Fundy, Canada	Non information provided	FVCOM	M$_2$ Tidal constituents	Undisturbed theoretical kinetic energy flux method. Disturbed drag coefficient method	18 kW/m^2. 6.9 GW	McMillian et al. (2006)
Canada		Tide2D	M$_2$ Tidal constituents	Undisturbed theoretical kinetic energy flux method		Tarbotton and Larson (2006)
Northwest Territories	From 2.7 m/s to 8.23 m/s. Please see reference for full details				35 MW	
British Columbia					4015 MW	
Quebec					4288 MW	
Nunavut					30567 MW	
New Brunswick					636 MW	
PEI					33 MW	
Nova Scotia					2122 MW	
Newfoundland					544 MW	
USA, East region.	From 0.5 to 3.39 m/s	Non information provided	Non information provided	Undisturbed theoretical kinetic energy flux method and technical method	10.35 kW/m^2	Electric power research Institute EPRI (June 2006),
USA, West region					6.5 kW/m^2	
UK, Portland Bill	3.6 m/s	TELEMAC 2D	12 main tidal constituents	Undisturbed theoretical kinetic energy flux method	Up to 730 kW per turbine	Blunden and Bahaj (2006)
Canada, Johnstone Strait	4.7 to 7.7 m/s	TIDE2D	M$_2$ Semidiurnal constituent	Disturbed drag coefficient method	1320 MW peak power	Sutherland et al. (2007)
Masset Sound, located in Haida Gwaii	2.5 m/s	One-dimensional model	M$_2$ tidal constituent	One-dimensional theoretical method	79 MW and 87 MW	Blanchfield et al. (2008)
Minas Passage, Bay of Fundy, Canada	3.28 m/s	FVCOM	M$_2$ Semidiurnal constituent	Undisturbed theoretical kinetic energy flux method and Disturbed drag coefficient method.	2.5 GW	Karsten et al. (2008)
Spain, Rıa de Muros	2.3 m/s	Delft3D-FLOW	Different forcing agents	Undisturbed theoretical kinetic energy flux method. Technical energy method	1.32x10^3 MWh/year	Carballo et al. (2009)
Chile, Chiloe Island.	Up to 2.1 m/s	Non information provided	Non information provided	Undisturbed theoretical kinetic energy flux method	10 kW/m^2.	Herrera et al. (2010)

Location	Current speed	Modelling approach	Boundary Forcing	Methodology used	Power or Power density	Reference
Malaysia, (see reference for all the sites)	0.8 to 1.2 m/s	The Princeton Ocean Model (POM)	TPXO data base of global tides	Undisturbed theoretical kinetic energy flux method and Technical energy method	Energy output (GWh/year)	Lim and Koh (2010).
Ireland	Above 1.9 m/s	MIKE 21	TOPEX Altimetry data set	Undisturbed theoretical kinetic energy flux method Technical energy method. Practical method.	230 TWh/year 10.46 TWh/year 2.633 TWh/year	O'Rourke et al. (2010).
Bay of Fundy, Canada	average spring tide excess 5 m/s	TELEMAC 3D	WebTide 10 tidal constituents	Undisturbed theoretical kinetic energy flux method	From 50 kW/m^2 to 80 kW/m^2	Cornett et al (2010)
Georgia Coast, USA	Mean from 0.34 to 1.07 m/s	ROMS	NOAA data set, ADCP, tidal level, bathymetry and tidal constituents measures	Undisturbed theoretical kinetic energy flux method and disturbed drag coefficient method.	500 W/m^2. See full paper for results details.	Defne et al. (2011)
USA coastline	1 m/s	ROMS	Q_1, O_1, K_1, S_2, M_2, N_2, K_2, M_4 and M_6. K_2	Undisturbed theoretical kinetic energy flux method	500 W/m^2	Georgia Tech Research Corporation (2011)
Canada, Bay of Fundy	More than 5 m/s	FVCOM	M_2 tidal constituent and WebTide Tidal Prediction Model (v0.7.1)	Disturbed drag coefficient method	7000 MW	Karsten et al. (2013)
Coastline, USA		HYCOM	NOAA's submarine cable transport data, Florida Atlantic University's (FAU) ADCP data at a high power density location. See reference for full details	Disturbed drag coefficient method	49 TWh/yr. 7.1 GW/km^2. See details for full figures and different estimated power scenarios.	Georgia Tech Research Corporation (2013)
UK, Pentland Firth	5 m/s	ADCIRC	M_2 and S_2 tidal constituents	Disturbed drag coefficient method	1.9 GW	Adcock et al. (2013)
UK, Anglesey Skerries	Up to 1.4 m/s	ADCIRC	M_2 and S_2 tidal constituents	Line sink of momentum.	269.6 MW per turbine	Serhadlıoğlu et al. (2013).
South Carolina, USA	0.87 m/s	ROMS 3D	Non information provided	Undisturbed theoretical kinetic energy flux method	610 MWh/month 371 MWh/month	Work et al. (2013)
Indonesia, Alas strait	1.2 m/s	The Princeton Ocean Model (POM)	OTPS, four semidiurnal (M_2,S_2,N_2,K_2), four diurnal tidal constituents (K_1,O_1,P_1,Q_1)	Undisturbed theoretical kinetic energy flux method	Annual energy yield (GWh). from 330 up to 640 GWh	Blunden et al. (2013).
New Zealand, Tory Channel	2 m/s	RICOM	7 Tidal constituents M_2, S_2, N_2, K_2, K_1, O_1, P_1.	Disturbed drag coefficient method	500 kW per turbine, estimate number of turbines 50 up to 600	Plew and Stevens (2013).
Pentland Firth, UK	3 m/s	ADCIRC	K_1, K_2, M_2, MU_2, N_2, NU_2, O_1 and S_2 tidal constituents	Undisturbed theoretical kinetic energy flux method	2.16 GW	Adcock et al. (2014)
Ireland, Bull mouth and Shannon Estuary.	2.02 m/s during spring tide	Measure data	Non information provided	Undisturbed theoretical kinetic energy flux method.	137.39 MWh and 2.16 MWh respectively	O'Rourke et al. (2014)

Location	Current speed	Modelling approach	Boundary Forcing	Methodology used	Power or Power density	Reference
Coast of New jersey, USA (please see reference for details)	1.26 m/s	Finite Volume Coastal Ocean Model (FVCOM)	OTIS	Undisturbed theoretical kinetic energy flux method	In between 250 to 3000 W/m^2, 395 MW	Tang et al. (2014)
Spain, Gibraltar strait.	2 m/s	MITgcm	M_2 S_2 O_1 K_1 Tidal constituents	Undisturbed theoretical kinetic energy flux method	Maximum of 1800 W/m^2	Calero et al. (2014)
France, Iroise Sea	From 2 m/s to 4 m/s.	Principal component analysis method	Current velocity time series recorded by High Frequency radars (HFR)	Undisturbed theoretical kinetic energy flux method	Kinetic power energy of 1.5 kW/m^2.	Thiébaut and Sentchev (2015)
Brazil, Sao Marcos Bay.	2.63 m/s	SisBaHiA	Q_1,O_1,M_1,P_1,K_1,J_1,MNS_2,$2N_2$,MU_2,N_2,NU_2. Tidal constituents	Technical energy method.	17.4 kW/m$^{2.}$ 9.2–11.2 MWh/m^2/year.	González-Gorbeña et al. (2015)
UK, Irish Sea	Above 2.5 m/s	ROMS	Ten tidal constituents (M_2, S_2, N_2, K_2, K_1, O_1, P_1, Q_1, Mf, and Mm).	Undisturbed theoretical kinetic energy flux method	4 Tera J within a 90 km^2 extent	Lewis et al. (2015).
Indonesia, Strait of Larantuka	3 to 4 m/s	Delft3D	TPXO Indian Ocean Atlas. 11 harmonic constituents	Undisturbed theoretical kinetic energy flux method	6 kW/m^2 20 GWh/year.	Orhan et al. (2015).
China, Hulu Islands	Max 2.0 m/s	Mike 21 (2D)	East Chinese Tidal Wave Mathematical Model	Undisturbed theoretical kinetic energy flux method. Technical energy method.	Mean 0.62 kW/m^2 and 1.81 kW/m^2	Gao et al. (2015).
Colombia, Buenaventura Bay.	Mean current speed 0.8 m/s	H2D	Not-revealed	Undisturbed theoretical kinetic energy flux method	100 W/m^2 and up to 250 W/m^2	Osorio et al. (2016)
Norway, Folda Fjord	Peak currents of 2.06 m/s	ADCP collected data	Predicted tide using T_TIDE (M2, M2, S2, N2 and K1),	Undisturbed theoretical kinetic energy flux method	4.1 kW/m^2.	Carpman and Thomas (2016)
Spain, Avilés Port.	0.35–0.4 m/s	CFD, ANSYS FLUENT V13.0,	Semidiurnal Tides	Undisturbed theoretical kinetic energy flux method	60 kWh/m^2 at the mouth of the channel	González-Caballín et al. (2016).
Pentland, Fifth UK	2 m/s	ROMS	Ten tidal constituents (M_2, S_2, N_2, K_2, K_1, O_1, P_1, Q_1, Mf, and Mm).	Disturbed drag coefficient method	1.7 kW/m^2, 2.2 kW/m^2 and 2.6 kW/m^2	Goward Brown et al. (2017)
Puget Sound, Canada	2 m/s during spring tide	FVCOM	Eight harmonic tidal constituents (S_2, M_2, N_2, K_2, K_1, P_1, O_1, and Q_1 from NOAA)	Undisturbed theoretical kinetic energy flux method with farm method	250 kW, 1550 kW, and 1800 kW	Wang and Yang (2017).
Uruguay	0.35 m/s	MOHID - Water Modelling System	13 tidal harmonic constituents obtained from the FES 2004 model	Undisturbed theoretical kinetic energy flux method	0.2 to 0.25 kW/m^2	Alonso et al. (2017)
Brazil, Baía de Todos os Santos	Max 1.0 m/s	ROMS	TPXO The main semi-diurnal (M_2,S_2,N_2 and K_2), diurnal (K_1,O_1,P_1 and Q_1)	Undisturbed theoretical kinetic energy flux method	1300 W/m^2	Marta-Almeida et al. (2017)

Location	**Current speed**	**Modelling approach**	**Boundary Forcing**	**Methodology used**	**Power or Power density**	**Reference**
France, W. Brittany coast.	From 1 m/s to 4 m/s	Data Analysis	High Frequency radars (HFR)	Undisturbed theoretical kinetic energy flux method. Technical energy method.	3 MW 1.2 MW.	Thiebaut and Sentchev (2017)
Channel Islands, UK and France.	>2.5 m/s mean spring tide	TELEMAC 2D	TPXO European Shelf 2008, nine tidal constituents (M_2, S_2, N_2, K_2, K_1, O_1, P_1, Q_1 and M_4)	Disturbed drag coefficient method	13.5 kW/m^2 5.1 GW	Coles et al. (2017)
Case of the Ouessant Island, France	>2.5 m/s	Observations	(French Navy Hydrographic and Oceanographic Service)	Technical energy method.	~ 0.9 MWh/m^2	El tawil el al. (2017)
France, English Channel.	1.5 m/s average	MARS2D	FES 2012, 115 Tidal constituents from tidal model cstFRANCE	Undisturbed theoretical kinetic energy flux method. Technical energy method	0.17 to 30.19. MW/km^2. 1.46 to 9.71 GW	Campbell et al. (2017)
France,	peak current speeds in excess of 2 m/s	Tidal harmonic database	10 primary harmonic constituents (M_2,S_2,N_2,K_2,K_1,O_1,P_1,Q_1, M_4 and MS_4),	Undisturbed theoretical kinetic energy flux method.	Power density ranges from 4 to 12 kW/m^2	Guillou et al. (2018)
El-jadida, Tarfaya and Tangier, Morocco	Max current speed of 2.3 m/s	SWAN 3D	Marine environment monitoring service. CMEMS database	Undisturbed theoretical kinetic energy flux method.	~ 22 kW, 19kW and 11 kW	Hazim et al., (2019)

Table 2.5. Power coefficient based on previous studies

Author and Publication year	**Proposal Value of the power coefficient** C_p
Fraenkel (1999)	0.5> C_p ≥0.35
Burton et al. (2001)	0.5> C_p ≥0.40
Lawn (2003)	C_p 0.3
Mellor (2004)	0.5> C_p ≥0.40
Blunden & Bahaj (2006)	C_p 0.3

Table 2.6. Drag coefficients associated to horizontal-axis marine turbines characterisation

Author and Publication year	**Proposal Value of the power coefficient** $\boldsymbol{C_b}$
Plew and Stevens (2013)	0.01, 0.02, 0.06
Adcock et al. (2013)	0.01, 0.05, 0.025
Karsten et al. (2013)	0.5 to 4.0
Coles et al. (2017)	0.025
Goward Brown et al. (2017)	0.0025
McMillan et al. (2008)	0.05

Chapter 3: Model configuration and validation

This chapter has been adapted from the following two publications:

> *Mejia-Olivares, C.J., Haigh. I.D., Wells, N.C, Coles, D.S., Lewis, M. and Neill, S.P, 2018. Tidal-stream energy resource characterisation for the Gulf of California, México. Energy, 156, 481-491. https://doi.org/10.1016/j.energy.2018.04.074*
>
> *Mejia-Olivares, C.J., Haigh. I.D., Lewis, M. and Neill, S.P, 2018. Sensitivity of bathymetry and choice of tidal constituents on tidal-stream energy resource characterisation in the Gulf of California, Mexico. Accepted and published with EWTEC 2019.*

3.1 Introduction

Hydrodynamic numerical models are important for mapping tidal energy resources as they can be used to predict tidal levels and tidal currents at every grid point over a spatial domain for any given period of time. Moreover, they can be used to determine how development of a tidal energy facility will influence the near-field and far field water levels and flow. In contrast, in situ measurements only record tidal levels and tidal currents at discrete locations, for specific periods of time. Furthermore, they can't be used to investigate how development of an energy facility will influence the hydrodynamic characteristics of a region. In addition, in situ tidal measurements are expensive and often difficult to obtain. Over the last 50 years or so, tidal models have increasingly been used for a verity of applications to improve understanding of tidal characteristics at different locations (Pugh and Woodworth, 2014). The different types of tidal models have been developed over the past 60 years are briefly reviewed in Section 2.1.6. Many previous studies have used numerical models to assess the tidal energy resource available in different parts of the world, and these studies have been reviewed in Sections 2.2.2.2 and 2.2.3.2.

This chapter describes the setup and validation of the hydrodynamic model used in objectives 1 and 2, and is structured into five main sub-sections, as follows. Section 3.2 (Methodology) provides a background to the modelling software and the model configuration and validation. The results of the validation are presented in Section 3.3. A discussion of the key points are and conclusions are given in Section 3.4 and Section 3.5, respectively.

3.2 Methodology

3.2.1 Modelling software: TELEMAC

A depth-averaged barotropic model was configured using the TELEMAC modelling suite of tools (Hervouet, 2007). The main reasons for choosing TELEMAC were (Jean-Michel, 2007): (1) its computing performance - parallel processing, using the University of Southampton's supercomputer, IRIDIS, optimized the simulation time; (2) its finite element method enabled variable mesh resolution to focus modelling effort in areas of interest; and (3) model inputs and outputs are compatible with a number of pre and post-processing software (e.g. Blue Kenue, Fudaa, MATISSE, Janet). TELEMAC is a popular model choice for tidal energy resource assessment and characterisation (e.g., Blunden and Bahaj, 2006; Cornett et al., 2010; Coles et al., 2017).

Its 2D component, TELEMAC-2D, utilized in this thesis, is based on the numerical solutions of the shallow water equations, or St Venant equations. It uses finite element techniques to solve the vertically integrated equations of momentum balance and the continuity equations (Jean-Michel, 2007). The shallow water equations are applicable where there is a scale relationship between the horizontal and vertical length scale and where the vertical velocities can be considered negligible and the pressure treated as hydrostatic. This assumption along with depth integration reduces the Navier-Stoke equations to incompressible flow.

3.2.2 Model configuration and domain

The depth-averaged barotropic TELEMAC model was configured to cover the Mexican Pacific coastal region and the GC (Figure 1.4a). The model mesh was generated using the Blue Kenue software and is shown in Figure 3.1. The mesh consists of 38,181 nodes and 133,779 elements. It has a resolution of 0.507° (~60 km) at the open boundary condition in the Pacific and increases to 0.042° (~5 km) at the entrance to the GC (Figure 3.1a). Within the GC the resolution increases to 0.0083° (~1 km) around the Midriff Islands (Figure 3.1c and d) and reduces to 0.025° (~3 km) resolution at the northern most reaches (Figure 3.1b).

The primary bathymetry data interpolated onto the model mesh was from the General Bathymetry Chart of the Oceans, 2014 version (GEBCO dataset, GEBCO_2014) (Kapoor, 1981) at 30 arc-second resolution (~900 m). In addition, higher resolution (~450 m) bathymetry data in northern (north of 27° to 32°) GC (Figure 3.2), was merged within the GEBCO gridded data (Figure 3.3e, 3.4f and a cross sectional area show in Figure 3.4c). This dataset was obtained from The Center for Scientific Research and Higher Education at Ensenada (CICESE). The bathymetry data sets were combined using a merge function in the ArcGIS software. Note, none of the points from either the GEBCO or CICESE data sets were omitted or altered. The inclusion of the higher-resolution bathymetry data in the northern GC significantly improved the tidal level and current validation, compared to using just the GEBCO_2014 bathymetry alone, as will be discussed later.

The open ocean boundaries (located between points A and B, shown in Figure 3.1a) were driven using tidal levels predicted from the TPXO 7.2 dataset (Egbert et al., 1994; Egbert and Erofeeva, 2002). TPXO is derived from OTIS (Oregon State University Tidal Inversion Software), which assimilates data from the TOPEX/Poseidon and Jason altimetry missions. This global model provides amplitudes and phases for the eight main diurnal and semi-diurnal constituents (M_2, S_2, N_2, K_2, K_1, O_1, P_1, Q_1), three non-linear constituents (M_4, MS_4, MN_4), and two long period constituents (Mf, Mm), at 1/4° resolution. The harmonic constituents were obtained from the OTIS Website (http://volkov.oce.orst.edu/tides/global.html) and subsequently the tide was predicted using the Tidal Model Driver (TMD) Matlab routines that include the 4.4-year perigean cycle and the 18.6-year lunar nodal cycle (Haigh et al., 2011).

3.2.3 Model validation

The model was validated against water levels measured from tide gauges and u and v current velocities measured by acoustic Doppler current profilers (ADCP). These datasets were obtained from CICESE. Data for 11 tide gauge stations were used, the locations/details of which are listed in Table 3.1 and shown in Figure 3.5a. Current measurements were also obtained from CICESE at 4 sites around the Midriff Islands in the GC, the locations of which are listed in Table 3.2 and shown in Figure 3.5b. These ADCP current measurements were available every hour through the water column and were collected using a 150 kHz and 75 kHz ADCP deployed 8 and 7 m above the seabed and the bin depth was 10 m (Lopez et al., 2008).

A harmonic analysis of the tide gauge records was undertaken using the T_TIDE software to extract just the astronomical tidal component (Pawlowicz et al., 2002). The depth averaged currents at each of the four ADCP site were also calculated. Again, a harmonic analysis was undertaken on the observed u and v velocity components, to extract just the astronomically driven tidal components. For validation, the model was run for the period from 27 November 2015 to 31 December 2015, and results were saved at every grid point every 10 minutes. This period was chosen, because a high percentage of observation data was also available for this time. The first three days were considered as model spin up and were not included in the subsequent analysis.

Different statistical methods were used to assess the performance of the hydrodynamic model in reproducing tidal levels and tidal currents at each observational site. To determine how accurately the model predicts both the tidal levels and currents in the region, the amplitude and phase of the main tidal constituents, extracted from both the measured and predicted water levels using T_TIDE, were compared. In addition, four error measures were used to quantify the model skill. For each of the time-series, the absolute difference between each 10-minute measured and predicted value was computed. The mean, equivalent to root mean square error (RMSE), and standard deviation of the absolute differences were calculated. The percentage error was derived by dividing the RMSE by the tidal-range or range of the tidal current magnitudes. Correlation coefficients between the measured and predicted time-series were also derived for each complete time-series.

3.2.3 Sensitivity testing

Many hundreds of model runs were undertaken to examine the sensitivity of the TELEMAC numerical model to different settings and inputs. In the first set of sensitivity runs, the grid domain and associated open tidal boundary conditions were altered. This allowed an assessment of how sensitivity the model results were to the location of the open boundaries and subsequent propagation of the tidal wave across the model domain. In the second set of the sensitivity runs, the resolution of the model mesh was altered. The grid resolution was gradual increased, to quantify if validation against observations improved with higher resolution. With higher resolution model run times increase significantly, so there is a balance between capturing approach resolution and ensuring the simulations can be made in appropriate time-scales. In the third set of sensitivity tests, different bed friction values (both uniform and spatially varying) and friction laws (e.g., Nikuradse, Manning and Chézy formula) were tested. In the fourth and final set of sensitivity tests, different bathymetric datasets were used. Three different bathymetric datasets were tested, two based on globally freely available bathymetric data (GEBCO and ETOPO) and the third a bespoke product created from freely available data and higher resolution datasets from the Mexican Government. These sensitivity tests are discussed in more detail later in Section 3.4. Moreover, a list of selection of undertaken simulation are showed in Tables B1 and C1 in Appendix B and C. In Section 3.3 the model validation is described only for the simulation that provided the best agreement with observation, and hence was subsequently used for the analyses described in Chapters 4 and 5. The TELEMAC steering file for the simulation that provided the best agreement with observations is shown in Appendix A.

3.3 Results

Here the results of the validation exercise are described. A comparison of the amplitude and phase of the four main tidal level constituents (M_2, S_2, K_1 and O_1) across the 11 tide gauge sites is shown in Figure 3.6, for the measured and modelled time-series. The results show good agreement for each of the main tidal constituents. The model predictions capture the range of amplitudes across the study area. The mean absolute error between the amplitude and phase for the main tidal constituents, across the 11 sites, are listed in Table 3.3. The mean amplitude differences are less than 7 cm for the main constituents, with the exception of K_1. The mean phase differences are 10° or less for M_2 and O_1, while the remaining constituents are less than 21° different.

As an initial assessment of the model performance, the predicted amplitudes and phases of the four main tidal constituents are compared to tidal constituents for the OTIS database. The OTIS model has been assimilated with satellite altimetry data and hence is considered as ‘ground truth’. The amplitudes and phases of the main semidiurnal (M_2, S_2) and diurnal constituents (K_1, O_1,) constituents are shown in Figures 3.7 to 3.10. Differences between the amplitudes of the M_2, S_2, K_1 and O_1 constituents are shown in Figures 3.11 to 3.14, respectively. There are small differences (~10 cm) in the amplitude of the M_2 and S_2 constituents in the Midriff area and in the northern most region (Figure 3.11 and 3.12 respectively) while within the GC the differences between K_1 constituents are negligible (Figure 3.13), but larger difference are apparent away from the study region near to the northern boundary of the model. The spatial pattern of the O_1 constituent is captured accurately by the TELEMAC model, although there is a small difference in phase in the northern most reaches of the GC (Figure 3.14).

A comparison of the measured and predicted tidal level time-series at a selection of the tide gauge sites are shown in Figure 3.15. The model predictions again show good agreement with measurements across the model domain. The model accurately captures the variation in both the tidal-range and tidal form (i.e. semi-diurnal and mixed) across the study domain, and for both spring and neap periods.

Four error measures were used to quantify the model skill at the 11 tide gauge sites, and these are listed in Table 3.4. The largest RMSE is at Guerrero Negro (0.26 m) while the smallest are at Ensenada (0.03 m), Cabo san Lucas (0.06 m) and Loreto and Manzanillo (0.07 m). The mean of RMSE across all sites is 0.11 m. The percentage errors are largest at La Paz (11 %) but are less than 10 % are the reminding 10 tide gauge sites. The larger error at La Paz could be a result of the fact that the tide gauge is in an enclosed bay with a complex bathymetry that is not accurately represented at our current model resolution (3 km in this region). The mean standard deviation error across the validation sites is 0.08 m and the mean correlation coefficient is 0.94. In conclusion, the model does a good job of reproducing tidal levels across the region.

A comparison of the depth-averaged amplitude and phase of the u and v tidal velocities components (estimated from the measured and predicted datasets at each of the validation sites) are shown in Figure 3.16 and Figure 3.17, respectively, for the four ADCP sites. There is reasonable agreement between the model predictions and the observational data. For the M_2 tidal current constituent, mean absolute errors across the four sites for the u and v components are below 0.01 m/s (Table 3.5). For S_2, the mean absolute error in the u amplitude is 0.01 m/s and is 0.19 m/s in the v component. The mean absolute phase error for M_2 and S_2 is less than 2° for both velocity components. The biggest phase errors were for the K_1 tidal constituents and these were 28° and 30° for the u and v velocity components, respectively (Table. 3.5).

A comparison of the measured and predicted u and v time-series velocities (Figures 3.18 and 3.19 respectively) shows good agreement at Ballenas channel (BC) and Delfin Basin (DEL), but currents speeds are underestimated at San Esteban (SE) and San Lorenzo (SL). The latter two sites lie in areas not covered by the high-resolution bathymetry data and this maybe the reason poorer agreement is obtained.

Similarly, four error measures were used to quantify the model skill at the four ADCP sites, and these are listed in Table 3.6. The largest RMSE of the u velocity component is at San Esteban (0.19 m/s) and San Lorenzo (0.18 m/s), while the smallest errors are at Delfin Basin (0.02 m/s) and Ballenas Channel (0.09 m/s). This equates to a percentage error of less than a 7 % error at Delfin Basin and Ballenas Channel, but 11 % error at San Esteban and San Lorenzo. As mentioned previously, the latter two sites lie in areas not covered by the high-resolution bathymetry data and this maybe the reason poorer agreement is obtained. RMSE and percentage errors in the v component are smaller than in the u component at San Lorenzo, San Esteban and Delfin, but are larger at Ballenas Channel (0.32 m, 25 %). The mean standard deviation across the four validation sites is 0.06 m/s and 0.08 m/s for the u and v velocities components, respectively. The mean correlation coefficient is 0.79 and 0.64 for u and v velocity components respectively. In general, these results demonstrate that the model performs reasonably well in reproducing the tidal currents in the Midriff area, particularly in areas where we have access to higher resolution bathymetry data.

3.4 Discussion

The previous results section has focused on describing the model run that gave the best overall validation, both in terms of tidal levels and tidal currents. The model has been validated against measured water level data within the domain area of the hydrodynamic model and currents measurement in the Midriff region, previously collected in 2003 and 2004 (Lopez et al., 2005). A detailed validation exercise is particularly important as it gives confidence in the model’s ability to reproduce the tidal levels and flows in the region with reasonable accuracy. Overall, it has been shown, based both on the visual comparisons and statistical analysis between the model predictions and the observations, that the model does a good job of reproducing the spatial distributions of both the amplitude and phase of the main tidal constituents and the combined tidal level and current time-series. The model predictions accurately capture the higher tidal amplitudes in the northern most reaches of the GC and the strong tidal currents in the Midriff region, giving confidence in using the model for this work. This section now discusses additional model runs that were undertaken to examine the sensitivity of the model to different settings and inputs. This section also outlines potential ideas for future work that could improve model performance and validation.

Many hundreds of model runs were undertaken to examine the sensitivity of the model to different settings and inputs. A list of selecting runs is given in Tables B1 and C1 in Appendices B and C, respectively. In the first set of sensitivity runs, the grid domain, and associated open tidal boundary conditions, were altered. This allowed an assessment of how sensitive the model results were to the location of the open boundaries and subsequent propagation of the tidal wave across the model domain. A variety of domain area shapes were test at the beginning of the simulations, some of them are show in Figure 3.20. One of the initial domain areas included the north coast of the Pacific Ocean (Figure 3.20a). However, this domain area had some instabilities at the upper west boundary (Figure 3.21c). Subsequently, the domain area was extended further north and east in order to include the amphidomic point located at approximately longitude 140° west, latitude 29° north. By including this point, I thought that tide would propagate better from this amphidromic point towards the Pacific coast. However, instabilities in the model domain remained. Interestingly, the model became stable when I used a circular boundary (see Figure 3.22d and 3.23), instead of a square boundary. The Eastern Tropical Pacific Ocean system, shown in Figure 3.24, exerts a significant influence on the movements of water around the entrance of the GC (Wyrtki, 1967; Baumgartner and Christensen 1985; Fiedler 1992; Strub and James, 2002a). The currents in this region experience considerable temporal variability. The seasonal variability of the Inter-tropical Converge Zone influences how far south the currents off the coast of California move and how far north the Coast Rica Current moves (Wyrtki, 1967; Fiedler, 1992). Due to that, I assumed that the domain area which covers the California Currents (CC) along the southern boundary and the Costa Rica currents (CRC) along the north boundary, would work better, and it did.

In the second set of sensitivity runs, the resolution of the model mesh was altered. An example of four different resolutions that I tested are shown in Figure 3.23. The grid resolution was gradually increased, to quantify if validation against observations improved with higher resolution. With higher resolution model run times increase significantly, so there is a balance between capturing approach resolutions and ensuring the simulations can be made in appropriate time-scales. The first simulation had a course mesh (Figure 3.23a); with a resolution of approximately 70 km outside of the GC and 5 km with the GC, with 6,031 nodes and 11,012 elements. I increased the resolution outside of the GC to 65 km, 60 km and 50 km, see Figure 3.23b, and Figures 3.23c and d, respectively, and also the resolution was increased inside the Gulf with each iteration. The final mesh had a resolution of 500 m in the north GC and Midriff region and 1 km resolution at the entrance of the GC (Figure 3.23c). The validation against observations generally improved with the higher resolutions meshes, but did not improve significantly between meshes 3 and 4. Also, mesh 4 took 18 hours to run a month simulation, compared to 12 hours for mesh 3. Hence, I decided to use mesh 3 for the subsequent analysis in Chapters 4 and 5.

In the third set of sensitivity tests, different bed friction values and friction laws were tested. Numerous sensitivity tests were undertaken to assess model perform using a range of uniform and spatially varying bottom friction coefficients and the different friction law options that are available in TELEMAC (e.g., Nikuradse, Manning and Chézy formula). I followed the guidance outlined by Arcement and Schneider (1989) for selecting friction values. I tested the Nikuradse formula and varied the bottom coefficient between 0.01 and 0.03 (mm). Then I tested the Manning law with bottom coefficients ranging of 0.01 to 0.04 ($m^{1/3}/s$). Furthermore, I also tested a variety of bottom coefficient utilising the Chezy law with values between 5 and 100 ($m^{1/2}/s$). Overall, differences between the model predictions and measurements were lowest when the Manning's law was used to define friction and when a spatially uniform value of 0.030 ($m^{1/3}/s$) was used; and hence this was used for subsequent simulations.

In the fourth and final set of sensitivity tests, different bathymetric datasets were used. To assess the sensitivity of the model predictions to bathymetry, the model was run three times for a 30-day period in December 2015, using just bathymetry data from two well-known and well-used sources: (1) GEBCO_2014 (Kapoor, 1981); and (2) ETOPO (NOAA, 2017), which are available at resolutions of ~900 m and ~775 m, respectively. A third run used the GEBCO data merged with the higher resolution data from CICESE (Figure 3.3c), for the Midriff region and the northern GC. The three model bathymetries are shown in Figures 3.25, 3.26 and 3.27, respectively. Percentage errors between predicted and measured tidal levels were calculated, for each of the three different bathymetries, at each of the 11 tide gauge stations, and are listed in Table 3.7. The results indicated that the percentage error are overall lower for the third run, where the GEBCO and CICESE bathymetric datasets are merger. A comparison of the u and v velocity components of the observations and model results using three bathymetry products are show in Figures 3.28 and 3.29. The results indicate that the predictions were more accurate when the combined bathymetry dataset (GEBCO merged with CICESE) was used. The RMSE improved, reducing from a mean of 25% to less than 11% for the GEBCO and CICESE merged dataset (Table 3.8). Therefore, and this will be stressed again in Chapters 4 and 5, the results caution the used of applying global bathymetric data products for tidal-energy resource assessment in regions where relatively little 'freely available' data is accessible.

Finally, potential future work is outlined that could improve help improve assessment of model performance and validation. The validation exercise has been undertaken using tidal levels at 11 tide gauge sites, with a reasonable spatial spread across much of the model domain. However, there were large gaps in the data record for some months. Therefore, in order to validate the model against observations, just the data from December 2015 was considered, consequently the model was run along for this month (as previously explained in Section 3.2.3). Moreover, ADCP observations data were only available from four sites in the vicinity of the Midriff region. Ideally, data from a much larger selection of sites, better spread across the model domain would be considered. Like all other resource assessment studies, there were certain limitation with regards to the existing data and its availability.

3.5 Conclusions

This chapter has described the configuration and validation of the depth-averaged hydrodynamic model that will subsequently be used in Chapters 4 and 5 to quantify the tidal-range and tidal-stream energy resource in the region. The model has been compressively validated against available measured water level and current meter data. Overall, it has been shown that the model accurately captures both tidal levels and tidal currents across the region and is therefore suitable for the energy resource assessments carried out in Chapters 4 and 5.

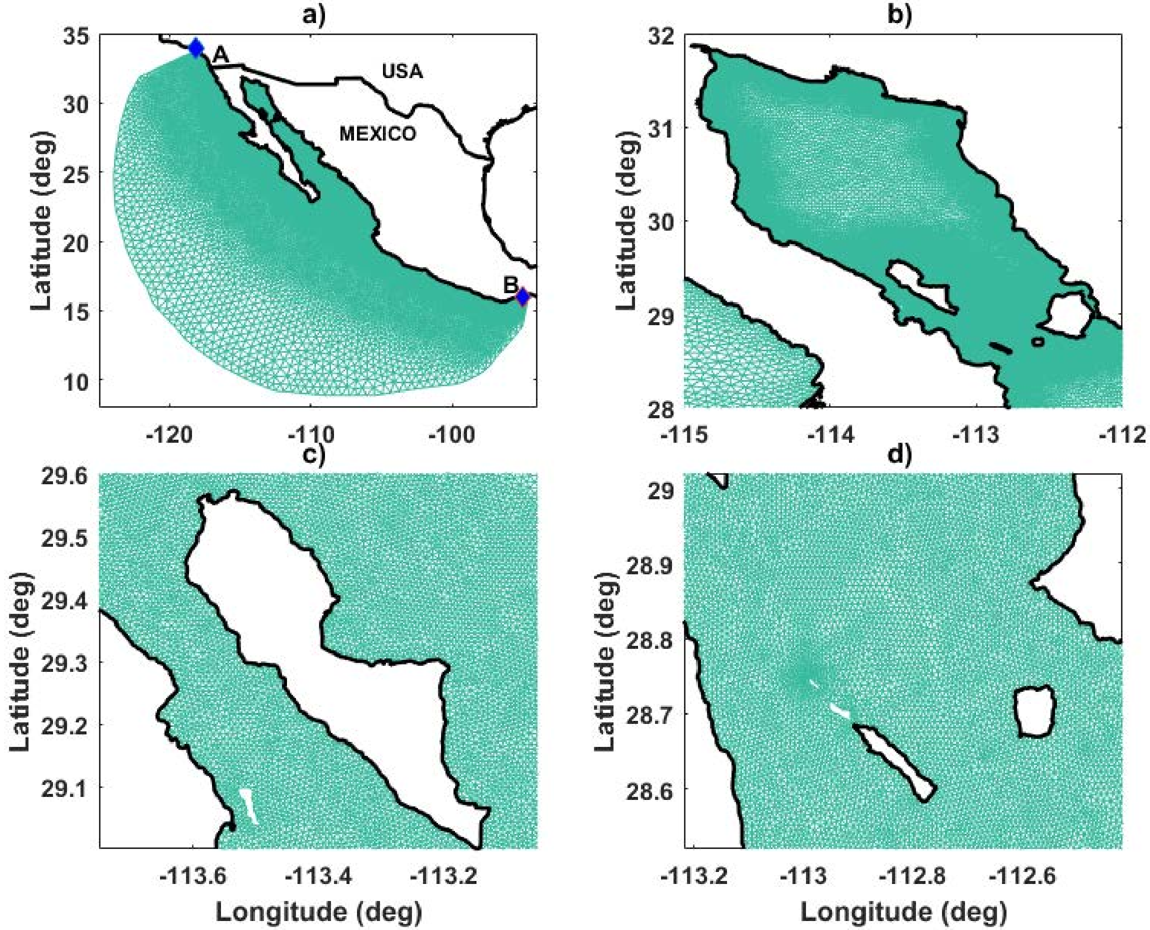

Figure 3.1. Model mesh for four regions: (a) the full domain; (b) the northern GC around the midriff Island (c) the central GC around Ballenas Channel; and (d) the central GC around San Lorenzo and San Esteban (San Lorenzo Passage). Blue Diamonds represent the northern and southern Boundary conditions.

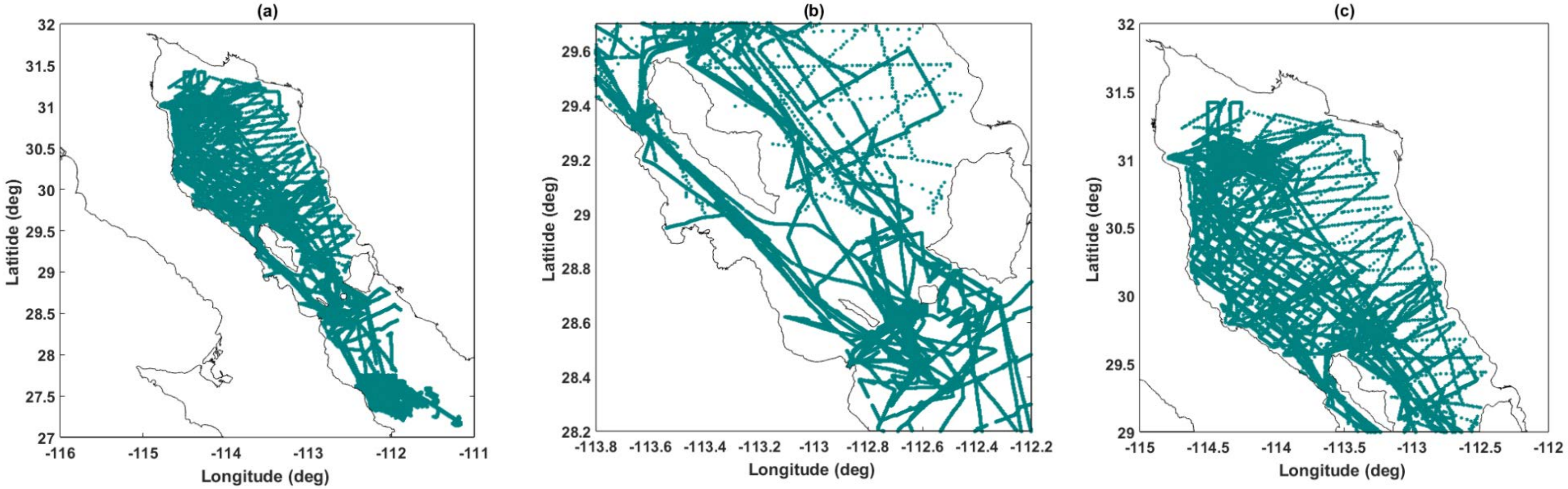

Figure 3.2. Bathymetry survey by CICESE research centre for the: (a) GC; (b) Midriff area; and (c) northern GC.

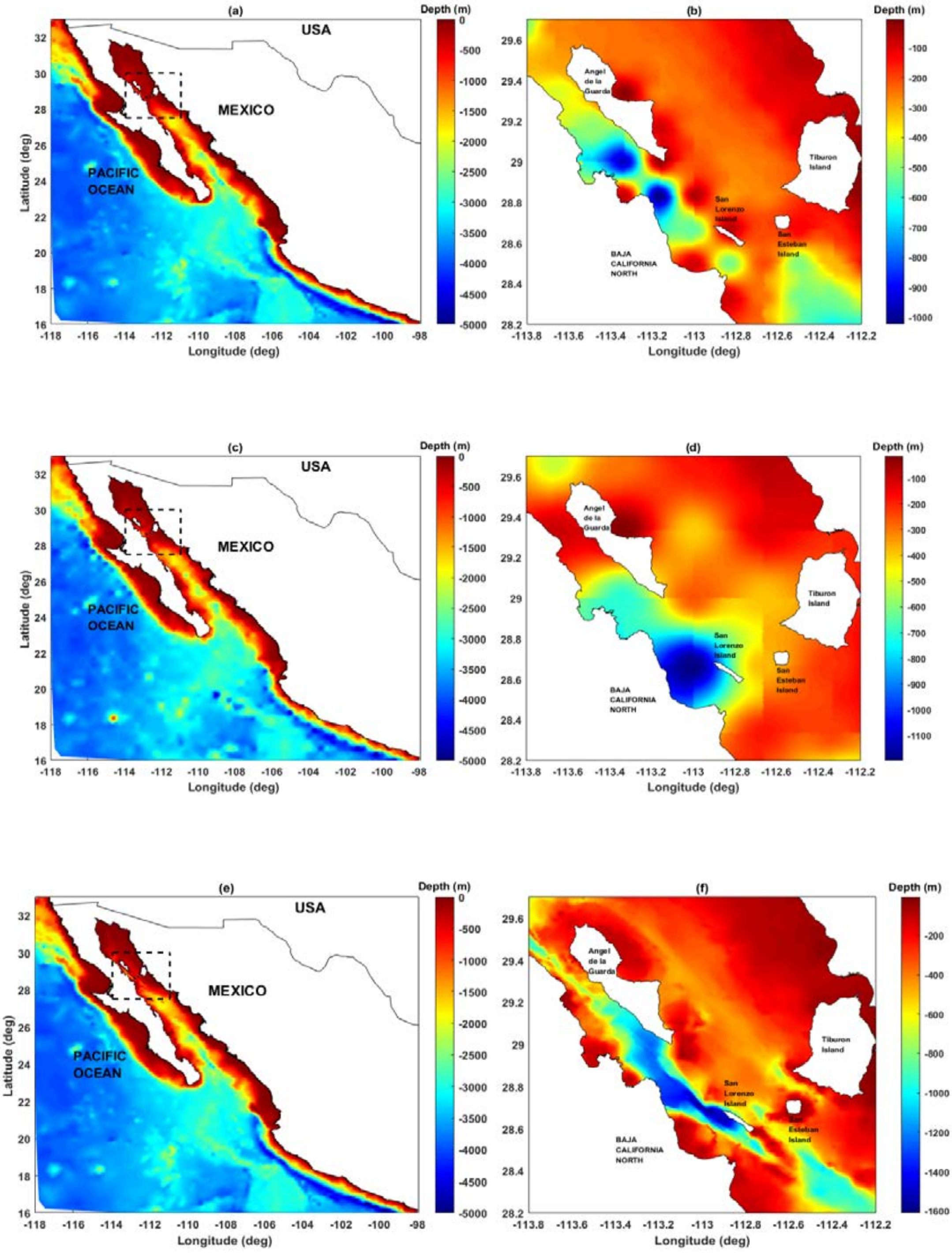

Figure 3.3. Model bathymetry created using (a, b) just GEBCO, (c, d) just ETOPO and (e, f) GEBCO and CICESE merged, for the (a, c, e) whole model domain and (b, d, f) just the Midriff area.

(a)

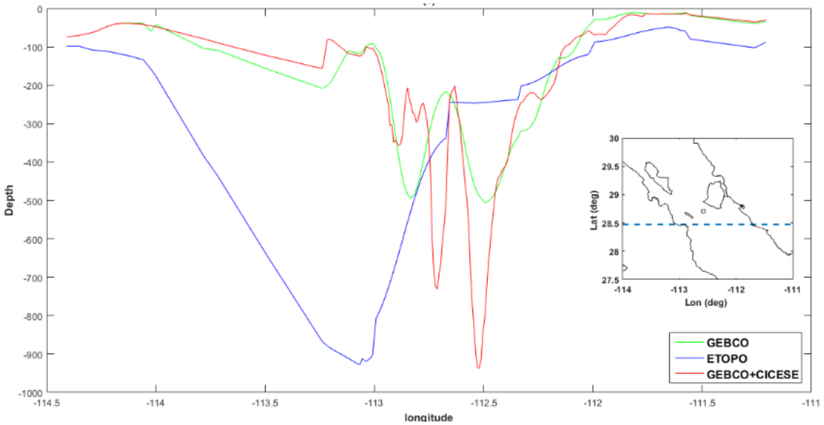
Depth
0
-100
-200
-300
-400
-500
-600
-700
-800
-900
-1000
-114.5
-114
-113.5
-113
-112.5
-112
-111.5
-111
longitude
Lat (deg)
30
29.5
29
28.5
28
27.5
-114
-113
-112
-111
Lon (deg)
GEBCO
ETOPO
GEBCO+CICESE

(b)

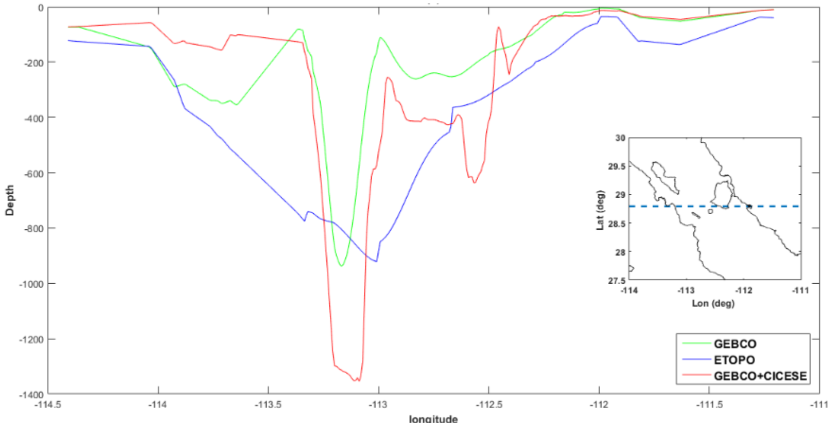
Depth
0
-200
-400
-600
-800
-1000
-1200
-1400
-114.5
-114
-113.5
-113
-112.5
-112
-111.5
-111
longitude
Lat (deg)
30
29.5
29
28.5
28
27.5
-114
-113
-112
-111
Lon (deg)
GEBCO
ETOPO
GEBCO+CICESE

(c)

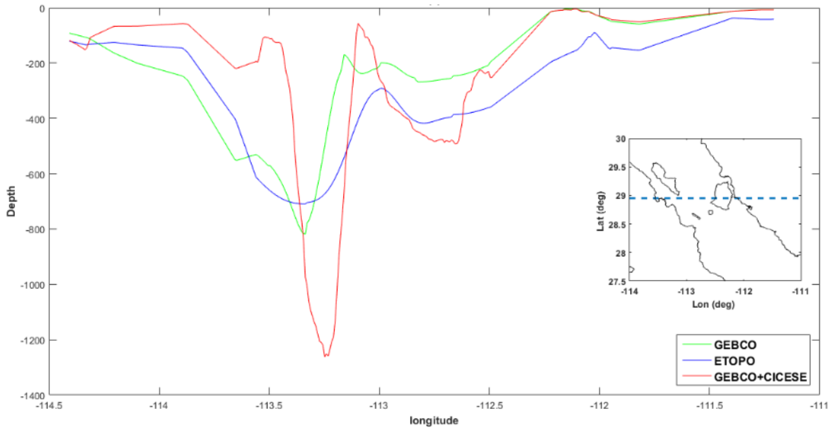
Depth
0
-200
-400
-600
-800
-1000
-1200
-1400
-114.5
-114
-113.5
-113
-112.5
-112
-111.5
-111
longitude
Lat (deg)
30
29.5
29
28.5
28
27.5
-114
-113
-112
-111
Lon (deg)
GEBCO
ETOPO
GEBCO+CICESE

(d)

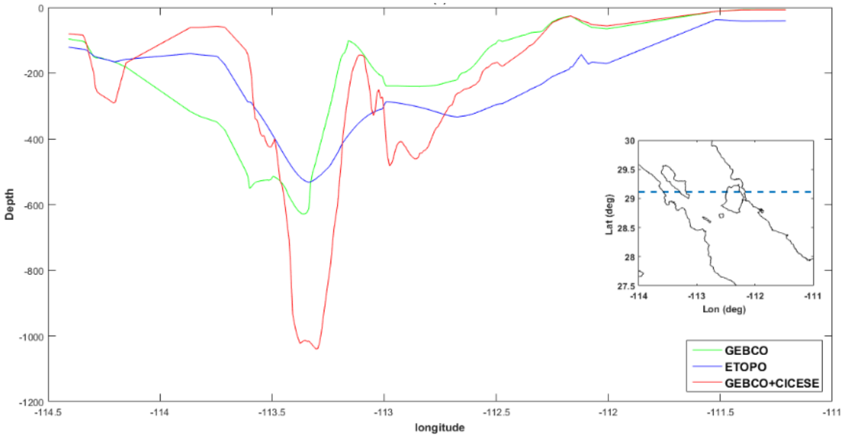
Depth
0
-200
-400
-600
-800
-1000
-1200
-114.5
-114
-113.5
-113
-112.5
-112
-111.5
-111
longitude
Lat (deg)
30
29.5
29
28.5
28
27.5
-114
-113
-112
-111
Lon (deg)
GEBCO
ETOPO
GEBCO+CICESE

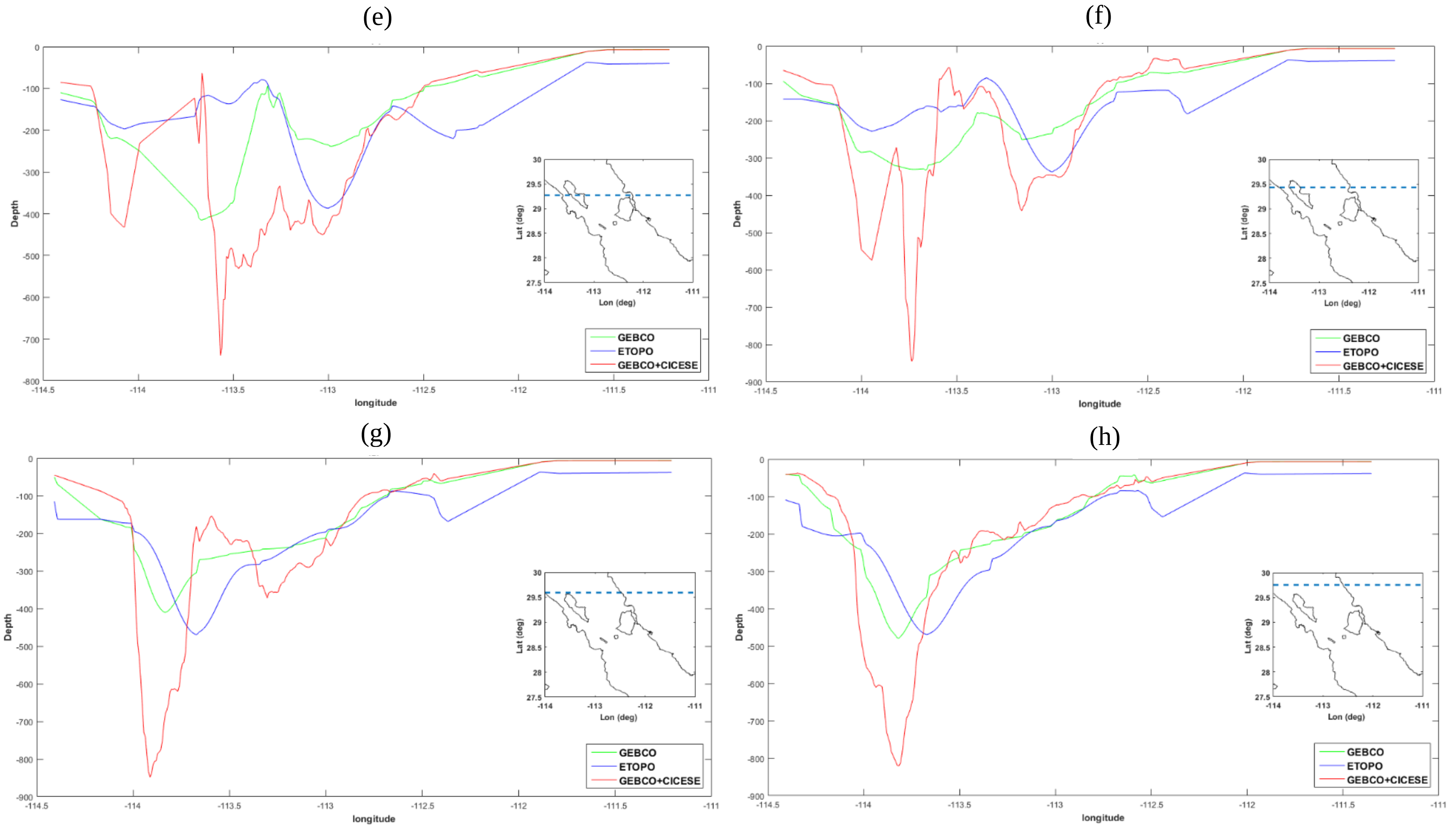

Figure 3.4. Bathymetric cross-sectional profile (location showed in inlay in panel a) considering: just GEBCO, just ETOPO and GEBCO merged with CICESE, data sets, Y axis is depth in m.

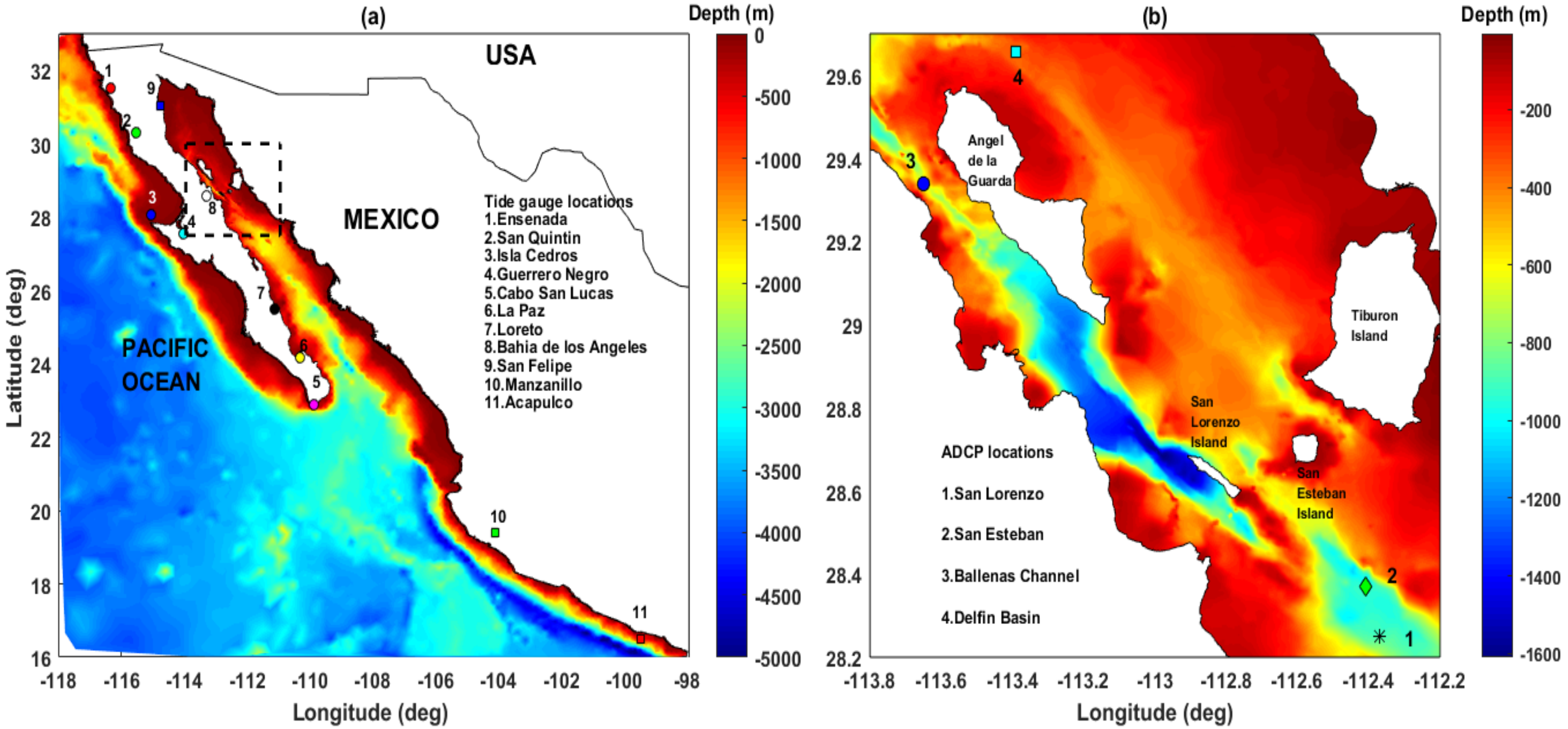

Figure 3.5. Location of the study area with water depth for the: (a) GC and the Pacific Ocean, with locations of the tide gauge sites; and (b) the Midriff region, with the locations of the ADCP sites.

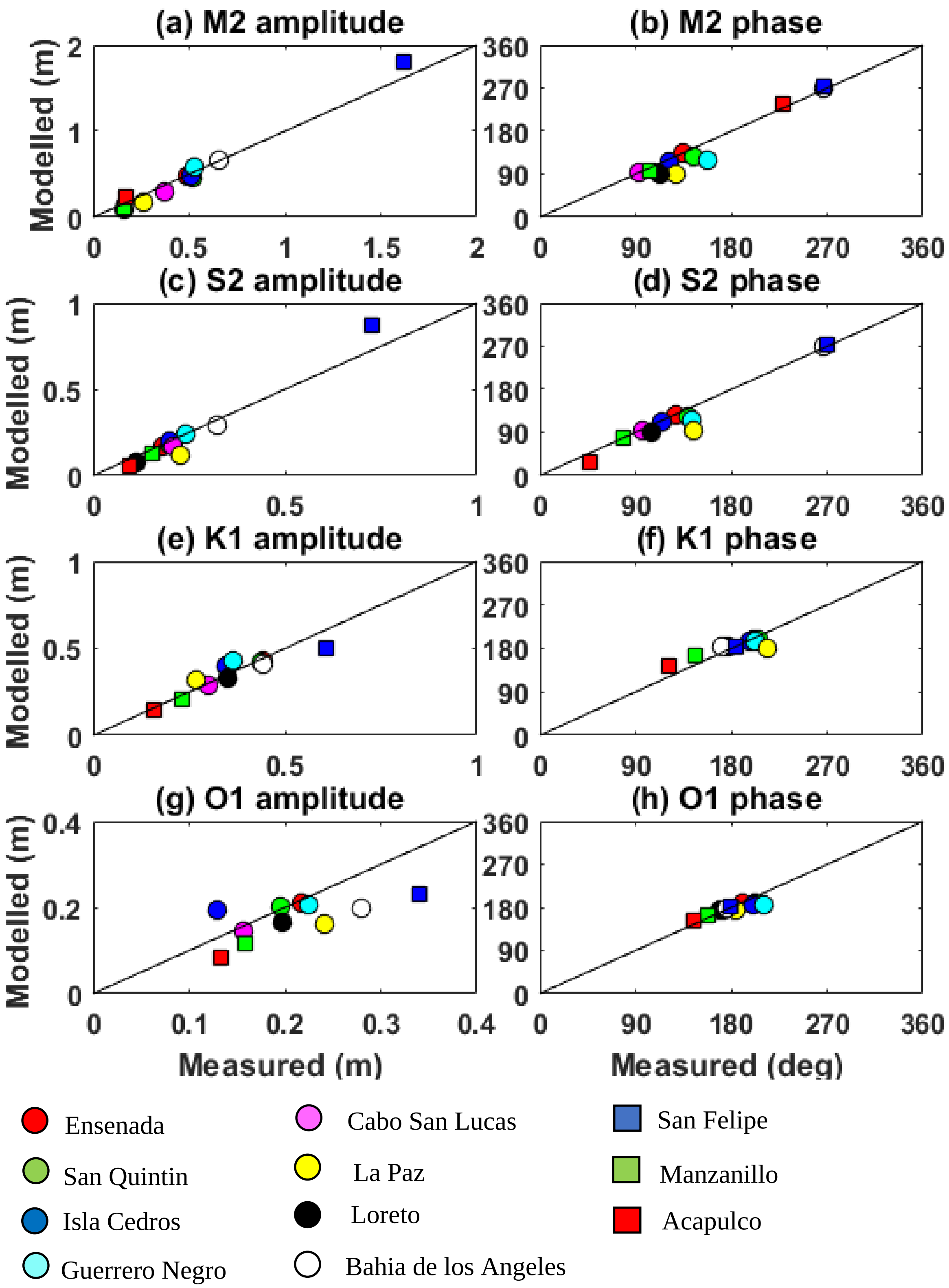

Figure 3.6. Comparison of the measured and predicted amplitudes and phases of the four main tidal constituents for the 11 tide gauge sites.

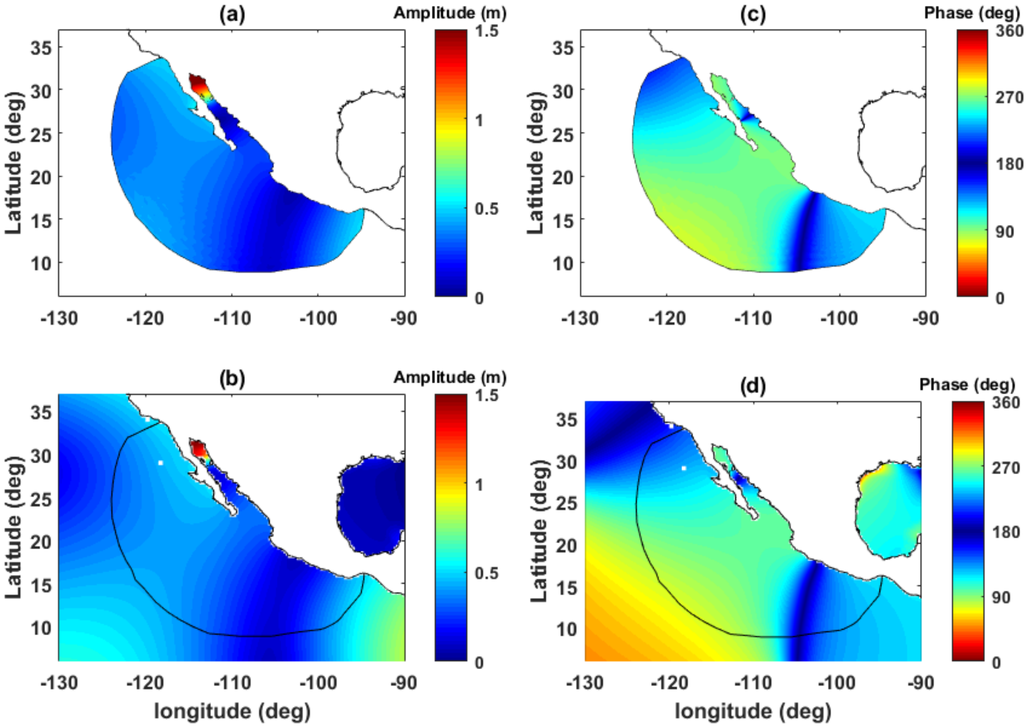

Figure 3.7. Tidal elevation amplitude M2 model (a) Otis model (b), phase M2 model (c) Otis model (d).

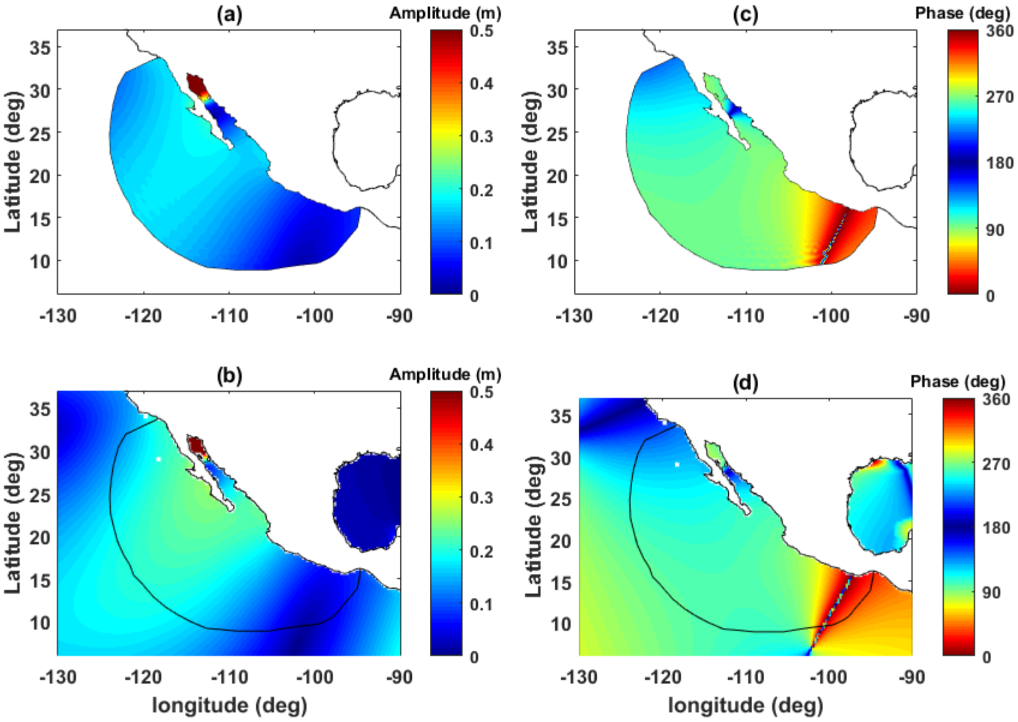

Figure 3.8. Tidal elevation amplitude S2 model (a) Otis model (b), phase S2 model (c) Otis model (d).

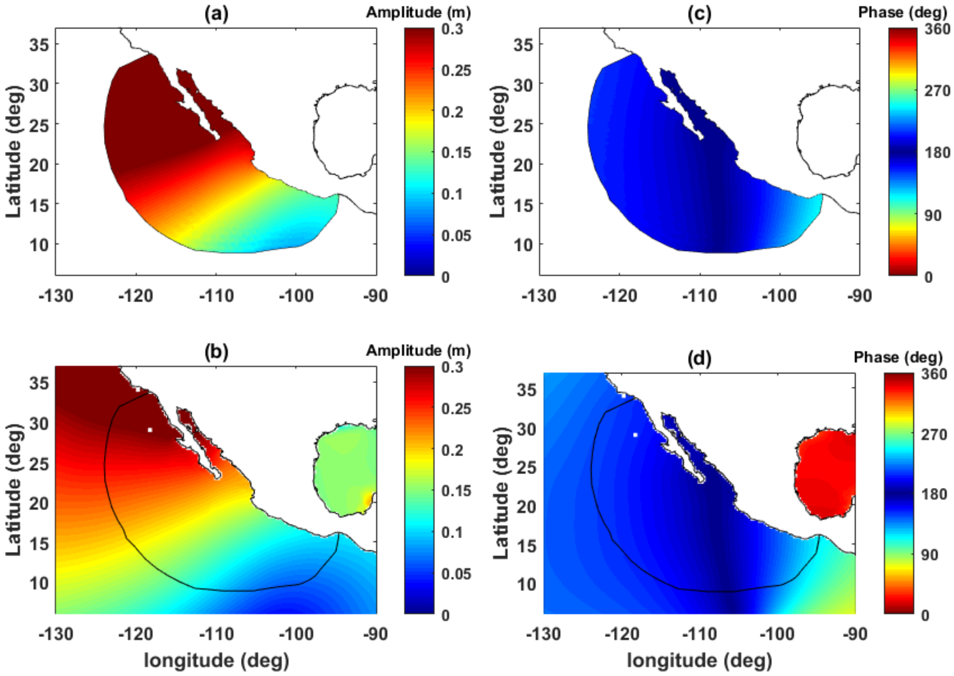

Figure 3.9. Tidal elevation amplitude K₁ model (a) Otis model (b), phase K₁ model (c) Otis model (d).

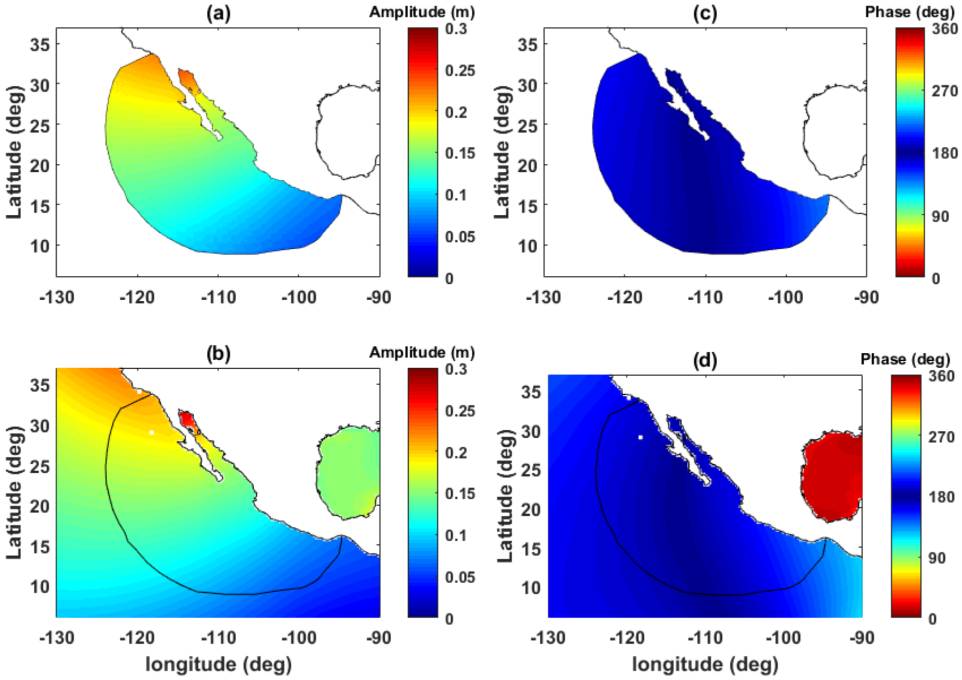

Figure 3.10. Tidal elevation amplitude O₁ model (a) Otis model (b), phase O₁ model (c) Otis model (d).

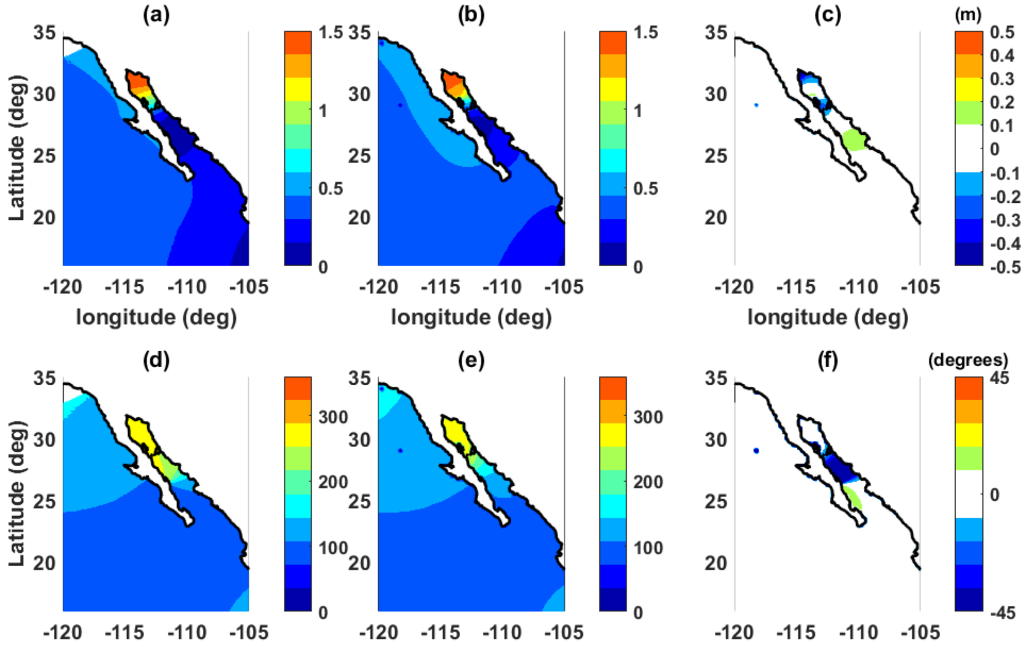

Figure 3.11. Differences between amplitude M_2 tidal constituent (a) Model, (b) Otis and (c) Differences model vs OTIS. Differences phase M_2 tidal constituent (d) Model, (e) OTIS and (f) Differences phase model vs OTIS.

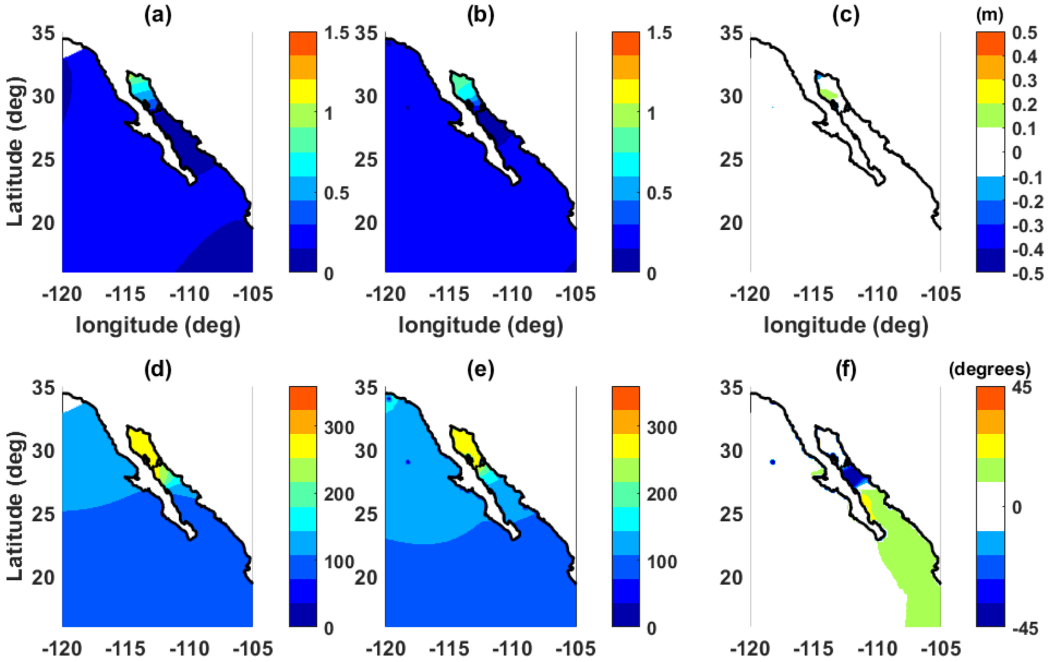

Figure 3.12. Differences between amplitude S_2 tidal constituent (a) Model, (b) Otis and (c) Differences model vs OTIS. Differences phase S_2 tidal constituent (d) Model, (e) OTIS and (f) Differences phase model vs OTIS.

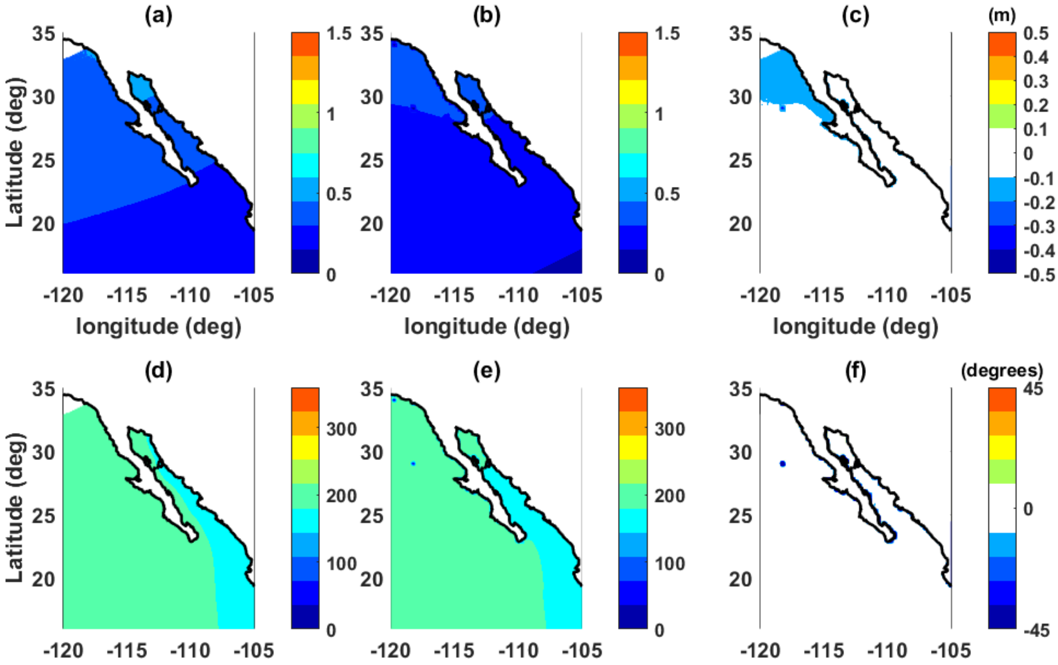

Figure 3.13. Differences between amplitude K_1 tidal constituent (a) Model, (b) Otis and (c) Differences model vs OTIS. Differences phase K_1 tidal constituent (d) Model, (e) OTIS and (f) Differences phase model vs OTIS.

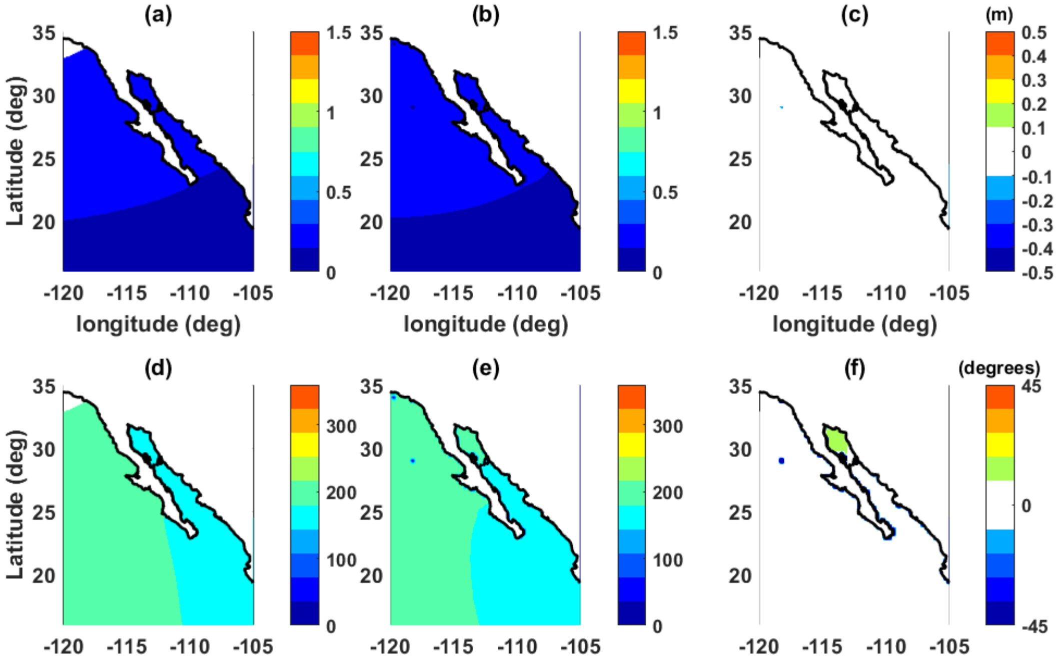

Figure 3.14. Differences between amplitude O_1 tidal constituent (a) Model, (b) Otis and (c) Differences model vs OTIS. Differences phase O_1 tidal constituent (d) Model, (e) OTIS and (f) Differences phase model vs OTIS.

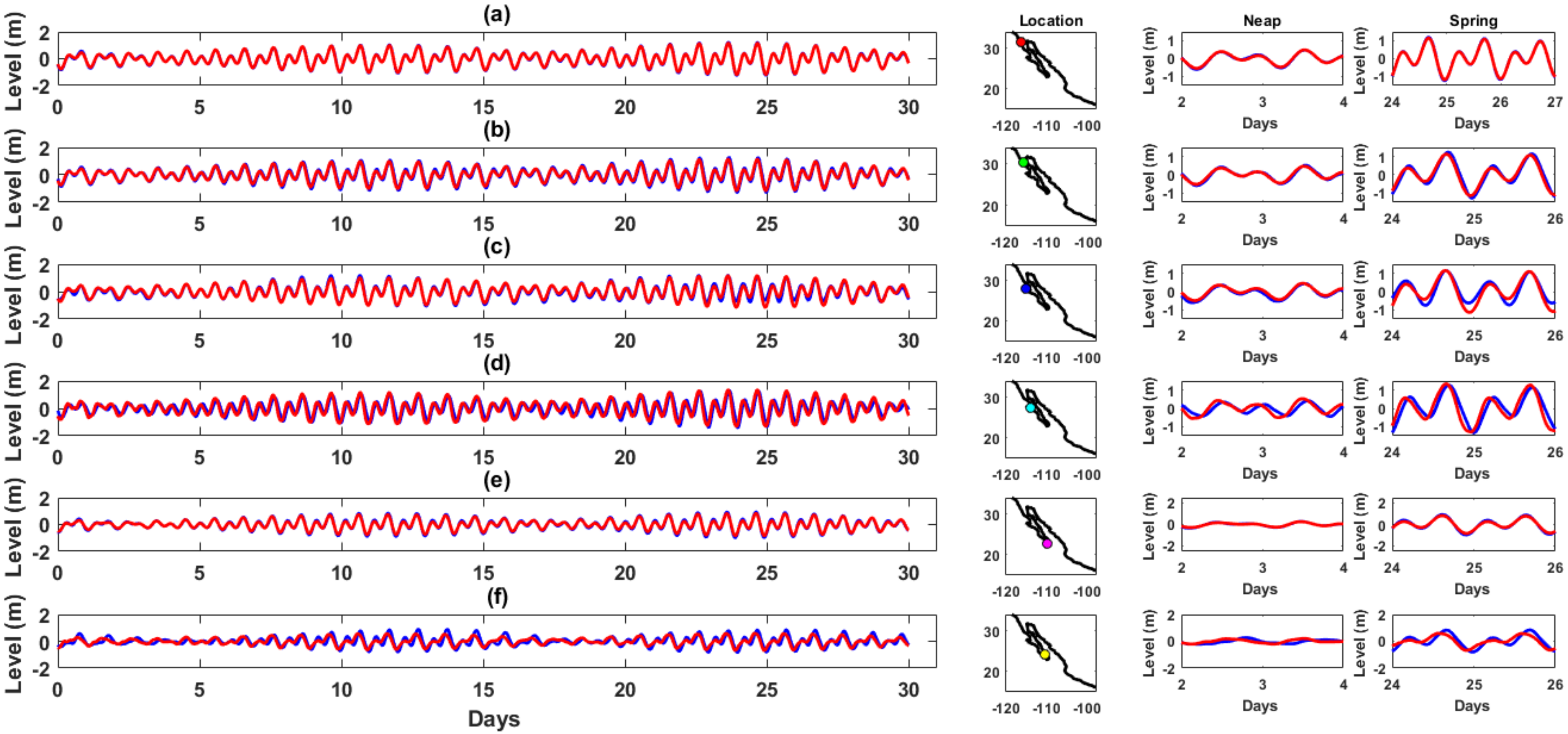
(a)
(b)
(c)
(d)
(e)
(f)
Level (m)
2
0
-2
0
5
10
15
20
25
30
Days
Location
30
20
-120
-110
-100
Neap
Spring
1
0
-1
2
3
4
24
25
26
27
Days

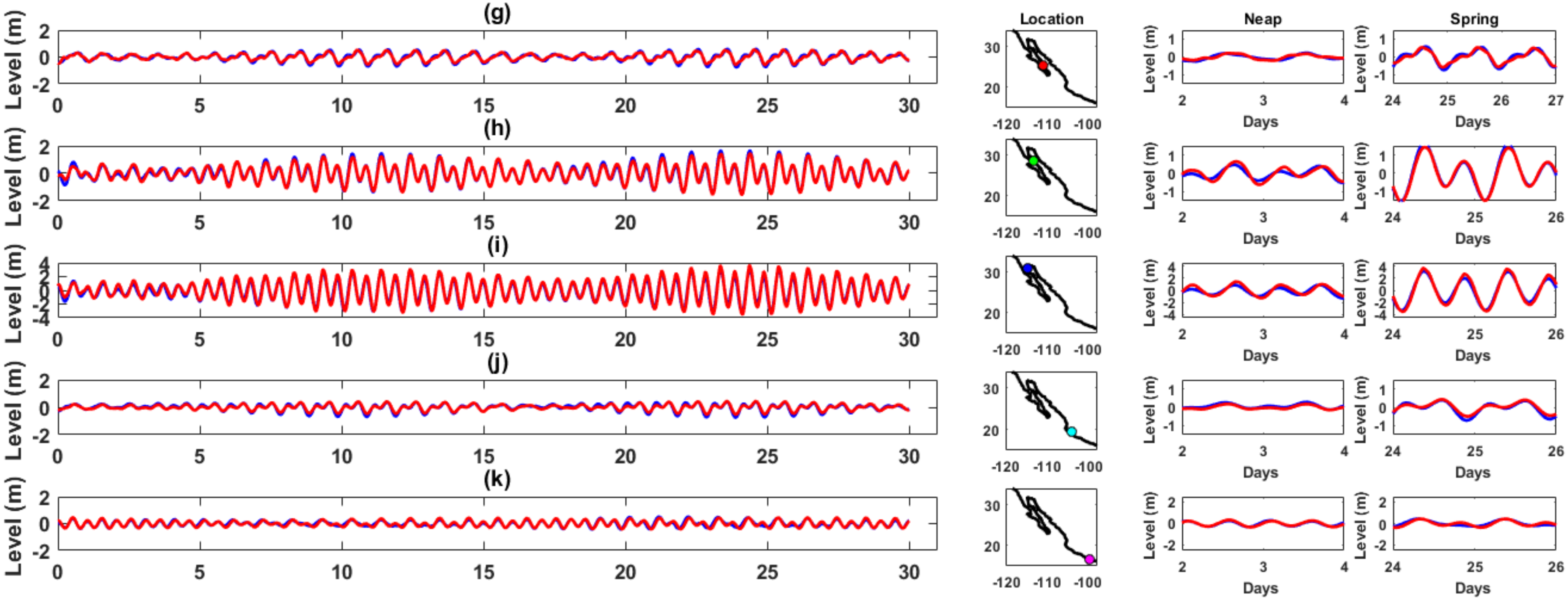

Figure 3.15. Comparison of the measured (blue) and predicted (red) tidal time-series at: (a) Ensenada; (b) San Quintin); (c) Isla Cedros; (d) Guerrero Negro; (e) Cabo San Lucas (f) La Paz; (g) Loreto; (h) Bahia de los Angeles; (i) San Felipe; (j) Manzanillo; (k) Acapulco.

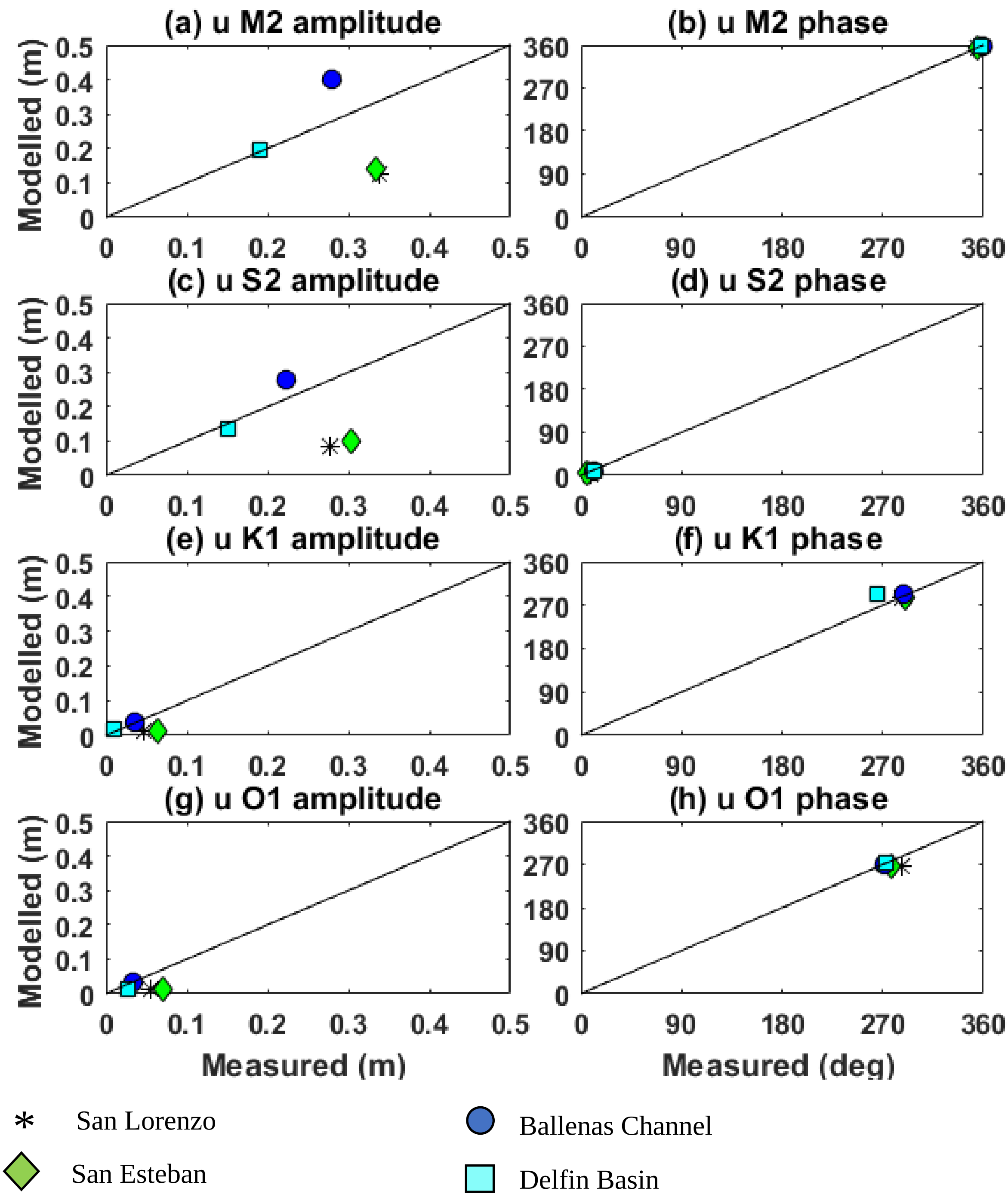

Figure 3.16. Comparison of the measured and predicted u velocity amplitudes and phases at the four ADCP sites for the: (a) M_2 amplitude; (b) M_2 phase; (c) S_2 amplitude; (d) S_2 phase; (e) K_1 amplitude; (f) K_1 phase; (g) O_1 amplitude; and (h) O_2 phase.

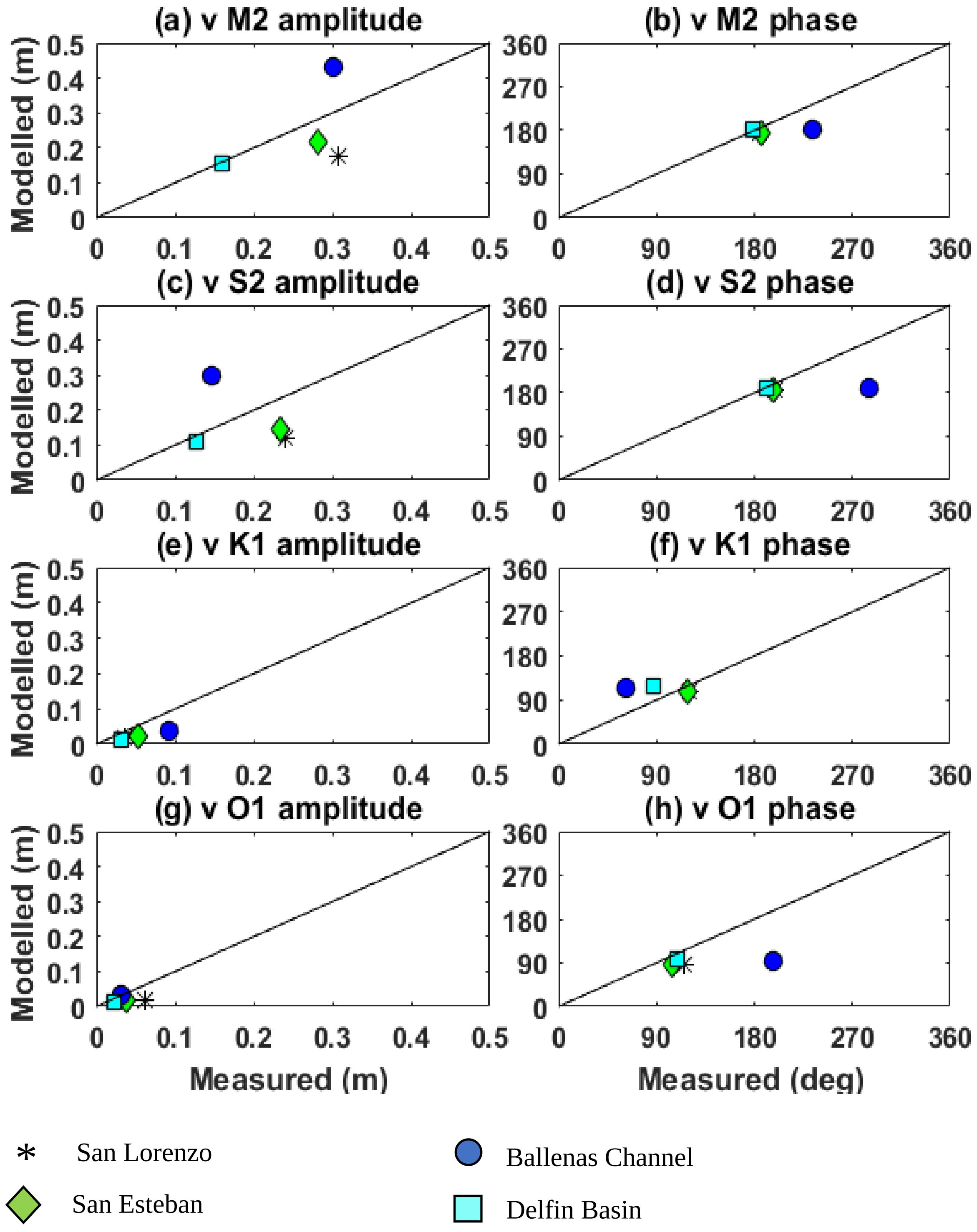

Figure 3.17. Comparison of the measured and predicted v velocity amplitudes and phases at the four ADCP sites for the: (a) M_2 amplitude; (b) M_2 phase; (c) S_2 amplitude; (d) S_2 phase; (e) K_1 amplitude; (f) K_1 phase; (g) O_1 amplitude; and (h) O_2 phase.

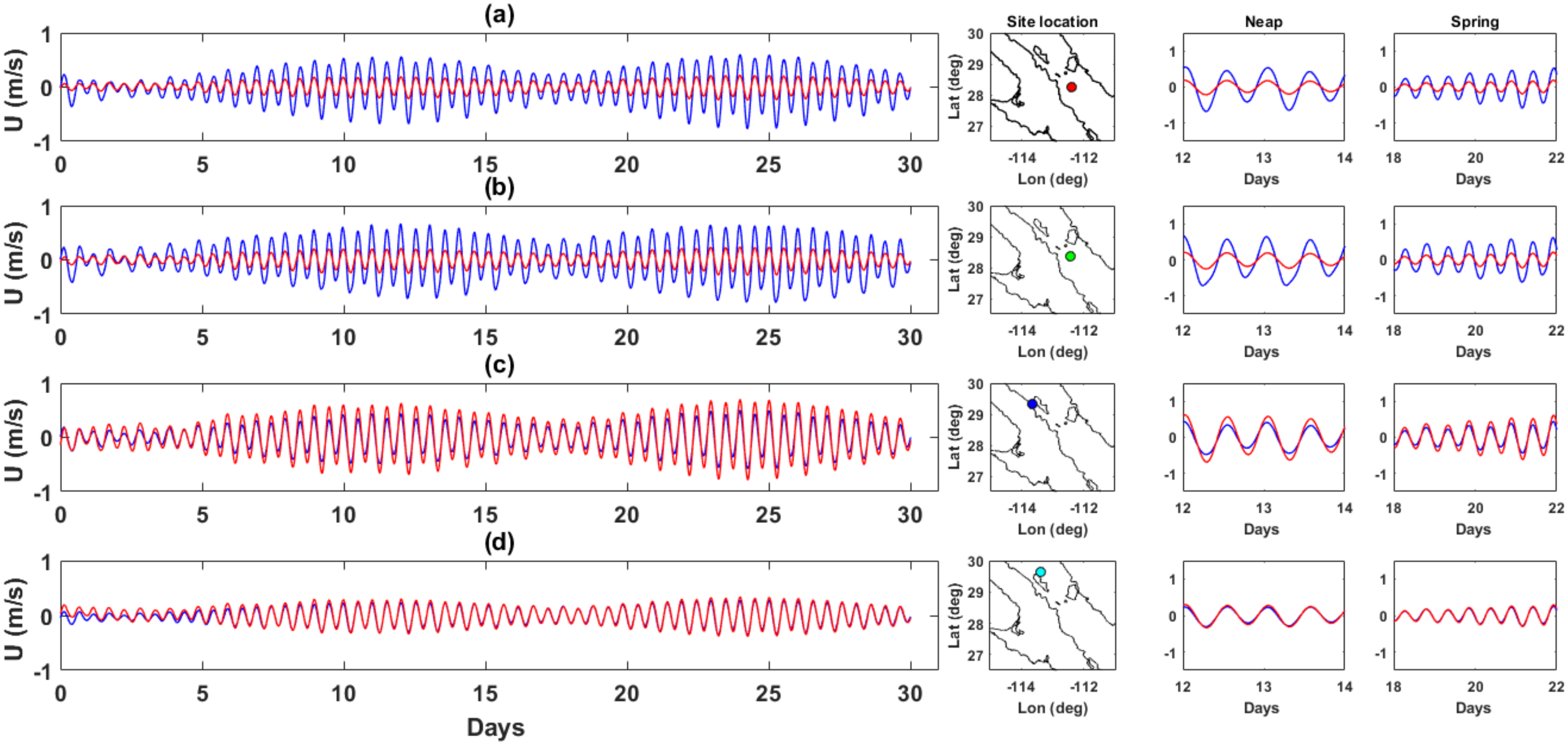

Figure 3.18. Comparison of the observations (blue) and model results (red) u velocity component (eastward velocity), neap and spring. (a) San Lorenzo (b) San Esteban, (c) Ballenas Channel and (d) Delfin Basin.

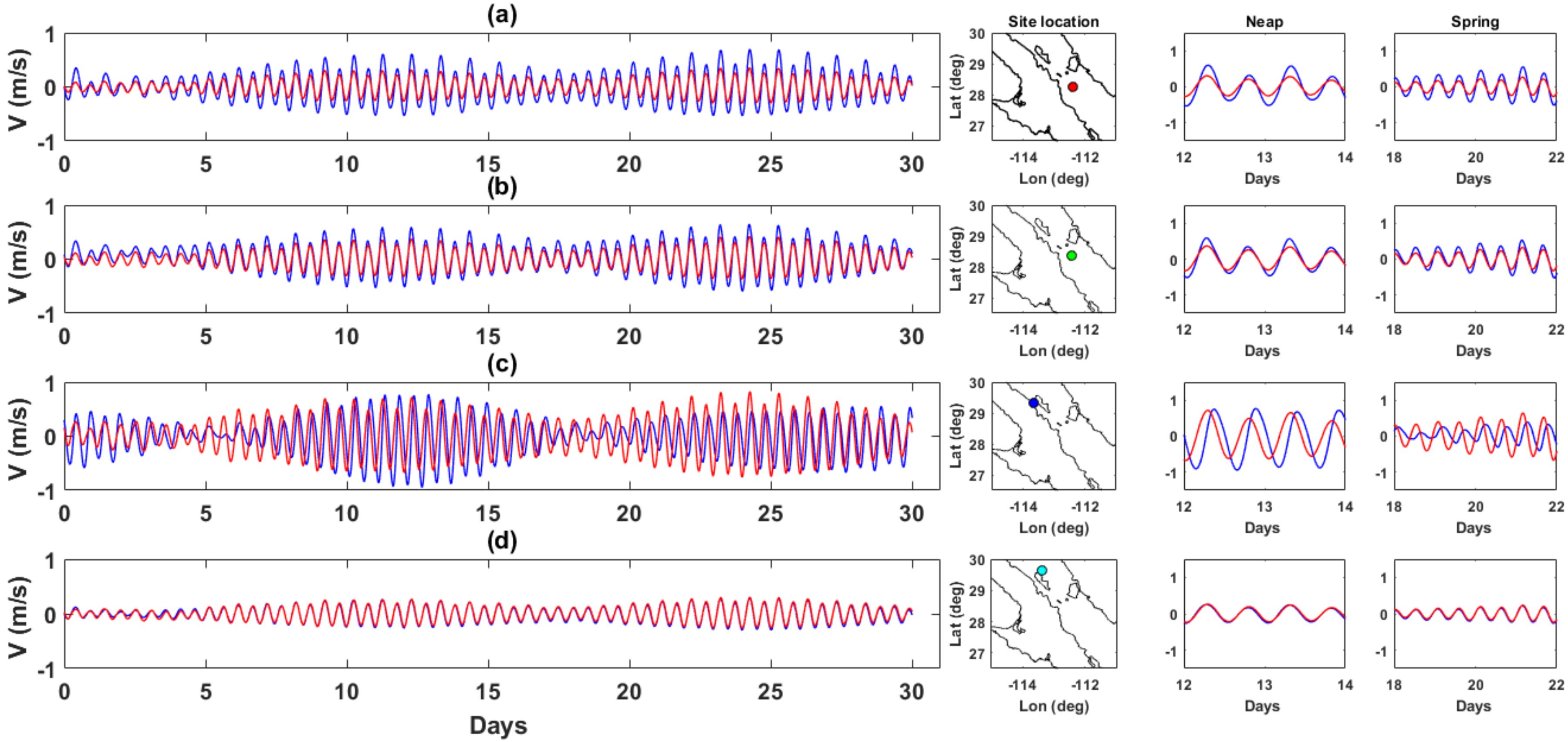

Figure 3.19. Comparison of the observations (blue) and model results (red) v velocity component (northward velocity), neap and spring. (a) San Lorenzo (b) San Esteban, (c) Ballenas Channel and (d) Delfin Basin.

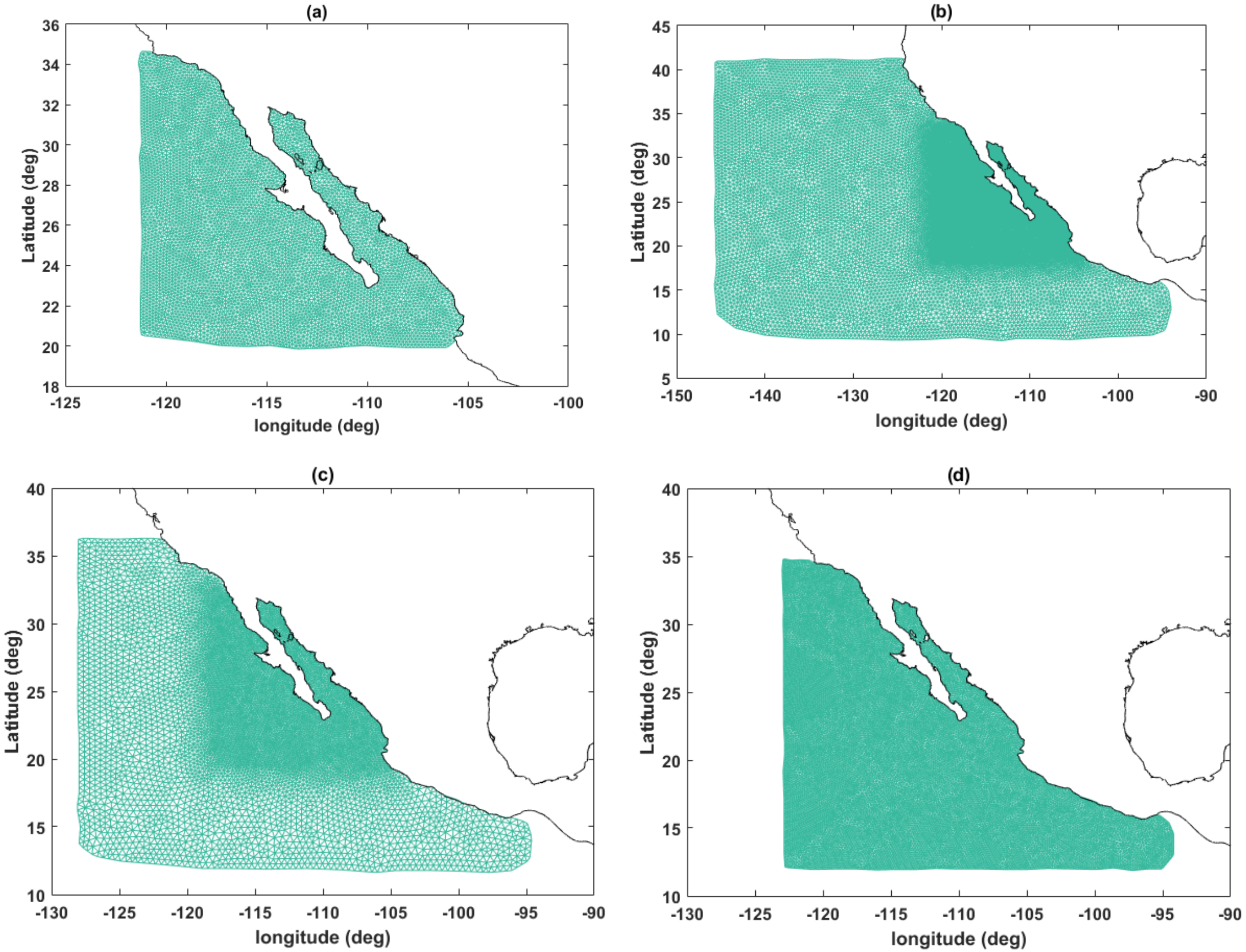

Figure 3.20. Example of different domain areas previously set up in around the GC.

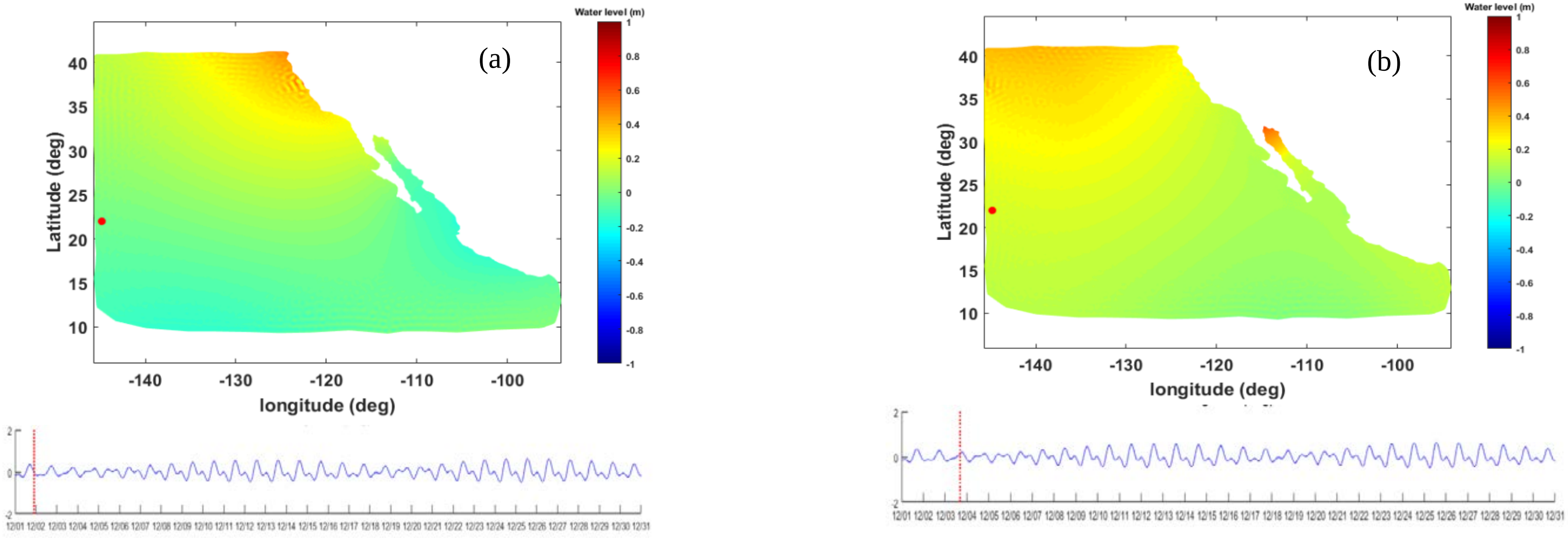

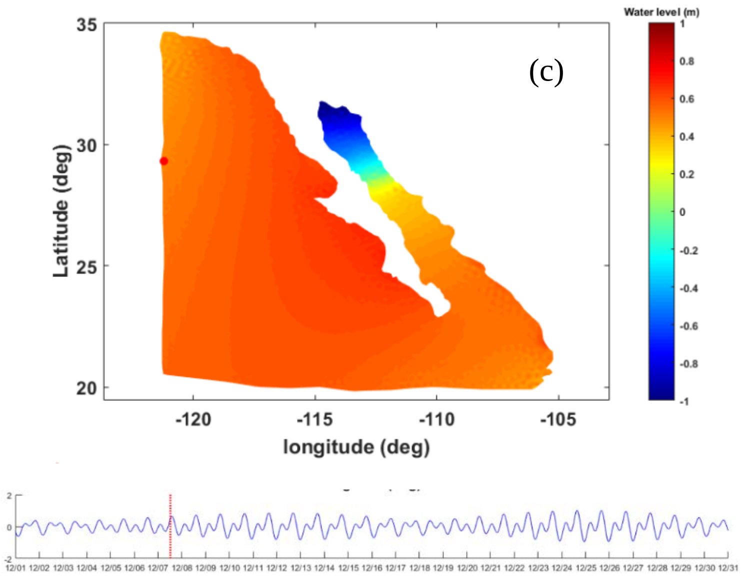

Figure 3.21. (a) Instabilities in the northern boundary (b) Instabilities in the open boundary and (c) instabilities in the west boundary conditions utilising different model domain.

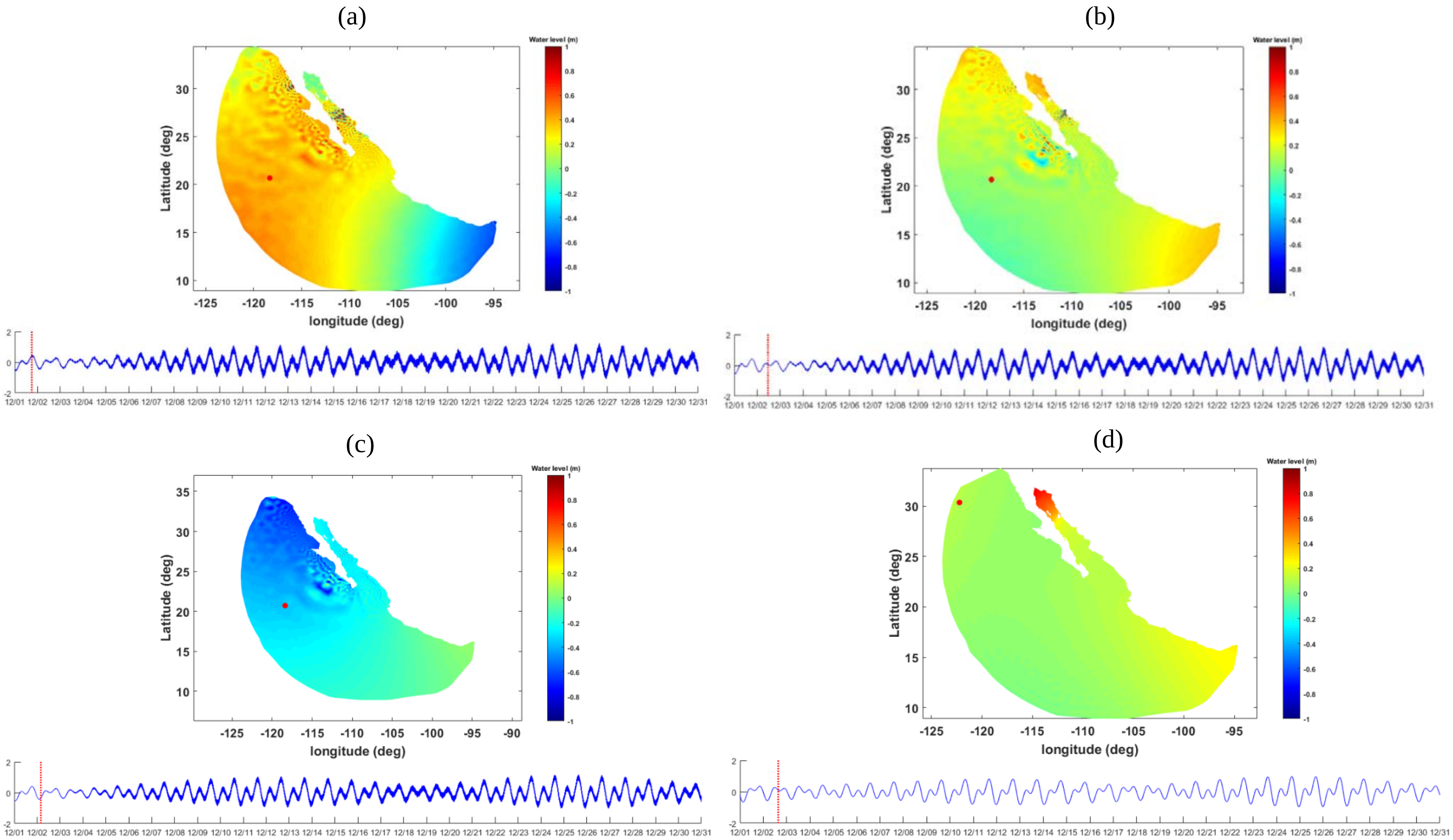

Figure 3.22. Model instabilities with rounded domain areas (a) Instable northern using 0.01 bottom coefficient (b) model instability using 0.015 (c) model instability in the central domain area using 0.018 (d) stable model final domain area using 0.030 bottom coefficient.

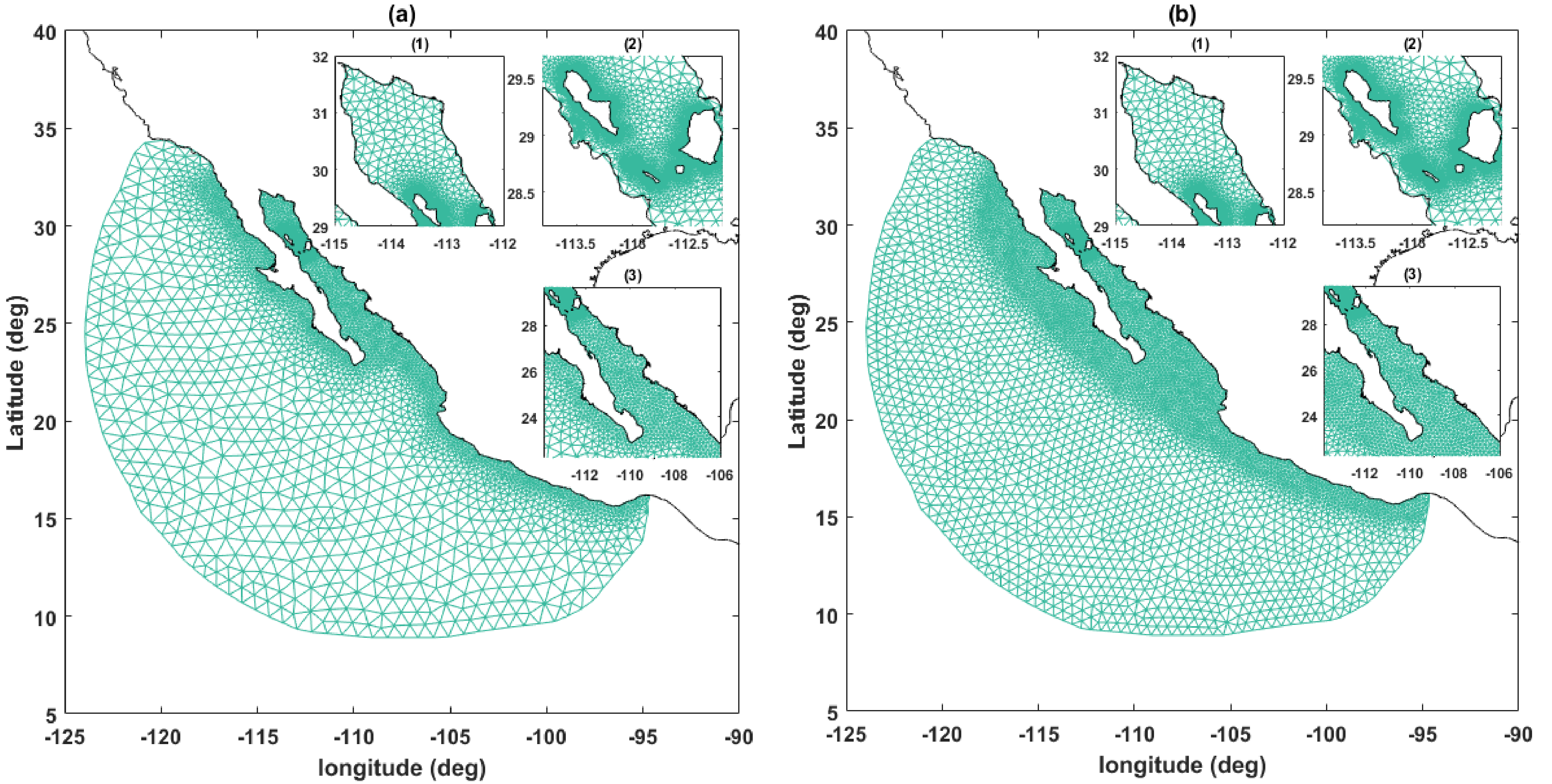
(a)
(b)
(1)
(2)
(3)
Latitude (deg)
longitude (deg)
40
35
30
25
20
15
10
5
-125
-120
-115
-110
-105
-100
-95
-90
32
31
30
29
-115
-114
-113
-112
29.5
29
28.5
-113.5
-113
-112.5
28
26
24
-112
-110
-108
-106

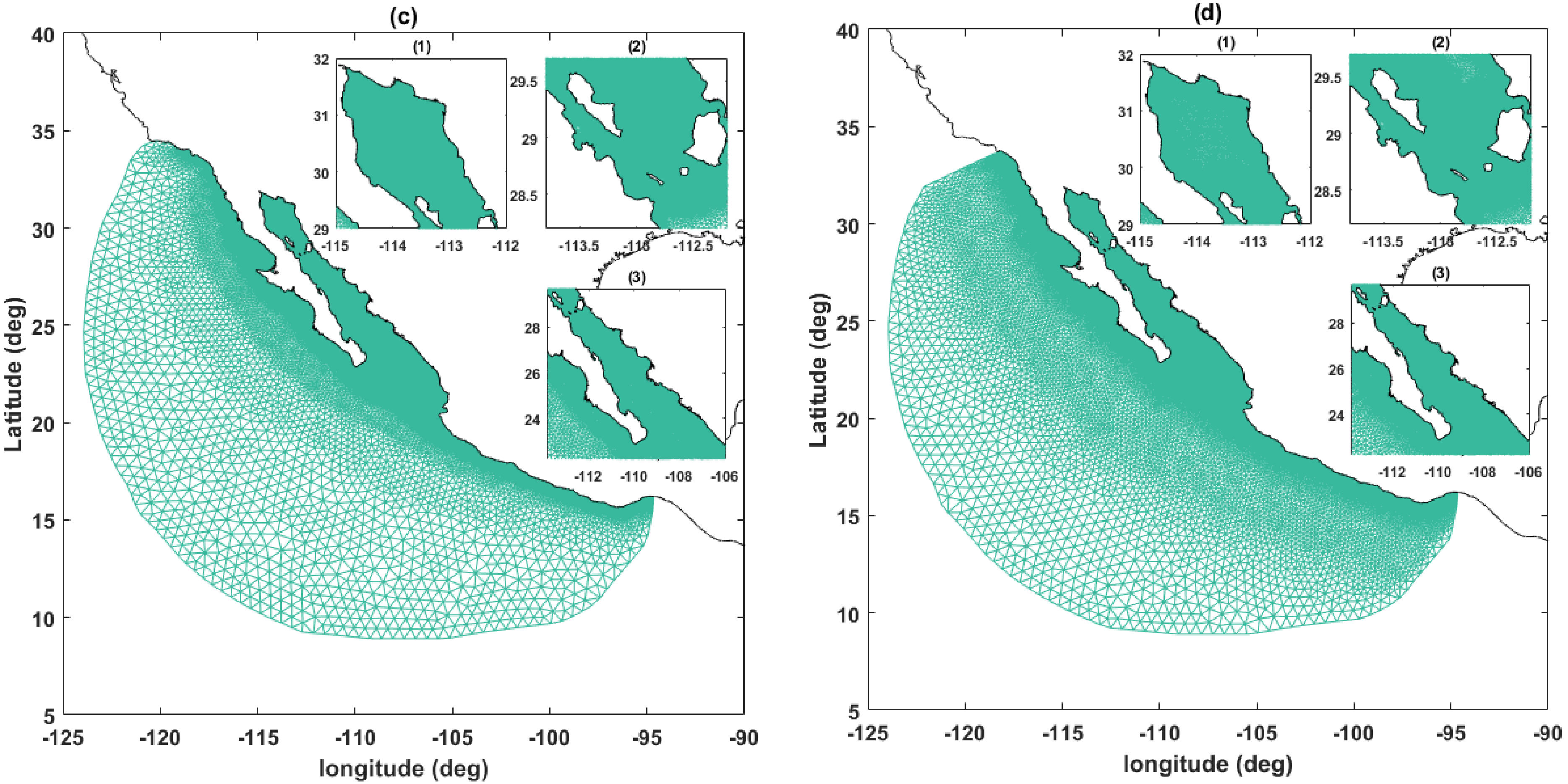

Figure 3.23. a) Square mesh resolution with 6031 nodes and 11012 elements (b) medium mesh resolution with 7797 nodes and 14498 elements, (c) Slightly refine mesh with 83969 nodes, 160757 elements (d) final refine mesh with 38181 nodes and 133779 elements; (1) Northern GC, (2) Midriff area and (3) Southern GC.

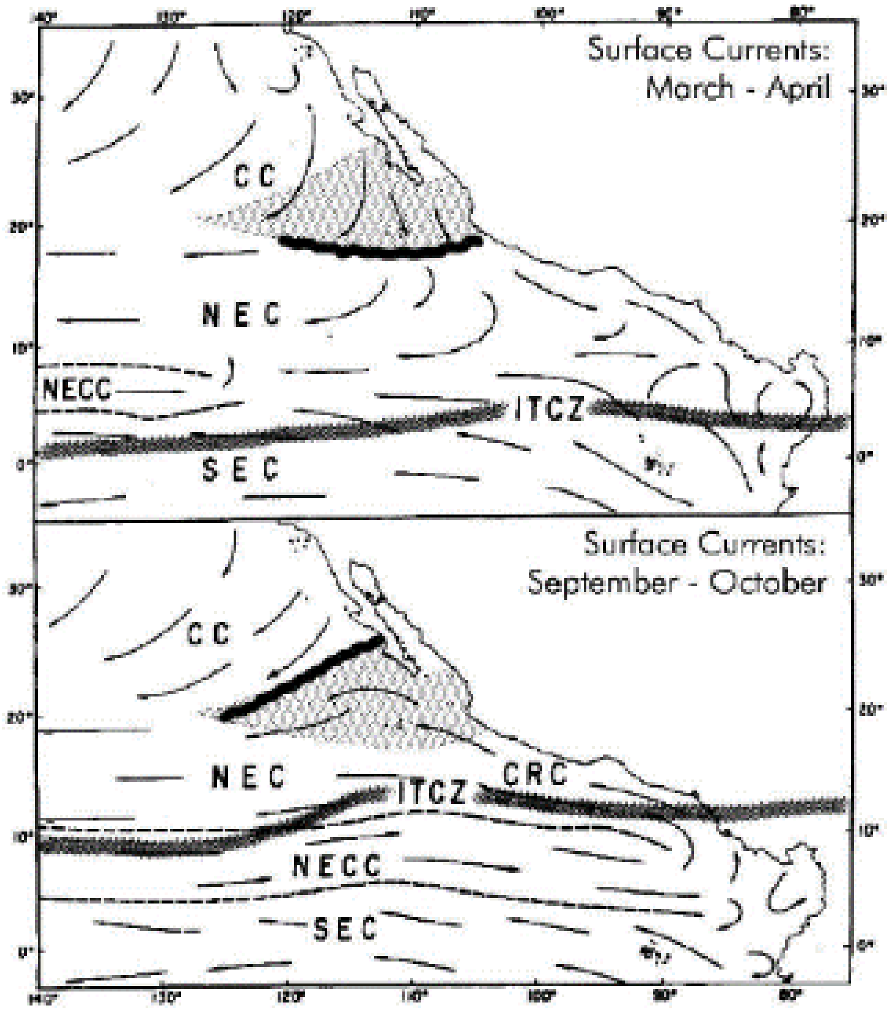

Figure 3.24. The California currents limitations in (a) and (b) are indicated by a wavy band. Based on Wyrtki (1965) and Baumgartner and Christensen (1985). NEC= North Equatorial Current. Inter-Tropical Convergence Zone, SEC= South Equatorial Current.

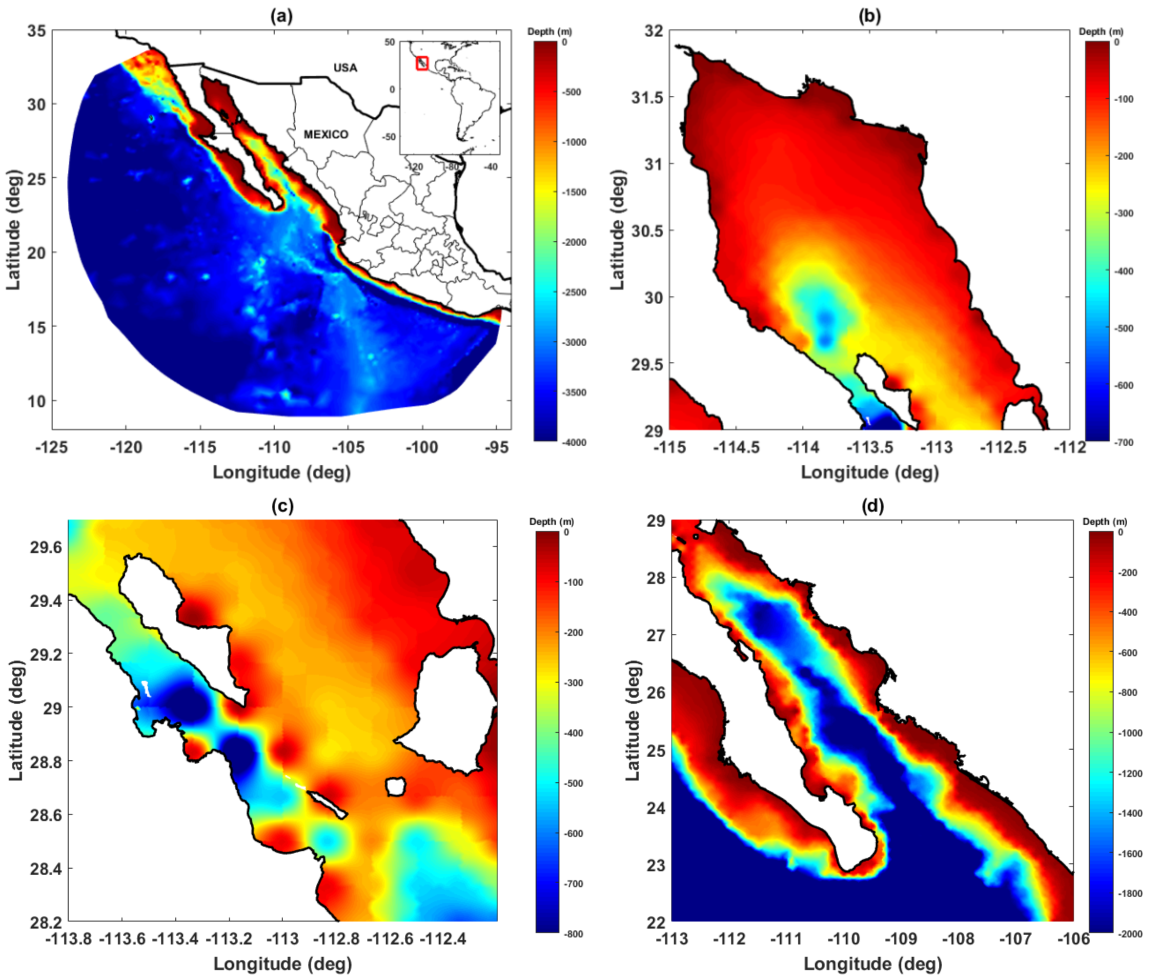

Figure 3.25. Bathymetry GEBCO alone, (a) All domain area, (b) Northern GC, (c) Midriff area, (d) Southern GC.

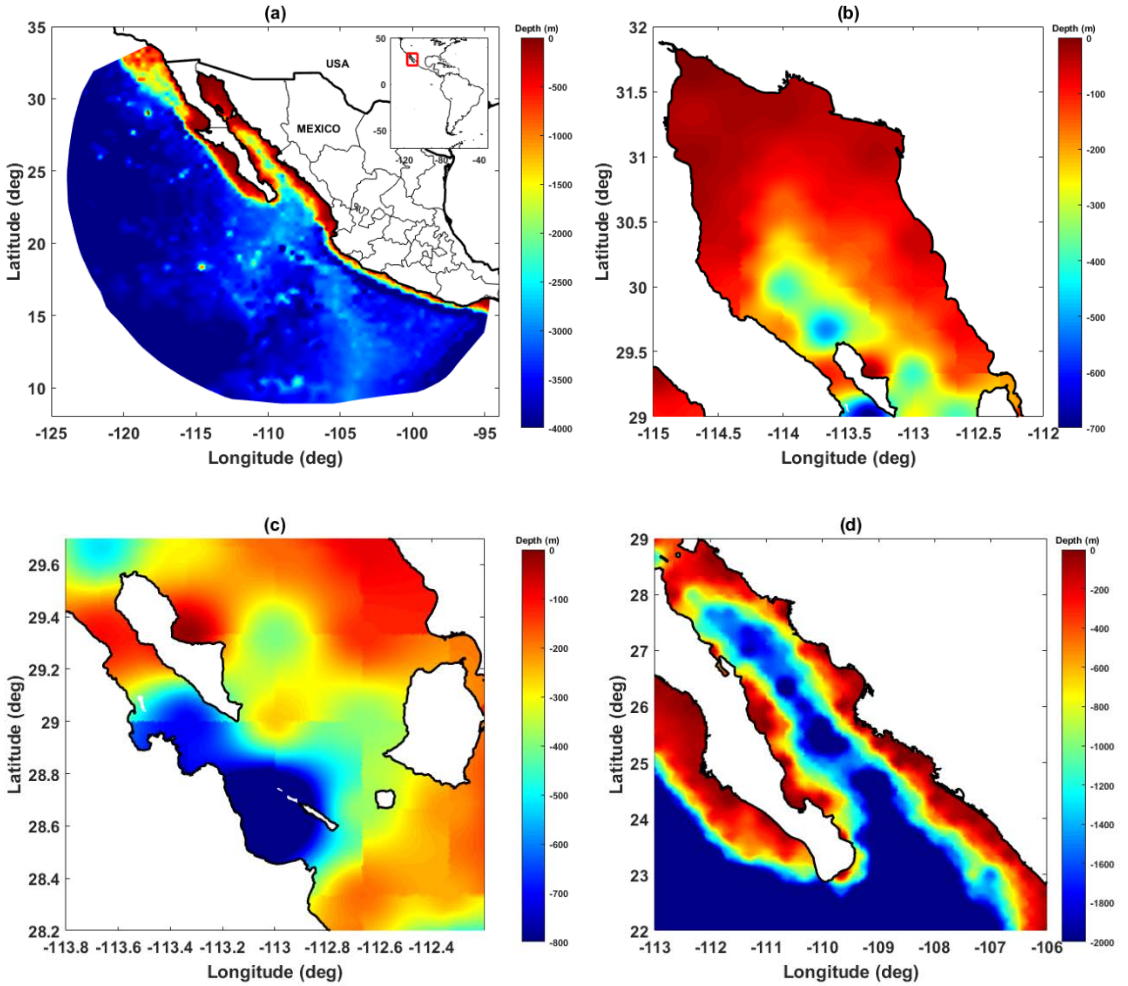

Figure 3.26. Bathymetry ETOPO alone, (a) All domain area, (b) Northern GC, (c) Midriff area, (d) Southern GC.

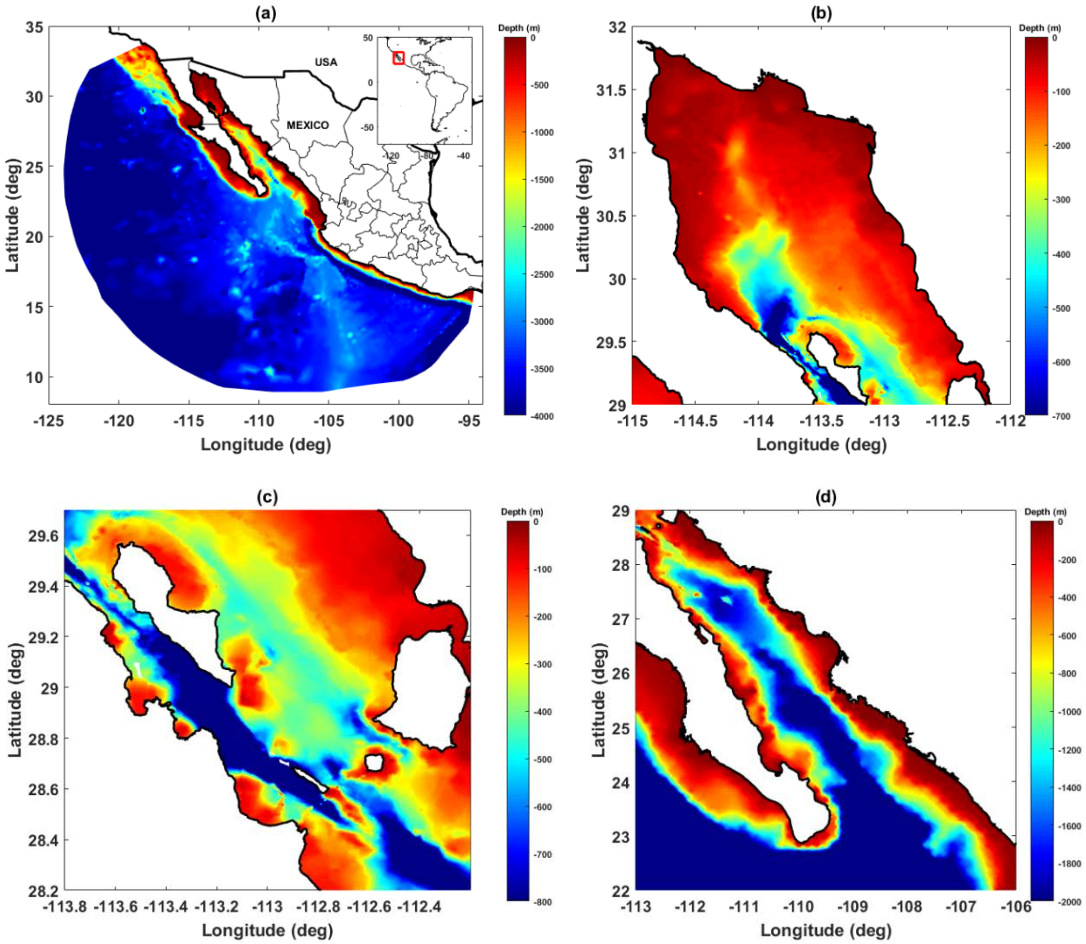

Figure 3.27. Bathymetry GEBCO plus CICESE, (a) All domain area, (b) Northern GC, (c) Midriff area, (d) Southern GC.

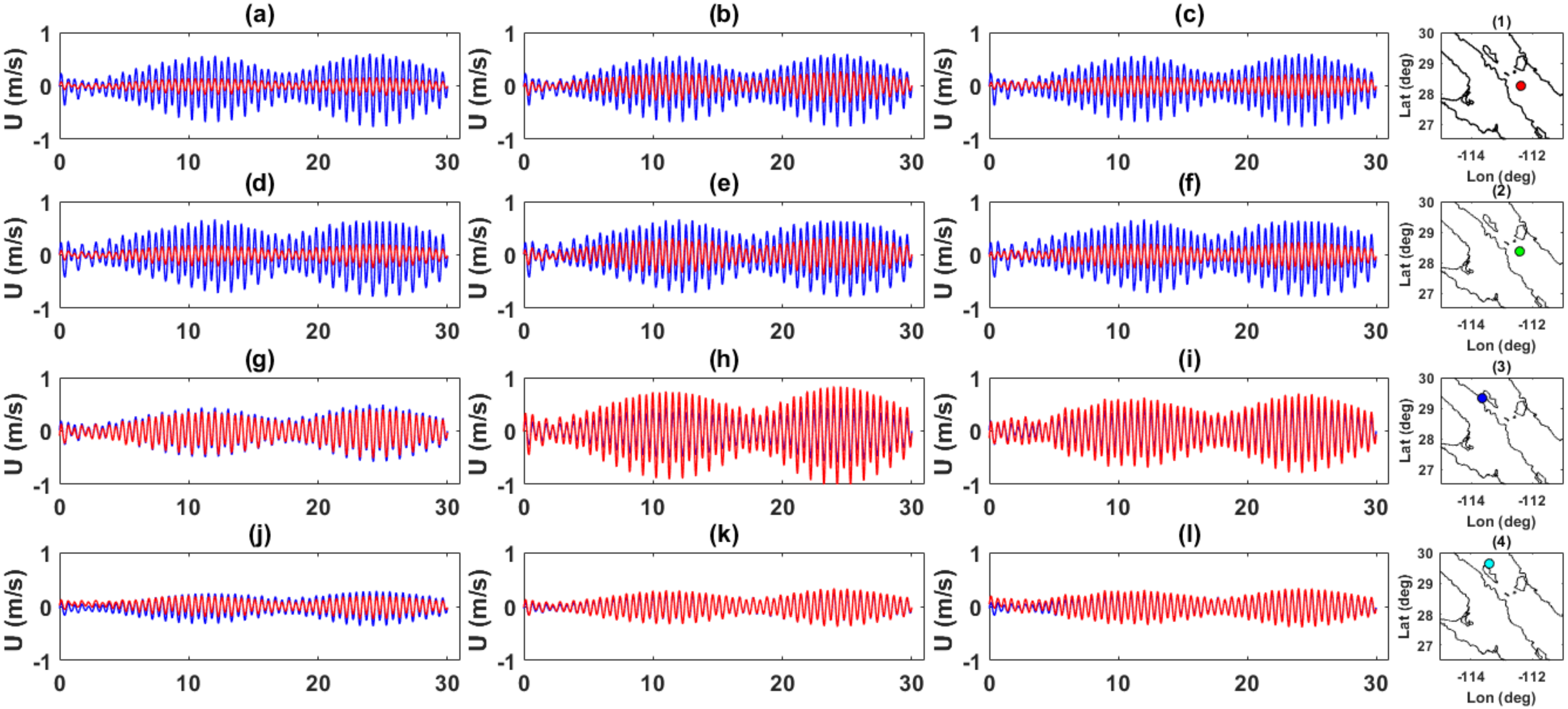

Figure 3.28. Comparison of the observations (blue) and model results (red) u north velocity component different bathymetry products as GEBCO (a,d,g,j), ETOPO (b,e,h,k) and GEBCO merged with CICESE (c,f,i,l) at (1) San Lorenzo (2) San Esteban, (3) Ballenas Channel and (4) Delfin Basin.

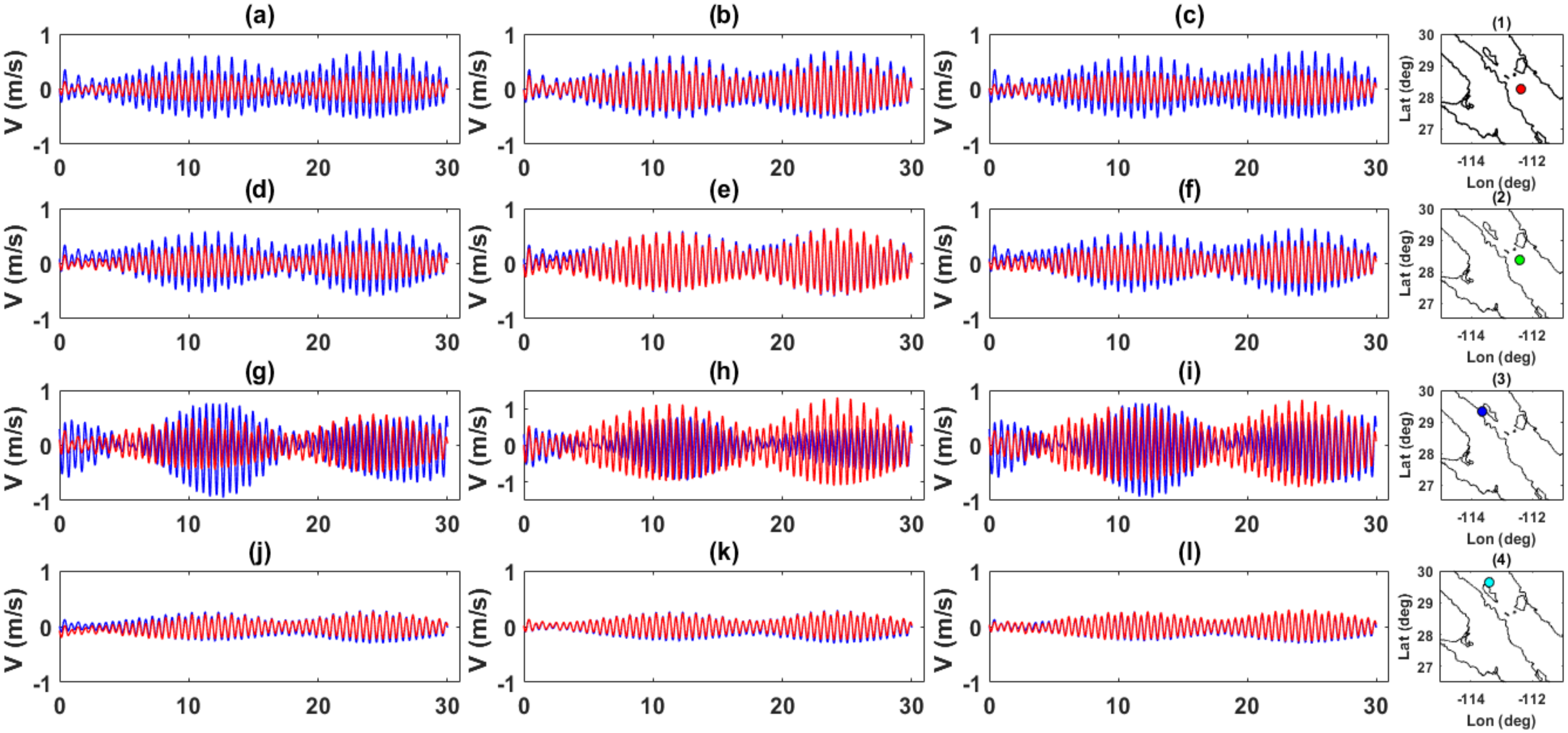

Figure 3.29. Comparison of the observations (blue) and model results (red) v east velocity component, different bathymetry products as GEBCO (a,d,g,j), ETOPO (b,e,h,k) and GEBCO merged with CICESE (c,f,i,l) at (1) San Lorenzo (2) San Esteban, (3) Ballenas Channel and (4) Delfin Basin.

Table 3.1. Details of the tide gauge records used for model validation

Site #	Site Name	Reference Code	Longitude (decimal °)	Latitude (decimal °)	Period	# of months
1	Ensenada	ENSM	-116.38	31.52	From January to December 2015	12
2	San Quintin	SNQN	-115.59	30.29		
3	Isla Cedros	ICDN	-115.11	28.05		
4	Guerrero Negro	GROM	-114.09	27.53		
5	Cabo San Lucas	CSLN	-109.54	22.52	From 24 of November to 31 of December 2015	1.5
6	La Paz	LPAZ	-110.35	24.16	From January to December 2015	12
7	Loreto	LTON	-111.80	25.48	23 of November to 31st of December 2015	1.5
8	Bahia de los Angeles	BLAN	-113.33	28.57	From January 2015 to December except June and July 2015	10
9	San Felipe	SNFN	-114.82	31.02	From January to December 2015	12
10	Manzanillo	MNZN	-104.17	19.38	From January to December 2015	12
11	Acapulco	ACAN	-99.55	16.5	24 of September to 31st of December 2015	1.5

Table 3.2. ADCP data records used for current validation

Reference Code	**Site Name**	**Depth device deployment and water depth in m**	**Longitude (decimal °)**	**Latitude (decimal °)**	**Period**	**Number of months -period**
SL	San Lorenzo	395/410	-112.37	28.25	From May 2003 to November 2004	18
SE	San Esteban	577/588	-112.41	28.37	From May 2003 to November 2004	18
BC	Ballenas Channel	578/595	-113.38	29.20	From May 2003 to November 2004	18
DEL	Delfin	337/354	-113.23	29.38	September 2005 to September 2006	13

Table 3.3. Mean absolute differences between the measured data and TPOX7.2 global ocean tidal model for the 11 validation sites.

Tidal constituent	Mean absolute error of the amplitude (m)	Mean absolute error of phase (°)
M_2	0.07	10
S_2	0.04	19
N_2	0.02	13
K_1	0.20	21
O_1	0.05	9
Q_1	0.00	20

Table 3.4. Statistic error measures for the 11 tide gauges stations.

Site number	Site Name	RMSE (m)	% Error	STD (m)	Correlation Coefficient
1	Ensenada	0.03	1.2	0.02	0.99
2	San Quintin	0.11	4.5	0.07	0.97
3	Isla Cedros	0.10	4.4	0.09	0.96
4	Guerrero Negro	0.26	9.6	0.15	0.84
5	Cabo San Lucas	0.06	3.0	0.04	0.99
6	La Paz	0.19	10.9	0.12	0.75
7	Loreto	0.08	5.9	0.05	0.95
8	Bahia de los Angeles	0.09	3.0	0.07	0.98
9	San Felipe	0.25	3.8	0.17	0.99
10	Manzanillo	0.07	6.1	0.05	0.94
11	Acapulco	0.07	7.7	0.05	0.91
All	**Mean**	**0.11**	**5.0**	**0.07**	**0.86**

Table 3.5. Mean absolute amplitude and phase from the main tidal constituents, estimated data and measured ADCP and tidal constituents across all sites

Tidal constituent	**Mean absolute error of the amplitude u velocity component (m/s)**	**Mean absolute error of the amplitude v velocity component (m/s)**	**Mean absolute error of phase (°) u velocity component**	**Mean absolute error of phase (°) v velocity component**
M_2	0.01	0.00	1	1
S_2	0.01	0.19	1	0
N_2	0.01	0.02	5	3
K_1	0.01	0.01	28	30
O_1	0.01	0.10	0	12
Q_1	0.00	0.00	21	12
All Mean	**0.01**	**0.05**	**9**	**10**

Table 3.6. Root mean square error of u and v velocity components

Site Name	**RMSE(m/s)**		**% Error u**	**% Error v**	**STD (m/s)**		**Correlation Coefficient**	
	u	v	u	v	u	v	u	v
San Lorenzo	0.18	0.12	11.3	8.5	0.13	0.08	0.99	0.97
San Esteban	0.19	0.10	11.5	6.7	0.13	0.07	0.97	0.94
Ballenas Channel	0.09	0.32	6.7	25.0	0.06	0.23	0.99	0.34
Delfin	0.02	0.03	2.7	3.7	0.02	0.02	0.99	0.98
Mean	**0.12**	**0.14**	**8.04**	**11**	**0.08**	**0.10**	**0.98**	**0.80**

Table 3.7. Statistic percentage errors measure of tidal level constituents for the 11 tide gauges stations using different bathymetry products.

Site number	**Site Name**	**% Error GEBCO**	**% Error ETOPO**	**% Error GEBCO merged with CICESE**
1	Ensenada	1.16	1.2	1.2
2	San Quintin	4.4	4.8	4.5
3	Isla Cedros	4.3	4.5	4.4
4	Guerrero Negro	9.4	8.9	9.6
5	Cabo San Lucas	2.10	2.7	3.0
6	La Paz	11.2	11.5	10.9
7	Loreto	6.3	4.5	5.9
8	Bahia de los Angeles	7	6.8	3.0
9	San Felipe	5.1	3.3	3.8
10	Manzanillo	6	6	6.1
11	Acapulco	7.4	7.4	**7.7**
All	**Mean**	**5.4**	**5.6**	**5.0**

Table 3.8. Root mean square error of u and v velocity components using different bathymetry products

Site Name	**% Error GEBCO u**	**% Error GEBCO v**	**% Error ETOPO u**	**% Error ETOPO v**	**% Error GEBCO merged with CICESE u**	**% Error GEBCO merged with CICESE v**
San Lorenzo	18.8	22.1	21.3	26.3	11.3	8.5
San Esteban	19.9	21.4	22.8	27	11.5	6.7
Ballenas Channel	24.8	31.1	38	50.3	6.7	25.0
Delfin	21.7	24	26.1	24.6	2.7	3.7
Mean	**21.34**	**24.7**	**27.1**	**32.1**	**8.04**	**11**

Chapter 4: Tidal-range energy resource assessment

This chapter has been adapted from the following publication:

> *Mejia-Olivares, C.J., Haigh. I.D., Angeloudis A., Lewis, M. and Neill, S.P, 2018. Tidal range energy resource assessment of the Gulf of California, Mexico. In review with Renewable Energy (Submitted 1st March 2019, under review with Renewable energy).*

4.1 Introduction

Tidal-range energy utilized the potential energy from the amplitude differences between two bodies of water, within the rise and fall of the tide (Neill et al., 2018). This potential energy can be harnessing thought the construction of a tidal barrage or tidal lagoon (Prandle, 1984; Baker, 2006, Hendry, 2017; Tidal Lagoon power. 2018). A detailed review of tidal-range energy has been given in Section 2.2.2. In summary, there are five commercial tidal power stations plant at France (The Rance), Russia (Kislaya Gubska), South Korea (Lake Shiwa), China (Jiangxia) and Canada (Nova Scotia). In recent decades, a large number of studies have identified, and carried out resource assessments, for many other sites around the world. These studies and the methods they utilized have been briefly explained in Section 2.2.2.2, Section 2.2.2.3 and summarized in Table 2.3.

To date, two studies have identified sites in the GC with potential for tidal-range energy (see Section 1.1 for details). However, these have used only limited data sets, basic methodologies and narrow scientific support for evaluating the resource. Therefore, in this chapter, the main focus is on carrying out a more detailed assessment of the theoretical tidal-range energy resource in the northern part of GC which has a relatively large tidal-range over 5 m (Marinone, 2003).

The overall objective of this chapter is to undertake a detailed quantification of the tidal-range energy resource in the northern reaches of the GC. To address this there are three sub-objectives, as follows:

1. To map how the tidal-range varies in the northern part of the GC;
2. To estimate the theoretical annual yield potential energy density in this region and how this resource varies subject to different bathymetry datasets while accounting for multiple tidal constituents; and
3. To determine the energy that can be generated technically whilst considering different operational strategies and certain tidal power plant technical specifications.

The structure of this chapter is as follows. Section 4.2 outlines the methodology used to assess the available power density and theoretical annual energy yield in the northern GC. The results for each of the three sub-objectives are then described in Section 4.3. Key findings are discussed in Section 4.4 and conclusions are given in Section 4.5.

4.2 Methodology for resource characterisation

This section describes how predictions from the barotropic model, previously described in detail in chapter 3, was utilized to estimate the theoretical and technical tidal-range energy resource in the GC.

4.2.1 Tidal level analysis

Using the validated model, I assessed tidal levels across the GC, with a focus on the northern region, to determine the location of the highest tidal levels and how they vary over time. The model was run for the period from 27 November 2015 to 31 December 2015 and results were stored at every grid point every 10 minutes. The first three days were considered as the warm up period and were discarded from the analysis. At each model grid point we undertook a harmonic analysis on the monthly predicted tidal level time-series, again using the T_TIDE software (Pawlowicz et al., 2002). I then used the tidal harmonics to predicted tidal levels for a full year, which saved the computation expense of running the high-resolution model for a year. I calculated the differences between the amplitude and phases of the main tidal constituents and used three error metrics to statistically assess model performance listed in Table 4.1, (see Section 3.3. for further details). I then calculate the annual maximum and mean tidal-range from the annual time-series at each grid point. I compared this to the maximum and mean tidal-range, just accounting for the M_2 and S_2 tidal constituents.

4.2.2 Methodology to assess the theoretical power density and annual energy yield

Next, the theoretical power density (per m^2) was quantified in the GC with a focus on the northern region because the highest tidal levels are observed here. I estimated the power density at each model grid point following the approach Prandle (1984) in which the theoretical power density (P $_{density}$) is given by:

$$P_{density} = \left(\frac{1}{2}\ Ag\rho\ H^2\right)/3600 \quad \text{(Units in Wh/m}^2\text{)} \qquad \text{(EQ. 4.1)}$$

Where A is the area of the impounded basin (in this case it was considered 1 m^2), ρ is the density of sea water (1025 kg/m^3), g is the acceleration due to gravity (9.81 m/s^2), and H (in m) is the head, normally defined as the water level differences between HW (high water) and LW (low water) peaks of a tidal elevation time series. The annual energy yield resource (P$_{annual}$) was then calculated as follows:

$$P_{annual} = \sum_{i=1}^{n} \left(\frac{1}{2}\rho g A H^2\right) \quad \text{(Units Wh/m}^2\text{)} \qquad \text{(EQ. 4.2)}$$

Where n is the accumulated water transitions from HW to LW, or LW to HW. The potential energy estimated by EQ. 4.1 was normalised by the impounded area to produce a metric that represents the spatially varying potential energy (i.e., the energy density, as $E = \rho g H^2$ in Ws/m^2).

In order to calculate the annual energy density, the head H was first extracted from each transition from high to low water and vice versa, from the elevation-time-series. In turn it was used to calculate the energy density for each consecutive flood and ebb tide and then accumulated for 1,411 transitions that are expected in a year (e.g., four transitions per day times 365 days in a year). The mean hourly power density for tidal-range power was calculated, by dividing the energy density from each transition by the duration between the elevation peaks.

I then undertook a series of sensitivity tests in which it was estimated and compared the theoretical power density for time-series derived from all considered tidal constituents (analysing monthly tidal predictions with T_TIDE gave 29 tidal constituents) and then just for the main semi-diurnal constituents, M_2 and S_2. I did this because several studies that have previously undertaken tidal energy resource assessments, just consider these two primarily constituents. Also, the estimated energy was compared from model runs that used: (1) just the GEBCO_2014 bathymetry; (2) just the ETOPO bathymetry; and (3) the GEBCO data merged with the higher resolution data from CICESE in the northern part of the GC.

4.2.3 Methodology to assess the technical extractable energy

Finally, it was determined the energy that can be generated technically whilst considering different operational strategies and certain tidal power plant technical specifications. The performance of a tidal-range power plant can be evaluated once a tidal signal is available that can be sufficiently representative of the outer water level evolution that the hydraulic structures will experience once the plant is constructed (Neill et al., 2018). For an early-stage assessment, this can be done in a manner that omits the influence of the structure on the localised hydrodynamics and assumes a constant impounded surface area with negligible water elevation variations in its interior (Prandle, 1984). This approach is known as 0-D modelling and has been applied on several occasions to assess the performance of tidal-range schemes (Burrows et al., 2009; Yates et al., 2013; Angeloudis et al., 2016a). The tidal power plant simulations employ a backward difference 0-D model based on the principles of continuity as implemented in Angeloudis et al. (2018), building on earlier operational modelling studies from Aggidis and Benzon (2013), and Lewis et al. (2017). Operation sequence algorithms dictate the flow through hydraulic structures and by extension (in the case of turbines) the power produced or consumed while pumping. There are multiple ways of operating a tidal power plant, as summarised in the schematics of Figure 4.1 which were produced using the parameters summarised in Table 4.2. For a more detailed description of the ebb-generation and two-way generation, the interested reader is directed in Angeloudis and Falconer (2016) and for two-way generation with pumping in Yates et al. (2013).

The operational algorithms employed in 0-D (Figure. 4.1) have previously been linked with 2-D hydrodynamic models to quantify hydrodynamic implications associated with the construction of tidal-range structures (Angeloudis et al., 2017, 2016b). Comparisons between the two approaches (0-D and 2-D) suggest that similar findings can be obtained when assessing small-scale projects under certain conditions. An excellent agreement has been observed for schemes that do not feature extensive intertidal regions upstream (Neill et al., 2018). In contrast, caution has been advised for larger schemes such as with the Severn Barrage STPG proposal in the UK (impounding approximately 573 km^2, Xia et al., 2010). Discrepancies have been reported in the case of designs that occupy significant proportions of estuarine regions that are tidally affected and with a substantial proportion of the impounded area comprising shallow water regions susceptible to drying. Larger impoundments are expected to correspond to a noticeable impact on the estuarine tidal resonance by compromising the established evolution and reflection of the tidal waves, thus markedly altering the downstream tidal conditions that drive the operation and dictate the extractable energy resource. In contrast, schemes that comprise extensive shallow water regions might experience non-linear and rapid surface area changes that would simply not be appreciated through a 0-D methodology.

Our approach hypothesises the deployment of a tidal lagoon plant at the four sites of interest shown in Figure 4.2b (Marker A San Felipe, Marker B Puerto Peñasco, Marker C Playa Encanto, and Marker D Gulf of Santa Clara). These specific locations were pre-selected due to the proximity with the nearest grids connectivity (later explained in the discussion section) and also the tidal-range is more than 5 m. A constant upstream surface area of 10 km^2 is assumed as in Lewis et al. (2017). This entails a scenario that would be expected for offshore tidal lagoon schemes (e.g. Cornett et al., 2013). As a result, the water volume impounded linearly varies with the water depth h. The impounded area A = 10 km^2 corresponds to a relatively small-scale tidal-range scheme. For example, the Swansea Bay tidal lagoon project within the Bristol Channel, UK, has been perceived as a pilot-scale project with a maximum surface area of 11.6 km^2 (Waters and Aggidis, 2016).

The formulations employed for the flow through hydraulic structures at every time step are outlined in Angeloudis et al. (2018) involving the orifice equation for sluice gates using a discharge coefficient of C_D = 1.0 (consistent with the sensitivity study of Bray et al., 2016) and a sluice gate cross-sectional area of A_s = 100 m^2. For the turbine parametrisation, representative hill charts are required to acknowledge the performance of low-head bulb turbine designs; this technology is typically installed for power generation from tidal-range structure proposals. The calculation process followed for the hill chart has been described by Aggidis and Feather (2012). In particular, it was assumed that generation will be facilitated by turbines with a capacity of 20 MW, a diameter D = 7.35 m in accordance with recent UK tidal-range energy studies (Angeloudis et al., 2016b; Petley and Aggidis, 2016; Waters and Aggidis, 2016). In Figure 4.3 the calculated 20 MW turbine hill chart is plotted together with an idealised representation from first principles. The idealised representation omits efficiency factors acknowledged by the hill chart and demonstrates how lower flows are predicted to generate an equivalent amount of power depending on the head difference H subjected to the turbine. A comparison between the two curves also suggests significant efficiency losses when generating at relatively low head differences; further compromising the generation during neap tides when H facilitated would be relatively lower. Moreover, the algorithms account for a minimum head difference that will be required to generate any energy, where in this case H_{min} = 1 m.

In the absence of detailed information about specific schemes at the potential sites in Figure 4.2b, certain assumptions must be included in relation to the tidal power plant configuration. Namely, the optimum number of turbines and sluice gates will vary for schemes at different locations according to the available potential energy, amongst additional constraints of a geomorphological, environmental and electrical nature. For our preliminary assessment I formulate the following expression to estimate the capacity *C* (in W):

$$C = \eta \frac{\rho g A \overline{H}^2}{T\ CF} \qquad \text{(Units in W)} \qquad \text{(EQ. 4.3)}$$

Where η is the overall generation efficiency, T = 44712 s is the tidal period, *CF* is the capacity factor and $\overline{H}$ is the mean annual tidal-range. It is generally acknowledged that approximately 27 – 55 % of the available energy resource can be harnessed (based on findings of Burrows et al., 2009 and more recently Angeloudis et al., 2018). Thus, it was assumed that the maximum potential energy that can be harnessed is subject to an efficiency of η = 0.50. The capacity factor of conventional single-basin tidal-range structures can accordingly vary between 0.15 – 0.25 depending on the operation performance. It is assume that any proposed scheme in the GC will aim for a value of *CF* = 0.20. In turn, the number of turbines N_t will be = C/P_{max} and assume for the sluice gate number $N_s = N_t/2$. These parametric relationships have been applied here on an empirical basis and site-specific optimisation will be essential for more comprehensive studies that also acknowledge the site bathymetry, marine spatial planning, economic and environmental constraints.

4.3 Results

The results of this chapter are described into three parts, each addressing a study objective as follows: (1) analysis of tidal-range at the northern GC and (2) the quantification of the theoretical annual energy yield utilizing different bathymetry products and varying the number of tidal constituents and (3) energy that can be generated technically, considering different operational strategies and certain tidal power plant technical specification.

4.3.1 Tidal-range variation

The first objective is to map how the tidal-range varies in the northern part of the GC. The annual maximum and annual mean tidal-range is shown in Figures. 4.4a and b, respectively. In the vicinity of the Midriff Islands the maximum tidal-range is in the order of 2 m. The tidal-range then increases moving north, with a maximum during spring tides of approximately 8 m in the northern most part of the Gulf (Figure 4.4a). The mean tidal-range is in the order of 5 m in the northern most part of the Gulf (Figure 4.4b and Table 4.3 in pre-selected sites). The annual maximum and annual mean tidal-range, calculated just using the M_2 plus S_2 tidal constituents, are shown in Figures 4.4c and d respectively. When I consider just the M_2 plus S_2 tidal constituents the annual maximum tidal-range reduce significantly from 8 to 5 m in the northern part of the GC (Gulf of Santa Clara region) while the annual mean tidal-range reduces from 5 to 4 m.

4.3.2 Energy density and annual theoretical resource

The second objective is to estimate the theoretical potential energy density as well as the theoretical annual energy yield in this region and how this resource varies subject to different bathymetry datasets while accounting for multiple tidal constituents. The annual maximum and annual mean power density for the region are shown in Figures. 4.5a and b, respectively. Power density varies spatially and reflects, as expected, the spatial distribution of tidal-range, shown in Figure 4.5. The maximum values are locate at the upper Gulf (opposite Gulf of Santa Clara) and are between 0.09 and 0.1 kWh/m^2. The water depth at these locations is less than 30 m. The power density is much lower around the Midriff region, ranging from 0.03 and 0.04 kWh/m^2. Here water depths vary between around 40 to 180 m. The annual mean power density in the upper Gulf is between 0.035 and 0.040 kWh/m^2 while in the middle and lower northern GC it is smaller, between 0.025 and 0.018 kWh/m^2, respectively.

Time series of tidal levels and potential energy density are shown in Figure 4.6 for four sites (the locations of which are shown in Figure 4.2b). I consider that these areas have potential for building a power plant or a lagoon, as the mean tidal-range exceeds 6 m and the topography and water depth are appropriate for the construction of a lagoon. There are slightly changes within the potential energy density for tidal energy extraction at the northern GC. Overall, the mean annual power density in those locations is in the range of 0.015 to 0.038 kWh/m^2.

Also, again for comparison purposes, the annual maximum and mean power density was estimated when using predicted tidal level time-series considering just the M_2 plus S_2 tidal constituents and results are shown in Figures 4.5c and d. Comparing Figure 4.5a with 4.7c, the maximum power density decreases by almost a half when just considering tidal levels predicted just using the M_2 plus S_2 tidal constituents, from 0.09 to 0.05 kWh/m^2. The mean power density decreases from 0.035 to 0.030 kWh/m^2 (Figures 4.5b and 4.5d).

It was also estimated the theoretical annual energy yield and the results are shown in Figure 4.7a. The potential annual energy yield ranges from 20 to 50 kWh/m^2. The maximum values are in the northern region of the GC and are around 45 and 50 kWh/m^2 in the vicinity of the Gulf of Santa Clara. At Puerto Peñasco, San Felipe and Playa Encanto the annual yield energy is lower, ranging from 30 and 35 kWh/m^2. In the southern reaches of the northern GC the annual yield energy is lower, between 20 to 25 kWh/m^2. In a similar way, it was compared the annual yield energy based on annual tidal predictions estimated using only the M_2 plus S_2 tidal constituents (Figure 4.7b). On average the resource is 10 to 13 kWh/m^2 bigger when considering all tidal constituents analysed, compared to just consider M_2 plus S_2.

I also estimated the annual energy yield considering a 10 km^2 basin area (results not shown). The annual yield is between 450 and 500 GWh/m^2 in the vicinity of the Gulf of Santa Clara. between 300 and 350 GWh/m^2 near to San Felipe and Puerto Peñasco and around 250 GWh/m^2 near to Playa Encanto.

Three different bathymetry products were used to estimate the theoretical annual energy yield and the contrasting results are shown in Figure 4.8. It is clear the resource estimates are underestimated when the freely available global bathymetry products (e.g., GEBCO and ETOPO) are used on their own. The ETOPO bathymetry gives a maximum resource of 28 kWh/m^2 (Figure 4.8b) in the northern region, while the GEBCO bathymetry gives a maximum resource of 20 kWh/m^2 in this area. These are almost 50% of that estimated when I combined the higher resolution CICESE bathymetry data with GEBCO.

4.3.3 Tidal power technical output

The third objective is to determine the energy that can be generated technically whilst considering different operational strategies and certain tidal-range power plant technical specifications. In Figure 4.6a-d I consider the tidal signal and the theoretical energy accumulated in each cycle in sites of interest in the GC. Figure 4.6e appends results to be used as a reference based on the theoretical energy from a site where a tidal lagoon proposal has been extensively studied, the Swansea Bay area in the Bristol Channel of the UK (Petley and Aggidis, 2016; Angeloudis et al., 2017). By observation, the GC is far less energetic in all four locations and this can also be appreciated in Table 4.4. The tidal-range is 30-38 % less than for the reference site in the UK. However, this difference corresponds to a 47-59 % reduction in the theoretical energy, attributed to the squared relationship between the tidal-range and the available theoretical energy (see EQ. 4.1).

Operational modelling sheds further insights into how tidal power plants would perform in the GC. The power output from each of the three strategies is summarised in Figure 4.9 where the intervals for power generation can be calculated more accurately. As with every tidal energy technology, far less energy is generated over neap tidal conditions, with shorter intervals of power generation. Ebb-only generation by restricting power generation to only a unidirectional flow, generates twice in a day. Two-way generation delivers four pulses of energy over 24 h which help distribute the tidal power contributions. Two-way generation with pumping corresponds to a superior performance but this comes at the requirement that energy is invested to pump water and increase the head difference that turbines will then generate from as illustrated in Figure. 4.9.

Even though it can be observed that energy can indeed be generated from the tides in the GC, there are significant efficiency losses as summarised in Table 4.4. The power plants consistently perform worse relative to the reference site, an aspect that is again connected with the lower head differences developed opposite the turbine structures. By observing the hill chart in Figure 4.3, the efficiency of practical turbine designs increases with an ascending head difference. The lower efficiency can be observed by the significantly greater discharge of Q_{chart} relative to Q_{ideal}, where in the latter hydraulic and other losses are not taken into account. More details on the bulb turbine performance efficiency for tidal-range structures can be found in Aggidis and Feather (2012). The best performing site in the GC is the Gulf de Santa Clara (Marker D Figure 4.2b) which delivers 50 %, 40 % and 33 % of the energy relative to the reference site for ebb-only, two-way and two-way with pumping strategies respectively.

4.4 Discussion

This work have undertaken a detailed quantification of the theoretical and technical tidal-range energy resource available in the northern part of the GC. Although a number of parameters are significant in tidal-range energy resource assessments, the most important is clearly tidal-range. In this study, I mapped tidal-range throughout the GC using results from a hydrodynamic numerical model. The maximum tidal-range is up to 8m in the northern most part of the GC, in the vicinity of the Gulf of Santa Clara and San Felipe Bay. However, the mean annual tidal-range is closer to 5 m in this area.

The annual energy yield ranges from 20 to 50 kWh/m^2 in the northern part of the GC. The maximum values are between 45 and 50 kWh/m^2 in the vicinity of the Gulf of Santa Clara, where the tidal-range is the largest. For comparison, the annual energy yield estimated for areas with the world's largest tidal-ranges by Neill et al. (2018) (e.g. Hudson Bay, Canada; Bristol Channel, UK; Patagonian Shelf; North-western Australian Shelf) is in the order of 100 kWh/m^2 or larger. Neill et al. (2018) suggest a minimum acceptable annual yield of 50 kWh/m^2, with a water depth of 30 m (based on construction costs of the embankment being prohibited in deeper waters. In the vicinity of the Gulf of Santa Clara and San Felipe Bay these criteria are just met.

In this section, it was determined the energy that can be generated technically at four key sites (shown in Figure 4.2b). It was considered different operational strategies and certain tidal-range power plant technical specifications. I contrasted these sites with the proposed tidal lagoon in Swansea Bay in the Bristol Channel of the UK, which has been extensively studies (e.g., by Angeloudis et al., 2017; Petley and Aggidis, 2016). The best performing of the four selected sites in the GC is Gulf of Santa Clara (Marker D in Figure 4.2b). This site would be capable of producing 50 %, 40 % and 33 % of the energy, relative to Swansea Bay, for ebb-only, two-way and two-way with pumping strategies, respectively.

In this study I have, for an early-stage assessment, used a 0-D modelling approach. This omits the influence of the structure on the localised hydrodynamics and assumes a constant impounded surface area with negligible water elevation variations in its interior (Prandle, 1984). The operational algorithms employed in 0-D (Figure. 4.1) have previously been linked with 2-D hydrodynamic models to quantify hydrodynamic implications associated with the construction of tidal-range structures (Angeloudis et al., 2017, 2016b). Comparisons between the two approaches (0-D and 2-D) suggest that similar findings can be obtained when assessing small-scale projects under certain conditions. An excellent agreement has been observed for schemes that do not feature extensive intertidal regions upstream (Neill et al., 2018). In contrast, caution has been advised for larger schemes such as with the Severn Barrage STPG proposal in the UK (impounding approximately 573 km^2, Xia et al., 2010). Discrepancies have been reported in the case of designs that occupy significant proportions of estuarine regions that are tidally affected and with a substantial proportion of the impounded area comprising shallow water regions susceptible to drying. Larger impoundments are expected to correspond to a noticeable impact on the estuarine tidal resonance by compromising the established evolution and reflection of the tidal waves, thus markedly altering the downstream tidal conditions that drive the operation and dictate the extractable energy resource. In contrast, schemes that comprise extensive shallow water regions might experience non-linear and rapid surface area changes that would simply not be appreciated through a 0-D methodology.

As it was previously highlighted in relation to tidal-stream energy within the GC (Mejia-Olivares et al., 2018), grid connectivity in the region presents a challenge. The nearest electricity connection point to the Mexican national network is located in Sonora County, which is ~450 km from Playa Encanto. North of the GC there are two electricity connection points on the Mexican/US border, but these are not connected to the national Mexican network. These points are located ~200 and ~370 km to San Felipe Bay. Difficult access to this region, due to its topography, lack of fresh water and dry weather make this area unattractive for urban development. Therefore, the tidal-range energy that could be could be converted into electricity from the GC might be more suitable for off-grid applications.

4.5 Conclusions

The aim of this chapter was to undertake a detailed quantification of the tidal-range energy resource in the northern reaches of the GC. This study used tidal level predictions from a depth-averaged barotropic hydrodynamic model, configured using the TELEMAC suite of modelling tools and the model was validated against tide gauge records, demonstrating good accuracy.

Model predictions showed that the maximum tidal-range is up to 8 m in the northern most part of the GC, in the vicinity of the Gulf of Santa Clara and San Felipe Bay. The mean annual tidal-range is closer to 5 m in this area. In the northern part of the GC the annual energy yield ranges from 20 to 50 kWh/m^2. The maximum values are between 45 and 50 kWh/m^2 in the vicinity of the Gulf of Santa Clara, where the tidal-range is the largest.

The used a 0-D modelling approach to estimate the energy that can be generated technically at four key sites in the norther GC, considered different operational strategies and certain tidal-range power plant technical specifications. Results showed that the site with the highest energy potential us Gulf of Santa Clara which produces 5 to 7 MW/km^2 utilizing ebb-generation scheme only while the two-way generation operational scheme produces 8 to 12 MW/km^2. Finally, the most energetic scheme calculation indicate that the most effective energy production is thorough using the two-way generation with pumping operational scheme with a maximum inner water elevation of 2.5 m. The maximum power generation is this region is range of 10 to 13 MW/km^2. This assessment has provided the most detailed estimate of the theoretical and technical tidal-range energy resource in the northern GC. It will provide the based for more detailed analysis to guide selection of suitable sites for tidal-range energy extraction in the region.

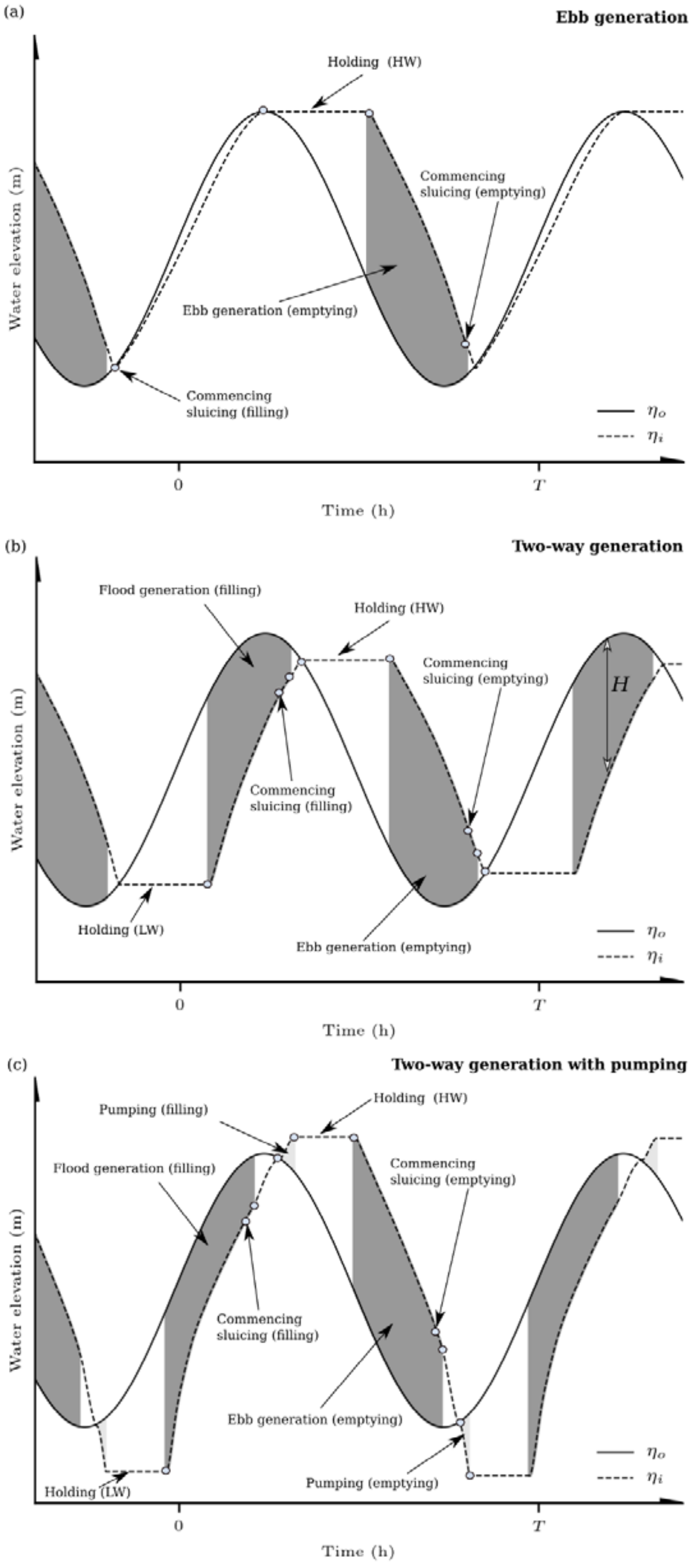

Figure 4.1. Typical operation strategies for a tidal power plant as simulated by our 0-D model: (a) one-way ebb generation (b) two-way generation (c) two-way generation with pumping. η_0 is the outer water elevation in the seaward side of the hydraulic structures.

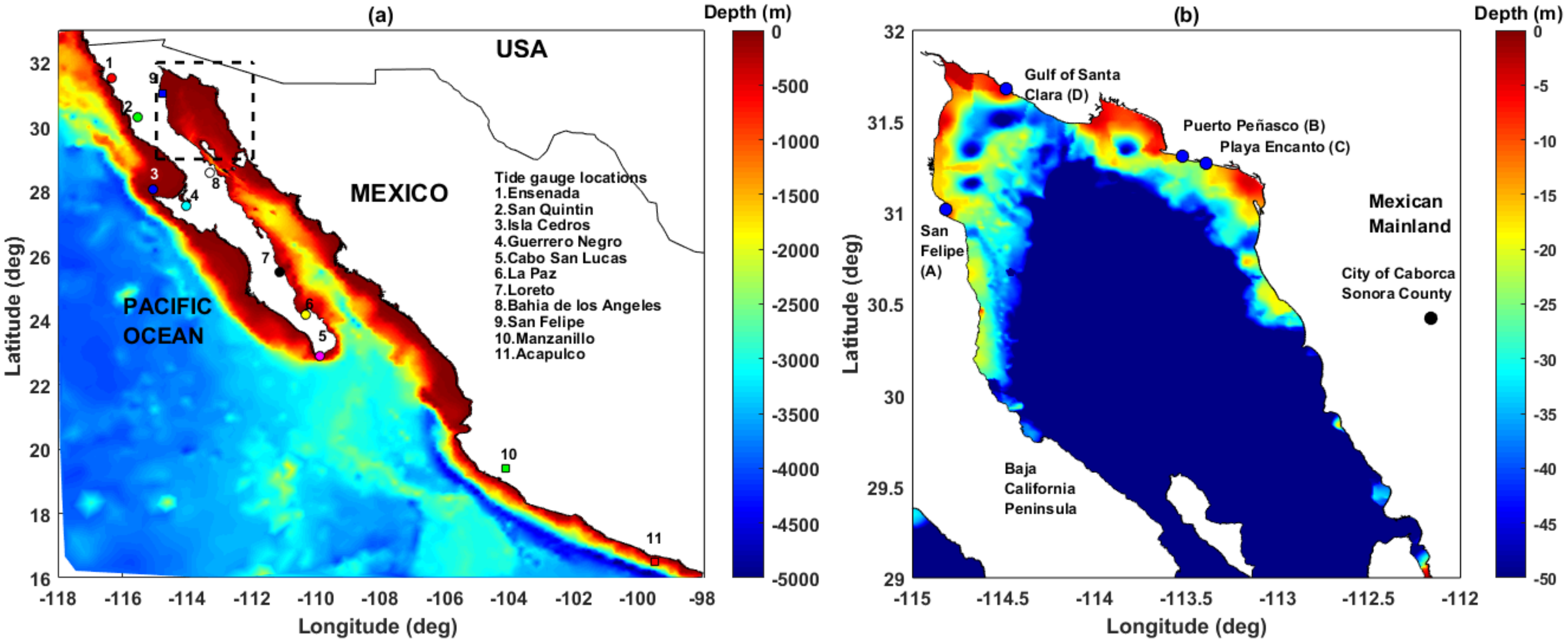

Figure 4.2. Location of the study area with water depths for the: (a) GC, with the locations of the tide gauge sites; and (b) the Northern GC. Blue dots are the location of the four pre-selected sites for tidal-range analysis.

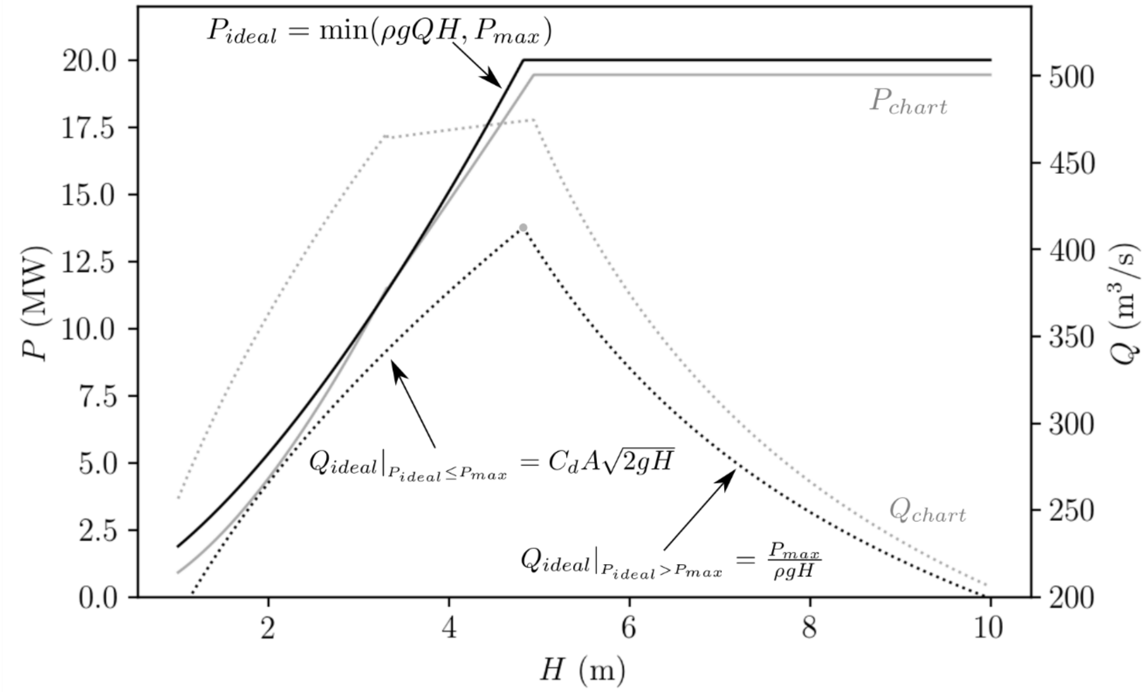

Figure 4.3. Idealised and calculated hill chart based on Aggidis and Feather (2012). The hill chart Power (P_{chart}) and Discharge (Q_{chart}) refers to a 20 MW 7.35 m diameter turbine as per the implementation of Angeloudis et al. (2018). For the idealised hill chart, Cd is the discharge coefficient (=1.0), P_{max} = is the turbine capacity (=20 MW) and AT the cross-sectional area of the turbine (assumed to be = π 7.352 /4 m^2) and H the head difference.

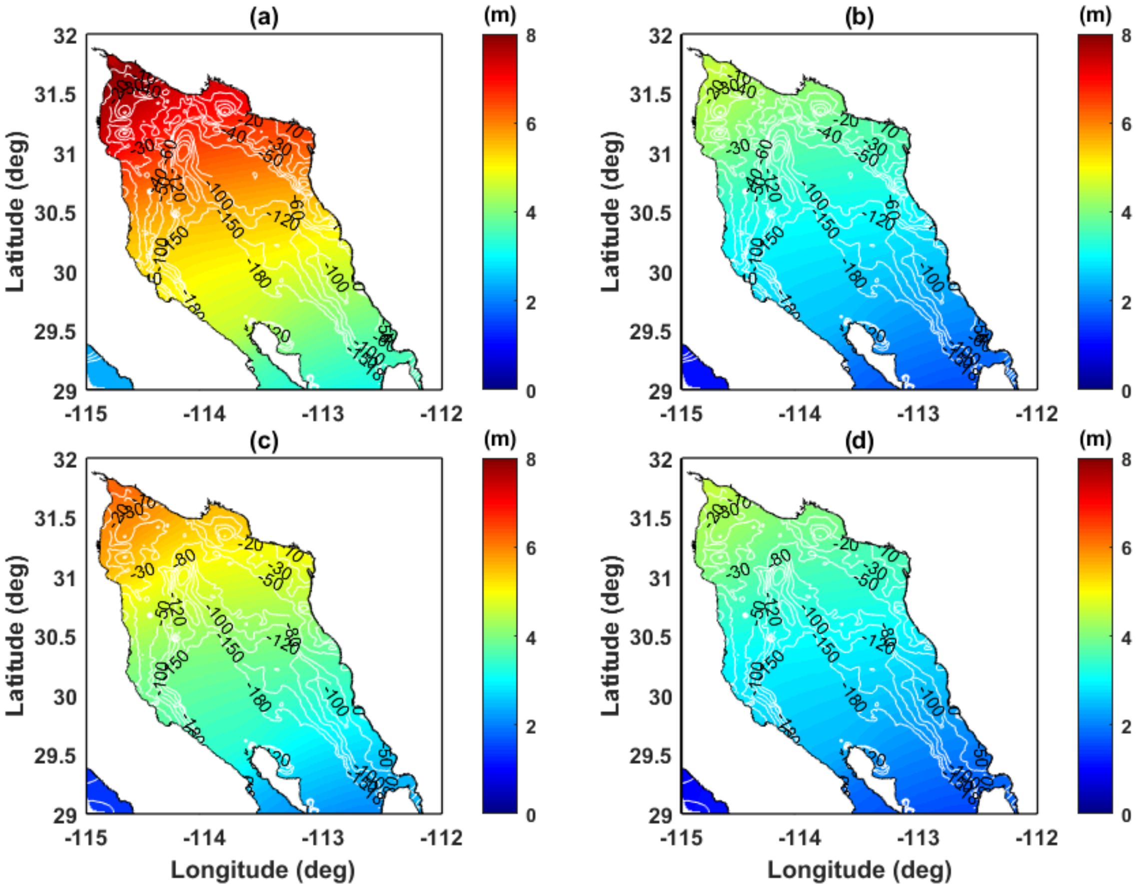

Figure 4.4. Annual max tidal-range and annual mean tidal-range for: (a,b) all model constituents and (c,d) just using the tide predict with the M_2 plus S_2 tidal constituents. All plots use the GEBCO data merged with the higher resolution data from CICESE, for the northern GC, for the model bathymetry. Bathymetry contours superimposed in m above.

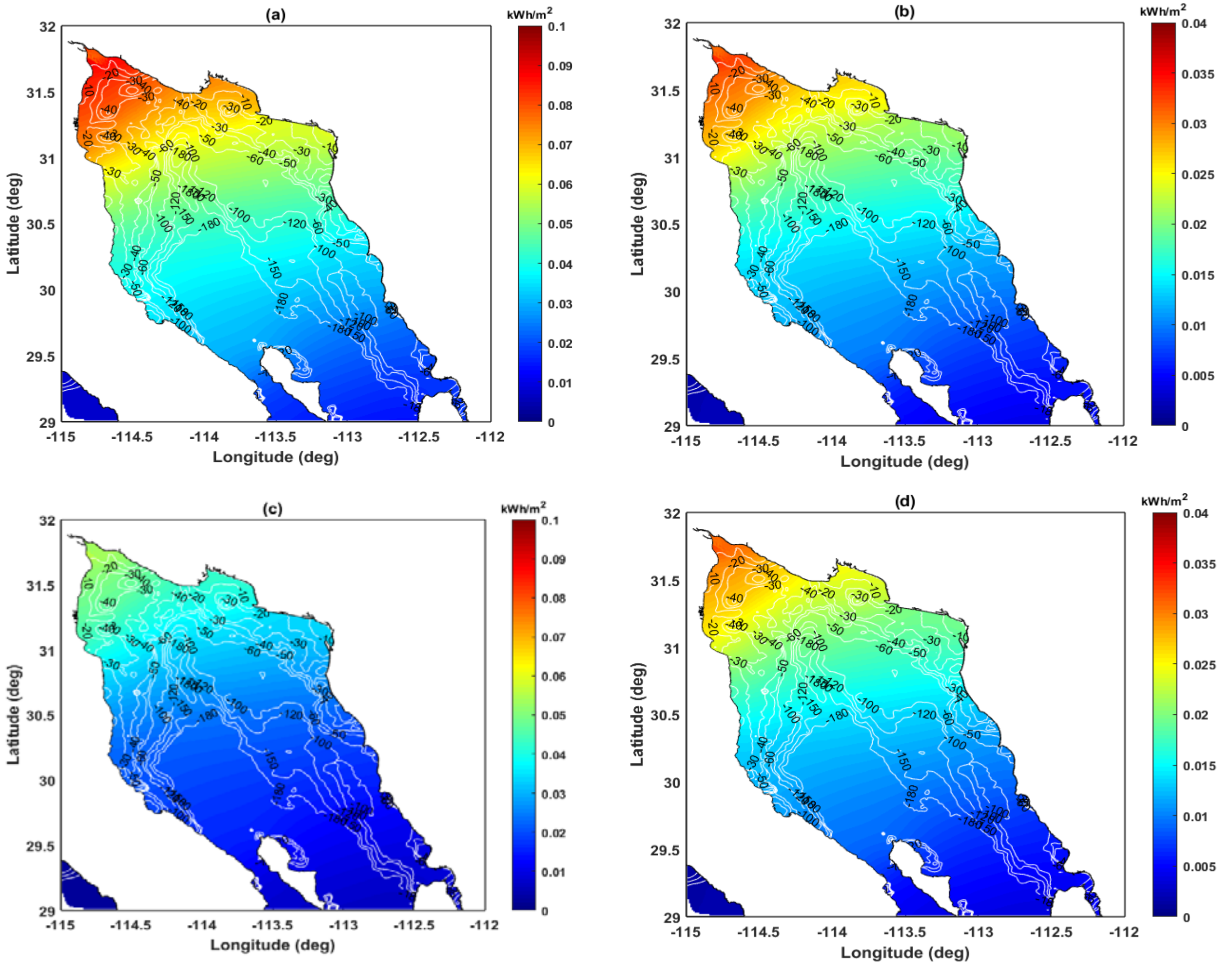

Figure 4.5. Annual max power density for: (a) all model constituents (c) using only M_2 plus S_2 tidal constituents. Mean power density (b) all model constituents (d) Using only M_2 plus S_2 tidal constituents. All plots use the GEBCO data merged with the higher resolution data from CICESE, for the northern GC, for the model bathymetry. Bathymetry contours superimposed in m above.

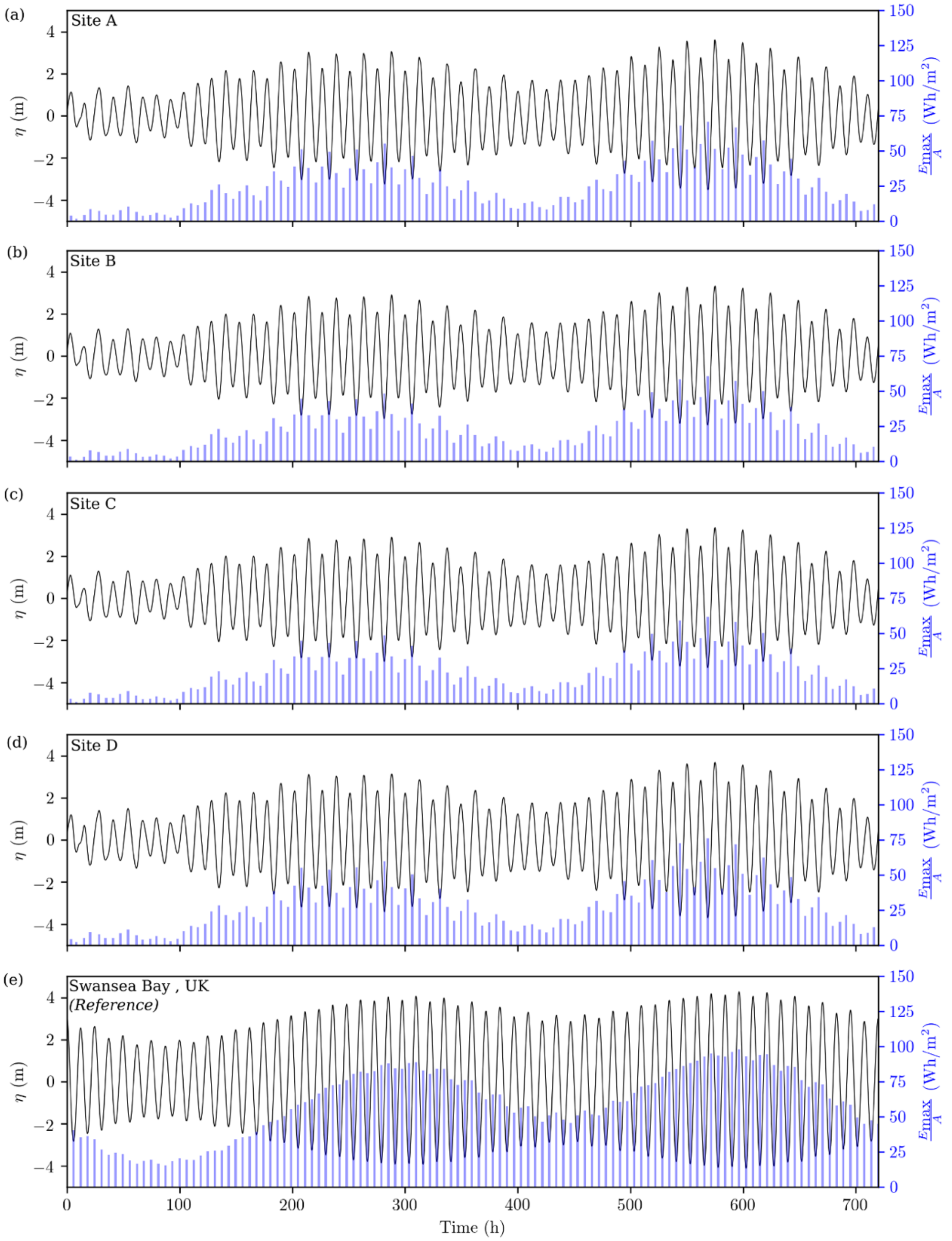

Figure 4.6. Monthly energy density and tidal levels at: (a) San Felipe, (b) Puerto Peñasco, (c) Playa Encanto, (d) Gulf of Santa Clara and (e) Swansea Bay, UK.

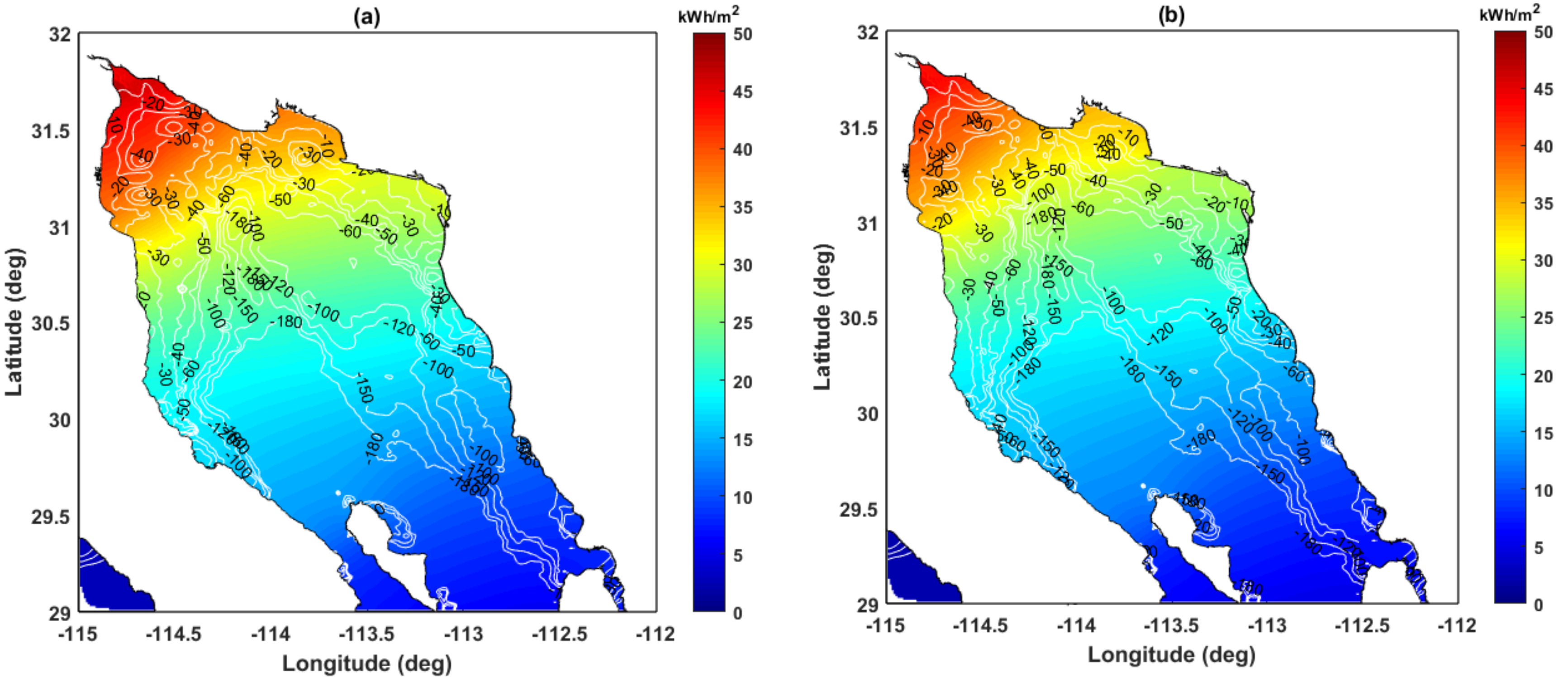

Figure 4.7. Annual energy yield (a) all model constituents (b) Using M_2 plus S_2. All plots use the GEBCO data merged with the higher resolution data from CICESE, for the northern GC, for the model bathymetry. Bathymetry contours superimposed in m above.

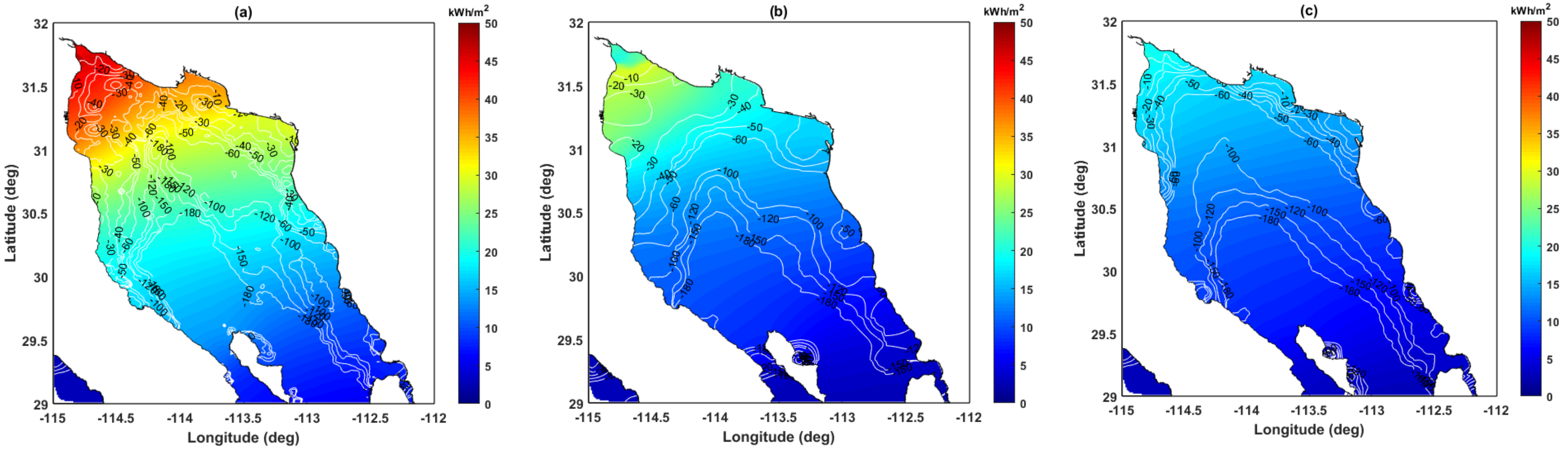

Figure 4.8. Annual energy yield using different bathymetry products: (a) GEBCO merged with CICESE (b) ETOPO and (c) only GEBCO. Bathymetry contours superimposed in m above.

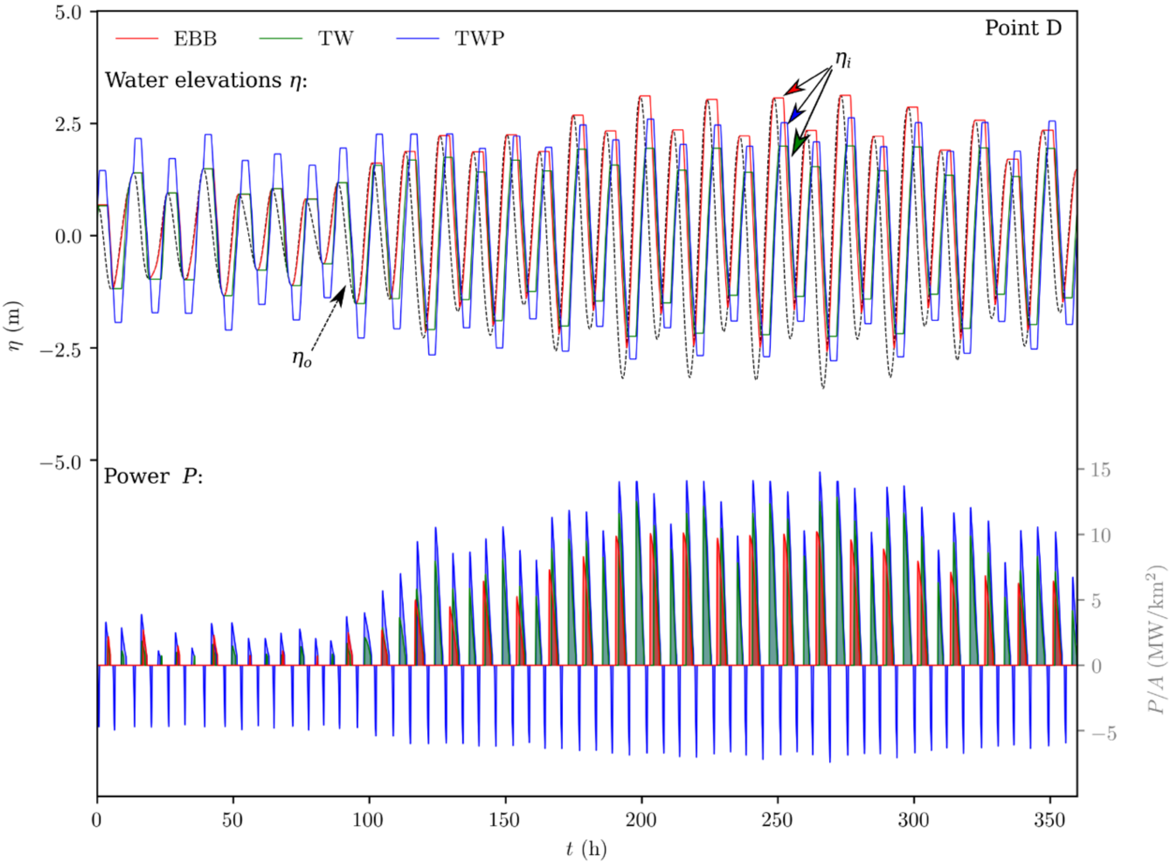

Figure 4.9. Water elevations and power produced for the three operational strategies for point D (Gulf of Santa Clara). EBB= Ebb-only generation, TW= Two-way generation, TWP = Two-way generation with pumping. η_i = inner water elevations, η_o = outer water elevation.

Table 4.1. Statistical validation error measures for the 11 tide gauges stations.

Site number	**Site Name**	**RMSE (m)**	**% Error**	**STD (m)**	**Correlation Coefficient**
1	Ensenada	0.03	1.2	0.02	0.99
2	San Quintin	0.11	4.5	0.07	0.97
3	Isla Cedros	0.10	4.4	0.09	0.96
4	Guerrero Negro	0.26	9.6	0.15	0.84
5	Cabo San Lucas	0.06	3.0	0.04	0.99
6	La Paz	0.19	10.9	0.12	0.75
7	Loreto	0.08	5.9	0.05	0.95
8	Bahia de los Angeles	0.09	3.0	0.07	0.98
9	San Felipe	0.25	3.8	0.17	0.99
10	Manzanillo	0.07	6.1	0.05	0.94
11	Acapulco	0.07	7.7	0.05	0.91
All	**Mean**	**0.11**	**5.0**	**0.07**	**0.86**

Table 4.2. Operational parameters used for the 0-D operational model for typical operational strategies employed in tidal-range power plants. EBB = One-way ebb generation, TW = Two-way generation, TWP = Two-way generation with pumping.

Operation specifications	Notation	EBB	TW	TWP	Units
Holding duration (ebb/flood)	$t_{h,e}$, $t_{h,f}$	3.50 / 0.00	3.00 / 3.00	2.00 / 2.00	H
Pumping duration (ebb/flood)	$t_{p,e}$, $t_{p,f}$	0.00 / 0.00	0.00 / 0.00	0.50 /0.50	H
Max Generation w/o sluicing (ebb/flood)	$t_{g,e}$, $t_{g,f}$	6.00 / 0.00	3.00 / 3.00	3.00 / 3.00	H

Table 4.3. Summary of sites considered for operational models in the Gulf of California, and a reference site based on the UK where tidal range projects have been considered. The table summarises, the mean tidal range, the annual energy per unit area, and the installed capacity calculated based on EQ. 4.3.

Marker	Site Name	Latitude (°)	Longitude (°)	$\overline{H}$ (m)	E_{yr}/A (GWh/km^2)	C/A (MW/km^2)
A	San Felipe	31.088	-114.740	4.37	45.2	15.8
B	Puerto Peñasco	31.287	-113.675	4.05	38.6	13.5
C	Playa Encanto	31.264	-113.812	4.08	39.2	13.7
D	Gulf of Santa Clara	31.489	-114.477	4.59	49.8	17.4
Reference	**Swansea Bay**	**51.58**	**-3.90**	**6.61**	**94.7**	**36**

Table 4.4. Technical annual energy output and operational efficiency for tidal range energy schemes at the selected sites along the coast of the Gulf of California. Table includes results from a reference site in the UK that has been identified as feasible for the deployment of the technology. In all cases the impounded area is = 10 km^2.

Site Marker	**Site Name**	**Ebb-only (EBB)**		**Two-way (TW)**		**Two-way with pumping (TWP)**	
		E_{yr} (Gwh)	**η (%)**	**E_{yr} (GWh)**	**η (%)**	**E_{yr} (GWh)**	**η (%)**
A	San Felipe	112	24.8	133	29.7	144	31.9
B	Puerto Peñasco	93	24.1	100	25.9	104	27.1
C	Playa Encanto	94	24.1	103	26.3	108	27.5
D	Gulf of Santa Clara	125	25.1	159	32	174	35
Reference	**Swansea Bay**	**250**	**26.4**	**393**	**41.1**	**520**	**55**

Chapter 5: Tidal-stream energy assessment

This chapter has been adapted from the following three publications:

> *Mejia-Olivares, C.J., Haigh. I.D., Wells, N.C, Coles, D.S., Lewis, M. and Neill, S.P, 2018. Tidal-stream energy resource characterisation for the Gulf of California, México. Energy, 156, 481-491. https://doi.org/10.1016/j.energy.2018.04.074*
>
> *Mejia-Olivares, C.J., Haigh. I.D., Lewis, M. and Neill, S.P, 2019. Sensitivity assessment of bathymetry and choice of tidal constituents on tidal-stream energy resource characterisation in the Gulf of California, Mexico. In review with Applied Ocean Energy*
>
> *Mejia-Olivares, C.J., Haigh. I.D., Lewis, M. and Neill, S.P, 2018. Sensitivity of bathymetry and choice of tidal constituents on tidal-stream energy resource characterisation in the Gulf of California, Mexico. Accepted and published with EWTEC 2019.*

5.1 Introduction

Tidal-stream energy exploits the kinetic energy of tidal currents, through the use of a variety of devices that are able to convert the linear velocity of the ocean's currents into a rotational torque (Bahaj, 2011). A detailed review of tidal-stream energy has been given in Section 2.2.3. In summary, there is only one commercial-scale scheme exploiting tidal-stream energy currently, the Strangford Lough scheme in North Ireland; but three pre-commercial array projects prototypes have been under construction since 2016 located at the following locations: (1) north of Caithness in the Pentland Firth and Orkney Waters, Scotland; (2) in the Bay of Fundy, in Canada; and (3) in Brittany, France (Marine Energy, 2016). In recent decades, a large number of studies have identified and carried out resource assessments, for many other sites around the world. These studies and the methods they utilized have been summarized in Section 2.2.3.2 and Section 2.2.3.3, respectively, and are listed in Table 2.4.

To date, no assessment of the tidal-steam energy resource has been produced for Mexico. However, peak spring tidal flows of over 1.5 m/s have been measured between the Midriff Islands in the GC (Badan-Dangon, 1991; Lopez et al., 2008). Therefore, this region holds promise for tidal-stream energy extraction. In contrast to other regions in which the tidal stream energy resource has been explored, the GC is relatively deep, and diurnal tidal constituents are typically larger; hence the resource characterisation is expected to contrast considerably from previously identified tidal stream sites.

Therefore, the overall objective of this chapter is to determine the potential theoretical tidal-stream energy resource available in the GC, Mexico. To address this overall objective there are three sub-objectives:

1. To map how the strength of tidal currents varies around the Midriff region of the GC;
2. To estimate the theoretical kinetic energy density in this region and determine the energy that can be generated technically;
3. To assess how this resource varies subject to different bathymetry datasets while accounting for multiple tidal constituents.

The structure of this chapter is as follows: Section 5.2 describes how the model described in Chapter 3, was used to assess current speeds and estimate the tidal-stream energy resource in the GC. The results for each of the three sub-objectives are then described in Section 5.3. Key findings are discussed in Section 5.4 and conclusions are given in Section 5.5.

5.2 Methodology

This section describes the used of the validated model described in detail in Chapter 3, to assess current speeds and estimate the energy resources of the region, including undertaking sensitivity tests using different bathymetry sources in the model while accounting for multiple tidal constituents.

5.2.1 Tidal currents analysis

Using the validated model, current speeds were assessed across the GC, with a focus on the Midriff region, to determine the location of the fastest currents, their magnitude and how the flows vary over a tidal cycle and a spring/neap period. To do this, tidal currents were simulated for a 30-day period in March 2015, when tidal currents are expected to be largest due to the large equinox tides that occur around that time each year (Pugh and Woodworth, 2014). Results were saved for each grid point every 10 minutes. Predicted u and v current velocities components were converted into speed and direction.

Current vector plots were produced over a single tidal cycle to examine the characteristics of tidal currents in the region. The maximum current speed was calculated for each grid point for the full 30-day period. Then maximum spring and neap, and ebb and flood current speeds were also calculated. The maximum neap velocity was calculated for the period from the 12-16 March 2015, and the maximum spring velocity was calculated for the period from the 19-23 March 2015. The maximum currents speed values in the ebb and flood period occurred around the 22 March 2015. Note, for this objective the focus is on depth-averaged currents; an assessment of how tidal currents vary with depth is given in Chapter 6.

5.2.2 Methodology to assess the kinetic energy resource

Next, the theoretical, undisturbed tidal-stream energy resource of the GC was quantified, with a focus on the Midriff region because the highest current speeds are observed here. The tidal stream energy resource was calculated using the tidal current harmonics from the simulated current speeds over the 30-day simulation period in March 2015. To avoid computational constraints, tidal current harmonics were used to predict the tidal currents for a full year, to obtain mean annual values of velocity and KPD, again using the T_TIDE software (Pawlowicz, et al., 2002). The instantaneous undisturbed 'theoretical' KPD (per unit area) was calculated following the approach of Fraenkel (2006), as follows:

$$P_{KPD} = \frac{1}{2}\rho V^{3} \quad \text{(Units in W/m}^2\text{)} \qquad \text{(EQ. 5.1)}$$

Where P_{KPD} represent the instantaneous undisturbed theoretical power density in kW/m^2 is, ρ is water density (1020 kg/m^3) and V is the depth-averaged current velocity (m/s). Turbine power output depends on the cube of current speed, highlighting the importance of high current speeds to tidal-stream energy resource. The KPD is defined as the average quantity of power per unit area available across a surface. In the case of marine current turbines, the cross-sectional area refers to the diameter or the swept area that is in direct contact with the incoming flow. Here, the theoretical KPD was calculated assuming no device interaction with the resource and assuming a one square meter cross-sectional area. An example of an instantaneous time-series of power density is shown in Figure 5.1b, for the location with the fastest current speeds in the GC for March 2015; the current speed for this month is shown in Figure 5.1a.

Then, a second analysis to estimate the maximum instantaneous undisturbed 'theoretical' power (P) in Watts (Myers and Bahaj, 2005) was undertaken, as follows:

$$P = \frac{1}{2}\rho A V^3 \qquad \text{(Units in W)} \qquad \text{(EQ. 5.2)}$$

Where ρ is water density (1020 kg/m^3), V is the depth-averaged current velocity (m/s) and A is the swept area of a tidal turbine (m^2). The instantaneous power represents the KPD multiplied by the swept area (down through the water column). The interpolated current speeds from our flexible mesh were interpolated onto a regular mesh, with a resolution of 5 km. As a first order approximation, the assumption of calculating A as being the water depth (allowing for 7 m clearance from the surface and 10 m clearance at the bottom) of each cell multiplied by the width of the cell was considered (see Figure 5.2). Although devices capable of a swept area in the order of 100 – 500 m (the typical water depths in our study area) are not currently being developed, this approach provides an estimate of the maximum theoretical resource available. It is important to stress that this is a significant over-estimation of the available resource, as it would not be possible to utilize the full water column at 100% efficiency. Never-the-less it provides a useful first approximation to inform industry and policy and demonstrates, as discussed later, that sites with slower tidal current speeds, but lower water, have a potentially large tidal stream energy resource. Also, in the future, the innovative development of emergence of tethered floating devices (i.e. 3rd/4th/5th/ generation tidal-stream devices) will be able to utilise this theoretical resource in greater water depths.

Then, a third analysis was undertaken to more realistically estimate the technical power (TP) using the technical and practical methods described in Section 2.2.3.3, which take into account characteristics of particular turbine designs (e.g., swept area, power coefficients, power rating, and cut in velocity speeds). The technical power (in kW/m^2) was calculated as follows (using an approach that is similar to that of Betz theory used for wind turbines; Betz, 1966):

$$TP = \frac{1}{2}\ \rho\, A\, V^3\, Cp \qquad \text{(Units W)} \qquad \text{(EQ. 5.3)}$$

Where A is the swept area of a tidal turbine (m^2), V is the depth-averaged current velocity (m/s), Cp is the power coefficient based on the turbine performance (dimensionless) and ρ is the water density (1020 kg/m^3). Table 5.1 list the: (1) swept diameter; (2) power rating; (3) velocity rating; (4) cut in velocity; and (5) power coefficient of 14 commercial or prototype power tidal stream energy devices that are currently being used or tested. The power coefficient quantifies the efficiency of the device. The cut in velocity indicates at what current speed the device can start generating energy. The velocity relating indicates the upper speed at which the device will only generate the power of the power relating. Here, four different devices from these 14 are considered, as follows: (1) the MCT device; (2) the SeaGen-S 2MW (Atlantis) twin rotor; (3) the Schottel Hydro d3; and (4) the Sabella D-10. These four devices are chosen as they cover the range of different device characteristics. The four chosen devices are shown in Figure 5.2. An example of an instantaneous time-series of technical power for the MCT device is shown in Figure 5.1c and 5.1d, for the location with the fastest current speeds in the GC for March 2015, before and after accounting for cut in and cut out speeds. For each device type, the technical power is estimated, in each 5 by 5 km interpolated grid cell, considering the characteristics of that specific device, summarised in Table 5.1. The technical power is then multiplied by the number of turbine devices it would theoretically be possible to deploy in that 5 by 5 km area. To avoid wake effects it is assumed, following Myers (2005), that the lateral spacing between turbines is 3 times the diameter of the devices while the longitudinal space is 15 times the diameter of the turbine. This is illustrated in Figure 5.4. First, the technical power was estimated assuming that it was only possible to have a single arrange of devices near to the surface. The second set of technical power estimates assumed devices could be installed throughout the water column. Devices needed to be separated by a distance equivalent to 3 times the diameter of the device in the vertical, allowing for 7 m clearance from the surface and at the bottom a quarter of the total depth at that site. This is illustrated in Figure 5.5.

5.2.3 Influence of bathymetry and different tidal constituents

Chapter 3 described how the model validation improved when higher resolution bathymetry data for the Midriff region (obtained from CICESE with a resolution of~450 m) was merged within the GEBCO dataset (~900 m resolution), compared to just using GEBCO alone. To explore how sensitive the results are to using different bathymetric datasets, three sensitivity tests were run. The model was run for a 30-day period in March 2015, using just bathymetry data from two well-known and well-used sources: (1) GEBCO_2014 (Kapoor, 1981); and (2)

ETOPO (NOAA, 2017), which are available at resolutions of ~900 and ~775 m, respectively. The maximum current speeds and the estimated 'theoretical' power, were compared from these two runs, to a third run which used the GEBCO data merged with the higher resolution data from CICESE, for the Midriff region. Further sensitivity tests were undertaken, in which the energy estimates using all the tidal constituents were compared with those computed using the tidal predicted from just the M_2 and S_2 constituents.

5.3 Results

The results are presented in three main parts: (1) analysis of currents speeds; (2) the three estimates of the theoretical, undisturbed tidal-stream energy resource, including estimates of technical power for four different types of devices; and (3) the results of the sensitivity tests in which we ran simulations with different model mesh bathymetries.

5.3.1 Currents speed analysis

Hourly current vector fields over a single spring tidal cycle when the maximum velocities occur (22 March 2015) are shown in Figure 5.6 for the Midriff region. Current speeds reach a maximum 3 hours after low water on the flood tide, and 3 hours after high water on the ebb tide, i.e. close to a classical standing wave. The location of Angel de la Guarda Island, to the east of the GC, and Tiburon Island, to the west of the GC, funnels the currents, first to the east of the GC, then to the west, on the flood tide; and vice-versa on the ebb tide.

The peak current speeds over the 1-month simulation are shown in Figure 5.7 (note the colour scale has been altered from Figure 5.6 to highlight regions with fastest currents), superimposed with bathymetry contours. Results show that maximum current speeds reach localised values of between 1 and 2.4 m/s at selected sites in the Midriff area. There are four main regions where current speeds exceed 1 m/s, the locations of which are marked on Figure 5.7. Current speeds are largest and reach a maximum of about 2.4 m/s in the deeper-water (~500 m) channel between the San Lorenzo and San Esteban Islands (Marker A, Figure 5.7). The distance between these two Islands is approximately 18 km. Current speeds of around 1.6 m/s are reached in the channel between the Baja California Peninsula and San Lorenzo Island (Marker B, Figure 5.7). The fast currents occur nearer to the main land. The distance between the Baja California Peninsula and San Lorenzo Island is around 17 km. Current speeds of around 1 m/s are reached in the Channel between San Esteban and Tiburon Islands (Marker C, Figure 5.7).

The distance between these two Islands is 12 km. Current speeds of 1 m/s also occur in the northern part of the Ballenas Channel between the Baja California Peninsula and Angel de la Guarda Island (Marker D, Figure 5.7). The average width of this channel is around 14 km. Maximum current speeds at just less than 1 m/s at the south-eastern tip of Angel de la Guarda Island. Time-series of current speeds, at the grid point with fastest current speeds in each of the four main areas is shown in Figure 5.8.

The area where current speeds are in the range 1 to 1.5 m/s is 1,431 km^2 within the horizontal area. Current speeds are between 1.5 and 2 m/s in an area 70 km^2 and are greater than 2 m/s in an area 35 km^2 horizontally. Sites with current speeds between 1 and 1.5 m/s are mostly situated in areas with depths greater than 100 m. Sites with velocities from 1.5 m/s and above 2 m/s are situated in depths over 120 m.

Maximum current speeds during a spring and neap period, and for the flood and ebb of a single tidal cycle, are shown in Figure 5.9. Tidal current speeds are up to 1 m/s slower during a neap tide (Figure 5.9b), compared to a spring tide (Figure 5.9a). Currents are slightly faster during the ebb tide (Figure 5.9d) compared to the flood tide (Figure 5.9c).

5.3.2 Tidal-stream energy resource assessment

The theoretical undisturbed tidal-stream energy resource in the GC was estimated for the first time. The instantaneous theoretical KPD for the maximum currents speed (over the 1-month simulation period) is shown in Figure 5.10, for the Midriff region. As expected this closely resembles the pattern of maximum current speeds, shown in Figure 5.7. In San Lorenzo Passage (the channel between the San Lorenzo and San Esteban Islands) (Marker A in Figure 5.7), the maximum instantaneous theoretical KPD reaches 5 kW/m^2. In the other three regions, mentioned above (and shown in Figure 5.7) the maximum instantaneous theoretical KPD ranges between 1.5 and 2.5 kW/m^2. Maximum instantaneous theoretical KPDs exceeds 1 kW/m^2 in an area of 384 km^2 in the horizontal area is between 1.5 and 2.5 kW/m^2 in an area of 314 km^2 and exceeds 2.5 kW/m^2 in an area of 35 km^2 horizontally. A better measure of the available energy resource, considering temporal variability, is annual mean KPD (per m^2). The annual mean KPD is shown in Figure 5.11a. The mean KPD range is between 0.55 and 0.65 kW/m^2 in San Lorenzo Passage. In the other three regions, the annual mean power density lies between 0.1 and 0.2 kW/m^2.

The annual maximum theoretical undisturbed mean power output was estimated, assuming, as a first order approximation, that tidal-stream turbines could utilize the full water depth (allowing for 7 m clearance from the surface and 10 m clearance at the bottom) and cross-sectional area of each grid cell (5 km width). The annual theoretical mean power output for the Midriff regions, is shown in Figure 5.11b. The maximum annual mean power output is now in the northern part of the Ballenas Channel between the Baja California Peninsula and Angel de la Guarda Island. This is because the greater water depths in this region (~500 m), allowing for a larger overall turbine surface area, countering the slower current speeds. Here the annual theoretical mean power output exceeds 200 MW. Whilst in the other three areas the annual mean power output is between 100 and 200 MW.

Next, a more realistically estimate of the tidal-stream energy resource was made. Here the technical power was estimated for four different devices, taking into account characteristics of the particular turbine design (e.g., swept area, power coefficients, power rating, and cut in velocity speeds). Technical power was estimated first, assuming just an array of devices near the surface, and second, assuming an array of devices down through water depth. The results from the MCT device are shown in Figure 5.12a, for the near surface array. In a 5 by 5 km grid it would be theoretically possible to install 1,482 turbines near the surface, as each turbine has a dimeter of 16 m. For the MCT devices power would only be generated for 36, 5 by 5 km grid cells. This is because, only 36 gird cells in this area have a current speed greater than the cut in speed of the device (1 m/s). The estimated total annual mean technical power is 251 MW. 70% of this power (174 MW), is generated at just one location; the grid cell at site A (see Figure 5.7). At two other grid cell the power exceeds 10 MW, and these account for 7% (19 MW) and 5% (14 MW) of the energy, respectively. The first of these grid cells is located next to site A and the other at Site B (Figure 5.12a). The technical power, calculated assuming that devices could be installed through the water depth is shown in Figure 5.12b. The estimated total annual mean technical power is now 322 MW. The estimated technical power for the grid cell at Site A is still 174 MW, because the water depth at this location (92 m) does not allow for more than 1 array in the vertical with a device of 16 m diameter. However, this site now accounts for 54% of the total energy of the region. Four locations now have technical power greater than 10 MW. The technical power is larger at the grid cells around Site D (see Figure 5.7), because the water depth here is larger.

The results for the SeaGen-S 2MW (Atlantis) twin rotor devices are shown in Figure 5.13a, for the near surface array. In a 5 by 5 km grid it would be theoretically possible to install 3,875 turbines near the surface, as each turbine has a dimeter of 10 m. Again, for this type of device, power would only be generated for 36, 5 by 5 km grid cells. This is because, only 36 gird cells in this area have a current speed greater than the cut in speed of the device (1 m/s). The estimated total annual mean technical power is 460 MW. 85% of this power (389 MW), is generated at just one location; the grid cell at site A (see Figure 5.7). At two other grid cell the power exceeds 10 MW, and these account for 2% (11 MW) and 2% (11 MW) of the energy, respectively. The technical power, calculated assuming that devices could be installed through the water depth is shown in Figure 5.13b. The estimated total annual mean technical power is now doubled to 779 MW. By utilising the water depth, ten locations now have technical power greater than 10 MW. The technical power is again larger at the grid cells around Site D (see Figure 5.7), because the water depth here is larger.

The results for the Schottel Hydro d3 device are shown in Figure 5.14a, for the near surface array. In a 5 by 5 km grid it would be theoretically possible to install 930 turbines near the surface, as each turbine has a dimeter of 20 m. Again, for this type of device, power would only be generated for 36, 5 by 5 km grid cells. This is because, only 36 gird cells in this area have a current speed greater than the cut in speed of the device (1 m/s). The estimated total annual mean technical power is 264 MW. 69% of this power (182 MW), is generated at just one location; the grid cell at site A (see Figure 5.7). At two other grid cell the power exceeds 10 MW, and these account for 7% (19 MW) and 5% (14 MW) of the energy, respectively. The technical power, calculated assuming that devices could be installed through the water depth is shown in Figure 5.14b. The estimated total annual mean technical power is now 304 MW. By utilising the water depth, five locations now have technical power greater than 10 MW.

The results for the Sabella D-10 device are shown in Figure 5.15a, for the near surface array. In a 5 by 5 km grid it would be theoretically possible to install 43,264 turbines near the surface, as each turbine only has a dimeter of only 3 m. For this type of device, power would only be generated for 41, 5 by 5 km grid cells. This is because, only 41 gird cells in this area have a current speed greater than the cut in speed of the device (0.9 m/s). The estimated total annual mean technical power is 431 MW. 80% of this power (347 MW), is generated at just one location; the grid cell at site A (see Figure 5.7). At two other grid cell the power exceeds 10 MW, and these account for 3% (12 MW) and 3% (12 MW) of the energy, respectively. The technical power, calculated assuming that devices could be installed through the water depth is shown in Figure 5.15b. The estimated total annual mean technical power is now increased significantly to 3,550 MW. By utilising the water depth, 24 locations now have technical power greater than 10 MW.

5.3.3 Bathymetry and tidal constituents sensitivity results

In this section, the results of the sensitivity tests are described. The maximum current speeds and the estimated ‘theoretical’ power from the three different bathymetry simulations, for the Midriff region (Figure 3.4c and 3.3f). Current speeds vary significantly while using the three different bathymetry products within the four main regions where current speeds exceed 1 m/s (Figure. 5.16). The largest current speeds were localised within San Lorenzo Passage reaching a maximum of about 2.4 m/s in the deeper-water (~500 m) for the combined GEBCO and CICESE bathymetry. In contrast, when using just GEBCO_2014 or ETOPO bathymetry products, the current speeds in this channel reduce to around 1.2 m/s and 0.8 m/s, respectively. Similarly, in the region of Ballenas channel (channel between Angel de la Guarda Island and the Baja California Peninsula) relatively large differences were found. Using the combined bathymetry dataset (Figure 5.16c) the flow speed was estimated to be around 1 m/s, whereas using GEBCO data only (Figure 5.16a) the current speed reduced to 0.5 m/s. However, the use of ETOPO bathymetry overestimated the current speed within Ballenas channel at around 1.8 m/s (Figure 5.16b).

The annual mean power are significantly underestimated when using just the GEBCO or ETOPO bathymetry data sources on their own for the Midriff region (Figure. 5.17). For the region with fastest current speeds, (San Lorenzo Passage) the annual mean power was 150 MW and 20 MW when using the GEBCO and ETOPO runs, respectively (Figures 5.17c and 5.17f). Whereas the annual mean power was calculated as ~200 MW when using the bespoke dataset (Figure. 5.17i). Similarly in the region between San Lorenzo and the Baja California peninsula (Marker B on Figure. 5.7) where the currents speeds are around 1.4 m/s the annual mean power was estimated of around 160 MW when using the combined bathymetry products whereas the resource reduces approximately to 80 MW and 40 MW when using GEBCO and ETOPO runs respectively. In the case of Ballenas channel the annual mean power estimated as 150 MW when using the combined bathymetry data however, the annual mean power was significantly overestimated as around 180 MW when using ETOPO bathymetry source (Table 5.3).

Next, different numbers of tidal constituents were utilise to analyse the quantification of the tidal-stream energy resource for the GC. The results of these tests are shown in Figure 5.18.

The annual mean KPD was estimated using only the S_2 tidal constituent (Figure 5.18c) which decreases by around a third in San Lorenzo Passage as compared with the calculation made using just the M_2 constituent (Figure 5.18a) from around 0.18 to 0.08 kW/m^2, while the maximum value reached was calculated as ~0.20 kW/m^2 where the fastest currents occur (Figure 5.20e).

Consequently, significant differences were found where the annual maximum theoretical undisturbed mean power was calculated utilising M_2 and S_2 on their own in San Esteban Passage. Using the M_2 tidal constituent, the estimation of the annual power is approximated between 90 and 100 MW (Figure 5.18b), while using S_2 tidal constituents the annual power reduced remarkably by more than half of around 15 to 20 MW (Figure 5.18d). Similarly, the annual mean power was calculated using M_2 plus S_2, where the results indicated an annual mean power range of 140 to 150 MW (Figure 5.18f). When taking into account predicted tidal levels, calculated using all 29 tidal constituents, the maximum annual mean was calculated in San Esteban Passage as ~200 MW (Figure 5.11b). Furthermore, the mean annual power reduces significantly where using just M_2 plus S_2 tidal constituent of around 140-150 MW. The annual mean power in San between Lorenzo Island and the Baja California peninsula (Marker B on Figure. 5.7a) was calculated of around 60 to 70 MW when using M_2 tidal constituents whereas the annual mean power increased almost the double (approximately 120 to 130 MW) when M_2 plus S_2 tidal constituents were included. Similarly, in the case of Ballenas (Marker D on Figure 5.7) the annual mean power reduces from 60 to 70 MW to 120 to 130 MW when using only M_2 and M_2 plus S_2 respectively (Table 5.4).

5.4 Discussion

In this chapter, the first detailed quantification of the theoretical tidal-stream energy resource available in the GC have been undertaken. Although a number of parameters are significant in tidal-steam energy resource assessments, the most important is clearly current speed. In this study, peak spring velocities were found to be between 1.0 and 2.5 m/s in four main areas centred in channels in the Midriff region of the GC. The San Lorenzo Passage shows the greatest potential for future tidal energy development, where flow speeds reach 2.4 m/s.

The maximum instantaneous KPD for the Midriff region is ~3 to 6 kW/m^2, but the mean annual KPD is much lower, ranging from 0.1 to 0.65 kW/m^2. For comparison, this represents only 10% of the maximum KPD available in the Bay of Fundy, the world’s largest tidal-range, and

7.5% of that predicted for Cape Spit (Cornett et al., 2010). It is currently unclear what level of annual mean KPD is needed for economic viability of tidal energy developments in the GC. This will be dependent on many factors, including (but not limited to) subsidy support, grid connection costs and technology cost reduction over time. For comparison, the 2011 UK tidal current resource assessment conducted by Black and Veatch (2005b) considered sites where the mean annual KPD exceeded 1.5 kW/m^2 in depths greater than 15 m. Clearly the KPD of the GC sites fall below this 1.5 kW/m^2 threshold. However, although the average KPD, and corresponding current speeds, are lower than recommendations for economic feasibility (2.5 kW/m^2) by Black and Veatch 2005b, the greater water depths (as discussed above), account for an overall greater power potential than for several sites in shallower water and with higher velocities. Depths at the GC sites far exceed that of 15 m and were found to occur in water depths of over 100 m, removing the constraint set by depth on allowable turbine swept area per turbine. As a comparison with other potential tidal-stream energy sites around the world, the deepest sites evaluated in these other studies are typically less than 80 m, and mostly less than 50 m.

Technical power estimates were made, considering four different devices, as follows: (1) the MCT device; (2) the SeaGen-S 2MW (Atlantis) twin rotor; (3) the Schottel Hydro d3; and (4) the Sabella D-10. When a near surface array only was considered, device 2 (SeaGen-S 2MW (Atlantis) twin rotor) gave the highest technical power for the region (460 MW). However, when devices down through the water column were considered, device 4 (Sabella D-10) gave the highest power (3,550 MW) please see Table 5.2 for summary results. Interestingly, this device gave between 3 and 10 times more energy than the other devices; as a result of the small diameter of the turbine (3 m) many thousands of turbines could theoretically be installed, utilising the deeper water depth in this region. With water depths varying between 72 and 540 m in this region, practical considerations regarding installation of turbines and mounting would clearly be a big issue.

Considerable research and development into tidal-stream energy has been carried out in the UK where the tidal energy sector is now on the verge of commercialisation. A clear example of this is the commissioning of the world’s first tidal stream array connected to the grid in Scotland (www.novainnovation.com) with an installed capacity of 3×100 kW. Phase 1A of MeyGen project in the Pentland Firth, Scotland (www.atlantisresourcesltd.com) represents great progress towards commercialisation within the marine energy sector worldwide. Both projects have deployed bottom-mounted tidal stream devices attached to the sea bed where the total water depth is <80 m. The UK plays host to 22 tidal device developers and 23 wave device developers (ORE Catapult, May 2018). A variety of new devices have been tested in UK waters. For instance, in October 2016 and after 15 years of development and construction, Orbital Marine’s SR2000 floating turbine (Figure 5.21) was deploy near Orkney Island. The turbine has the following characteristics: 16 m diameter, 2 MW rated power, cut-in current speed of 1 m/s, and rated current speed of 3 m/s. This turbine can operate continuously producing over 3,200 MWh of electricity with a maximum load factor of 38%. This type of turbine offers a variety of new benefits. For example, it provides full on-site access resulting in a low cost of maintenance, and an easy mooring system that does not need a level seabed as required for bottom mounted installations. In addition, no specialist vessel is required for maintenance (UK Marine energy 2019). Similarly, in 2014, Ocean Flow Energy (www.OceanflowEnergy.com) deployed a floating device at Sanda Sound in Scotland. This device had a rated power capacity of 1.2 MW and it operates into a water depth of 22 m. However, due to the lack of research funding the tidal testing programme ended. In the case of the GC where the maximum current speed are between 1 and 2.4 m/s this kind of devices would not be feasible as a result of the rated current speed. For this reason, alternative devices need to be developed considering lower speeds as well as the water depth within the GC.

Current tidal-stream turbines projects have focused on utilising devices where the current speed is greater than 2.5 m/s. However, less energetic sites in the world which have current velocities lower than 2.5 m/s have been overlooked (see Table 5.5) resulting in a reduction of opportunities for implementing large-scale commercialisation. Moreover, lower speed structural devices would provide a significant cost reduction as a result of utilising less raw materials and also the cost of maintenance would be reduced. Therefore, developing new devices would be necessary to be able to generate electricity in waters where the current speed is relatively lower. To date, a few projects around the world have started to identify suitable sites for turbine deployment in lower current speeds. For instance Minesto UK has currently identify a potential location at west of Anglesey, North Wales where the tidal flows are between 1.5–2 m/s mean peak flow at a depth of 80 to 100 m (https://minesto.com/projects/holyhead-deep). Therefore, Minesto has developed a new floating device DG500 (Figure 5.22) which is the first low-velocity tidal energy device project worldwide that will be gradually tested at Holyhead in two main stages. The first stage consists of testing the device base on operational functionality, verification and testing the control system. The second stage would move forward to testing electricity generation and looking to commercial demonstration of an array which have an installed capacity of 10 MW. Finally, this gradually expansion of testing prototypes of new device prototypes would contribute to marine energy sector because once the technology was proved, Minesto could imported that cut in edge technology to any other suitable location where the requirements are matched.

Therefore, the analysis of the distribution of the undisturbed KPD suggests that the four sites identified in this initial resource assessment of the GC are unsuitable for 1st generation tidal stream turbine technology. However, with investment and development in appropriate technology suitable for deeper water locations, sites within the GC could become feasible development opportunities in the future. This would also allow other similar sites to be utilized to increase the practical available resource worldwide. As occurred with wind energy (Bahaj, and Myers, 2004) new global markets should promote investment in tidal-stream energy extraction research (Bahaj, 2013). Prototypes, trials and knowledge of deep and low flow extraction devices will actively help to close the deep flow energy extraction knowledge gap. New technologies capable of operating at these deeper depths, and new energy policies can help reduce the current costs of marine energy extraction to open up opportunities at deeper, lower flow sites. It is also acknowledged in Black and Veatch (2005b) that ‘technologies specifically designed for low power density sites (such as the Minesto device) could potentially result in lower power density sites becoming economic’.

Only the theoretical undisturbed tidal-stream energy resource for the GC was calculated here. To further this study, effects such as array scale blockage (Garrett and Cummins, 2008), array-array interaction (Bourban et al., 2013; Coles et al., 2017), wake-turbine interaction (Abolghasemi et al., 2016) and array optimisation (Funke et al., 2016) also need to be considered. This relies on implementing additional drag terms in the momentum equations to simulate turbine drag. Select past numerical modelling studies have included the effect of turbine drag (Neill et al., 2009; Ahmadian et al., 2012; Neill et al., 2012; O’Donncha et al., 2013; Goward Brown et al., 2017). Therefore, one important consideration, for future work, would be to determine flow reduction across the GC as a result of tidal stream energy extraction, and consideration for optimal array layout. Nevertheless, this simple approach has allowed a first estimate of the annual mean and maximum theoretical tidal-stream energy resource to be estimated and will help inform the industry and policy, upon which more detailed further studies can be built.

The results within this work show that there are significant temporal variations in current speeds, and hence, the energy resource, over single tidal cycles (i.e. tidal asymmetry) and longer periods. These are due to the fact that tides in the Midriff region are mixed in form, as a result of relatively large semi-diurnal and diurnal tidal constituents. These factors, particularly the tidal asymmetry, need to be taken into account when planning for future device installations (Neill et al., 2014). In addition, it has been shown that correctly predicting tidal currents requires accurate, high resolution bathymetric data. Results thus caution the used of applying global bathymetric data products for tidal-energy resource assessment in regions where relatively little ‘freely available’ data is accessible.

Due to the complexity of setting up a full three-dimensional baroclinic model, and the associated longer model run times, an initial resource assessment was undertaken here based on results from a depth-averaged tidal model. The potential tidal-stream energy sites were identified in water depths >100 m, where three-dimensional flows will clearly be important. Previous oceanographic studies (e.g., Lavın and Organista, 1988; Alvarez-Borrego and Lara-Lara, 1991) have shown that the GC is subject to strong seasonal stratification, which will influence the vertical structure of tidal currents. Three-dimensional tide flows are analysed in Chapter 6.

Grid connectivity in the region presents a challenge. The nearest electricity connection point for the three southern sites was identified more than 35 km away at Kino Bay (near Guaymas II shown in Figure 6.26), requiring any cabling to cross the complex mountains on Tiburon Island. For the northern site, in the Ballenas channel, the closest connectivity point is that of Bahia de Los Angeles, more than 40 km south-west. Furthermore, the difficult access to the region due to its topography, dry weather and lack of fresh water make this area unattractive for urban development. Therefore, the tidal-stream energy that could be converted into electricity from the GC might be more suitable for off-grid applications.

5.5. Conclusions

The overall objective of this chapter was to undertake the first tidal-stream energy resource assessment for the GC in México. In contrast to other regions in which the tidal stream energy resource has been explored, the GC is relatively deep, and diurnal tidal constituents are typically larger. Hence the resource characterisation was expected to contrast considerably from previously identified tidal-stream sites.

Model predictions show peak current speeds of up to 2.4 m/s in the Midriff area and its straits. Key findings indicated that there are four main locations where the tidal current speeds exceeded 1.0 m/s: (1) in channel between the San Lorenzo and San Esteban Islands – here maximum current speeds are close to 2.4 m/s; (2) in the channel between the Baja California Peninsula and San Lorenzo Island; (3) in the Channel between San Esteban and Tiburon Island; and (4) in the northern part of the Ballenas Channel between the Baja California Peninsula and Angel de la Guarda Island.

The maximum instantaneous undisturbed 'theoretical' KPD in the Midriff region was estimated to be between 3 and 6 kW/m^2, but the mean annual KPD is much lower, ranging from 0.1 to 0.65 kW/m^2. However, as the sites with tidal current speeds typically exceed 100 m in water depth, then the maximum undisturbed theoretical annual mean power was estimated of to be 100 to 200 MW. Therefore, it was found that the tidal energy resource to be large, but new turbine technologies would be required to exploit these 'second generation' resource regions.

Technical power was estimated for four device types, first assuming just an array of devices near the surface, and second an array of devices down through the water depth. The estimated total annual mean technical power varied between 251 and 460 MW, considering just a near surface area, and between 304 and 1030 MW if the full water column was utilised. For the surface area, the best majority of the energy was generated at just one site (Site A).

Whereas the model simulations are based on localised refined bathymetry datasets, global and freely available bathymetry data products under-resolve the resource by 75 %. The variability of the resource, using a limited number of tidal constituents to predict the tidal current annually, indicates that the M_2 constituent, as expected, plays an important role into the energy calculation and contributes more than 50 % of the total energy resource, while the S_2 constituent contributes less (~20 %).

This assessment has provided an overall first order estimate of the available tidal-stream energy resource in the GC. It will provide a basis for more detailed analyses to guide selection of suitable sites for tidal–stream energy extraction in the region.

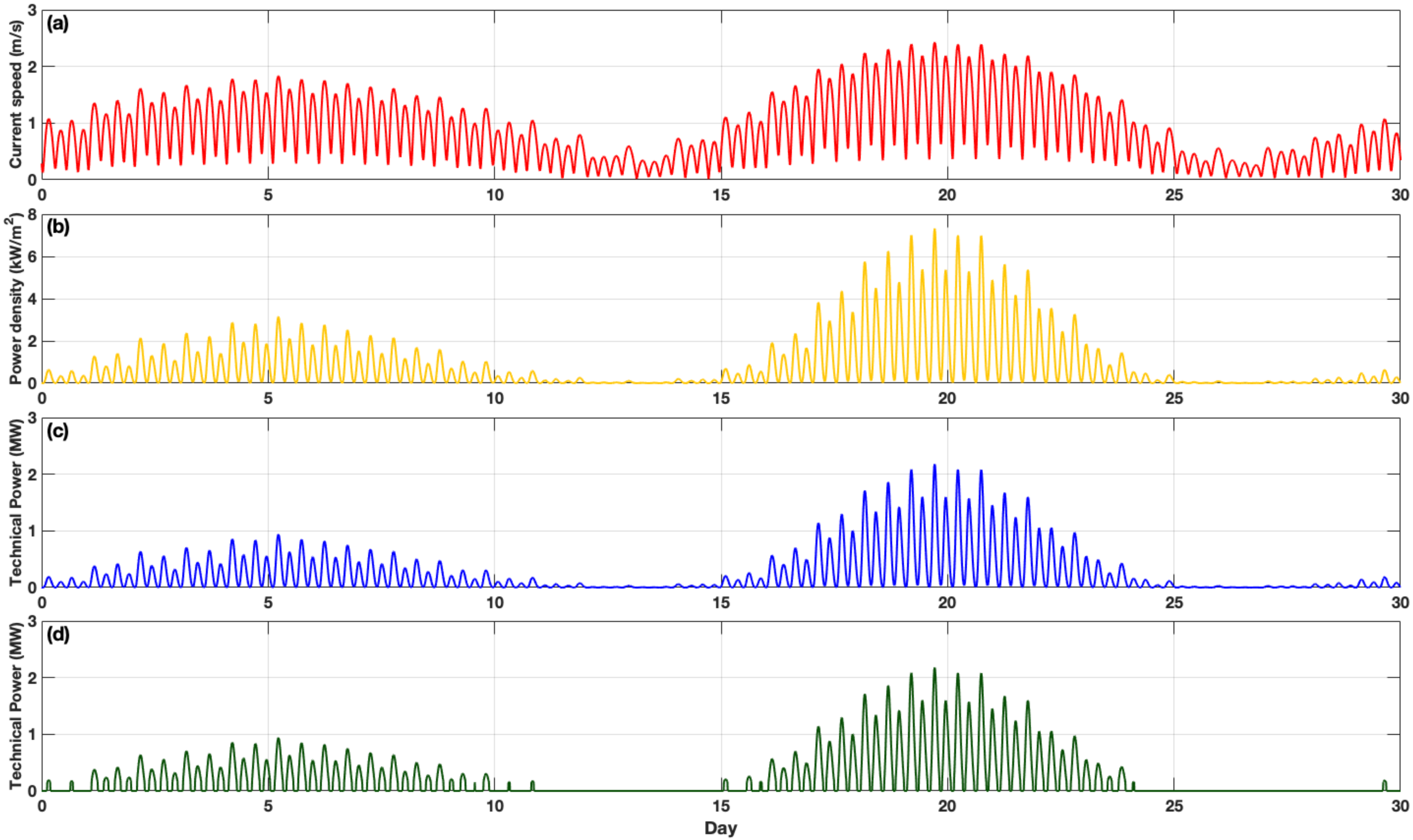

Figure 5.1 . (a) Current speed; (b) tidal stream power density; (c) technical power, without cut in and cut out speeds accounted for, and (d) technical power, with cut in and cut out speeds account for, for March 2015, at the location in the Midriff region with the fastest current speeds.

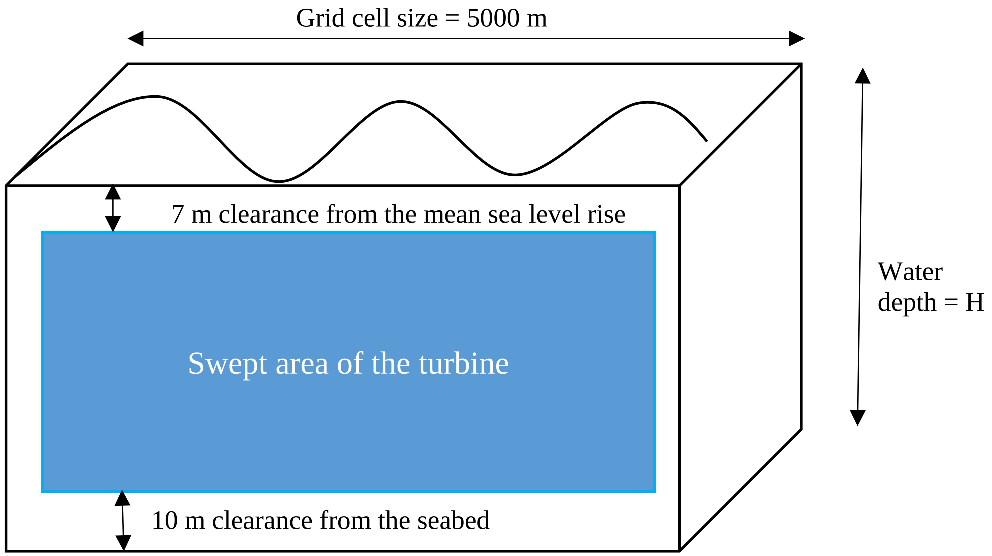

Figure 5.2. The theoretical Kinetic power density assuming the majority of the water depth could be utilized. Note, diagram not to scale.

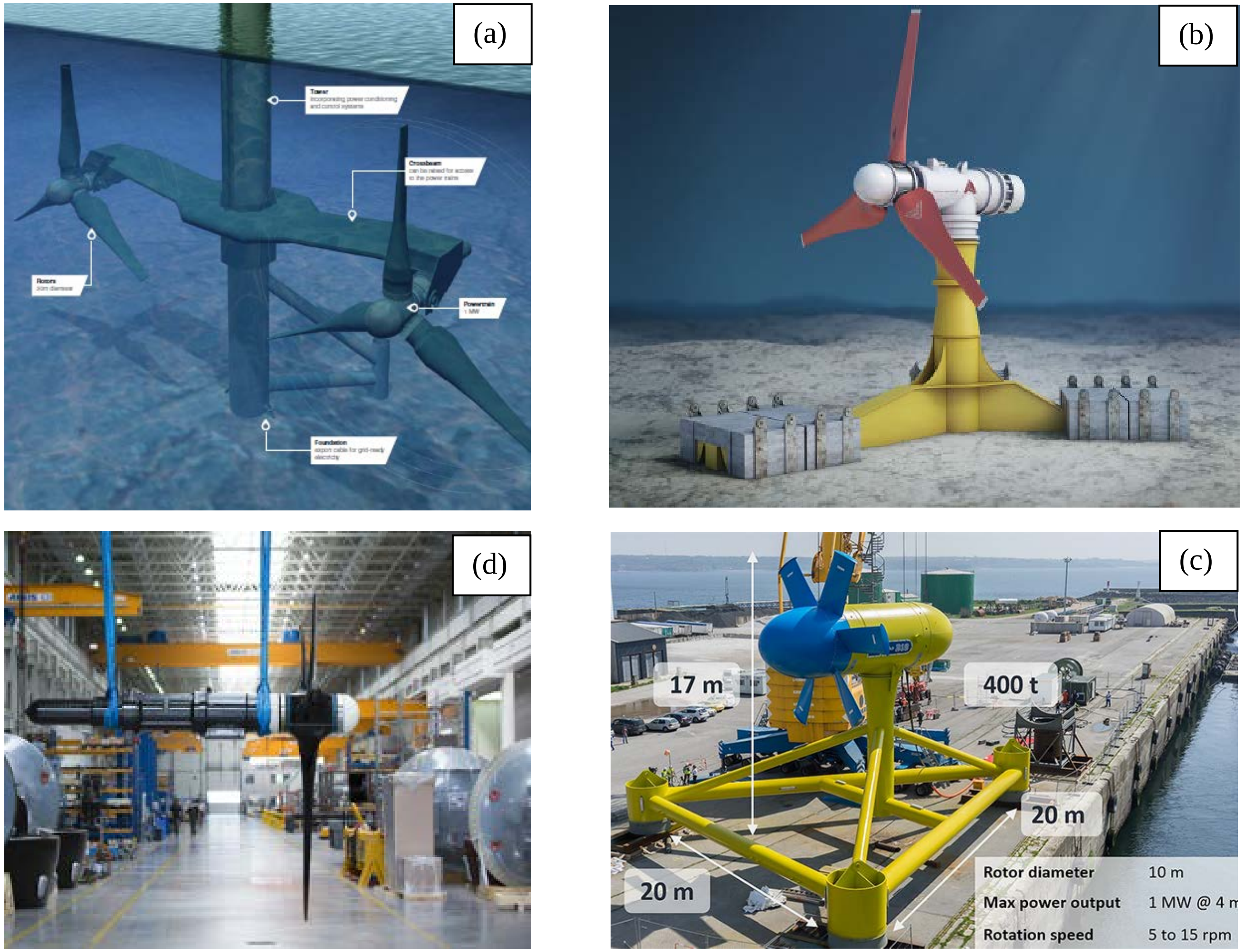

Figure 5.3. Devices used to estimate the technical power: (a) the MCT device; (2) the SeaGen-S 2MW (Atlantis) twin rotor; (3) the Schottel hydro d3; and (4) the Sabella D-10.

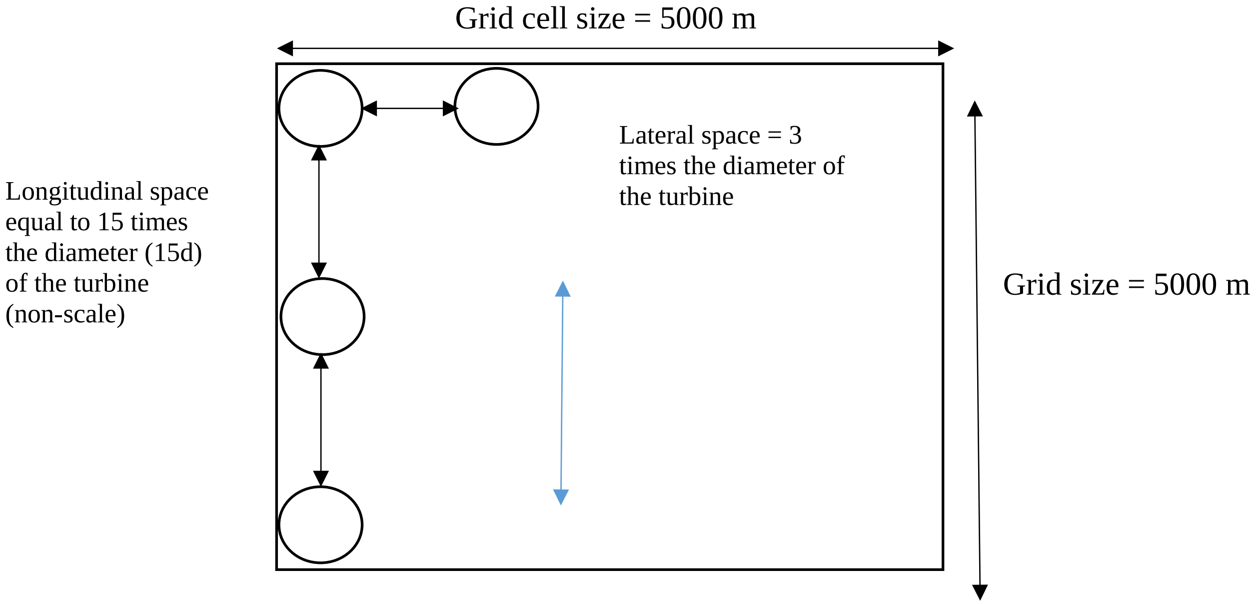

Figure 5.4. The assumed turbine array configuration considering the lateral and longitudinal spacing proposed by Myers (2005). Note, diagram not to scale.

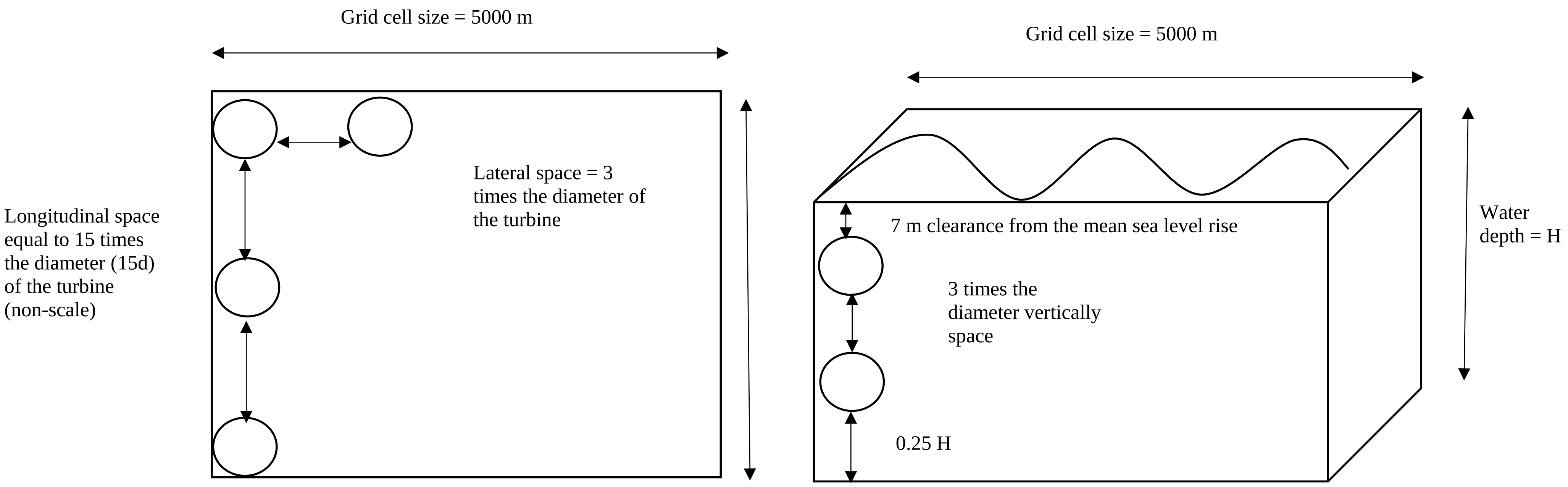

Figure 5.5. The assumed turbine array configuration considering the lateral and longitudinal spacing proposed by Myers (2005) and spacing of turbines down the water column. Note, diagram not to scale.

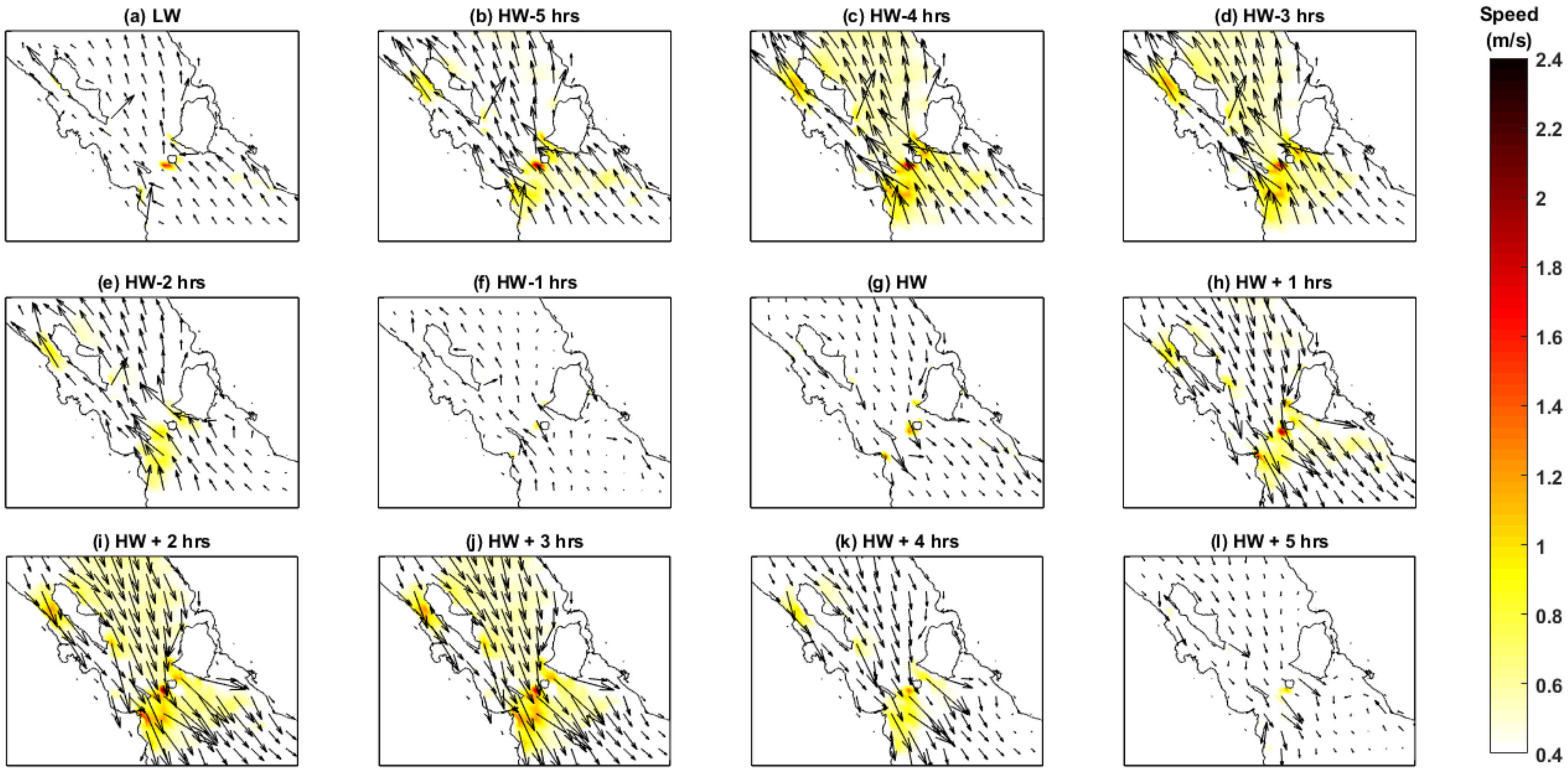

Figure 5.6. Velocity vectors (black arrows) and current speeds (background colour) over a single tidal cycle on the 22nd March 2015 for the Midriff region in the GC. a) Low Water b) High water - 5 hours c) High water -4 hours d) High water -3 hours e) hours e) High water – 2 hours f) High water – 1 hour g) High water h) High water + 1 hour i) High water + 2 hours j) High water + 3 hours k) High water + 4 hours l) High water + 5 hours.

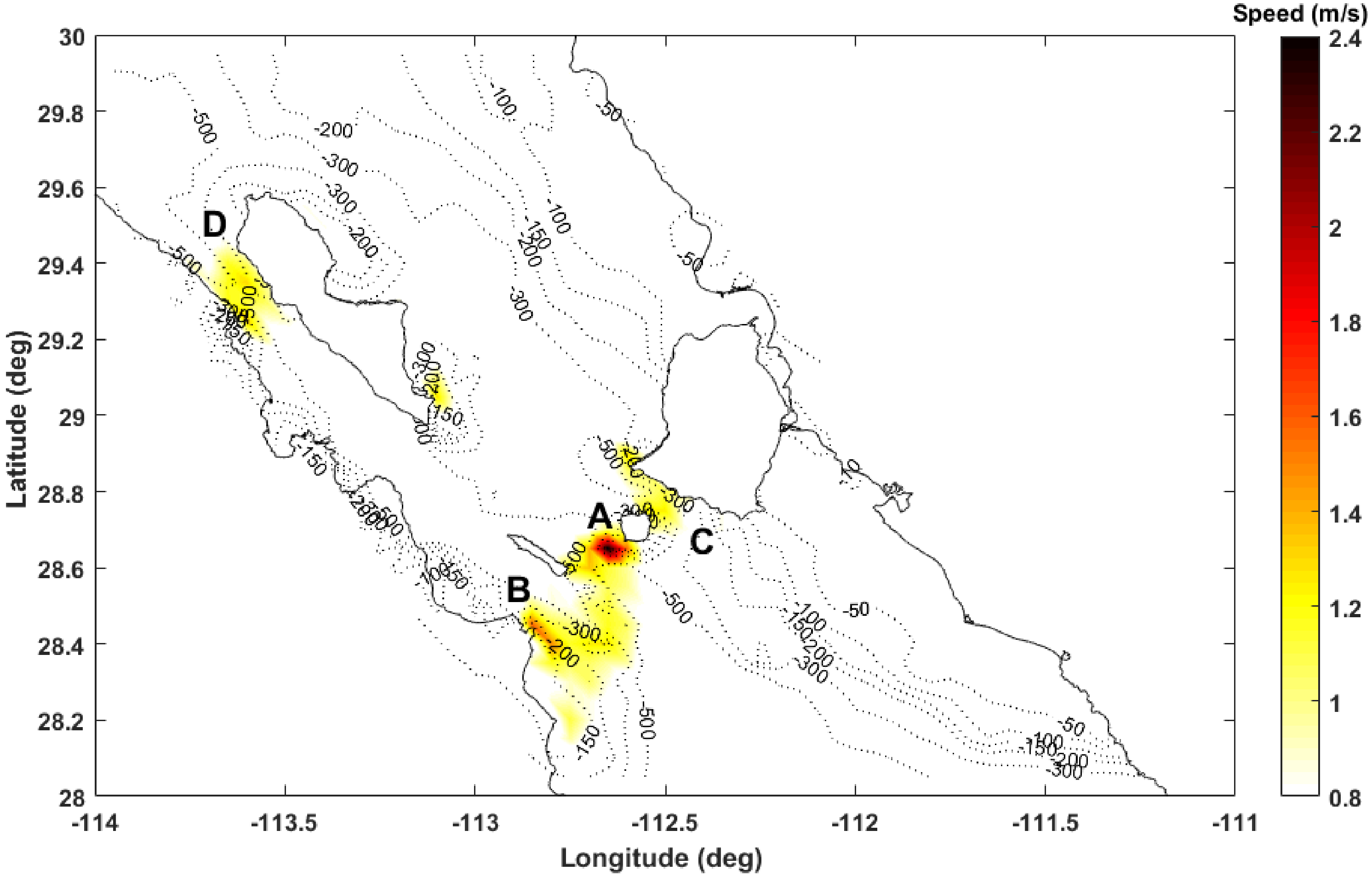

Figure 5.7. Maximum current speeds in the Midriff area during March 2015.

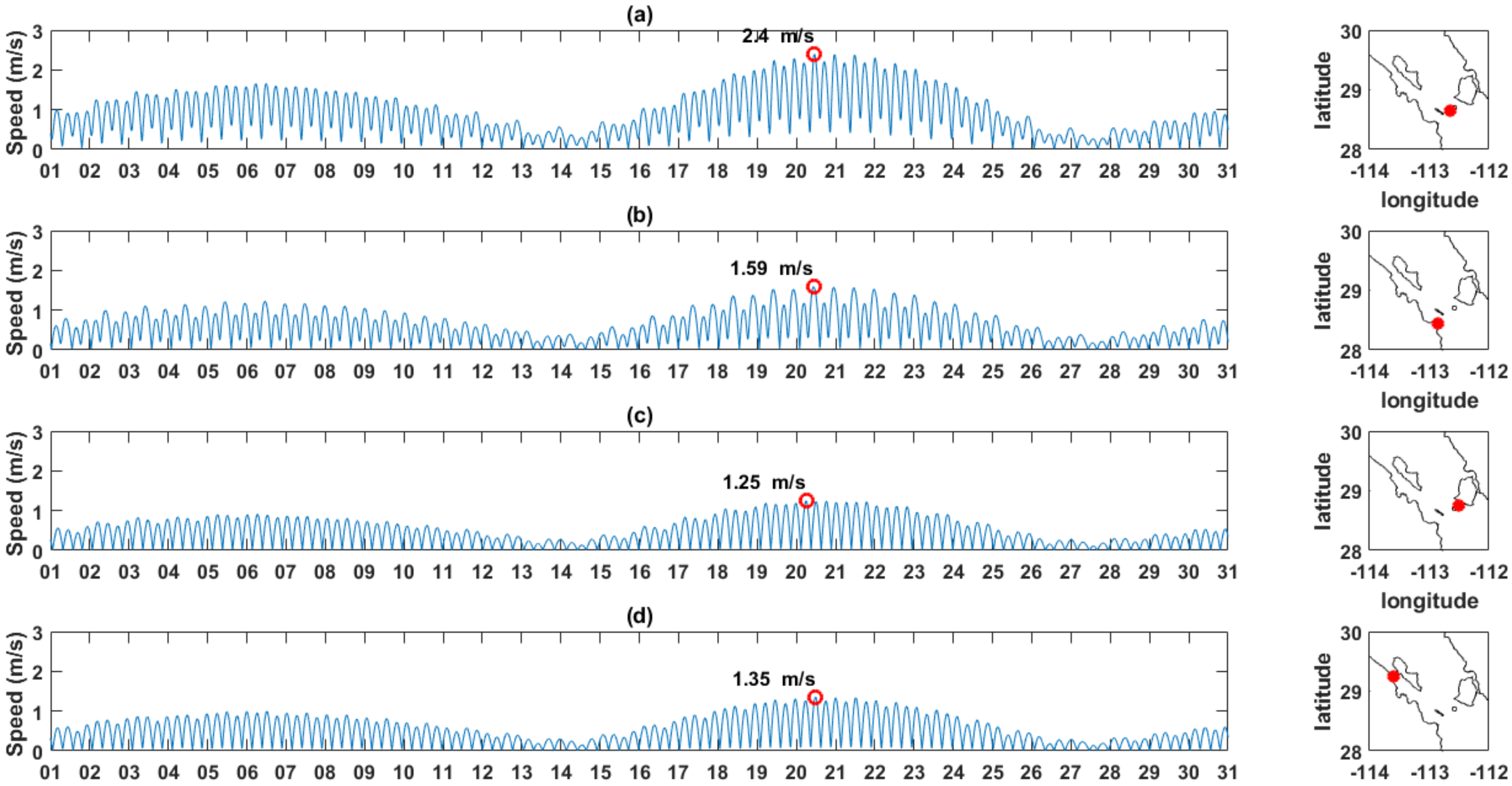

Figure 5.8. Time series of currents speeds in the four regions with the largest current speeds Sites location between (a) San Lorenzo (SL) and San Esteban (SE) Islands, (b) Baja California peninsula and San Lorenzo (SL) Island, (c) San Esteban (SE) and Tiburon Islands and (d) Baja California Peninsula and Angel de la Guarda Island.

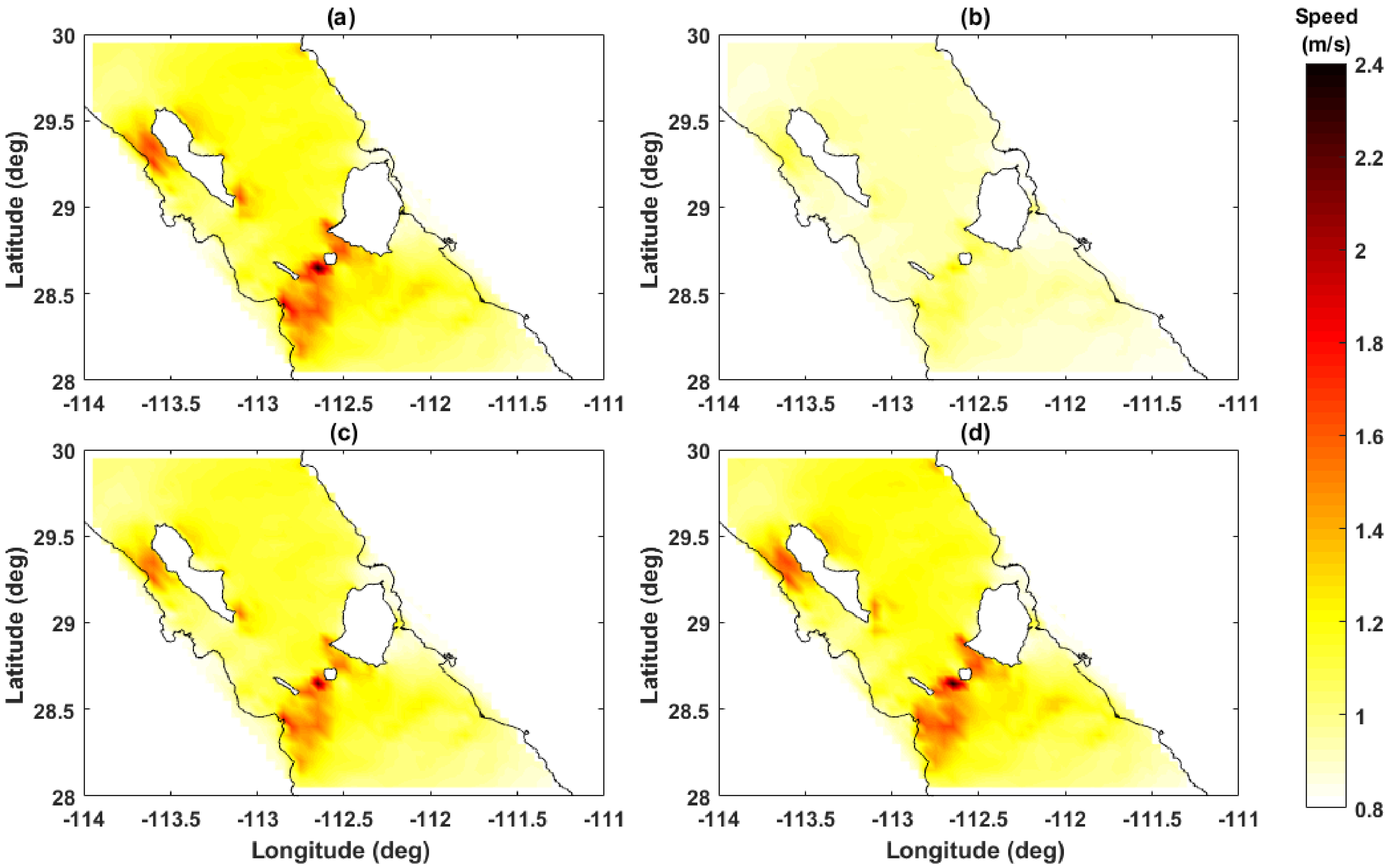

Figure 5.9. Maximum current speed for the (a) spring, (b) neap periods, and for the: (c) ebb and (d) flood tide, for the Midriff region in the GC.

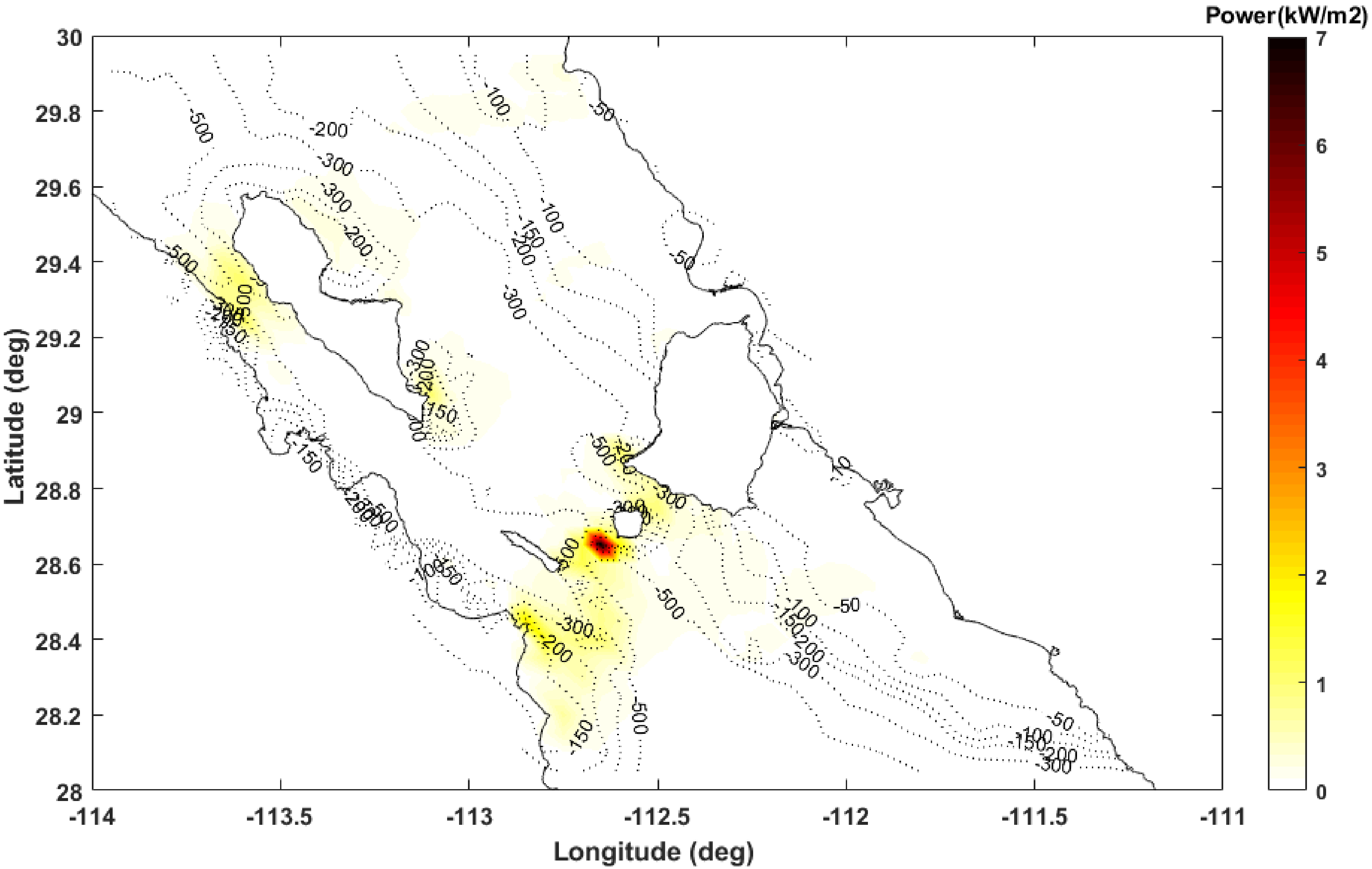

Figure 5.10. Maximum instantaneous undisturbed KPD, for the Midriff region in the GC.

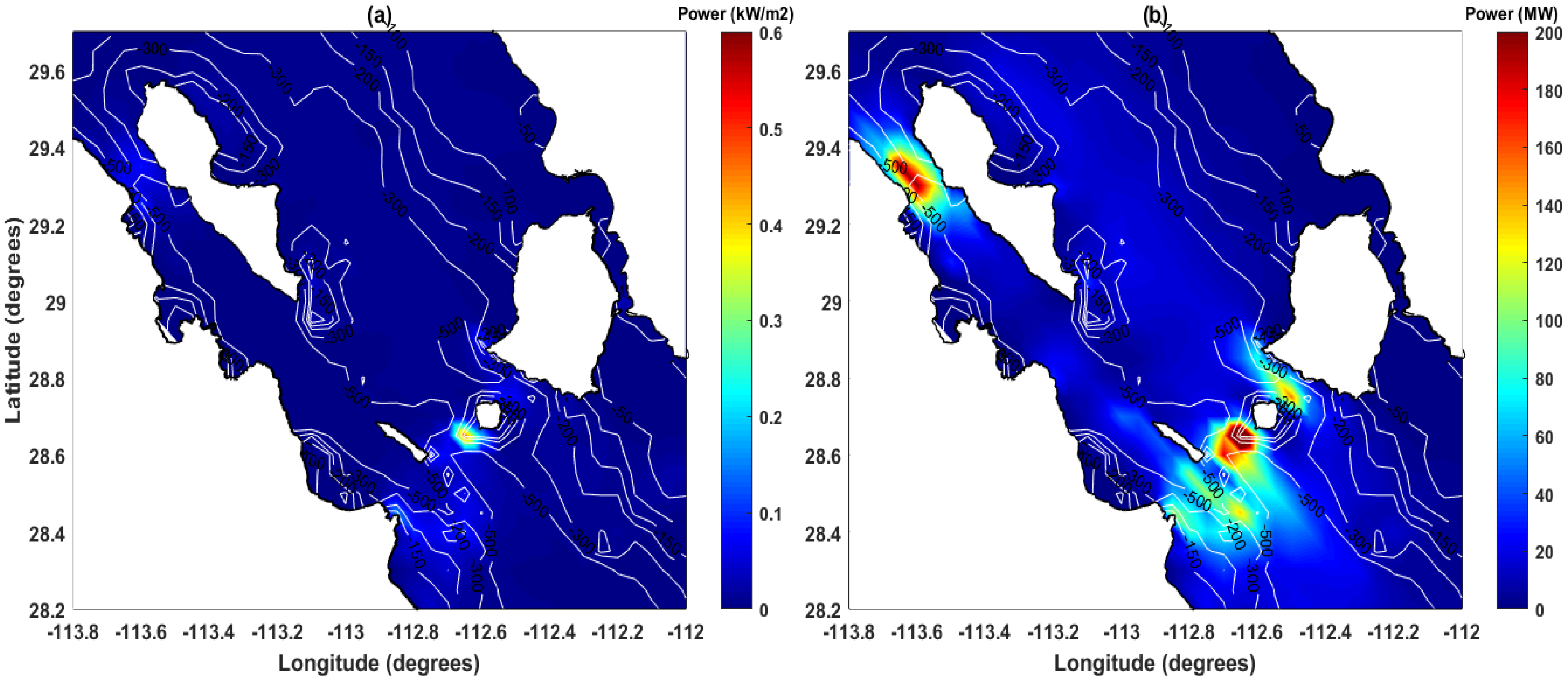

Figure 5.11. (a) Annual mean KPD, and (b) Annual theoretical mean power, for the Midriff region in the GC. Bathymetry contours are overlaid as white lines.

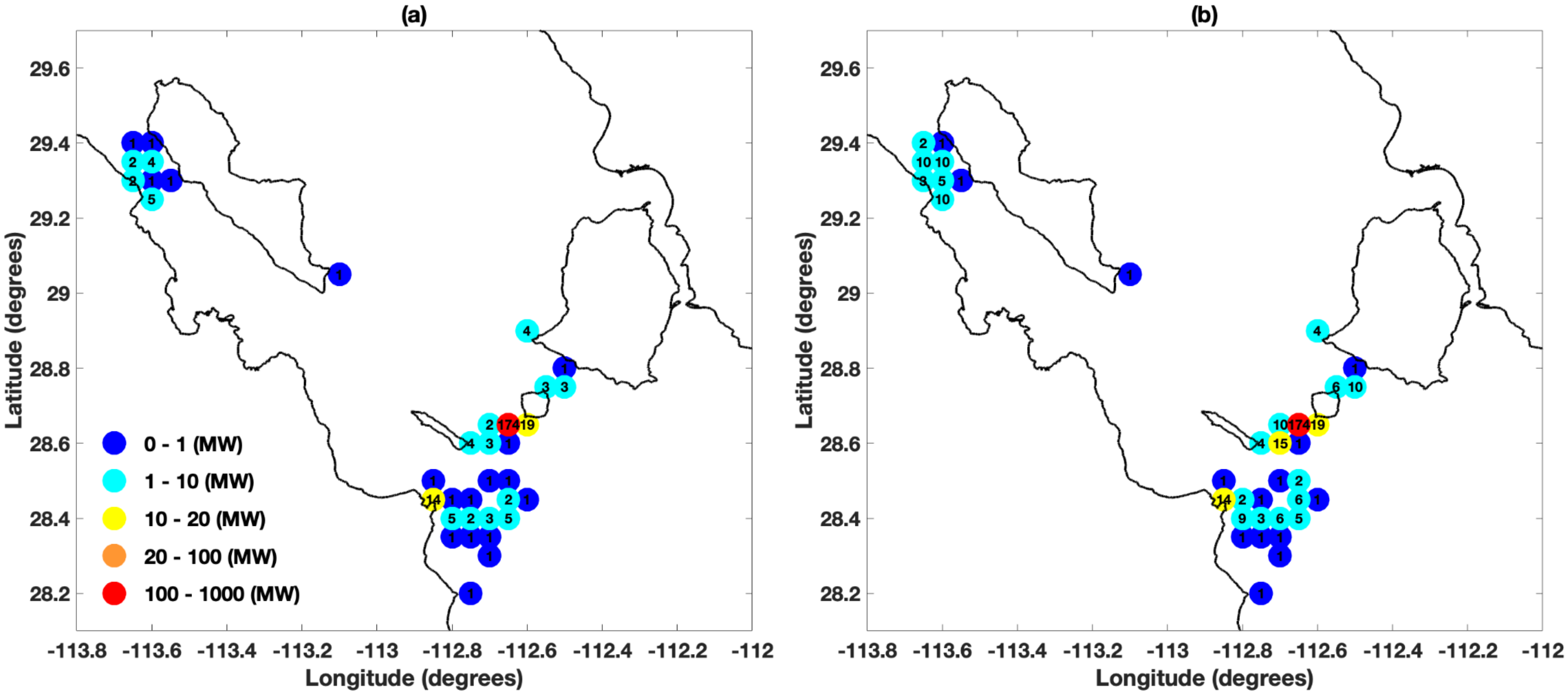

Figure 5.12. Mean annual tidal-stream technical power for each 5 by 5 degree model grid cell for the MCT device, assuming: (a) an array of devices near the surface with lateral spacing between turbines being 3 times the diameter of the devices while the longitudinal space is 15 times the diameter of the turbine; (b) arrays down through the water column, with devices separated by a distance equivalent to 3 times the diameter of the device in the vertical, allowing for 7 m clearance from the surface and at the bottom a quarter of the total depth at that site.

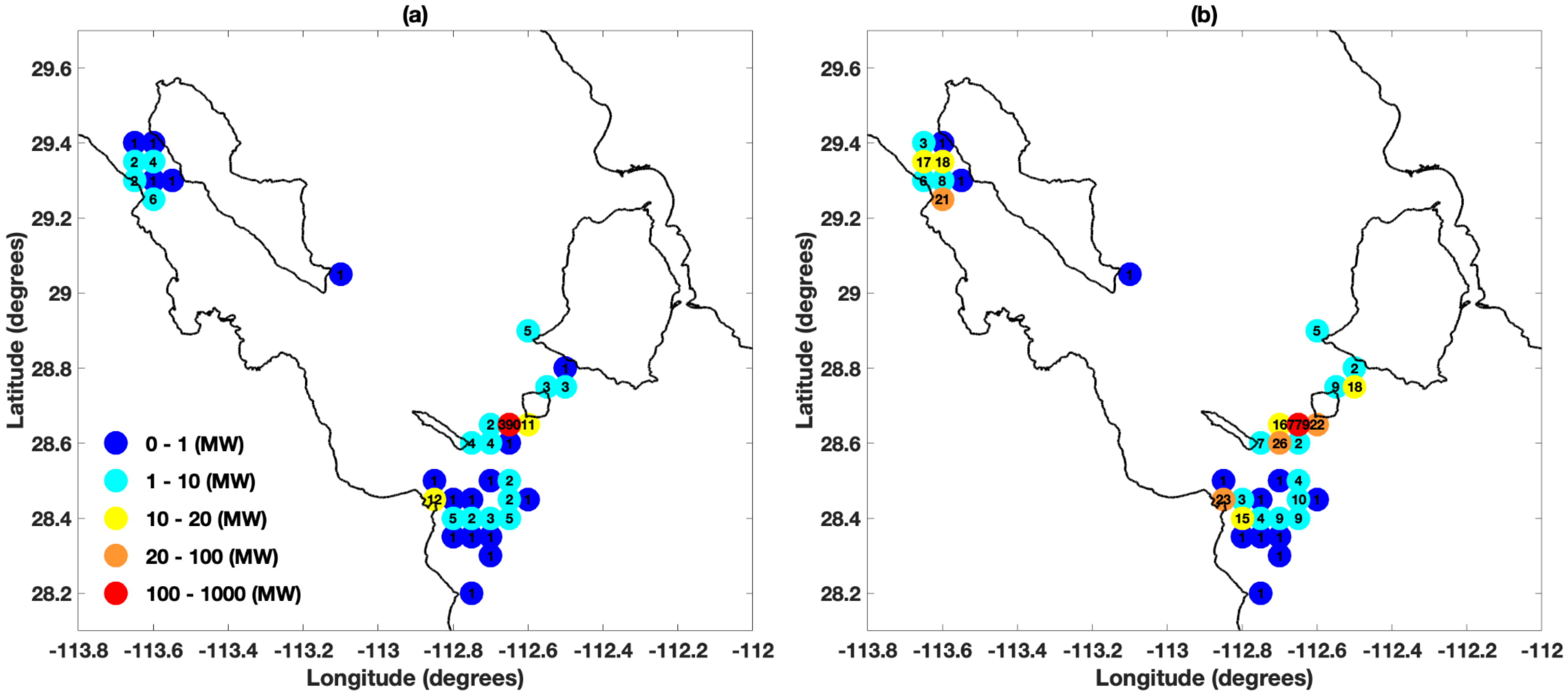

Figure 5.13. Mean annual tidal-stream technical power for each 5 by 5 degree model grid cell for the SeaGen-S 2MW (Atlantis) twin rotor device, assuming: (a) an array of devices near the surface with lateral spacing between turbines being 3 times the diameter of the devices while the longitudinal space is 15 times the diameter of the turbine; (b) arrays down through the water column, with devices separated by a distance equivalent to 3 times the diameter of the device in the vertical, allowing for 7 m clearance from the surface and at the bottom a quarter of the total depth at that site.

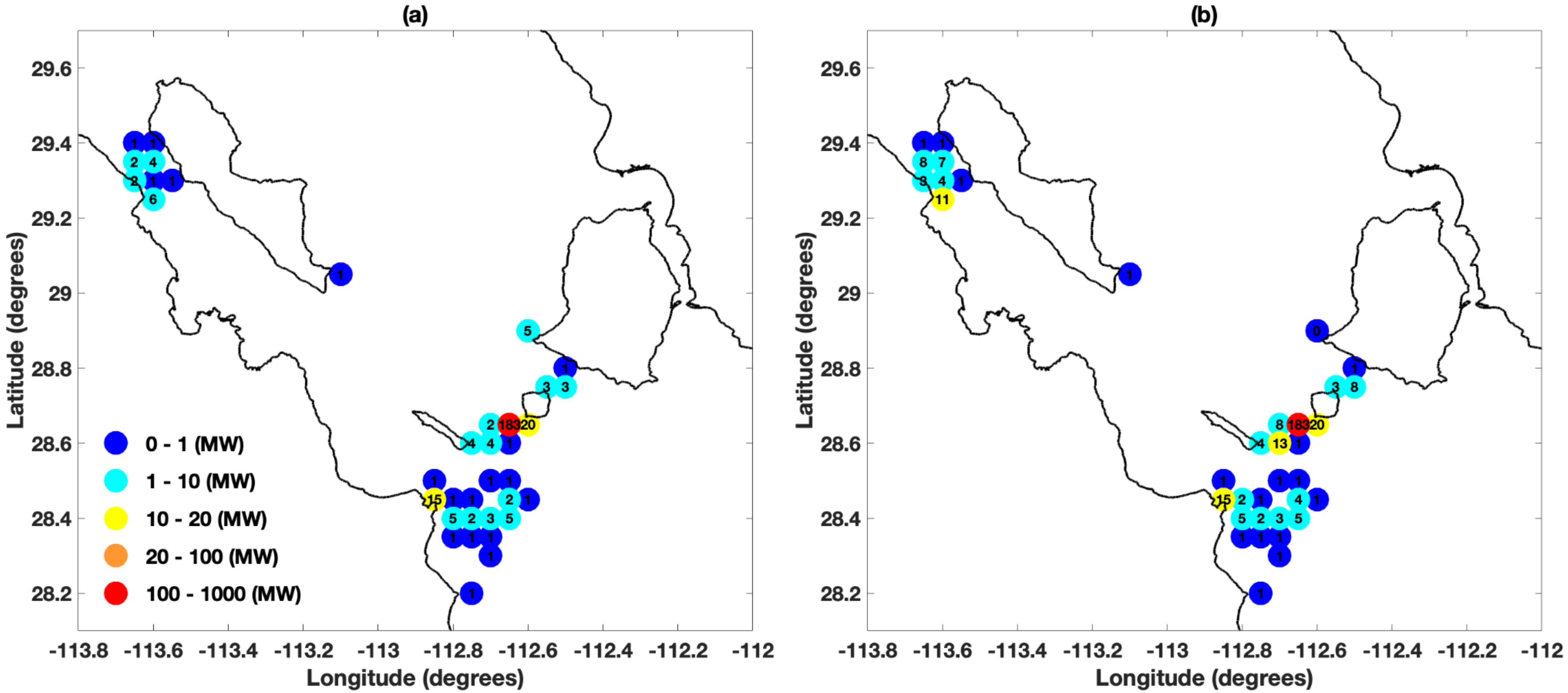

Figure 5.14. Mean annual tidal-stream technical power for each 5 by 5 degree model grid cell for the Schottel hydro d3 device, assuming: (a) an array of devices near the surface with lateral spacing between turbines being 3 times the diameter of the devices while the longitudinal space is 15 times the diameter of the turbine; (b) arrays down through the water column, with devices separated by a distance equivalent to 3 times the diameter of the device in the vertical, allowing for 7 m clearance from the surface and at the bottom a quarter of the total depth at that site.

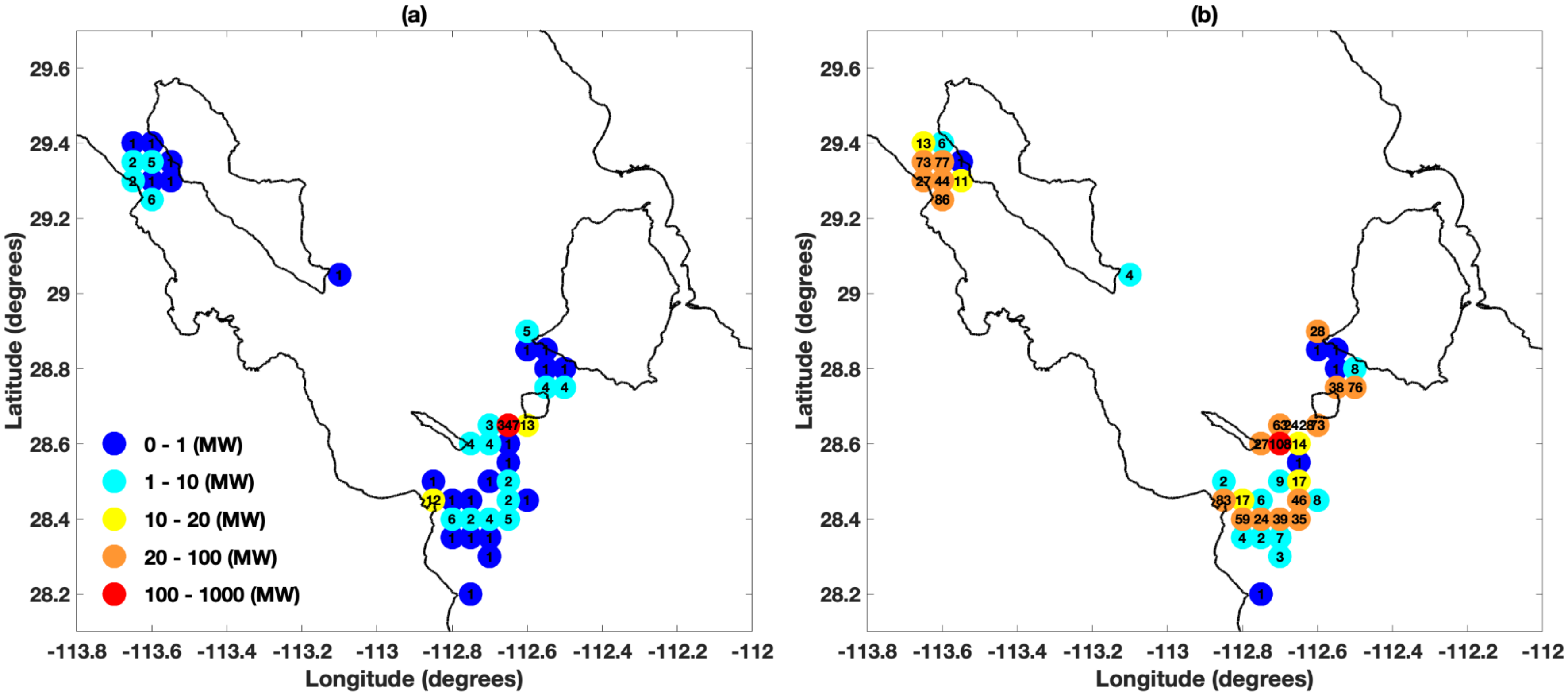

Figure 5.15. Mean annual tidal-stream technical power for each 5 by 5 degree model grid cell for the Sabella D-10 devices, assuming: (a) an array of devices near the surface with lateral spacing between turbines being 3 times the diameter of the devices while the longitudinal space is 15 times the diameter of the turbine; (b) arrays down through the water column, with devices separated by a distance equivalent to 3 times the diameter of the device in the vertical, allowing for 7 m clearance from the surface and at the bottom a quarter of the total depth at that site.

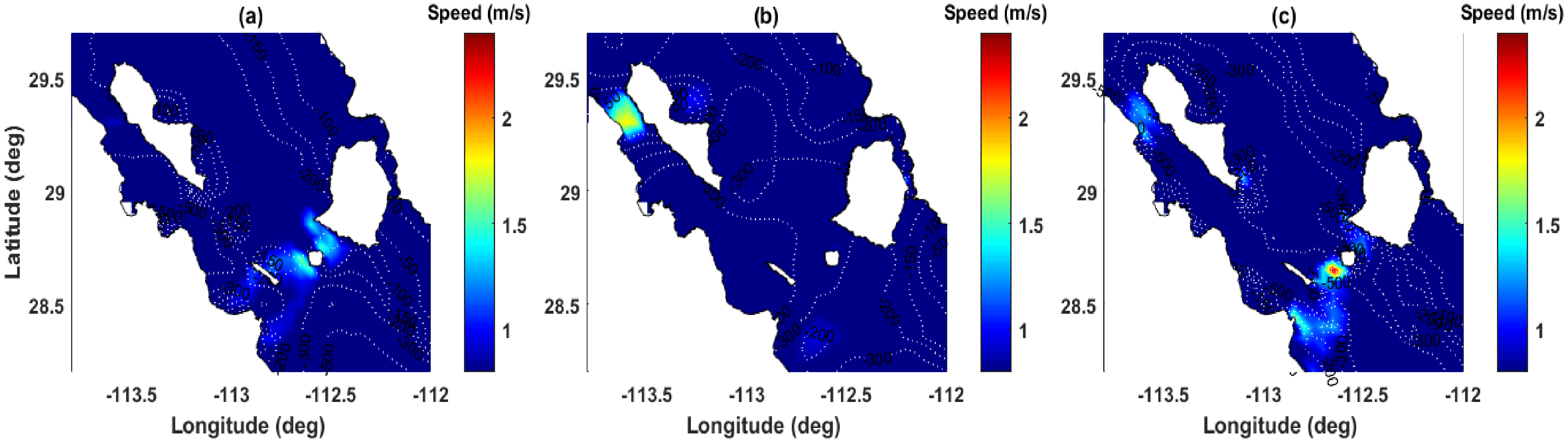

Figure 5.16. Maximum current speed calculated using: (a) just GEBCO data, (b) just ETOPO data (c) GEBCO merged with CICESE. Bathymetric contours are superimposed in m. All figures include the 29 tidal constituents originally used the model set up in chapter 3.

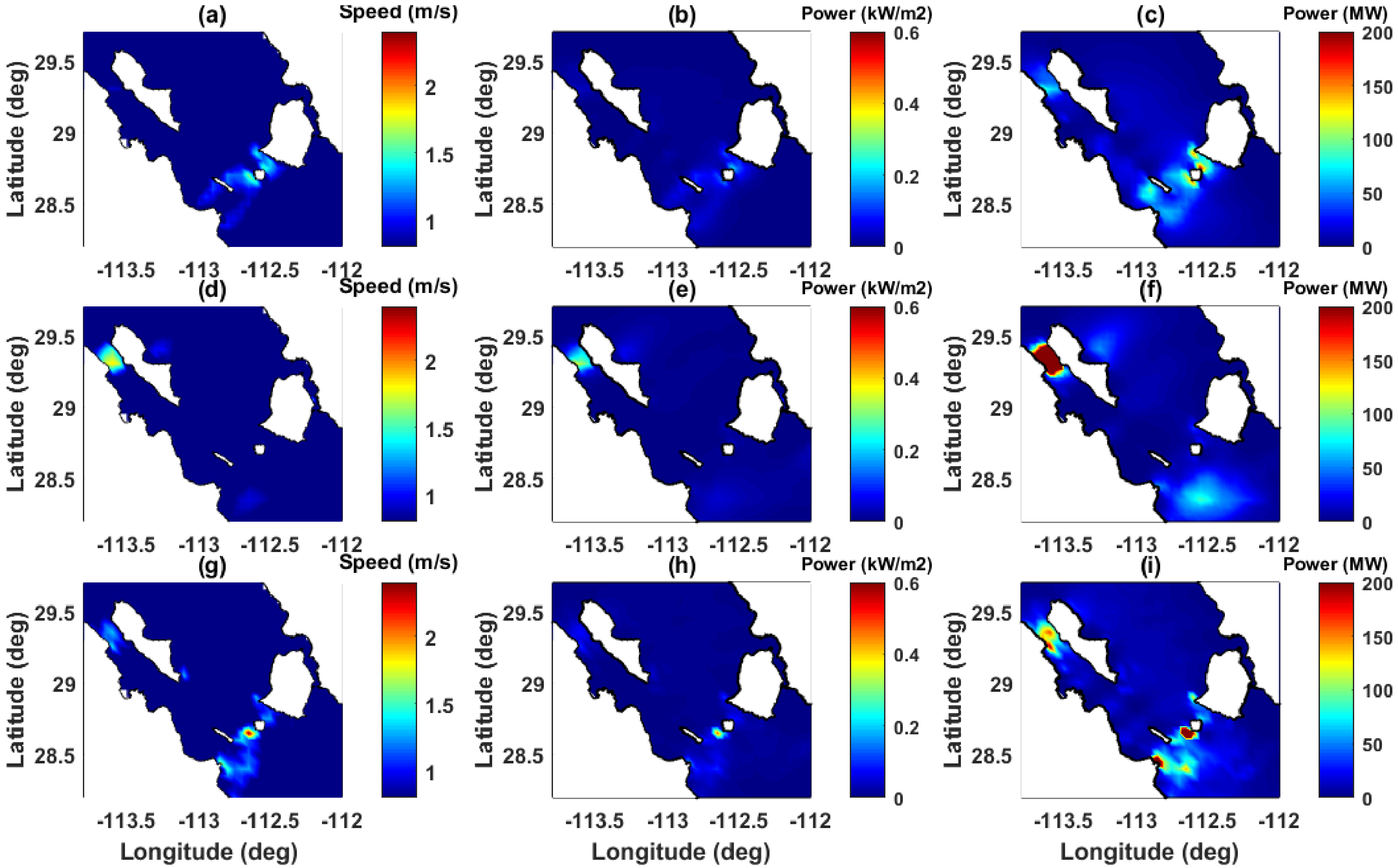

Figure 5.17. (b,e,h) Annual mean KPD, (c,f,i) Annual mean power and (a,d,g) Maximum current speeds for (a,b,c) GEBCO only; (d,e,f) ETOPO only; and (g,h,i) GEBCO data merged with the higher resolution data from CICESE, for the Midriff region.

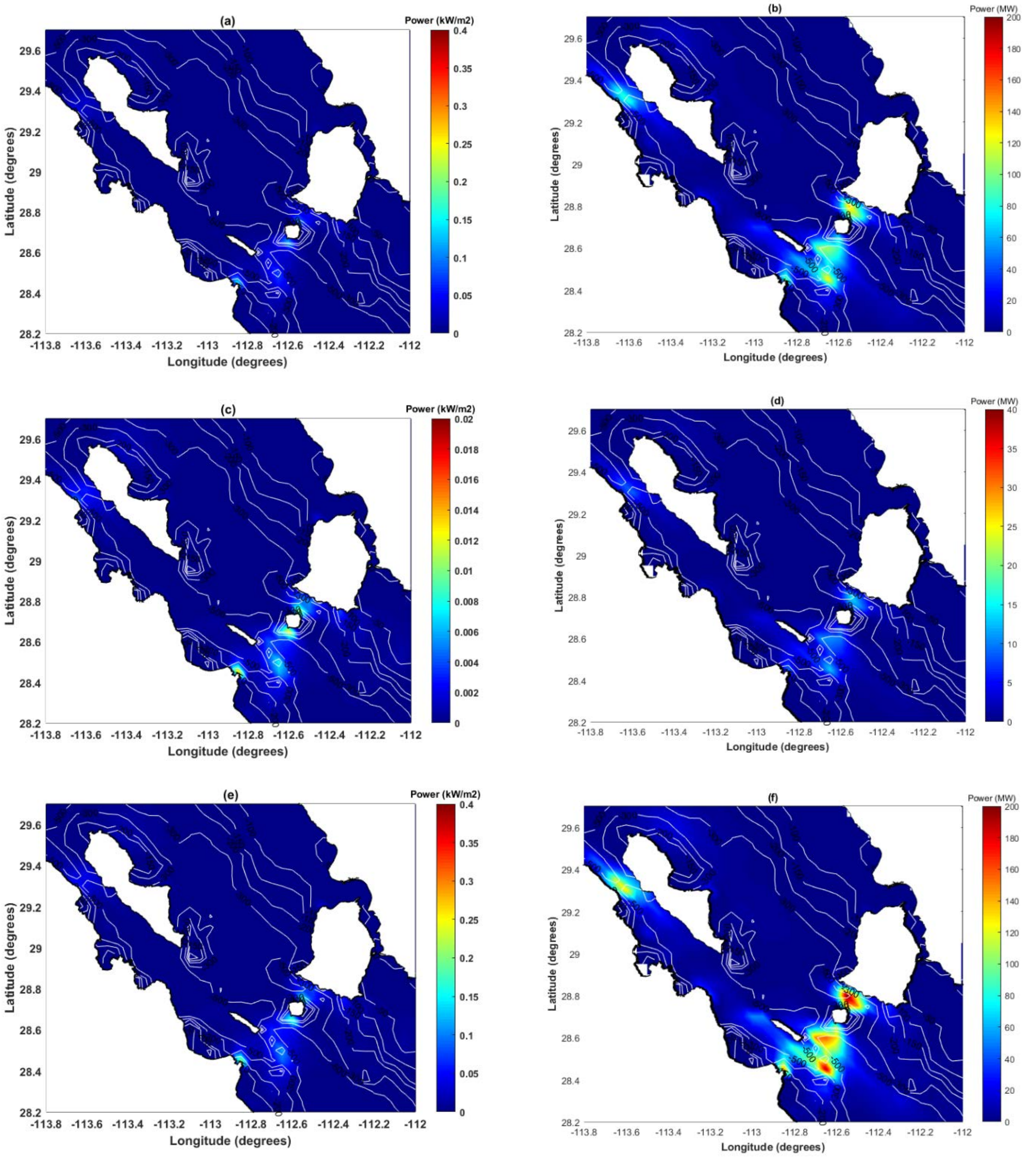

Figure 5.18. Annual mean KPD (a) just the M_2 constituent, (c) S_2 constituents (e) M_2 plus S_2 constituents. Annual theoretical mean power for (b) just the M_2, (d) S_2 constituents (f) M_2 plus S_2 constituents. All plots use the GEBCO data merged with the higher resolution data from CICESE, for the Midriff region, for the model bathymetry. Bathymetric contours superimposed in m above.

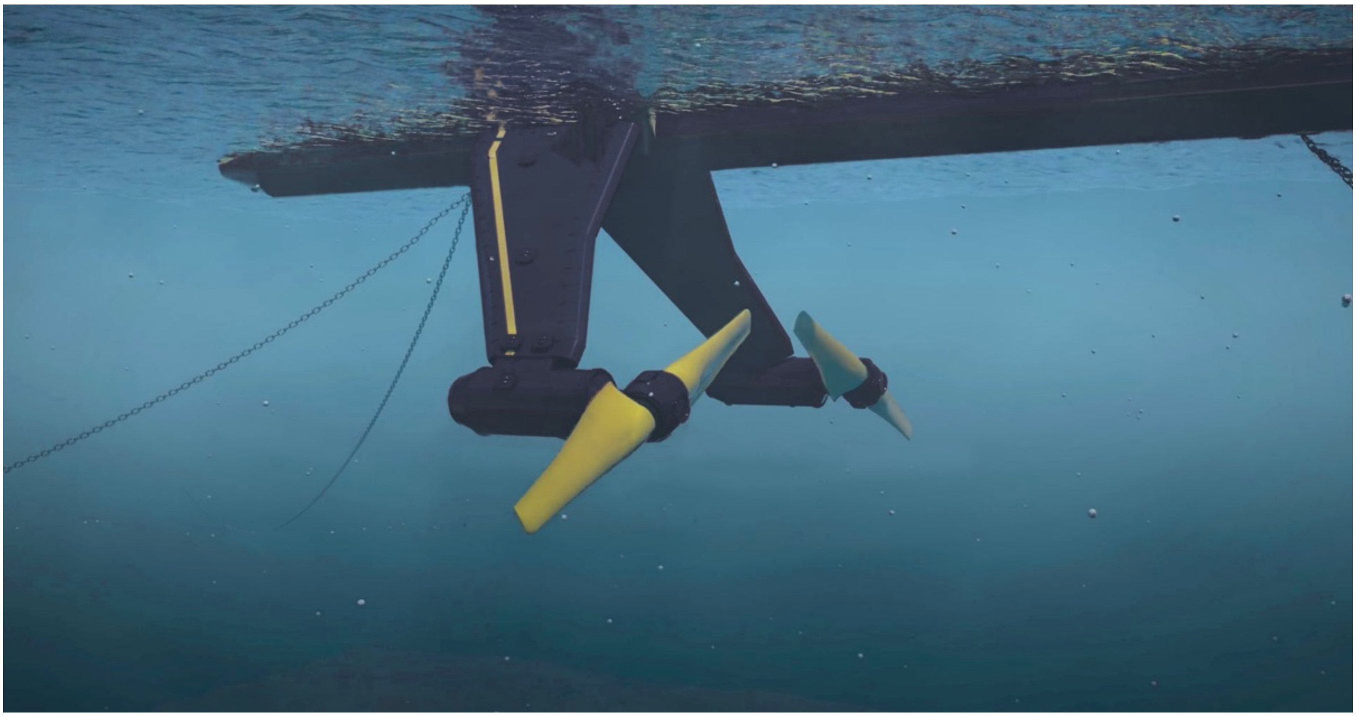

Figure 5.19. Orbital O2 2MW Underwater View.
Source https://orbitalmarine.com/technology-development/orbital-o2.

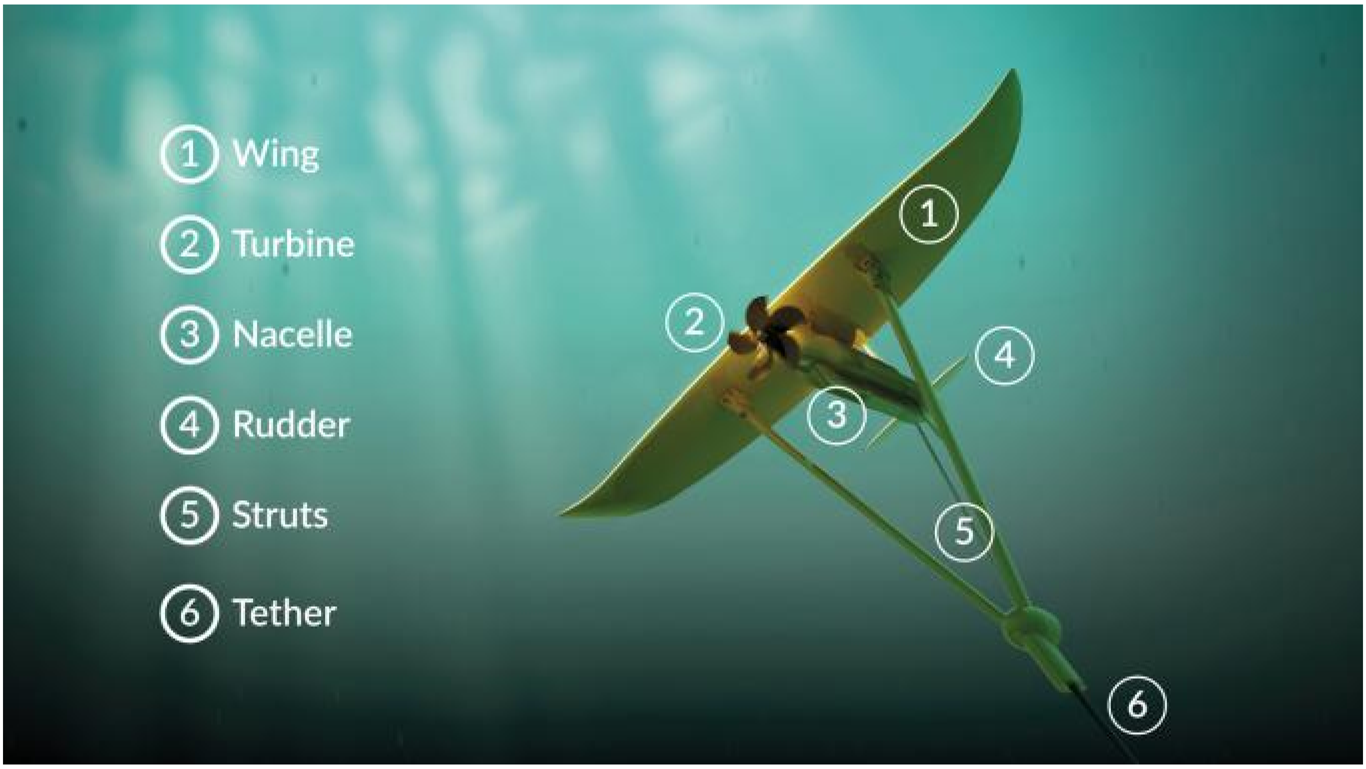

Figure 5.20. DG500: Power rated 0.5 MW, Water current velocity 1.2-2.4 m/s, Installation Depth 60-120 m, Turbine diameter 1.5 m. Source: https://minesto.com/our-technology.

Table 5.1 List of current commercial and prototypes devices.

Device Name	Swept diameter (m)	Power rated (kW)	Velocity rated (m/s)	Cut in velocity (m/s)	CP estimated	Source
MCT	16	600	2.5	1	0.3719	Lewis et al. 2015
Alstom	18	1000	2.7	1	0.3888	http://www.emec.org.uk/about-us/our-tidal-clients/alstom/
Minesto	43.43*	500	1.2	0.4	0.3804	Buckland et al., 2015
sabella D-10	10	1000	4	1	0.3874	https://www.sabella.bzh/en/projects/d10
sabella D-15	15	2300	4	1	0.396	https://www.offshorewind.biz/2014/12/17/sabella-conducting-d15-tests-at-insean/
SeaGen-S 2MW (Atlantis) twin rotor	20	1000*	2.5	1	0.3967	https://www.atlantisresourcesltd.com/wp/wp-content/uploads/2016/08/SeaGen-Brochure.pdf
Atlantis AR1000	18	1000	2.65		0.4112	Roberts et al., 2016. https://simecatlantis.com/2013/03/25/atlantis-resources-corporation-completes-testing-of-the-ar-1000-tidal-turbine-at-narec/
Voith	16	1000	2.9		0.3971	Roberts et al., 2016.
Openhydro 200Kw	10*	200	2.5		0.3155	Polagye et al., 2010, Roberts et al., 2016.
Minesto DG-8	85.19*	110	1.3		0.0171	Roberts et al., 2016.
Minesto DG-14	155.54*	850	1.73		0.0168	Roberts et al., 2016.
Schottel hydro d3	3	70	3.7	0.9		www.schottel.de/schottel-hydro/sit-instream-turbine
Schottel hydro d4	4	62	3.1	0.8		www.schottel.de/schottel-hydro/sit-instream-turbine
Schottel hydro d5	5	54	2.6	0.7		www.schottel.de/schottel-hydro/sit-instream-turbine

Table 5.2 Summary of the array configuration (MW)

Device Name	Swept diameter (m)	Power rated (kW)	Cut in velocity (m/s)	Number of devices in 5 by 5 km grid utilising lateral and longitudinal spacing	Mean annual Power (MW) for near surface array	Mean annual Power (MW) for near array utilising water depth
MCT	16	600	1	1482	251	322
Sabella D-10	10	1000	1	3875	460	1030
SeaGen-S 2MW (Atlantis) twin rotor	20	1000	1	930	264	304
Schottel Hydro d3	3	70	0.9	43264	431	3550

Table 5.3. Annual mean theoretical power (MW) by location using different bathymetry products. (A) San Lorenzo Passage. (B) channel between the Baja California Peninsula and San Lorenzo, (C) Channel between San Esteban and Tiburon Island and (D) Ballenas Channel between the Baja California Peninsula and Angel de la Guarda Island.

Site Marker	GEBCO	ETOPO	GEBCO merged with CICESE
A	~120	~20	~200
B	~80	~40	~160
C	~140	~10	~40
D	~70	~180	~150

Table 5.4. Annual mean theoretical power (MW) by location using different tidal constituents with GEBCO merged with CICESE. (A) San Lorenzo Passage. (B) channel between the Baja California Peninsula and San Lorenzo, (C) Channel between San Esteban and Tiburon Island and (D) Ballenas Channel between the Baja California Peninsula and Angel de la Guarda Island

Site Marker	M_2 tidal constituent	S_2 Tidal constituent	M_2 plus S_2 Tidal constituent
A	90 - 100 MW	15 – 20 MW	140 -150 MW
B	60 – 70 MW	8 – 10 MW	120 - 130 MW
C	120 – 130 MW	10 – 15 MW	140 – 160 MW
D	60 – 70 MW	10 – 12 MW	120 – 130 MW

Table 5.5. List of locations where the current speed are lower than 2.5 m/s

Location	Current speed	Reference
USA, East and west coast.	1.5 m/s	Hagerman et al. (2006)
Canada, East and west coast.	average flow speed of 2.11 m/s	Cornett (2006)
Spain, Rıa de Muros	2.3 m/s	Carballo et al. (2009)
Chile, Chiloe Island.	Up to 2.1 m/s	Herrera et al. (2010)
Malaysia	0.8 to 1.2 m/s	Lim and Koh (2010).
Ireland	Above 1.9 m/s	O'Rourke et al. (2010).
Georgia Coast, USA	Mean from 0.34 to 1.07 m/s	Defne et al. (2011)
USA coastline	1 m/s	Georgia Tech Research Corporation (2011)
UK, Anglesey Skerries	Up to 1.4 m/s	Serhadlıoğlu et al. (2013).
South Carolina, USA	0.87 m/s	Work et al. (2013)
Indonesia, Alas strait	1.2 m/s	Blunden et al. (2013).
New Zealand, Tory Channel	2 m/s	Plew and Stevens (2013).
Straits of Malacca, Malaysia	2 m/s	Chong et al., (2013)
Ireland, Bull mouth and Shannon Estuary.	2.02 m/s during spring tide	O'Rourke et al. (2014)
Coast of New jersey, USA	1.26 m/s	Tang et al. (2014)
Spain, Gibraltar strait.	2 m/s	Calero et al. (2014)
France, Iroise Sea	From 2 m/s to 4 m/s.	Thiébaut and Sentchev (2015)
China, Hulu Islands	2 m/s	Gao et al. (2015).
Colombia, Buenaventura Bay.	Mean current speed 0.8 m/s	Osorio et al. (2016)
Norway, Folda Fjord	Peak currents of 2.06 m/s	Carpman and Thomas (2016)
Spain, Avilés Port.	0.35–0.4 m/s	González-Caballíin et al. (2016).
Pentland, Firfth UK	2 m/s	Goward Brown et al. (2017)
Puget Sound, Canada	2 m/s during spring tide	Wang and Yang (2017).
Uruguay	0.35 m/s	Alonso et al. (2017)
Brazil, Baía de Todos os Santos	Max 1 m/s	Marta-Almeida et al. (2017)
France, W. Brittany coast.	From 1 m/s to 4 m/s	Thiebaut and Sentchev (2017)

France, English Channel.	1.5 m/s average	Campbell et al. (2017)
Cozumel channel, Mexico	2 m/s	Alcérreca-Huerta et al, 2019
El-jadida, Tarfaya and Tangier, Morocco	Max current speed of 2.3 m/s	Hazim et al., (2019)

Chapter 6: Synthesis, implications and future work

This chapter provides a synthesis and discussion of the main findings from Chapters 4 and 5, in light of important considerations when identifying a suitable tidal energy site. Furthermore, additional analysis is undertaken to provide further insight. In particular this chapter: (1) describes the results from an analysis of the three-dimensional structure of tidal currents in the central region of the GC (Section 6.1); (2) discusses the possible environment impacts that might arise in the GC if tidal energy schemes were developed at the sites identified (Section 6.2); (3) briefly explores whether knowledge of the phase relationship between tidal energy sites could be exploited, leading to firm power supply to the electricity grid (Section 6.3); (4) proximity to grid connection is briefly discussed in regards to the locations of the sites identified in Chapters 5 and 6 (Section 6.4); and finally, (5) five main areas of possible future work that would enhance this study, are discussed (Section 6.4).

6.1 3D structure of water column and implications

In Chapters 3, 4 and 5, a depth averaged numerical model has been used to evaluate the theoretical tidal-range and tidal-stream energy resource available in the GC, Mexico. The use of the two-dimensional approach was justified, given that no comprehensive assessment of tidal energy had been undertake from the Gulf of California before now; and the goal of this study was to carry out a first order estimate of the theoretical tidal-range and tidal-stream energy resource available, to identify future sites that could then be subsequently examined in more detail. However, tidal currents are three-dimensional (3D), as Goward-Brown et al. (2017) point out, and contain non-linear features. Hence the 3D nature of tidal currents should be characterised. This is particular the case here, for the GC, as the water depth at the tidal-stream sites identified in the Midriff region are relatively deep (>400 m) compared to the sites examined in the majority of other tidal-stream energy assessments. Furthermore, the GC is known to be stratified at certain times of the year (e.g. Marinone, 2000), which will clearly impact 3D tidal current flows.

To consider the 3D nature of tidal currents around the Midriff region of the GC, and how they might impact the findings of Chapter 6, we utilize here current predictions from the layerwise vertically integrated Hamburg Shelf Ocean Model (HAMSOM) developed by Backhaus (1983, 1985) and later adapted to the GC by Marinone (2003). The model is described in detail in Marinone et al. (2009). The model domain has a rectangular mesh size of 2.5’ x 2.5’ (3.9 km x 4.6 km). The number of layers in the vertical depends on the local depth, but 12 nominal layers are used, with lower levels at 10, 20, 30, 60, 100, 150, 200, 250, 350, 600, 1000 and 2000 m. The model is forced at the open boundary with the seven main semidiurnal and diurnal tidal constituents (M_2, S_2, N_2, K_2, K_1, O_1, and P_1), in addition to the semi-annual (Ssa) and annual (Sa) components. The model is also forced with climatological heat and fresh water fluxes at the air–sea interface and hydrography at the Gulf’s mouth. The model was extensively validated against observations.

The 3D model grid is coarser than the 2D model grid mainly used in this thesis, and hence doesn’t resolve the tidal currents to the same level of accuracy, particularly in the Midriff region. For example, at the 2 sites (A and B shown in Figure 5.7) where the highest tidal-currents were observed in the GC in Chapter 5, the 3D HAMSOM model underestimates the depth averaged current speeds, compared to the 2D TELEMAC model predictions (see Table 6.1). However, at the other 2 sites (C and D shown in Figure 5.7) where high tidal-current speeds were also observed, the coarser 3D model agrees well with depth averaged predictions from the 2D model (see Table 6.1).

Here, the tidal-currents from the 3D HAMSOM were extracted (using the interface available at http://gulfcal.cicese.mx/map.php) at select points to consider the 3D nature of tidal currents around the Midriff region. In total, currents were selected at 68 locations, shown in Figure 6.1. At each of these 68 locations, u and v current velocities were extracted at -5, -125 and -300 m for March 2015; these three water depths were chosen initially to gain a first order assessment of changes through the water column. The water levels and current speeds at -5 m, 125 m and 300 m are shown in Figure 6.2 at Point A (location shown in Figure 5.7). Interestingly, the fastest currents are not observed at the time of highest tidal range. This is because the tide is mixed in form at this location, with periods of diurnal and semidiurnal tides. Instead, the highest current speeds are observed when the tide is most strongly semi-diurnal, for example around the 20th March 2015 (Figure 6.3). Current speeds are similar at -5 and -125 m water depth, but are much lower at -300m water depth. Current vectors at all 68 locations are shown in Figure 6.4, every hour from 10:00 to 21:00 on the 20th March 2015, when the highest currents were observed. There are clear differences in both current speed and direction with depth. Current speeds at -300 m are typically less than at -5 and -125 m. The maximum u and v velocities, and current speeds over March 2015, are shown in Figure 6.5 for -5, -125 and -300 m water depth. As expected v velocities are greater than u velocities at most locations, because of the north/south direction of the flow in the GC. U and v velocities, and current speeds reduce with depth, and are largest at -5 m for most locations.

To assess changes in velocities down through the water column in more detail, u and v velocities were extracted at each of the 12 model levels (e.g., 10, 20, 30, 60, 100, 150, 200, 250, 350, 600, 1000 and 2000 m) at the four locations (A, B, C and D, shown in Figure 5.7) with the fastest current speeds. The u and v velocities were then interpolated to give velocities every 20 m through the water column. U and v velocities and current speeds are shown in Figure 6.6 through the water column on the day with the highest (Day 20) maximum current speeds. The velocities change considerably with depth, which has important implications for tidal-stream energy extraction. U and v velocity and current speeds are typically highest in the upper 200 m of the water column, and then subsequently reduce with depth (Figure 6.6a, b,c). Current speeds near the bottom of the water column are typically around half of that at the surface. With the v velocity and current speed, the phase changes with depth are minimal. Interestingly, however, there is a phase lag with depth for the u velocities (Figure 6.6a). Peak u velocities at the bottom occur several hours after the peak velocities in the upper water column. This is shown clearly in Figure 6.7a. Figure 6.7d, e and f shown the velocity changes with depth, after subtracting the depth averaged current. Again, it is evident that current speeds in the upper 200 m of the water column exceed the depth average current, whereas current speeds below 200 m are less than the depth averaged current.

Changes in velocities down through the water column are shown for locations B, C and D, in Figures 6.8 and 6.9, Figures 6.10 and 6.11 and Figures 6.12 and 6.13, respectively. Again, it is evident that there are significant changes in current speed with depth. At Point B, current speeds are around 4 times faster in the upper layers of the water column, compared to the deeper layers (Figure 6.8c). Current speeds in the upper 50 m of the water column exceed the depth average current, whereas current speeds below -50 m are less than the depth averaged current (Figure 6.9e). Interestingly, at Point C the u velocities are out of phase, between the surface and bottom (Figure 6.10a and 6.10b). At Point C, the current speeds are fastest between -200 and around -50m, and are slower at the surface. At Point D, the currents at the bottom are around a third of the speed of the currents at the surface (Figure 6.11c). Current speeds in the upper -150 m of the water column exceed the depth average current, whereas current speeds below -150 m are less than the depth averaged current (Figure 6.9e).

This analysis has shown that current velocities varying considerably with depth, and the vertical profile varies depending on site. Hence, if any of these sites are chosen for tidal-stream extraction a more detailed analysis of the 3D nature of the current speeds needs to be undertaken. Goward-Brown et al. (2017) also stress the importance of 3D flows for reducing uncertainty in environmental resource assessments, for the Pentland Firth. At the four sites, considered here, the current speeds are fastest in the upper water column (Point A – upper 200m; Point B – upper 50 m; Point C – upper 200 m; and Point D – upper 150 m).

6.2 Impacts

There are many advantages of tidal energy, but there are also several possible negative impacts. In light of the results of Chapters 4 and 5, the potential negative impacts that might arise in the GC if tidal energy (both range and stream) schemes were developed at the sites identified are discussed here.

First environmental impacts are considered. Four sites in the northern GC were identified as being potentially suitable for tidal-range energy extraction and a further four suites were identified in the Midriff region as being suitable for tidal-stream extraction. However, the majority of these sites are located in areas that have been designated by the United Nations Educational, Scientific and Cultural Organization (UNESCO) as being a World Heritage Site. The ‘Islands and Protected Areas of the Gulf of California’ World Heritage Site comprises 244 islands, islets and coastal areas that are located in the Gulf of California in north-eastern Mexico (Figure 6.14). This region is home to 695 vascular plant species, more than in any marine and insular property on the World Heritage List, and 891 fish species, 90 of them endemic. Moreover, this region contains 39% of the world’s total number of species of marine mammals

(Figure 6.15) and a third of the world's marine cetacean species. Therefore, construction and operation of any tidal-energy scheme would need to minimise the environmental impacts in this important and sensitive area.

The northern most part of the GC, encompassing the Colorado River Delta, is part of the Biosphere Reserve. This is the largest aquatic reserve in Mexico (9,347 km^2) and is divided into core, buffer, and Vaquita (*Phocoena sinus, "little cow in English"*) Refuge areas, shown in Figure 6.16. Within the core zone and the buffer zone changes in ground use, habitat modification and construction are prohibited, as is harm to marine mammals (CONANP, 2007). Several Mexican government institutions have some jurisdiction over the biosphere reserve, including: the National Protected Natural Areas Commission (CONANP); National Ecology Institute (INE); National Fisheries Institute (INP); National Aquaculture and Fisheries Commission (CONAPESCA); Ministry of the Environment and Natural Resources (SEMARNAT); Federal Environment Protection Office (PROFEPA); National Commission for Use and Knowledge of Biodiversity (CONABIO);and the Mexican Navy (SEMAR). Therefore, construction of any tidal-range energy projects within the northern GC region would need to compliance with legislation of these organisations.

The Midriff region is particularly important in regard to marine mammal migration. For example, Figure 6.17 shows the satellite derived track of Fin Whales throughout the year (Jimenez Lopez et al., 2019). Construction of a tidal-stream array could impact on the migration of Fin Whales and other marine mammal species. In such a high productivity region, the noise generated by the turbines could also negatively impact fish and marine mammal species in this area. An improved understanding is therefore required of the likely environmental consequences of the associated changes in underwater noise due to tidal turbines. Lepper and Robinson (2016) assess in detail the measurement of underwater operational noise emitted by wave and tidal-stream energy devices. An extensive Environmental Impact Assessment (EIA) would need to be undertaken, prior to the construction of a tidal energy scheme. EIA is the process by which information about the environmental effects of a project is collected, assessed and evaluated, and is used in reaching a decision about whether a proposed development should be approved.

Second, changes to sediment pathways and concentrations are considered. Any construction of tidal-energy schemes, particularly tidal-range barrages, need to consider changes to sediment pathways, suspended sediment concentrations and water quality. Sediment supply has altered over the last century in the upper Gulf, as a result of the building of more than 20 dams in the upper Colorado River (Getches, 2003). This has resulted in a reduction of fresh water into the upper gulf from 18 to 8 billion m^2. There has also been a significant reduction in sediment supply from 160 billion kg of sediments deposited a year to 12 billion. The reduction of fresh water and changes in sediment supply have caused losses of wetlands, riparian vegetation, and estuarine habitat, leading to a decrease of fish and wildlife populations. Construction of large-tidal barrages could further alter the sediment pathways and supply in the upper GC. The high tidal range in the northern GC and strong tidal currents creates a significant amount of suspension sediments within the water column in this region (Lulch-Cota et al., 2007). The suspended sediment concentrations in this region could be enhanced during the construction phase of a tidal-range barrage. This could negatively impact on the diverse ecosystems and important fisheries in this area. There are high levels of nutrients in the region (Bustos-Serrano and Castro-Valdez, 2006) as a consequence of high sea surface temperature (Castro et al., 1994), and this results in high biodiversity. Therefore, it is important to consider how construction of a tidal energy scheme might influence the nutrient structure and in turn influence the marine ecosystems in the area.

Third, impacts to shipping are considered. Construction of tidal-range barrages and tidal-stream arrays could impact shipping routes and increase collisions. The main cargo shipping routes for the GC are shown in Figure 6.18. The majority of the shipping routes are limited to the southern part of the GC. However, a few cargo ships travel northwards and cross between the Islands of the Midriff region on route to Puerto Libertad, Sonora. Construction of tidal-stream arrays at Points A, B and C (Location of points shown in Figure 5.7) in this region would clear have implications for these shipping routes. The northern part of the GC contains several small communities (e.g. Santa Clara, population 2700; Puerto Peñasco Sonora, population 31,000; and San Felipe population 13,000) and the main economic activity of the local inhabitations is fishing. In the GC there are more than 20,000 registered (and many unregistered) artisanal fishing boats (~7 m length open-deck fiberglass) and 1,500 larger industrial trawl and seine vessels (Cisneros-Montemayor and Vincent, 2016). Again, construction of both tidal-range barrages and tidal stream arrays, could impact the routes of these fishing vessels. Further, detailed assessment of these factors is needed.

6.3 Phase relationships and intermittency

Although tides and tidal currents are predictable, this form of energy is intermittent (Neill et al., 2016). Tidal energy is only created at certain times of the day and is variable throughout the 14-day spring-neap period and longer. As Neill et al. (2016) pointed out, the timing of high and low water, and flooding and ebbing tidal currents, varies considerably along coastlines. For example, it is low water at one end of the Gulf, while it is high water at the other end. An interesting question therefore is, could knowledge of the phase relationship between tidal energy sites be exploited by aggregating the electricity generated by a number of geographically distributed sites, leading to firm power supply to the electricity grid. Put another way, could we implement schemes at different sites wisely to produce 24 hours of electricity a day.

In this section an assessment of the timing of high and low water, and flooding and ebbing tidal currents, is undertaken for the four tidal-range sites in the northern GC identified in Chapter 4 (Figure 4.2b) and the four tidal-stream sites in the Midriff region identified in Chapter 5 (Figure 5.7), that have the potential for tidal-range and tidal-stream energy respectively. Tidal levels, predicted by the 2D TELEMAC model, at the four tidal-range sites in the northern GC are shown in Figure 6.19a for the spring tide on the 19th March 2015. The instantaneous technical power estimated by the 0D model (see Chapter 4) is shown in Figure 6.19b, for a two-generation scheme. These power calculations assume an impounded area of 1 km^2, as an illustration. The phase of the tide varies little across the four identified sites, which is expected given these are in relatively close proximity in the north region of the GC. Hence, the aggregated power from all four sites, shown in Figure 6.19c, does not lead to a firm power supply. Instead, there are four distinct periods of generation in any given day for the two-way generation scheme and four periods, each of around 3 hours, where power generation is zero.

Similar results are shown in Figure 6.20, for the four tidal-steam sites in the Midriff region of the GC. Tidal current speeds at the four sites are shown in Figure 6.20a for the spring tide on the 19th March 2015. The technical power is shown in Figures 6.20b, for these four sites. These power calculations were made, following the approach applied in Chapter 6, assuming a SeaGen Device (see Table 5.1 and Figure 5.2a). The power was calculated here assuming there would be 12 turbines, each with a 16 m diameter, power coefficient of 0.37, cut in speed of 1 m/s, cut out speed of 2.5 m/s and a power rating of 600 kW. The phase of the tide current varies little across the four identified sites, which is again expected given these are in relatively close proximity in the north region of the GC (there is a small phase difference between site D and the other three sites, because site D is located further north, Figure 5.7). Hence, the aggregated power from all four tidal-steam sites, shown in Figure 6.20c, does not lead to a firm power supply. Like for the four tidal-range sites, there are four distinct periods of generation in any given day and four periods, each of around 1 hour, where power generation is zero.

If one considers tidal-range and tidal stream schemes separately, it is not possible to generate a form power supply through a day from the four tidal-range and four tidal-stream sites identified in Chapters 4 and 5, respectively. However, if one considers tidal-range and tidal-stream sites together, it is possible to generate a more consistent supply, although still with periods of little electricity generation. This is because, as shown in Figure 6.21a, where is a phase-lag between the power generated by the tidal-range sites, compared to the tidal-stream sites. Figure 6.21b shows the power aggregated across the tidal-range and tidal stream sites. There are now four-hour windows when a relatively constant and high power supply is available. However, there are still four 30-minute windows with zero power generation. The results indicate that by combining different tidal-range and tidal-stream schemes the intermediate time would reduce, producing a more consistent energy supply over any given day.

The estimated technical tidal-range and tidal stream power over a 14-day spring/neap period in March 2015 is shown in Figures 6.22 and Figure 6.23, respectively. The aggregated power over this 14-day period is shown in Figure 6.24. Due to the large different between neap and spring tidal range and tidal currents, power generation is virtually zero during neap tides. Hence, clearly intermittency is an issue in the GC over longer periods.

Timing assessments have been undertaken for the UK by Burrows et al. (2009c) for tidal-range power. They, examined basin level variations for Morecambe Bay. Their results indicate that the best water delay for a two-way tidal-level generation scheme is around 1.28 hrs while for flood and ebb only schemes, delays are 2.98 hrs and 2.6 hrs respectively, resulting in an efficiently time of generation of around 2/3rds over two tidal cycles (e.g. 1 day). Burrows et al. (2009c) also assessed tidal barrage solutions for eight major estuaries in order to determine power outputs using different operational schemes, combining different number of turbines as well as providing an overall idea of the most suitable delay for holding water. Results suggested that energy capture could be improve by modifying the minimum head generation head. Xia et al. (2010) assess different operating modes for a proposed Severn tidal-range Barrage. Their results indicated that the process of power generations varies significantly when utilising different operational schemes. For an ebb only tidal-range scheme the power generation is 5.5 hours a day with a maximum power of 5.8 GW, while for flood generation scheme the power generation lasts 3.6 hours with a maximum power of 5.4 GW, within a typical mean spring tidal cycle. Using a two-way generation scheme, they find that the total time for power generation is 7.2 hours with a maximum power output of 3.8 GW and 4.5 GW for tidal-ranges of 4 and 4.4 m, respectively. More recent studies of timings have been undertaken for different potential sites, as follows: Mersey Estuary (Aggidis and Benzon, 2013), Severn estuary (Bray et al., 2016; Angeloudis and Falconer, 2017) in the UK, and Bacanga estuary in Brazil (Leite Neto et al., 2015). Aggidis and Benzon (2013) find that the starting head is one of the most important parameters to optimize the operation of the tidal barrage. By varying the starting head, they estimated a 20% of energy increase compared to that predicted by Burrows et al. (2009a). For a proposed tidal-range power plant in Bacanga estuary in Brazil, Leite Neto (2015) showed it was possible to improve the operational time from 34% to 38% by varying the operational levels of the reservoir. Angeloudis and Falconer (2017) analysed the energy outputs for proposed tidal lagoons in Swansea Bay, Cardiff and the Severn using different hydraulic structure representation (i.e., flow discharge, flow area, turbine efficiency and sluices gates specifications) and operational sequences (flood only, ebb only, two-way generation). They demonstrate that the best generation time for two-way schemes is by reducing the maximum holding time.

Several studies have assessed timing in regard to tidal-stream energy generation (e.g., Bahaj and Myers, 2004; Myers and Bahaj, 2005; Blunden and Bahaj, 2006; Carballo et al., 2009; Lim and Koh, 2010; O'Rourke et al., 2010; Defne et al., 2011; Work et al., 2013; Iyer et al., 2013; Adcock et al., 2014; Tang et al., 2014; Thiébaut and Sentchev, 2015; González-Gorbeña et al., 2015; Gao et al., 2015; Lewis et al., 2015). For example, Dafne et al. (2011) estimate tidal-stream energy generation for sites along the coast of the Georgia. They found that electricity was only likely to be generated for around 3,000 hours (125 days) in a year. Iyer et al. (2013) examine the phasing of tidal currents at different locations around the UK. For instance, they show that Islay and Pentland Firth are in phase while the Race of Alderney is out of phase for approximately 1 hour, resulting in a significant reduction when the aggregate daily power is calculated. Adcock's et al. (2014) results highlight the variability in the power over a month at Pentland Firth.

Although tides are periodic and predictable, the results presented here, along with findings from other authors show that it is important to consider the phasing of the tide and consider the spatial and temporal variability of the tidal energy resource. Knowledge of the phase relationship between tidal energy sites could be exploited by aggregating the electricity generated by a number of geographically distributed sites, leading to a more firm power supply to the electricity grid.

6.4 Grid connectivity

As mentioned earlier in this chapter, proximity to a grid connection is one of the important considerations when identifying whether a site is suitable for tidal energy extraction or not. In this section this issue is briefly discussed in regards to the locations of the sites identified in Chapters 5 and 6.

In the northern GC region electricity production is challenging due to the limited national grid network in this region. The nearest electrical connection point to the Mexican national network is located in Sonora County, which is ~450 km from Playa Encanto. North of the GC there are two electricity connection points on the Mexican/US border, but these are not connected to the national Mexican network. These points are located ~200 and ~370 km to San Felipe Bay. Difficult access to this region, due to its topography, lack of fresh water and dry weather make this area unattractive for urban development. Therefore, the tidal-range energy that could be converted into electricity from the GC might be more suitable for off-grid applications. Another important consideration with regard to tidal-range power is the initial development costs. Even though this technology is well-proved technically the cost of building a tidal power station or tidal lagoon is highly expensive. For example, the Swansea lagoon project cost was initially estimated to be in the order of £1bn (Waters and Aggidis, 2016b) while the Severn Barrage project would cost £38bn (DECC, 2010). It is important to consider these costs in regards to the feasibility of the project as well as the profits and revenues of the initial investment.

In terms of tidal-stream energy, four locations have been identified as being suitable sites for energy extract in the GC and these are all located in the Midriff region. As mentioned earlier, current speeds and water depths at these locations, mean the sites are currently not suitable for current ‘first generation’ devices. However, the industry is testing ‘second generation’ devices (e.g., floating devices and hydrofoil). If these could be designed to utilise the full water depth and cross-sectional area of the channels in which the highest currents are located, then these sites could provide a potentially large and important energy resource for Mexico; especially in the northern west region of the country, where electricity generation is limited.

Grid connectivity in the region presents a real challenge, because of the complexity of the required cabling from the existing electrical network. The existing electricity network is shown in Figure 6.25. This network, which includes a permanent interconnect between the USA and Mexico, has been in operation since 1999. However, in 2015 energy production figures indicated that the Baja California North has a limited energy production with only 5 % of the national electricity demand (13,122 GWh) while Baja California South’s energy production is much lower at only 1 % (2,546 GWh) (PRODESEN, 2016). Therefore, the Northern Baja California region presents important challenges to distribute electricity locally as well as exporting electricity throughout the northwest border (CEE, 2013). The nearest counties, (Sonora and Sinaloa at the Mexican Mainland), which both produce 8 % of the National demand (21,642 GWh), offer relatively promising electricity grid connections (Figure 6.25 and 6.26). Thus, the nearest electricity connection point for the four potential sites for tidal-range energy extraction are located at San Felipe, Santa Clara, and Puerto Peñasco cities requiring any cabling to connect any future power plant project to distribute electricity into the Main national network. Therefore, the grid connectivity for the tidal-range power plant potential project needs to be taken into account for future off-grid applications.

6.5 Further work

There are six main areas of possible future work that would enhance this study. These are summarised in the paragraphs below.

Further model validation: As discussed in Section 6.2, the hydrodynamic model used in this study was comprehensively validated against water level measurements from 11 tide gauge sites and current-meter data from four sites in the Midriff area. The tide gauge sites were reasonably spread across the study area. However, tide gauge sites were lacking along the east GC coast and there were no sites in the Midriff region. To provide greater confidence in model predictions in these areas, it would be necessary to have measurements in these locations. Future work could consider deploying pressure sensors in these areas for shorter term periods (at least one month). Validation of tidal currents was restricted by the lack of current meter data across the study area. During the study, data from only four locations was available in the Midriff region and these sites were not located in the four areas found to have the highest tidal currents. In the future, it would be beneficial to deploy ADCP's within the areas of highest tidal currents. This would also allow for a detailed assessment of the 3D nature of the tidal flows in these areas.

Three-dimensional modelling: For objectives 1 and 2 a depth-averaged hydrodynamic model was used to provide an initial theoretical tidal-range and tidal-stream energy resource estimates, to identify potential energy extraction sites and inform industry and policy. In the case of tidal-range a depth averaged model is appropriate. However, results from this thesis demonstrated that the potential sites for tidal-stream energy extraction are located in relatively deep water (>100 m) and there is considerable variability in the tidal currents with depth (see Section 6.1). Previous studies by Simpson et al. (1994), Argote et al. (1995), Palacios-Hernandez et al. (2002), Lavin and Marinone (2003), Marinone (2003, 2006, 2007, 2008) and Zamudio et al. (2011), have shown that there is often strong stratification in the water column in the central Gulf, and therefore it is likely that this region has strong 3D flows. Therefore, future studies should apply 3D hydrodynamic model in order to better understand the 3D structure of the tidal flow and hence, more accurately assess the potential tidal-stream energy resource of the region.

Furthermore, the problem with kinetic energy extraction in stratified tidal current is currently unknown as the physics of the turbulence mixing is not well understood and altering the mixing in such flows may have a significant influence on the bio-system. This study has indicated that an example site in the Midriff region at the GC which is suitable speed for kinetic energy extraction would be suitable for studying these effects; this is site A (see Figure 5.7) in San Lorenzo Passage where the current speed reach over 2.4 m/s. Within this region strong mixing occurs which help to bring colder, nutrient-rich water to the surface. The turbulence created by strong tidal currents also as a Physical pump that carries $C0_2$ from deep water to the surface. Consequently, this area has higher levels of phytoplankton making the area suitable for sea birds and mammals. Therefore, analysis of the tidal mixing and stratification changes as a result of the turbines need to be undertaken in order to clear clarify the potential impacts within the GC.

Representing turbine arrays within the 3D model: Given the limited previous assessments of tidal-range energy, and lack of any prior assessment of tidal-stream energy, this thesis focused on provided an overall first order theoretical estimate of the available tidal-range and tidal-stream energy resource in the GC. Building on this strong foundation, a more realistic assessment of the resource is now needed, which accounts for actual energy devices and the array interaction. Effect such as, array scale blockage (Garrett and Cummins, 2008), array-array interaction (Coles et al., 2017), wake-turbine interaction (Abolghasemi et al., 2016) and array optimisation, need to be considered. This could be done by implementing additional drag terms within the hydrodynamic model, following the approach previously applied by, for example, Neill et al. (2009), Ahmadian et al. (2012), Neill et al. (2012), O'Donncha et al. (2013) and Goward-Brown et al. (2017). One way of simulating the presence of an array turbine within the model mesh, is to increase the bottom friction coefficient factor in the region of interest, as proposed by Blunden et al. (2006). This involves a number of steps. First, a polygon is selected identifying the region of interest (as show in Figure 6.27). Secondly, the coordinates of the polygon are included within the subroutine "dragfo" in TELEMAC, as shown in Appendix D. Third a friction coefficient is defined. This could be based on the previous studies listed on Table 2.6. Finally, a simulation is run, ideally for a one month. The velocities within this polygon can then be used estimate the theoretical and practical power. Moreover, following the approach of Coles, et al. (2017), the velocities can be compared with and without including the friction.

Hydrodynamic changes: Particularly in the case of tidal-stream energy in the Midriff region, an important consideration for future work would be to determine flow reduction as a result of different array designs. A key limitation with the Gulf, is the dimensions (i.e., width and length) of the channels between the islands, where the highest speeds are located. For example, the channel between the San Lorenzo and San Esteban Islands, which has the fastest maximum tidal currents (~2.5 m/s) is 18 km in width. In the case of tidal-range energy an important consideration previously described in section 2.2.2.2 for future projects would be to determine the potential tidal range changes which can have significant impacts as a result of building a tidal lagoon scheme. Furthermore, Hydrodynamic changes in tidal currents, tidal levels and discharges could be investigated, similarly as previous studies within the Bristol Channel (Burrows et al. 2009b; Falconer et al. 2009).

Environmental impact assessment: Future work could carry out a detailed environmental impact assessment to determine how develop of a tidal lagoon or turbine array would influence various aspects of the dynamics of the GC. For example, the study could assess the influence of a turbine array on: (1) sediment transport; (2) coastal erosion; (3) marine animal migration as a result of the turbine presence and noise; and (4) variation in the stratification of the water column and changes in nutrients (Lopez et al., 2006, 2008; Marinone, 2008); these issues have been reviewed in Section 6.2. In regard to the latter two points, the region is home to more than 40 colonies of sea lions (Aurioles-Gamboa and Zavala-Gonzalez, 1994) and 17 species of seabird that commonly breed in the Midriff Islands. Every year, 11 seabird species immigrate to the region (Velarde and Anderson, 1998). Also, a considerable number of intertidal invertebrate species have been identified in the region (Brusca, 1980) and 875 species of fish (Findley, 1996). Therefore, sensible environmental studies need to be carried out before taking any decisions on construction**.**

Moreover, additional environmental impacts need to be carried out regarding to the noise of the devices, there is relatively quality data that describe how the noise could affect certain species during and after the devices being commissioner. Numerous locations and methods have been reported by Robinson and Lepper (2013). For instance, there is strong evidence that the radiated noise as a result of the revolution speed and operational mode could have negative implications for perception capability especially for marine mammals, consequently there is a potential risk for collision with movement components of the turbine (Hastie et al., 2018). Therefore, a details analysis of different frequencies band of devices could be necessary to analyse and compare with the acceptable decibels the mammal species in the GC can tolerate within any immigration disruption. However, there is still uncertainty about the environmental impacts as a result of deployed devices can affect the mammal species (Inger et al., 2009).

Assessment of grid connectivity: As previously mentioned in Sections 4.4, 5.4 and 6.4, grid connectivity and energy storage present key challenges in the Northern and Midriff area of the GC region. Further work could assess the most suitable supplies include transformers, medium voltage switchgear, associated civil engineering works and power converters base on the most current available innovative engineering designs. Moreover, both on land and on the sea bed it is essential to explore routes for cabling as well as the onshore or offshore power conversion which could provide the electricity safely and reliably into the local distribution grid.

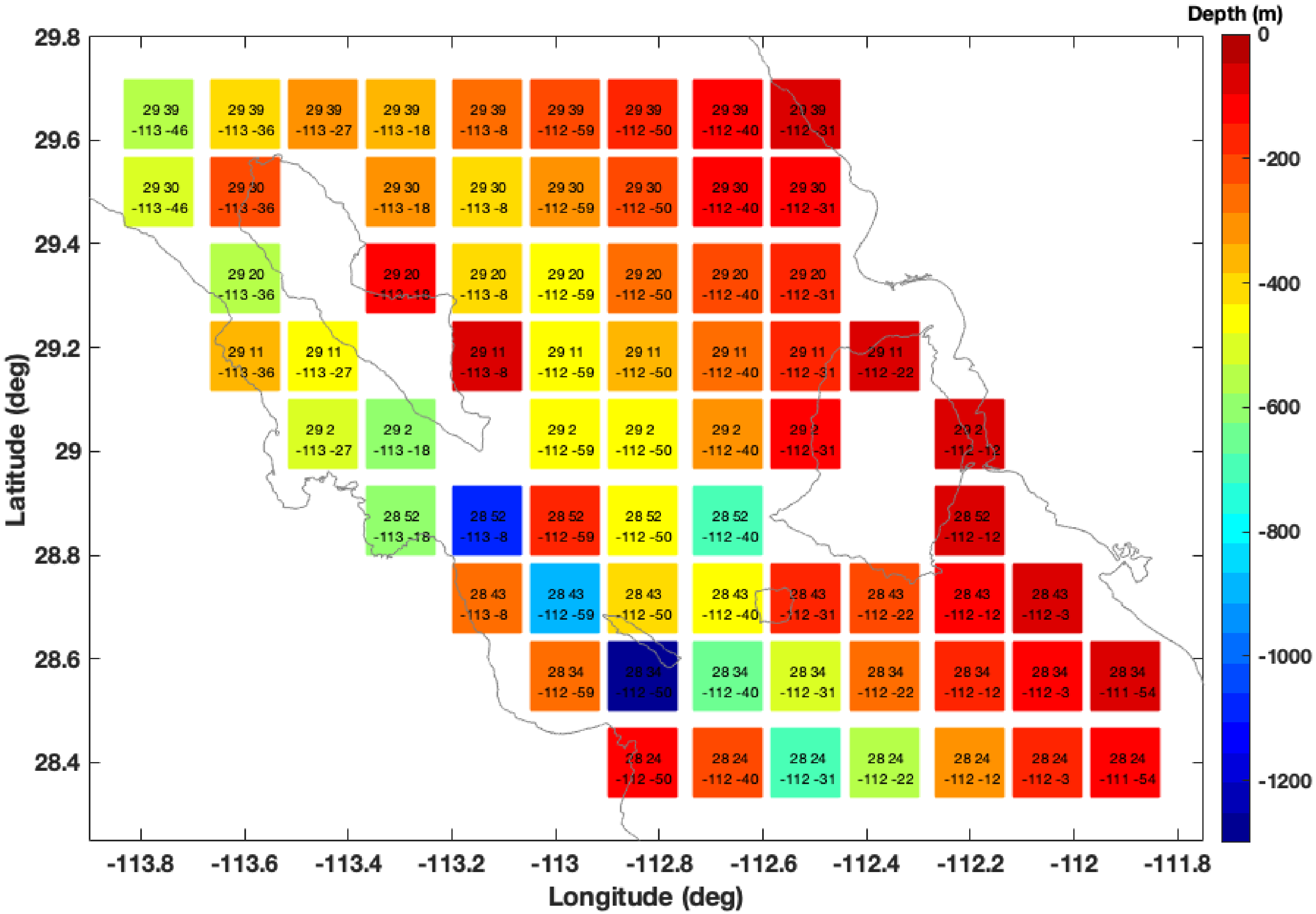

Figure 6.1. Grid points at which data was selected from the HAMSOM model.

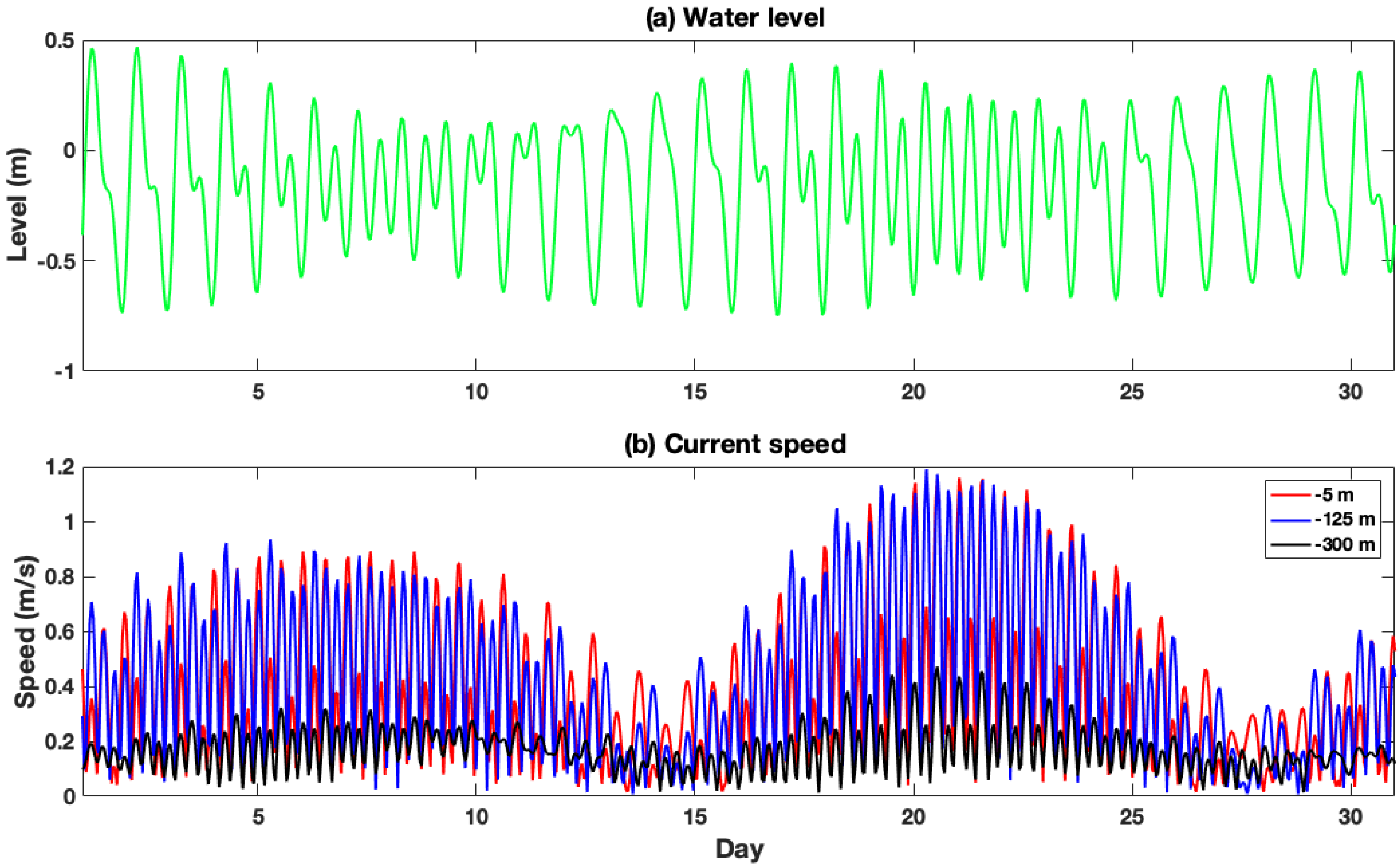

Figure 6.2. (a) Water level and (b) current speed at -5 m, 125 m and 300 m at Point A (location shown in Figure 5.7) for March 2015.

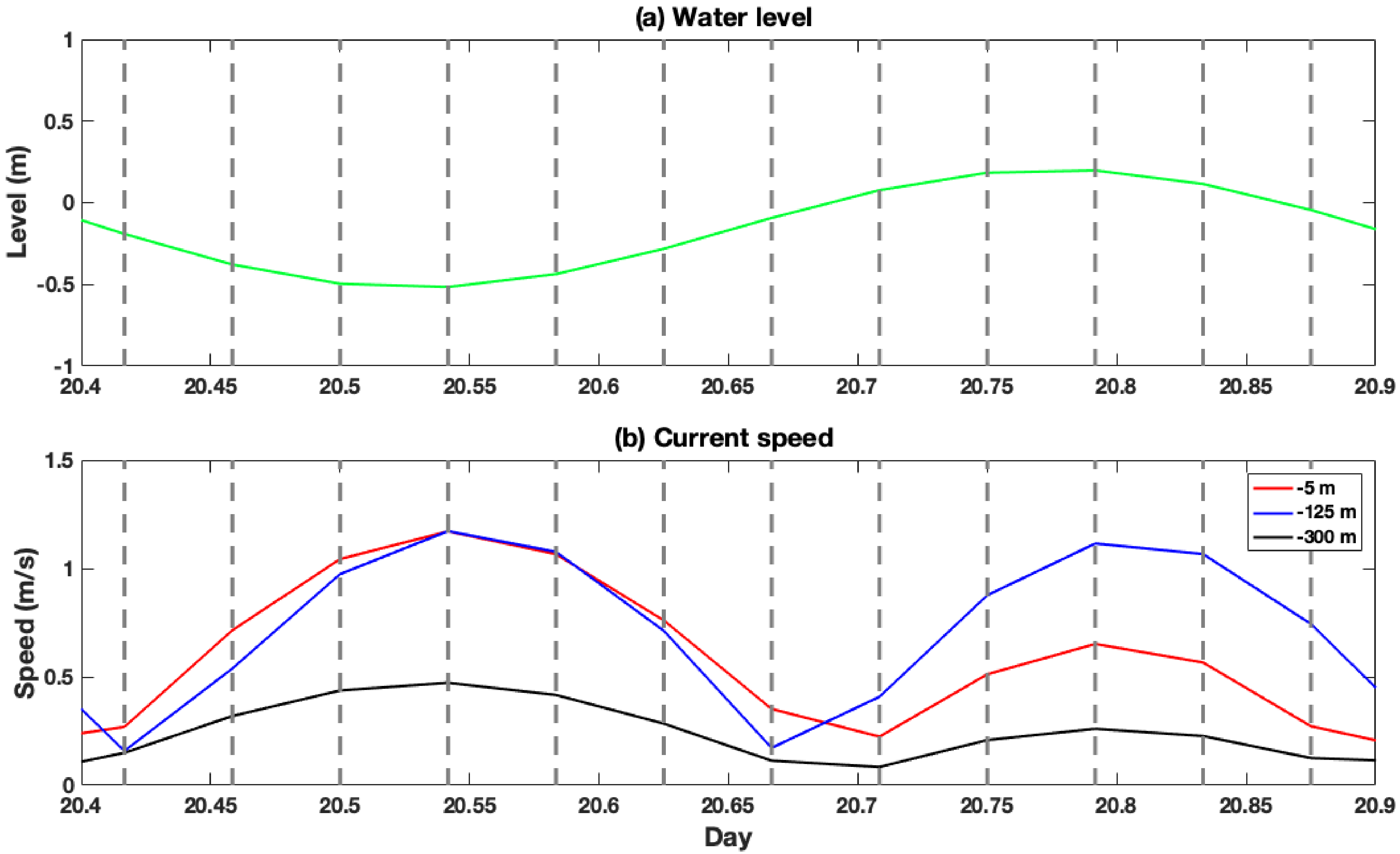

Figure 6.3. (a) Water level and (b) current speed at Point A (location shown in Figure 5.7) for 19th March 2015.

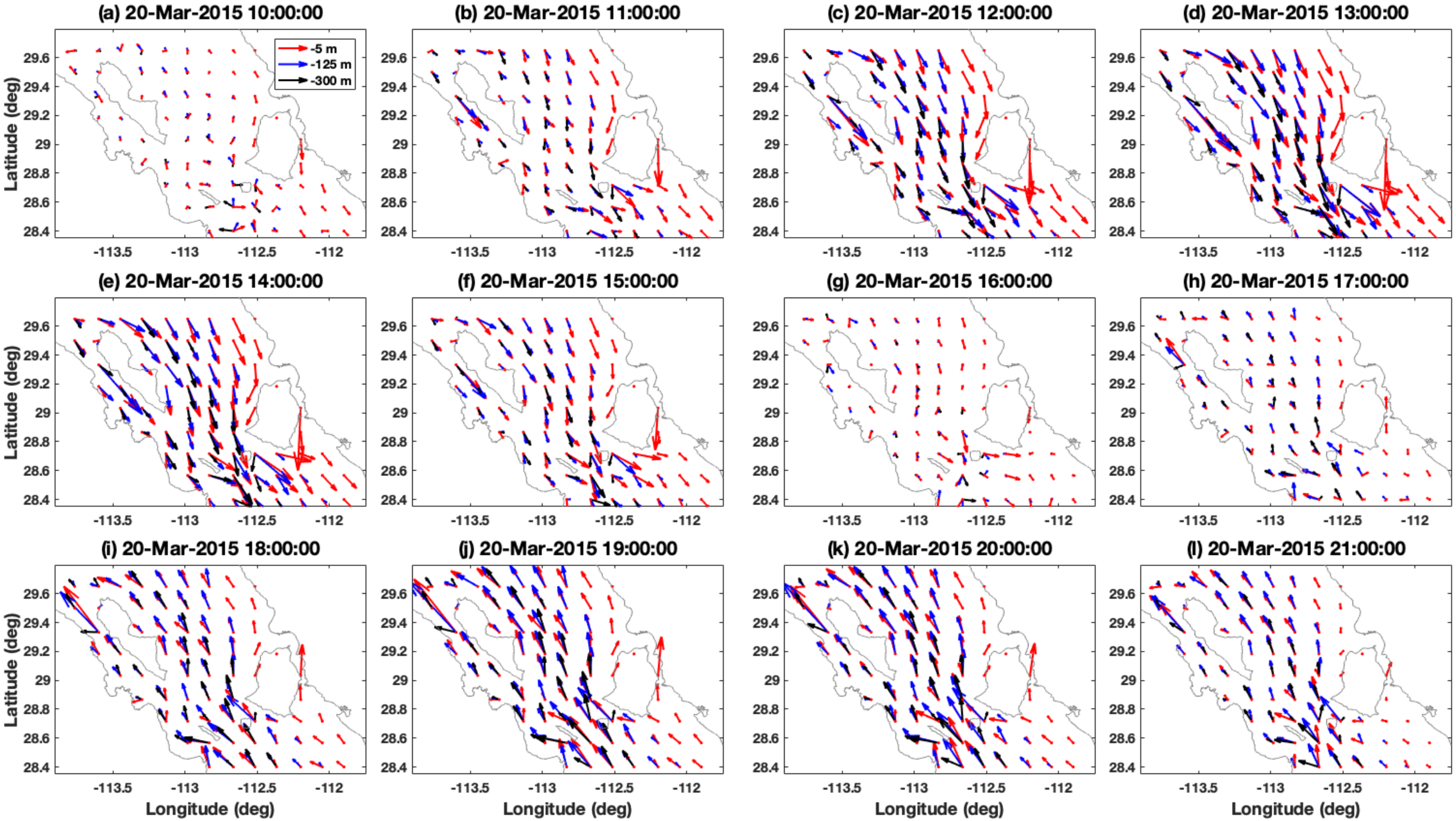

Figure 6.4. Current vectors at -5 m (red), -125 m (blue), -300 m (black) every hourly from 10:00 to 21:00 19th March 2015.

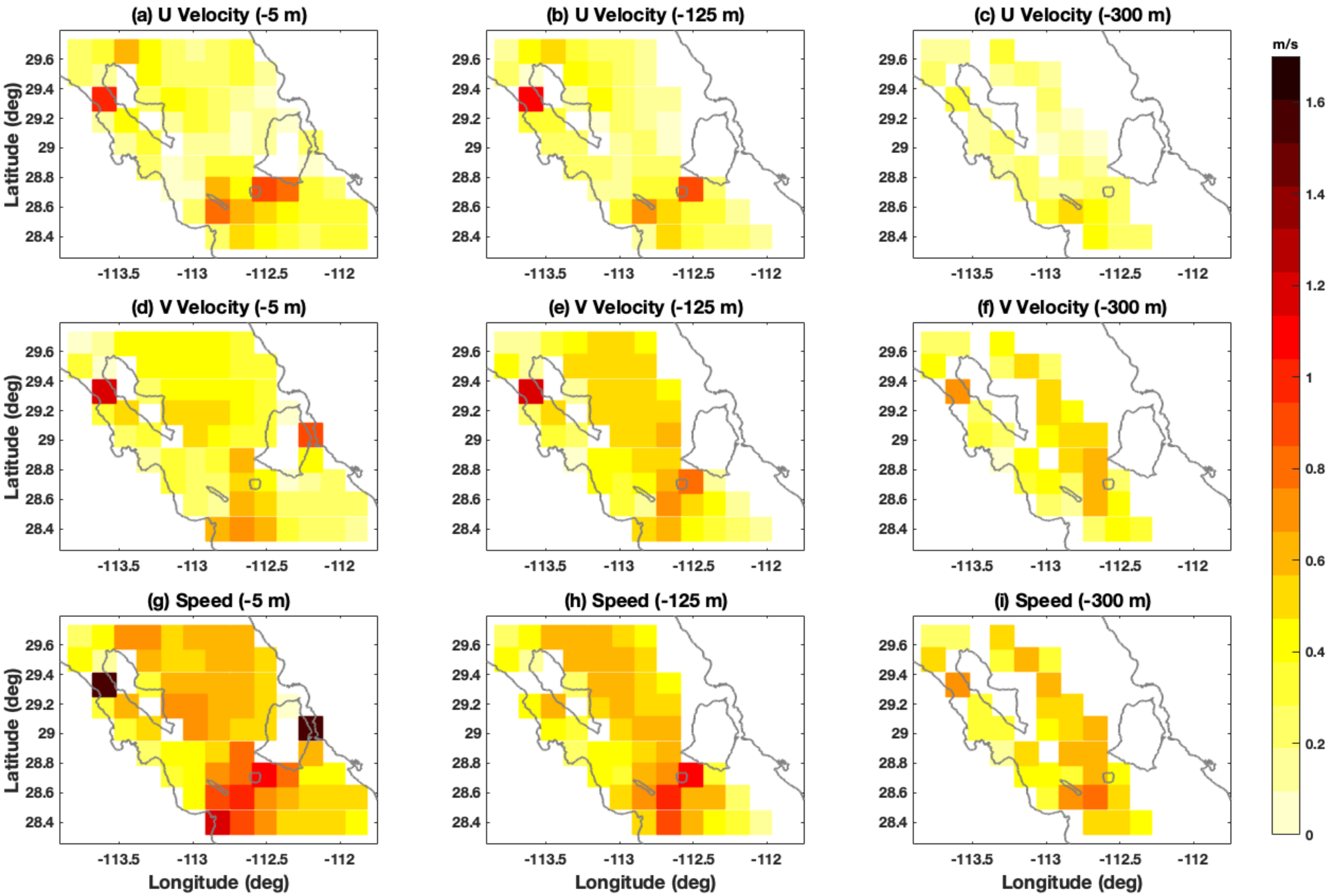

Figure 6.5. Maximum (a,b,c) u velocity; (d,e,f) u velocity; and (g,h,i) current speed at (a, d, g) -5 m; (b,e,h) -125 m and (c,f,i) -300 m for March 2015.

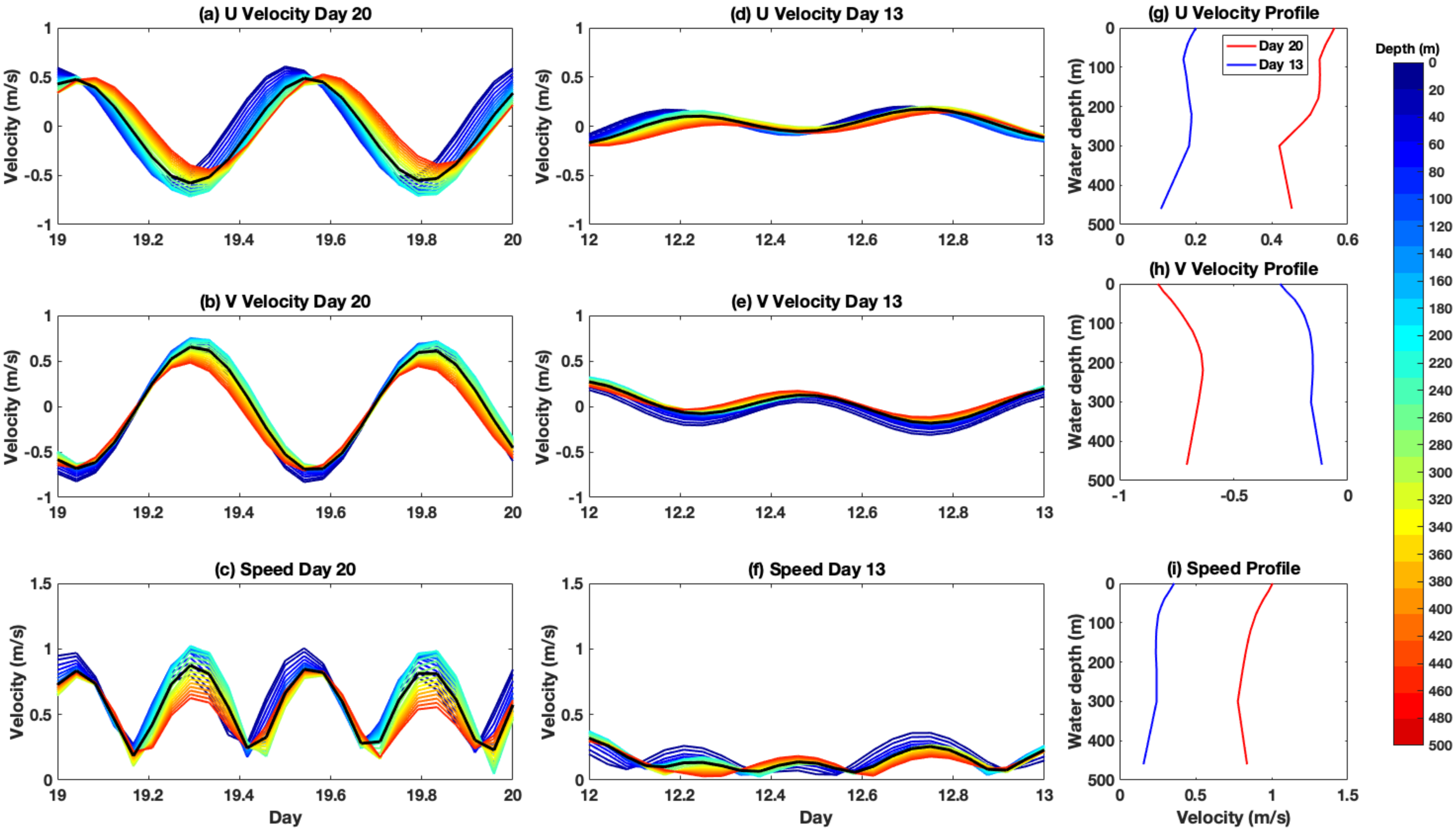

Figure 6.6. Time-series of (a,d,g) u velocity; (b,e,h) v velocity; and (c,f,i) current speed at different water depths, for (a,b,c) Day 20; and (d,e,f) Day 13 for Point A (location shown in Figure 5.7); (g,h,i) velocity depth profiles for maximum currents on Day 20 and Day 13 for Point A. Black line on panels a to f shows depth averaged current.

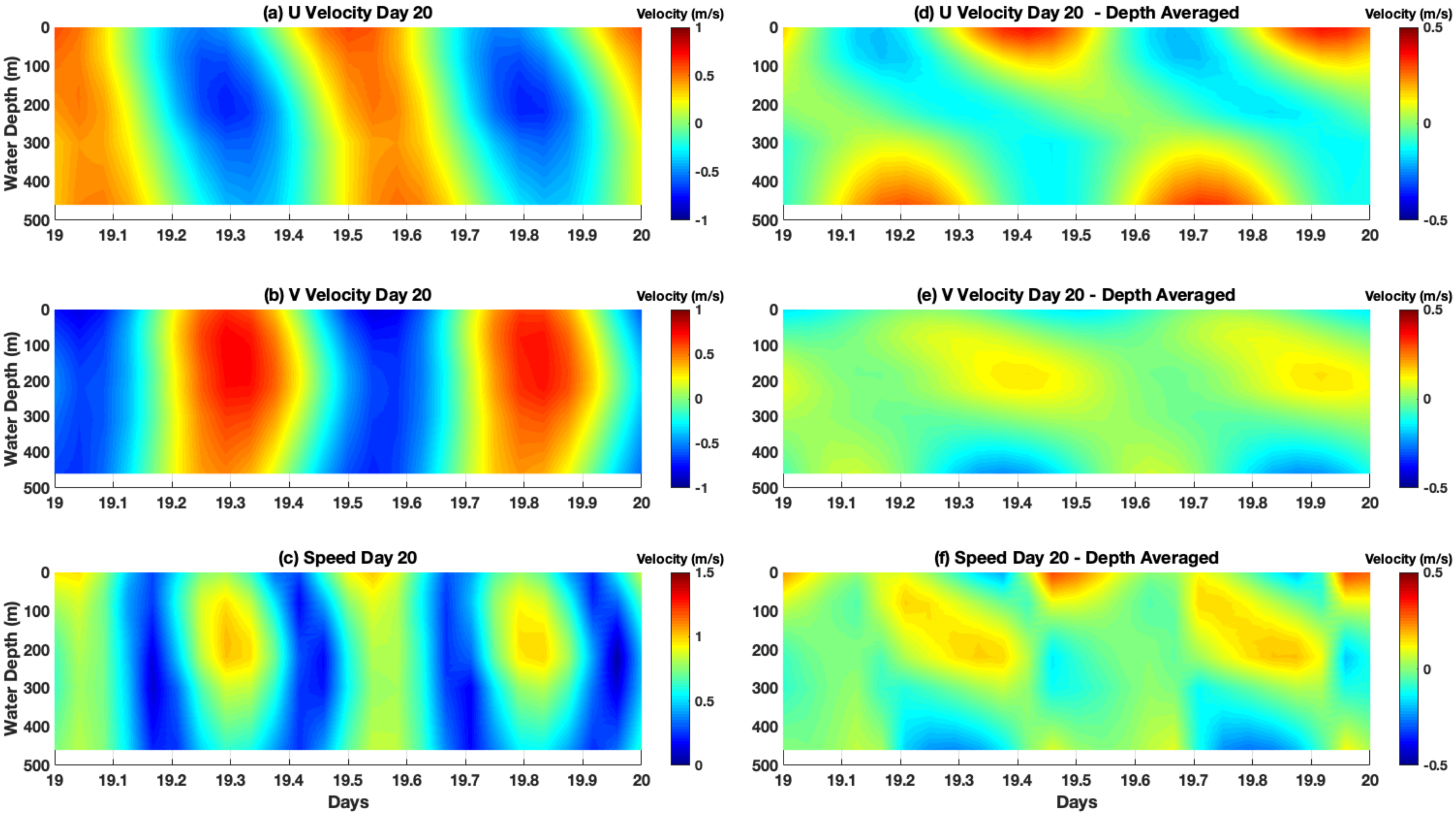

Figure 6.7. Time-series of (a,d,g) u velocity; (b,e,h) v velocity; and (c,f,i) current speed at different water depths, for Day 20 for Point A (location shown in Figure 5.7).; and (d,e,f) velocities after subtracted the depth average velocity.

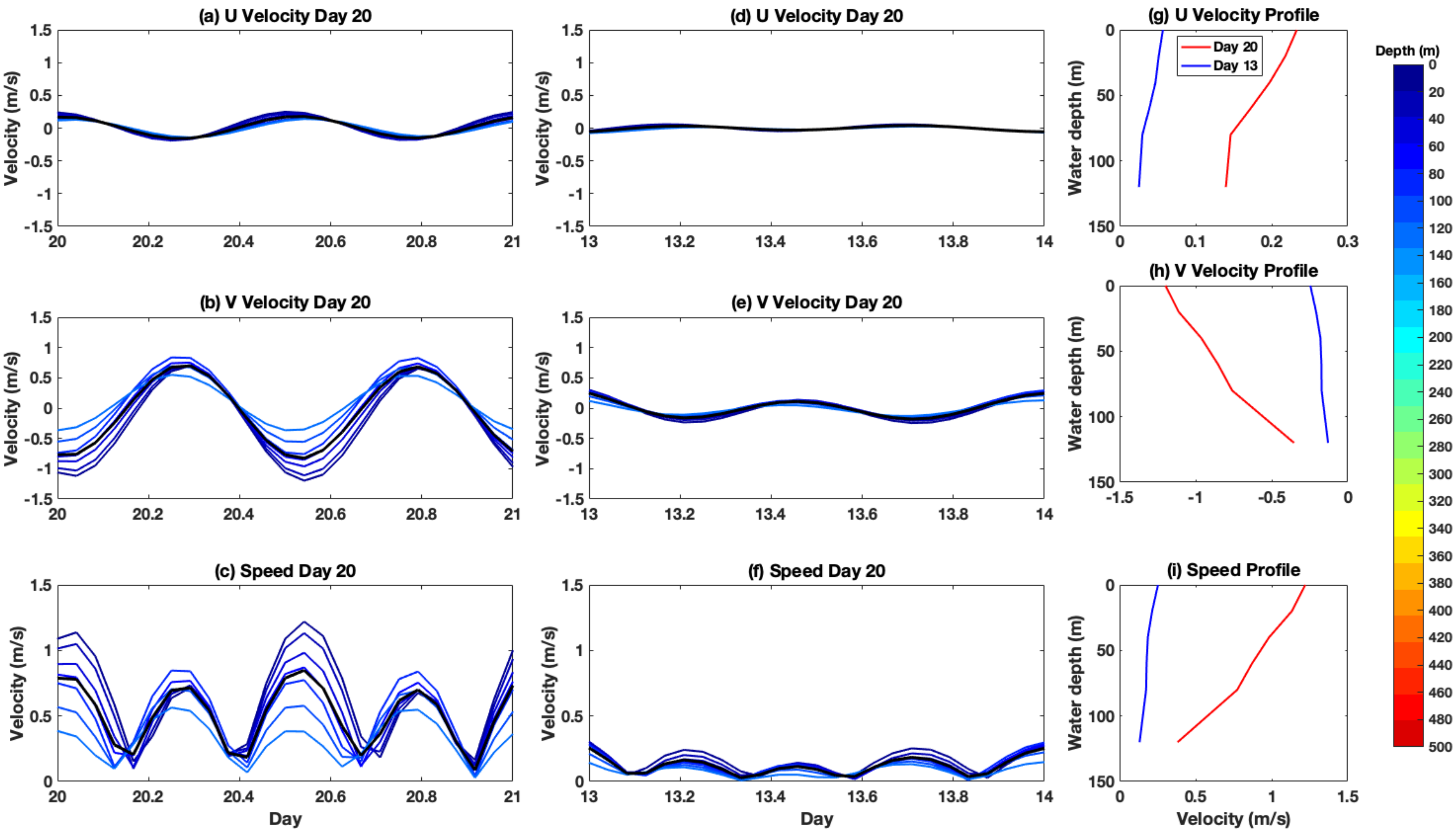

Figure 6.8. Time-series of (a,d,g) u velocity; (b,e,h) v velocity; and (c,f,i) current speed at different water depths, for (a,b,c) Day 20; and (d,e,f) Day 13 for Point B (location shown in Figure 5.7); (g,h,i) velocity depth profiles for maximum currents on Day 20 and Day 13 for Point B. Black line on panels a to f shows depth averaged current.

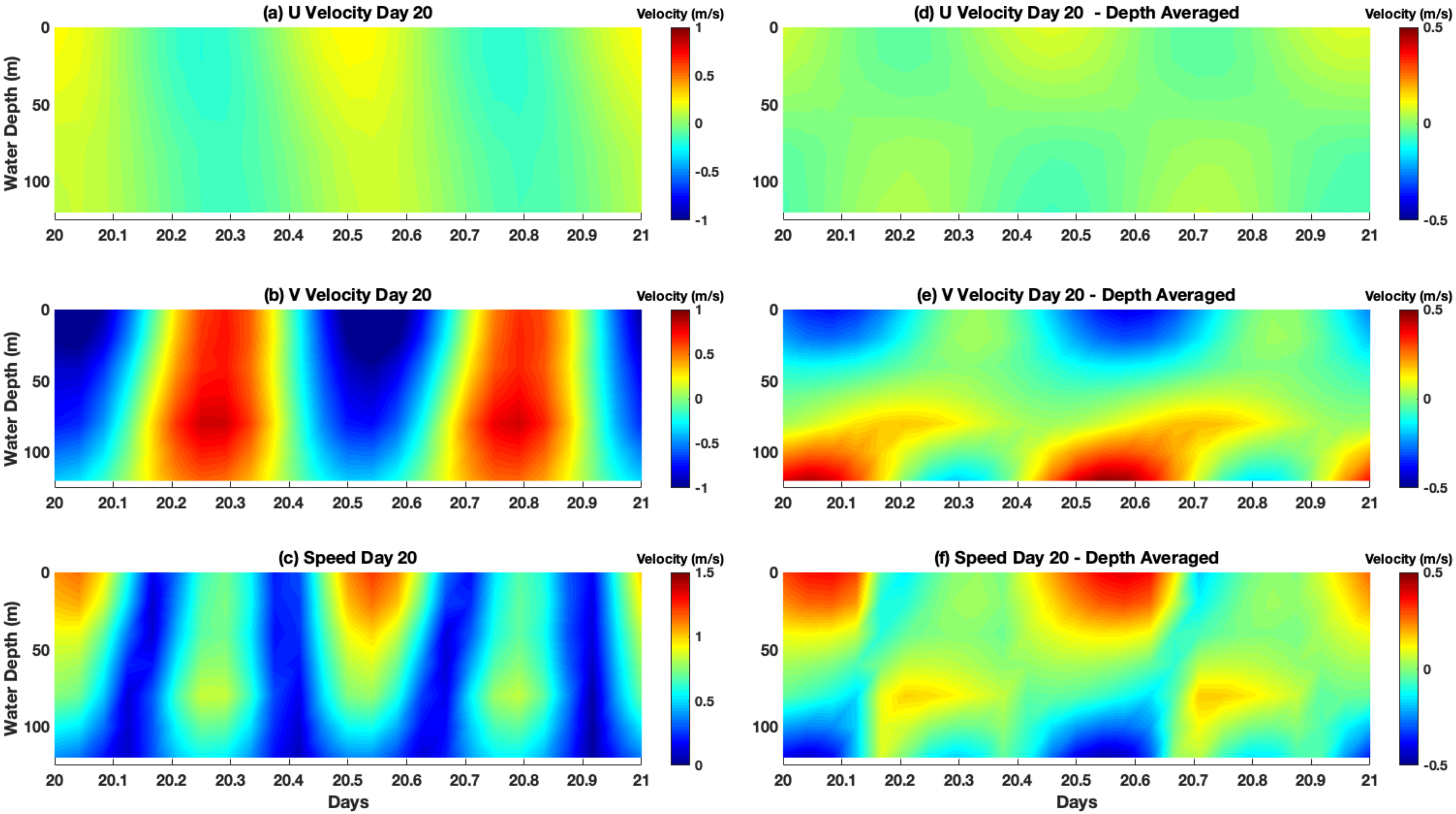

Figure 6.9. Time-series of (a,d,g) u velocity; (b,e,h) v velocity; and (c,f,i) current speed at different water depths, for Day 20 for Point B (location shown in Figure 5.7).; and (d,e,f) velocities after subtracted the depth average velocity.

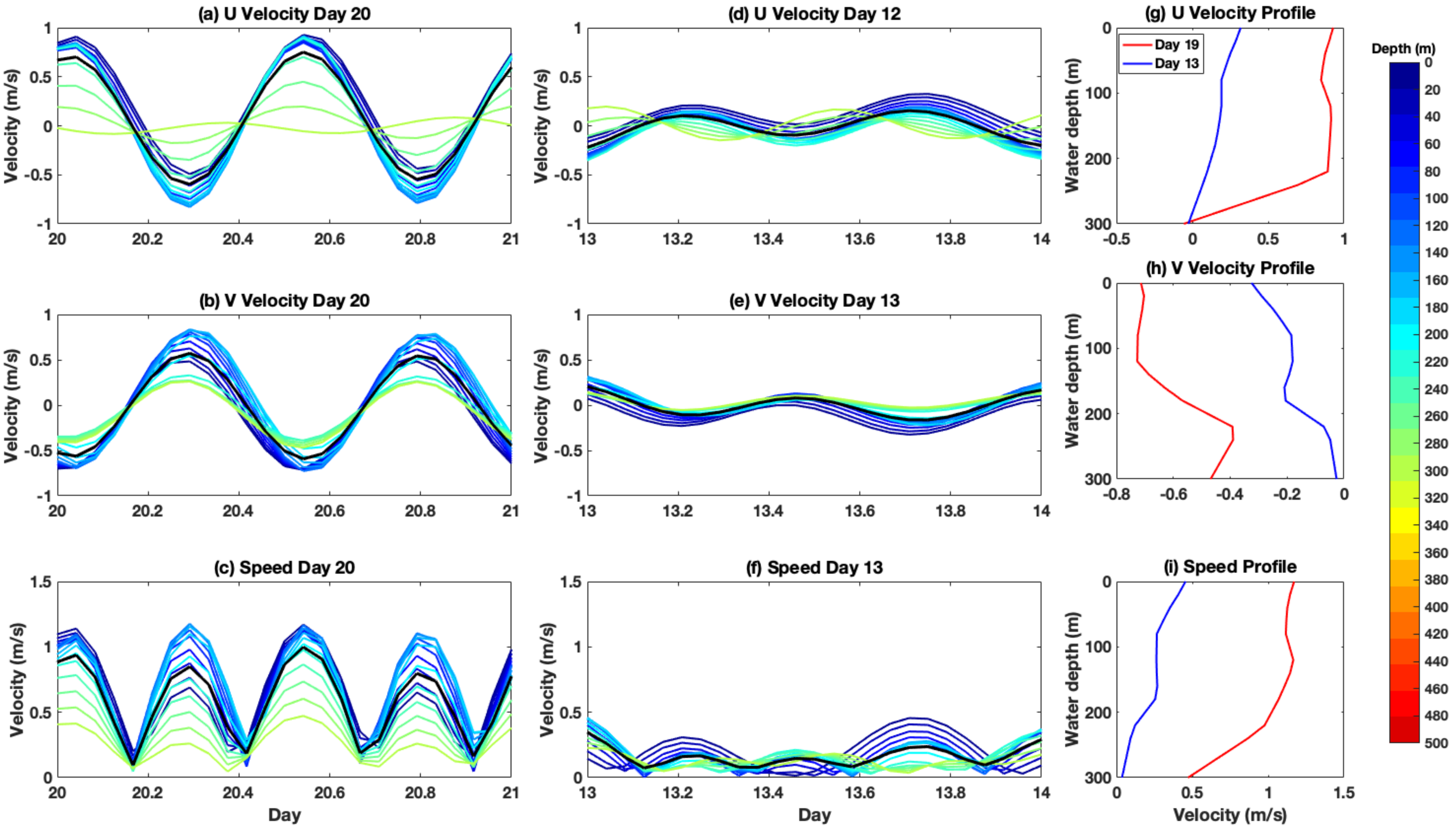

Figure 6.10. Time-series of (a,d,g) u velocity; (b,e,h) v velocity; and (c,f,i) current speed at different water depths, for (a,b,c) Day 20; and (d,e,f) Day 13 for Point C (location shown in Figure 5.7); (g,h,i) velocity depth profiles for maximum currents on Day 20 and Day 13 for Point C. Black line on panels a to f shows depth averaged current.

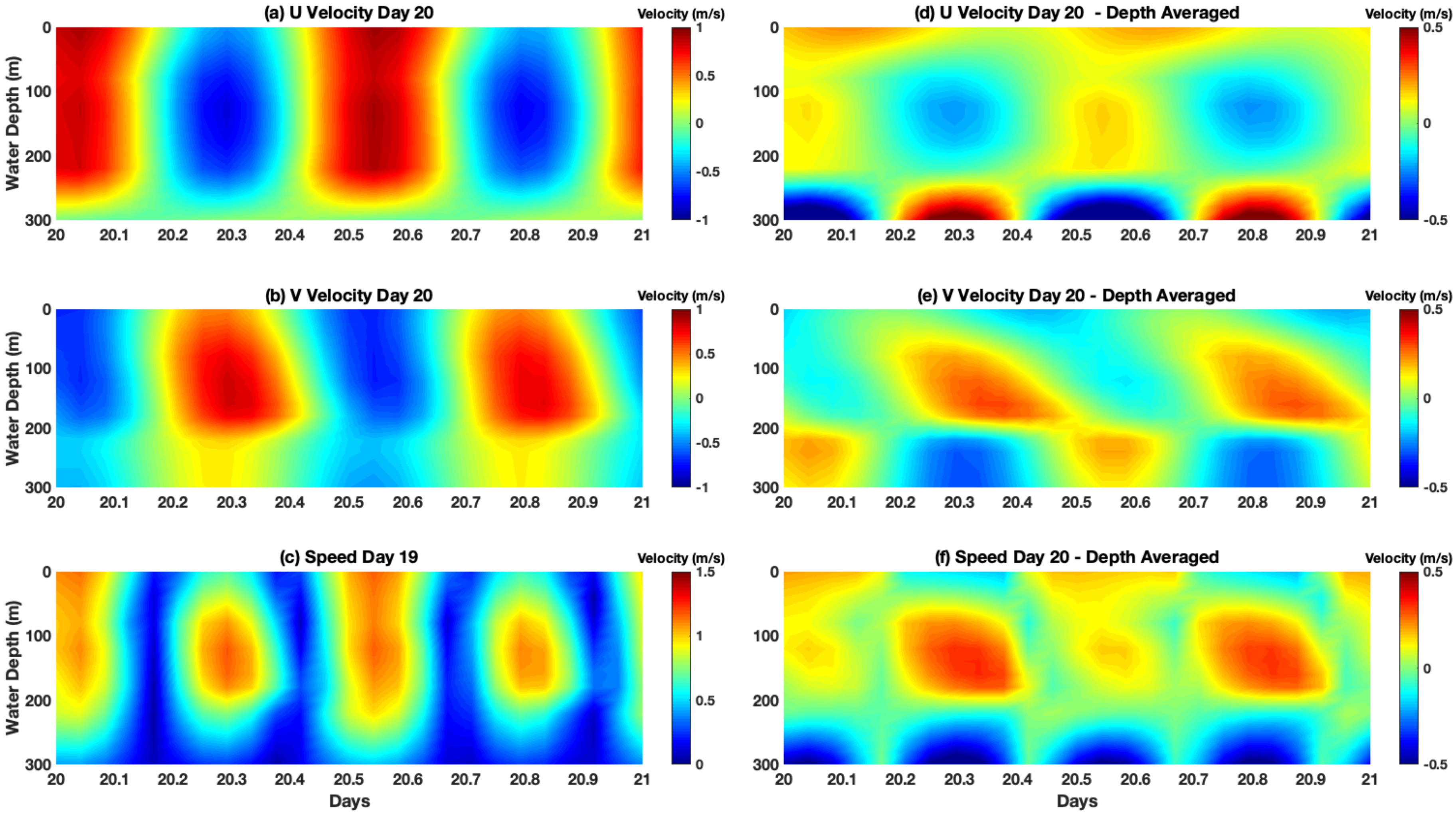

Figure 6.11. Time-series of (a,d,g) u velocity; (b,e,h) v velocity; and (c,f,i) current speed at different water depths, for Day 20 for Point C (location shown in Figure 5.7); and (d,e,f) velocities after subtracted the depth average velocity.

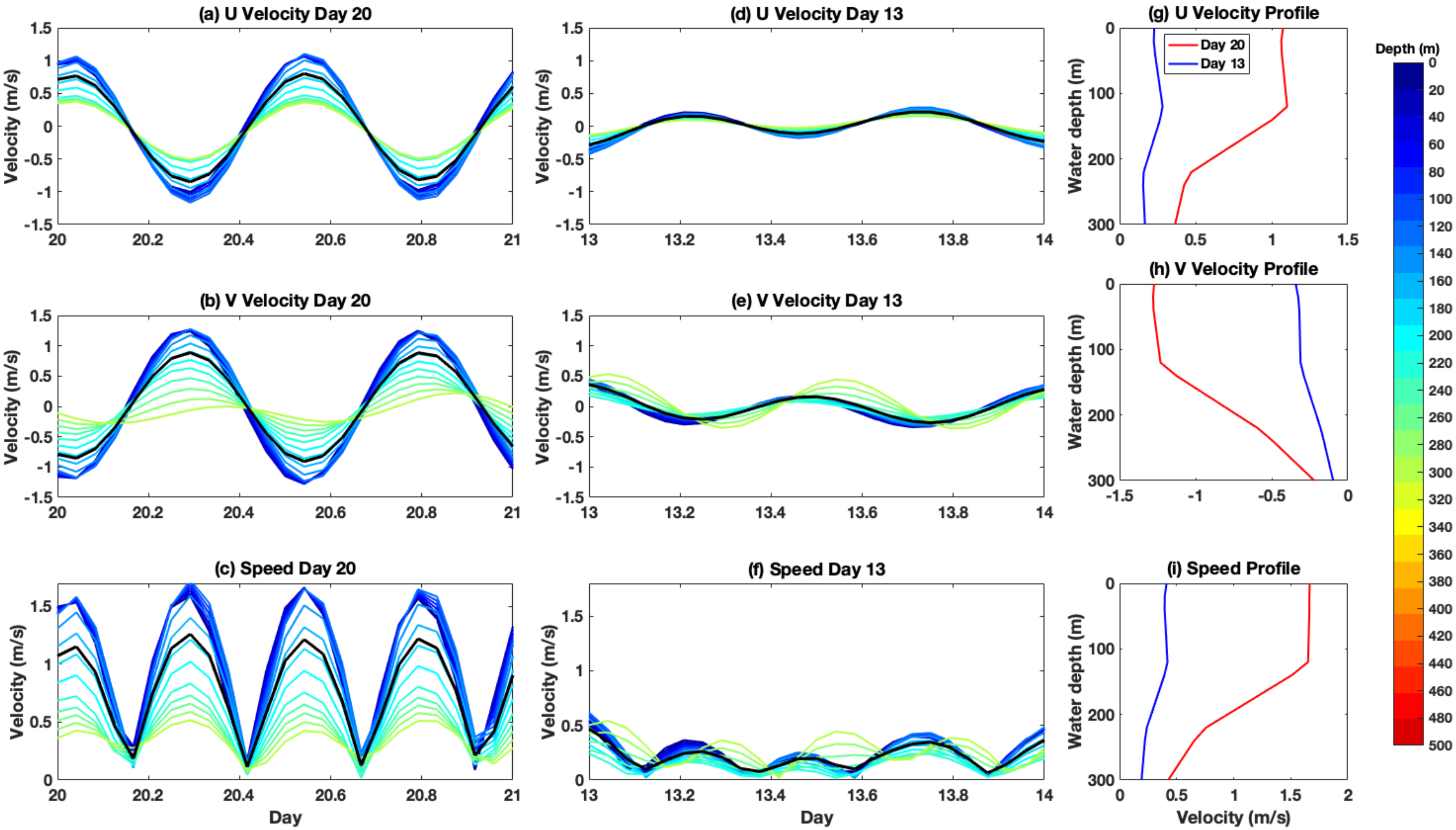

Figure 6.12. Time-series of (a,d,g) u velocity; (b,e,h) v velocity; and (c,f,i) current speed at different water depths, for (a,b,c) Day 20; and (d,e,f) Day 13 for Point D (location shown in Figure 5.7); (g,h,i) velocity depth profiles for maximum currents on Day 20 and Day 13 for Point D. Black line on panels a to f shows depth averaged current.

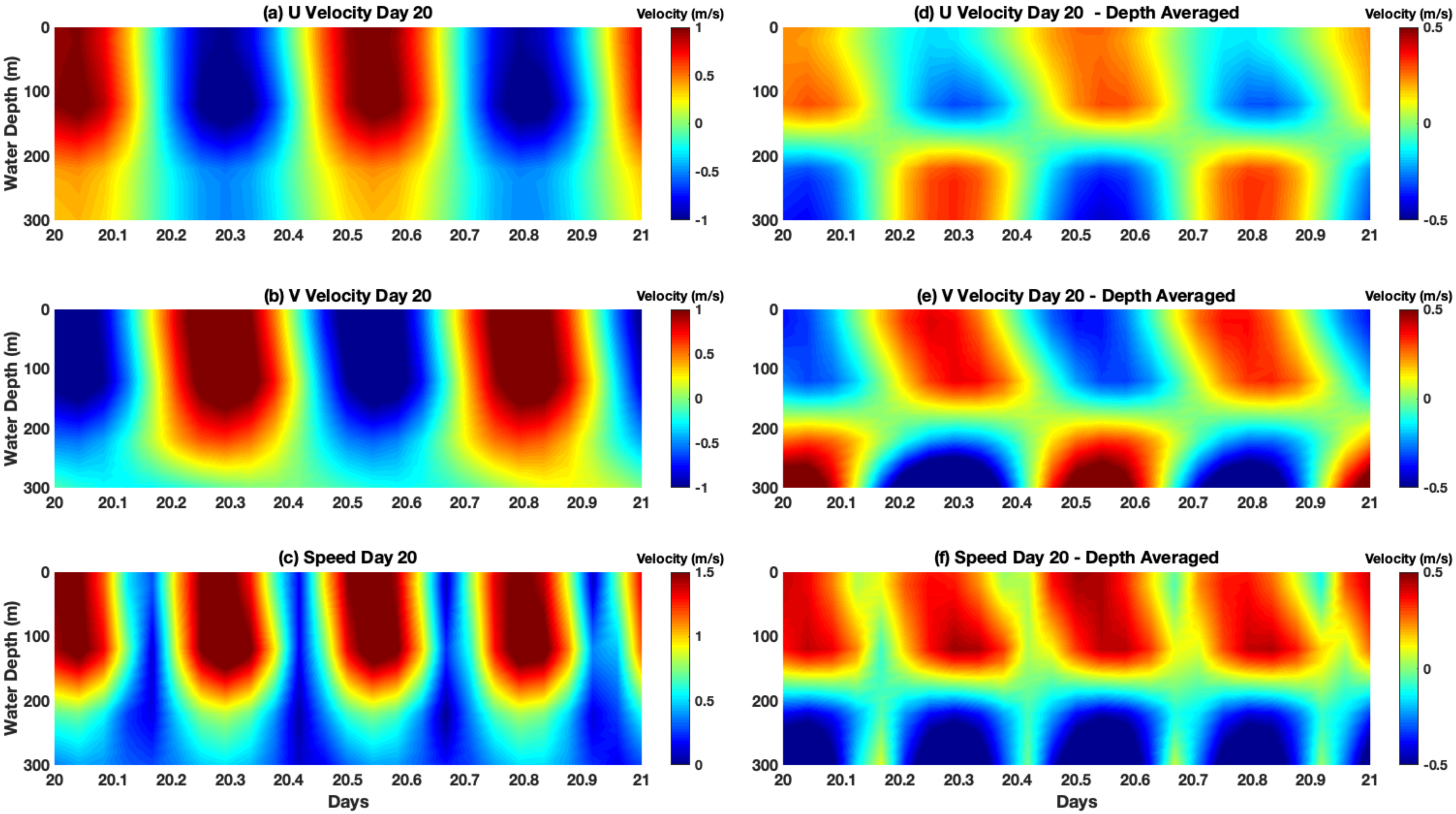

Figure 6.13. Time-series of (a,d,g) u velocity; (b,e,h) v velocity; and (c,f,i) current speed at different water depths, for Day 20 for Point D (location shown in Figure 5.7); and (d,e,f) velocities after subtracted the depth average velocity.

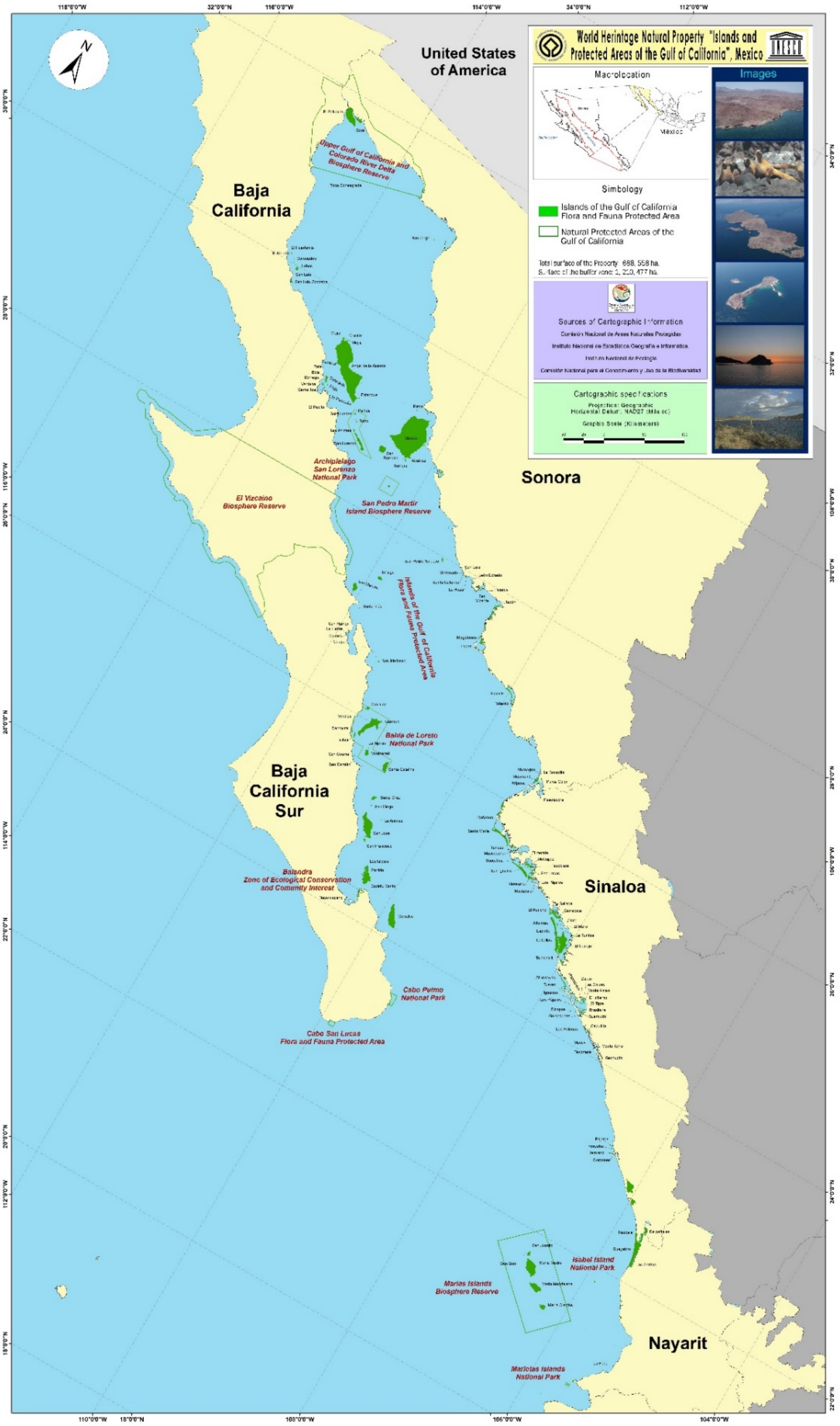

Figure 6.14. Protected area of the Gulf of California.
Source: https://whc.unesco.org/en/list/1182/documents/

Green Turtle
Whale
Blue Whale
Oliver Ridley Turtle
Great White shark
Tuna

Bigeye Tuna
Skipjack Tuna
Shark
Sea Turtle
Vaquita
Grey Whale

Whale Shark
Fin whale
Loggerhead turtle
Leatherback Turtle
Sea Whale

Figure 6.15. A selection of the mammal species found in the GC. Source: https://www.worldwildlife.org/places/gulf-of-california.

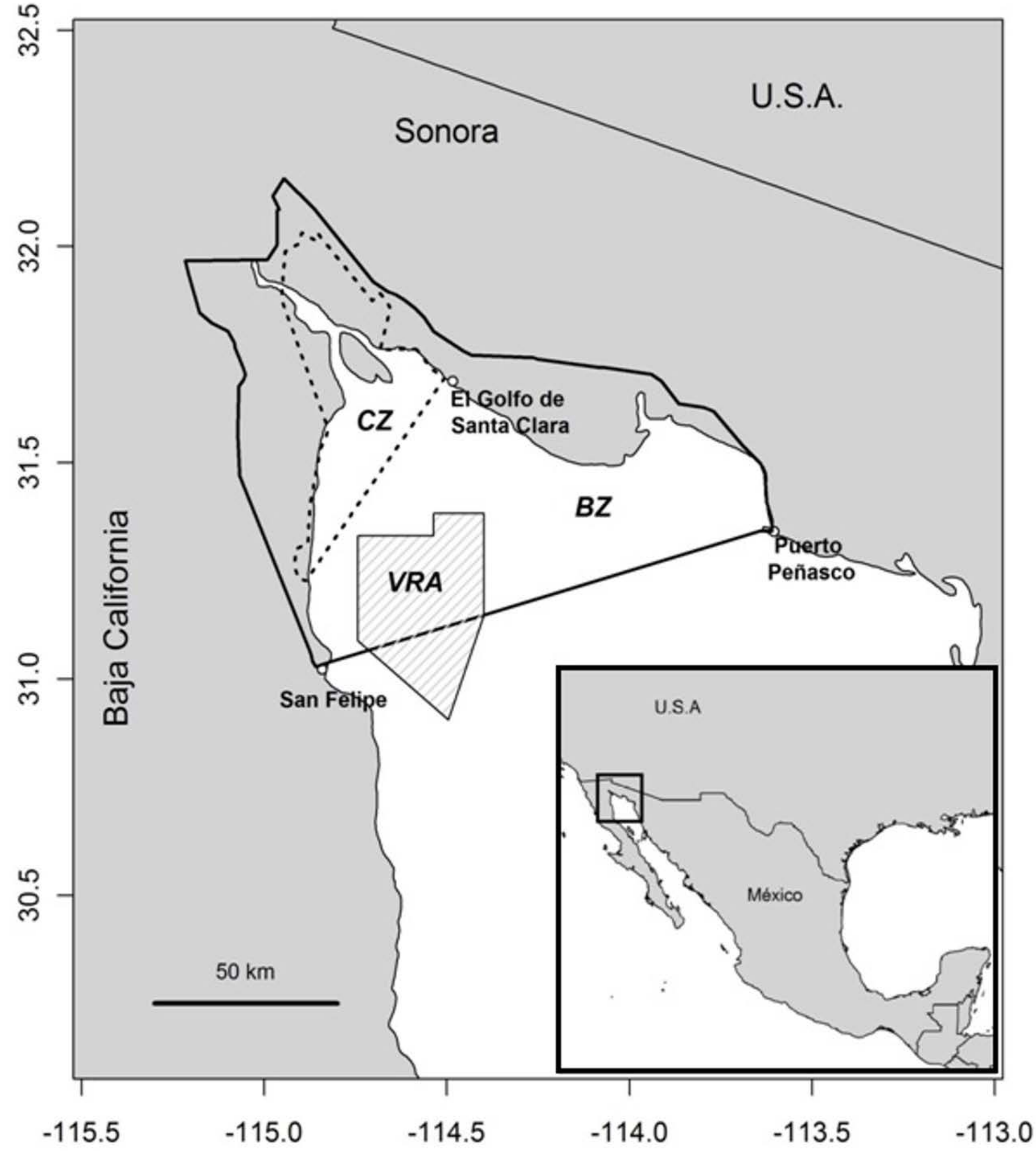

Figure 6.16. Upper Gulf of California and Colorado River Delta Biosphere Reserve, including the core zone (CZ), buffer zone (BZ), and vaquita refuge area (VRA). Source: Cisneros-Montemayor and Vinvent (2016).

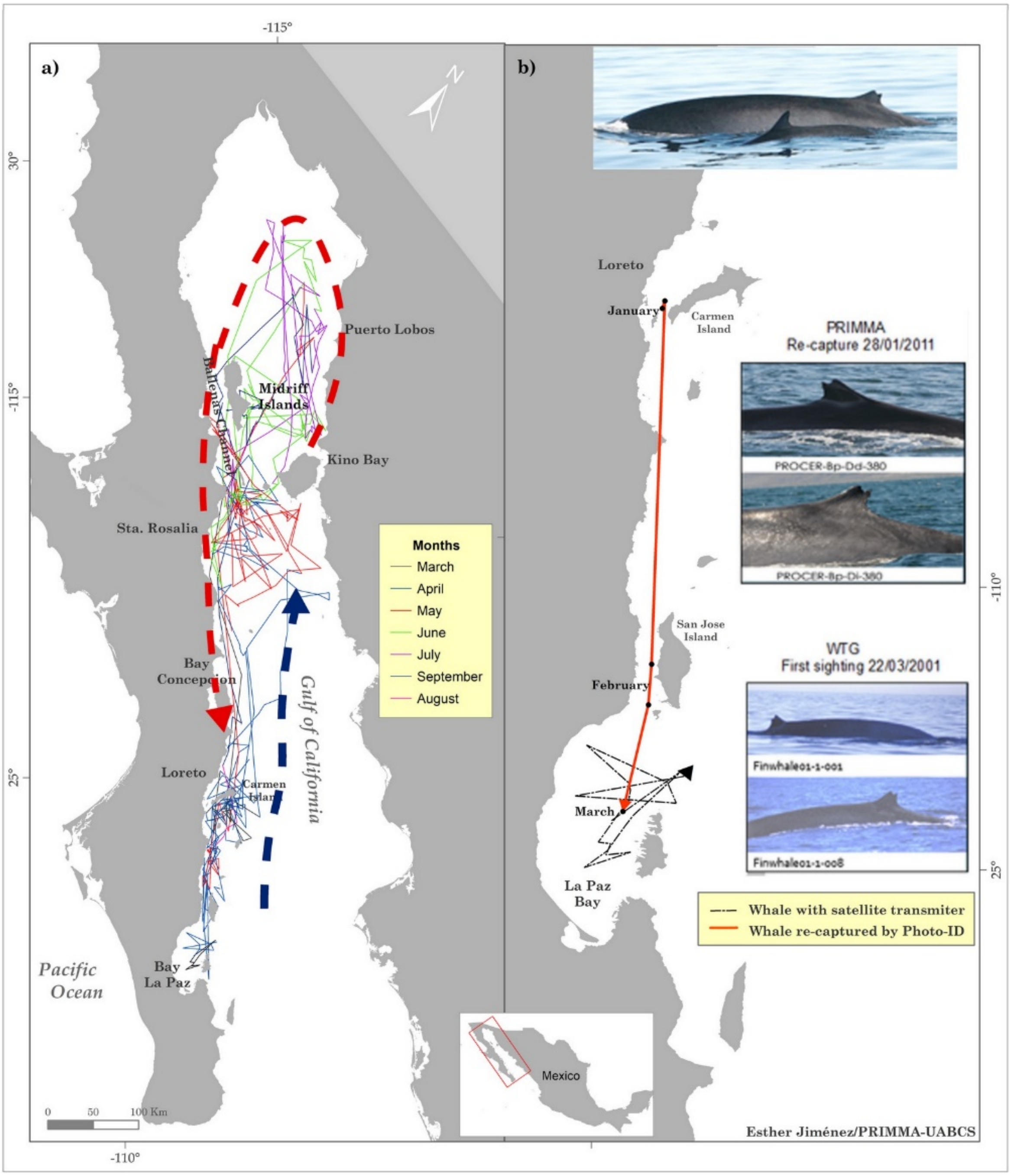

Figure 6.17. Migration routes of Fin whales. Source: Jimenez Lopez et al. (2019).

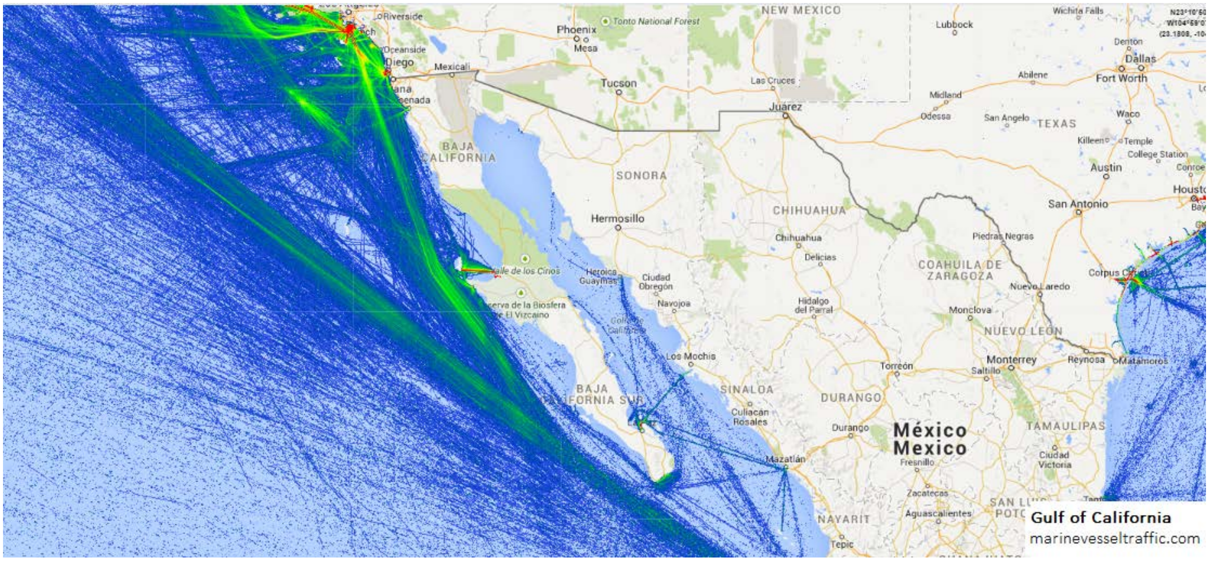

Figure 6.18. Shipping routes in the Gulf of California. Source: http://www.shiptraffic.net/2001/04/gulf-of-california-ship-traffic.html

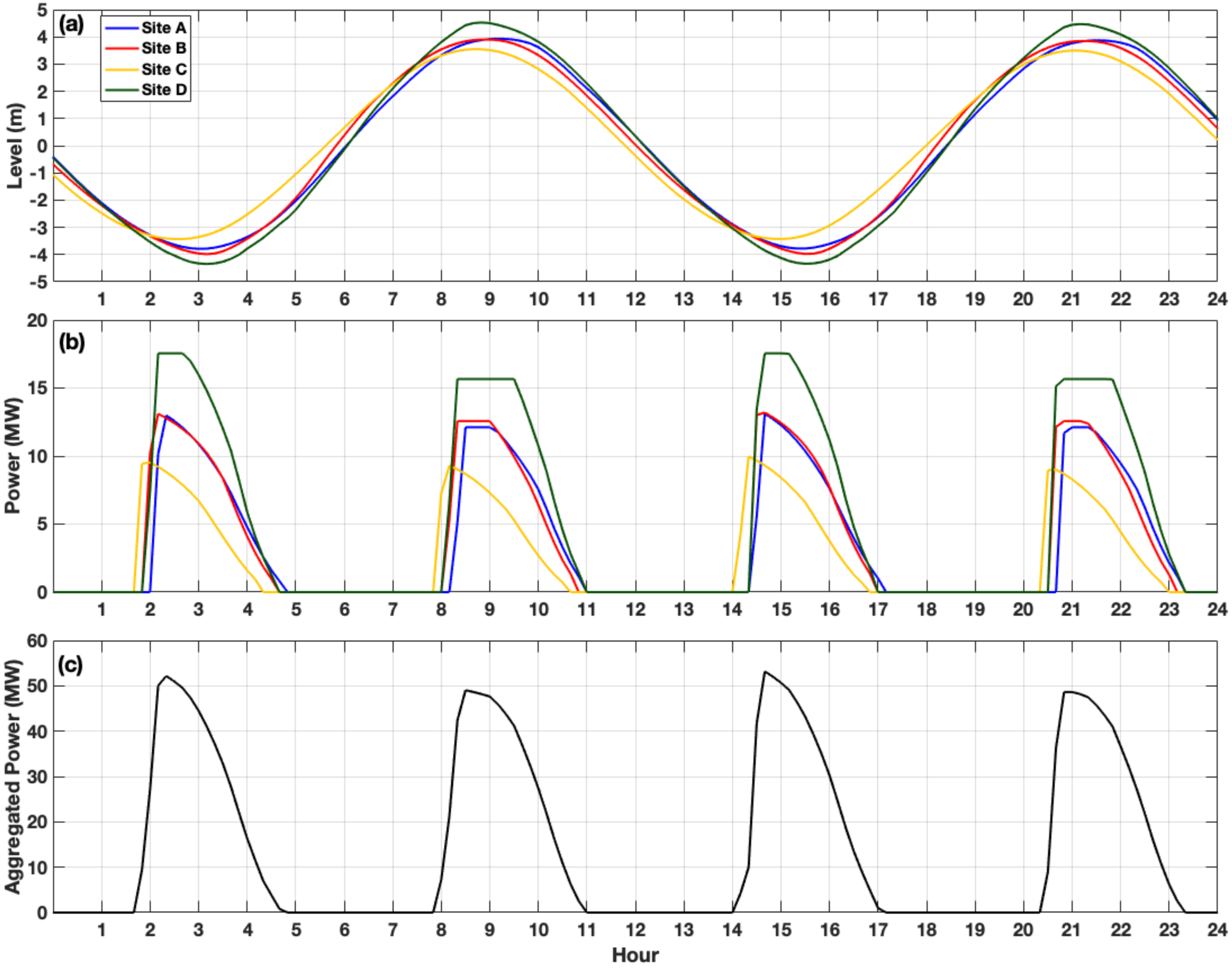

Figure 6.19. (a) Tidal level; (b) tidal-range power; and (c) aggregated tidal-range power, at the four identified northern sites, for the spring tide on 19th March 2015.

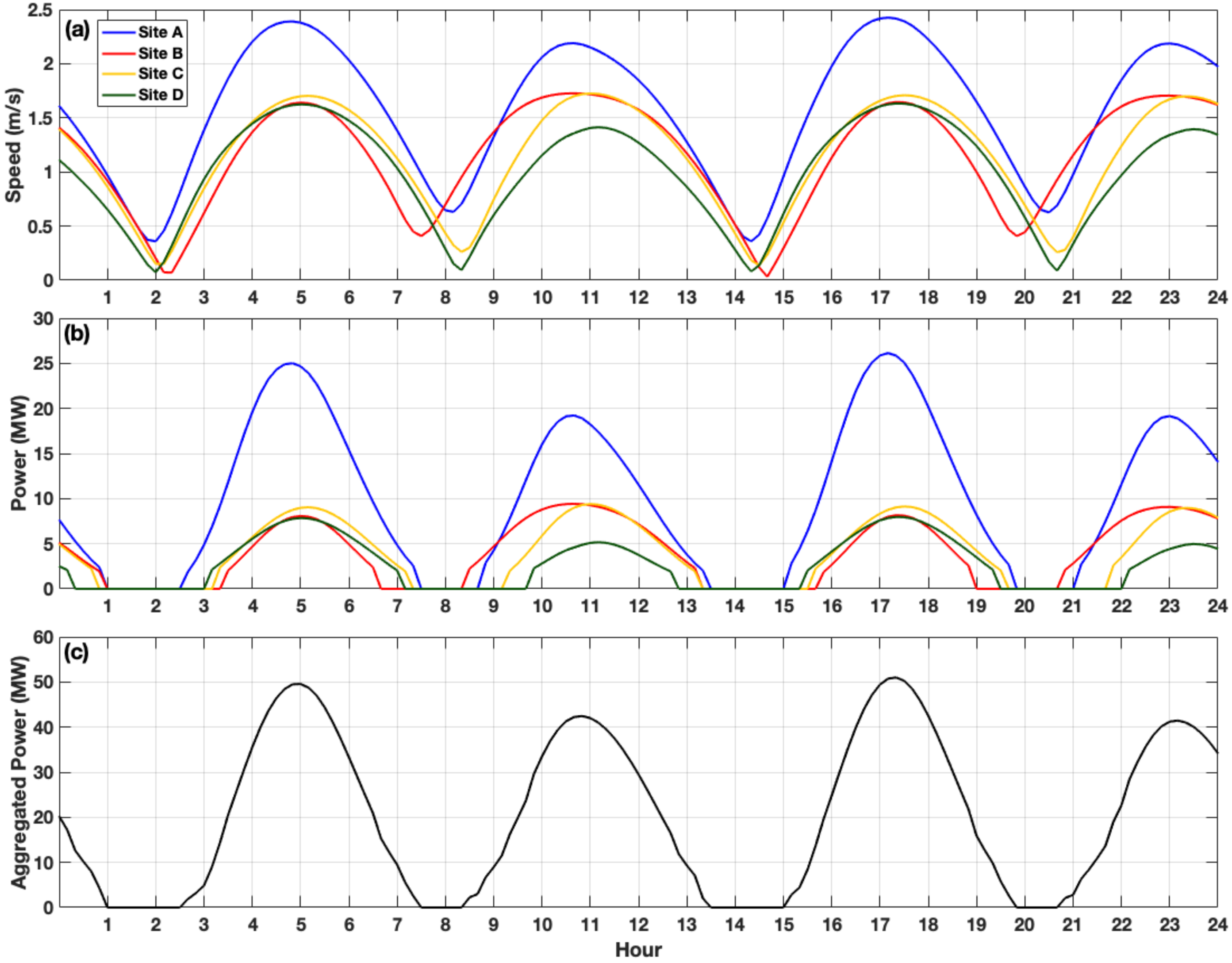

Figure 6.20. (a) Tidal current speed; (b) tidal-stream power; and (c) aggregated tidal-stream power, at the four identified in the Midriff region, for the spring tide on 19th March 2015.

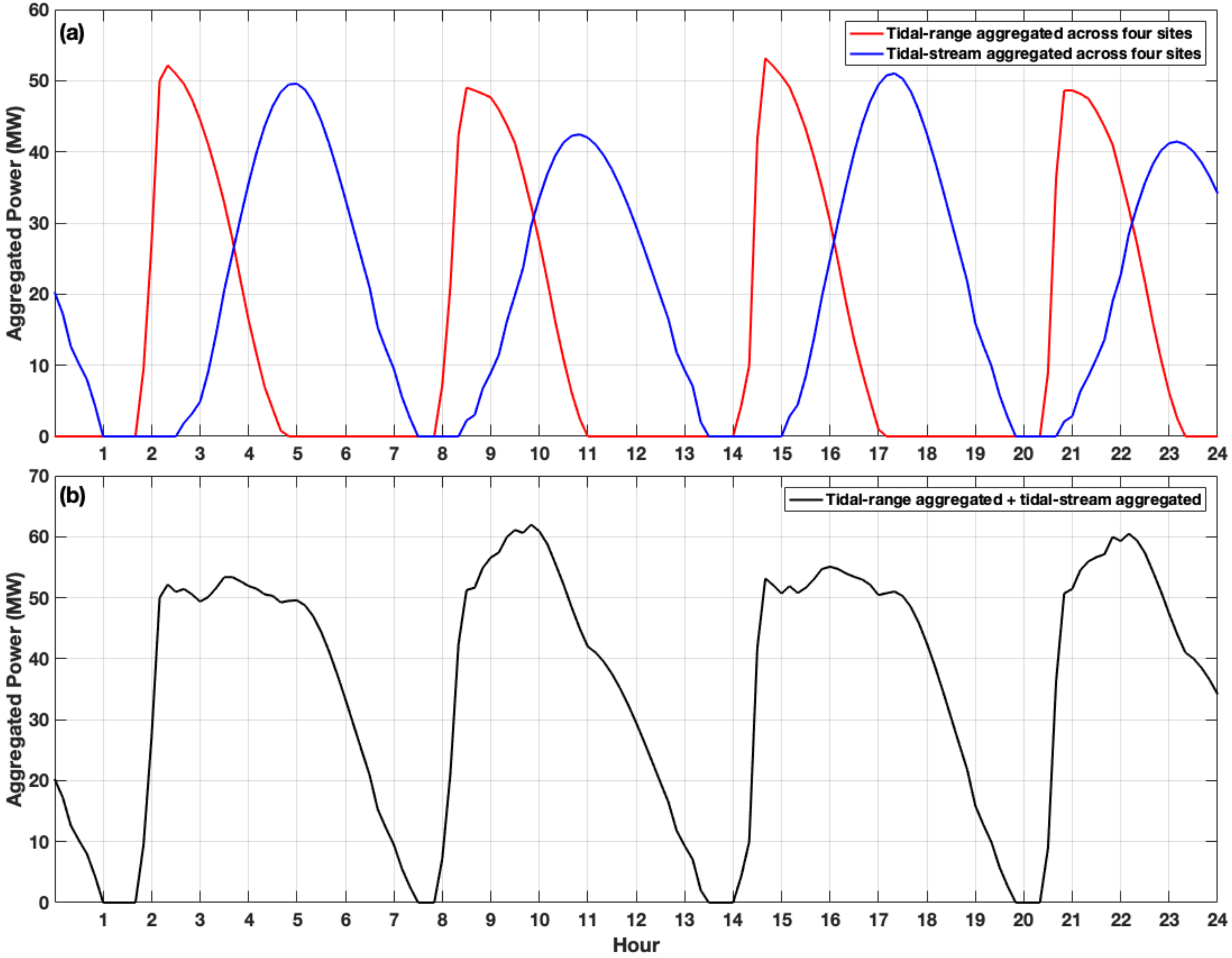

Figure 6.21. (a) Aggregated tidal-range power (red) across the four northern sites and aggregated (tidal-stream power (blue) across the four Midriff sites; (b) tidal-range and tidal stream aggregated power, for the spring tide on 19th March 2015.

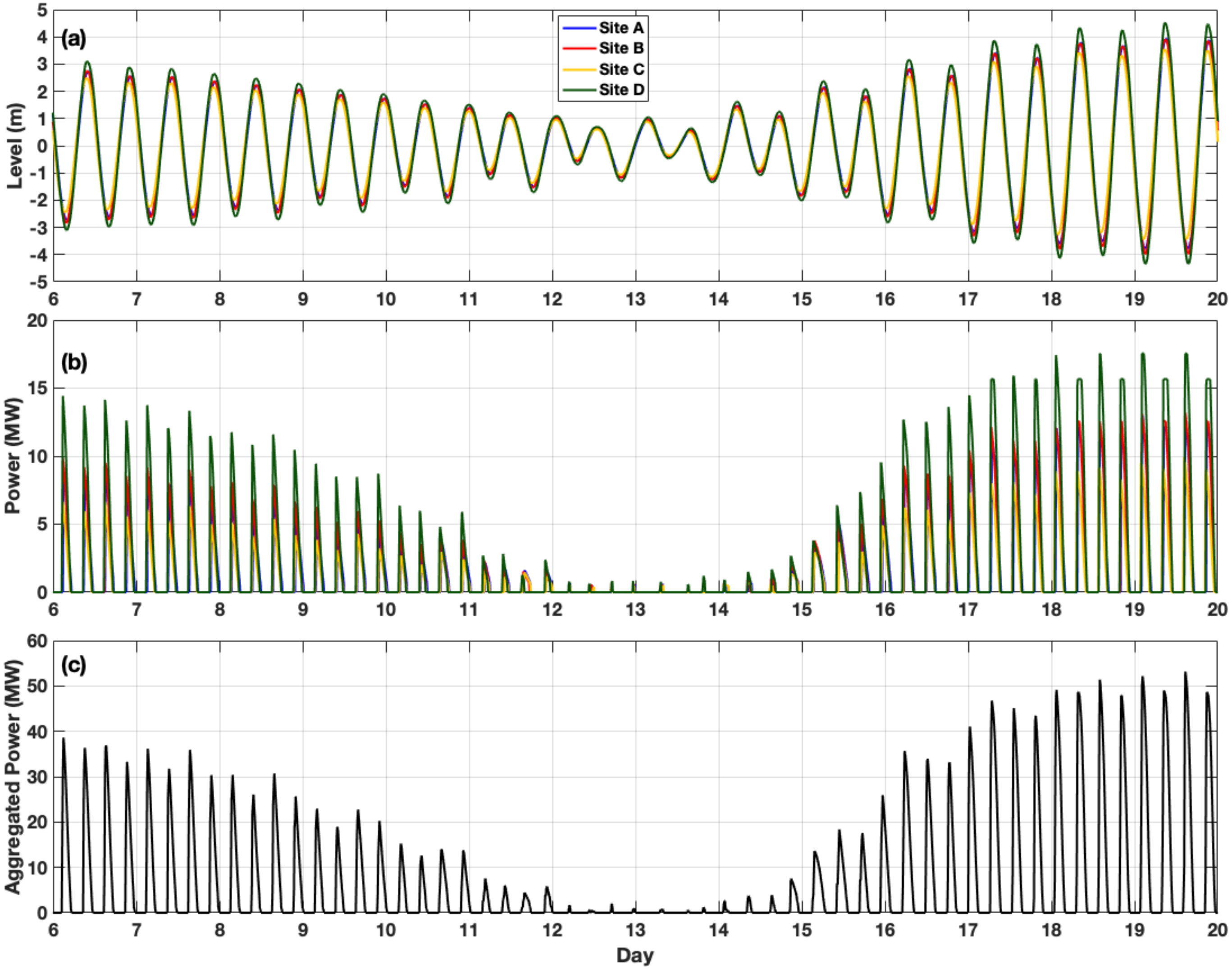

Figure 6.22. (a) Tidal level; (b) tidal-range power; and (c) aggregated tidal-range power, at the four identified northern sites, for a 14-day spring/neap tidal cycle in March 2015.

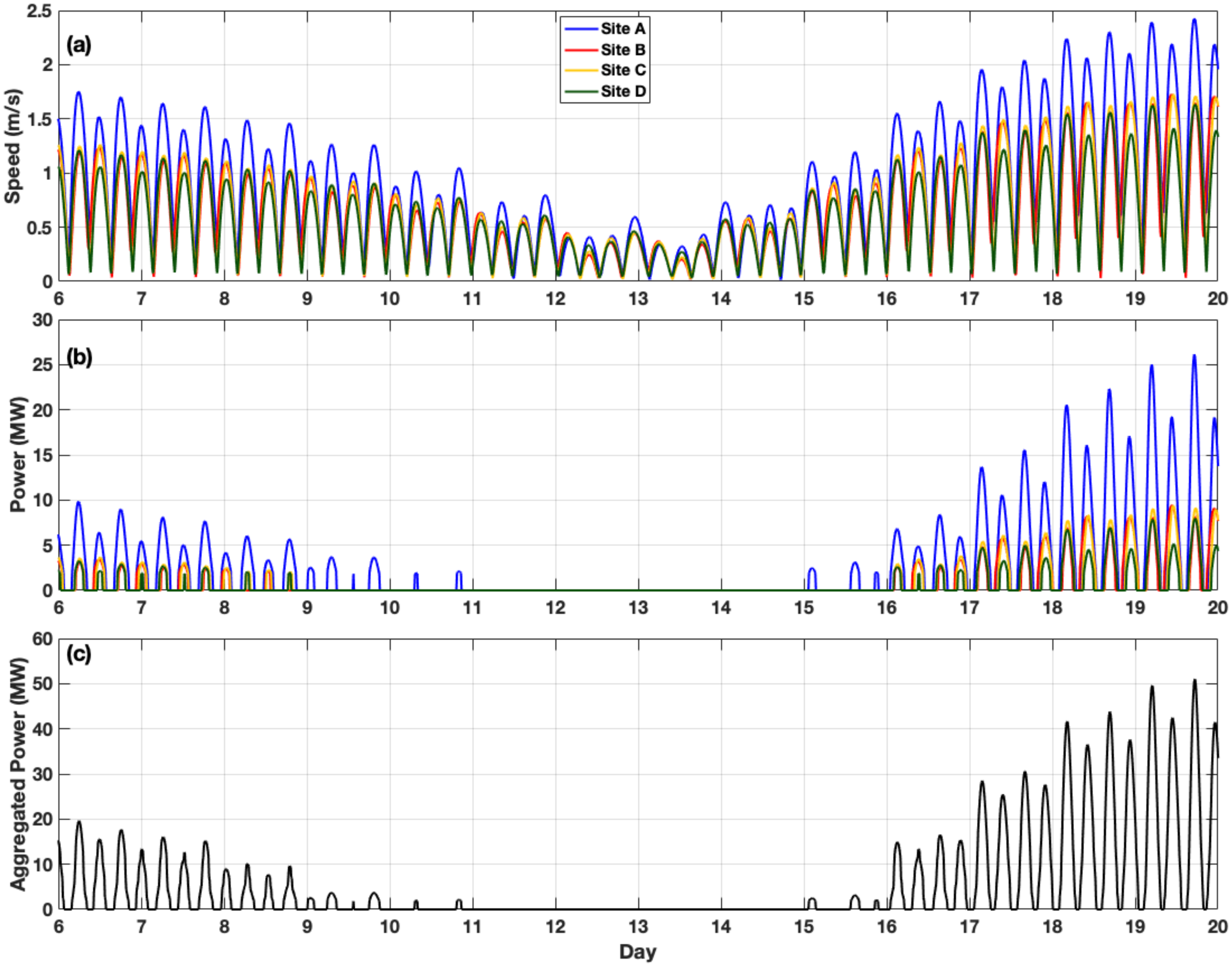

Figure 6.23. (a) Tidal current speed; (b) tidal-stream power; and (c) aggregated tidal-stream power, at the four identified in the Midriff region, for a 14-day spring/neap tidal cycle in March 2015.

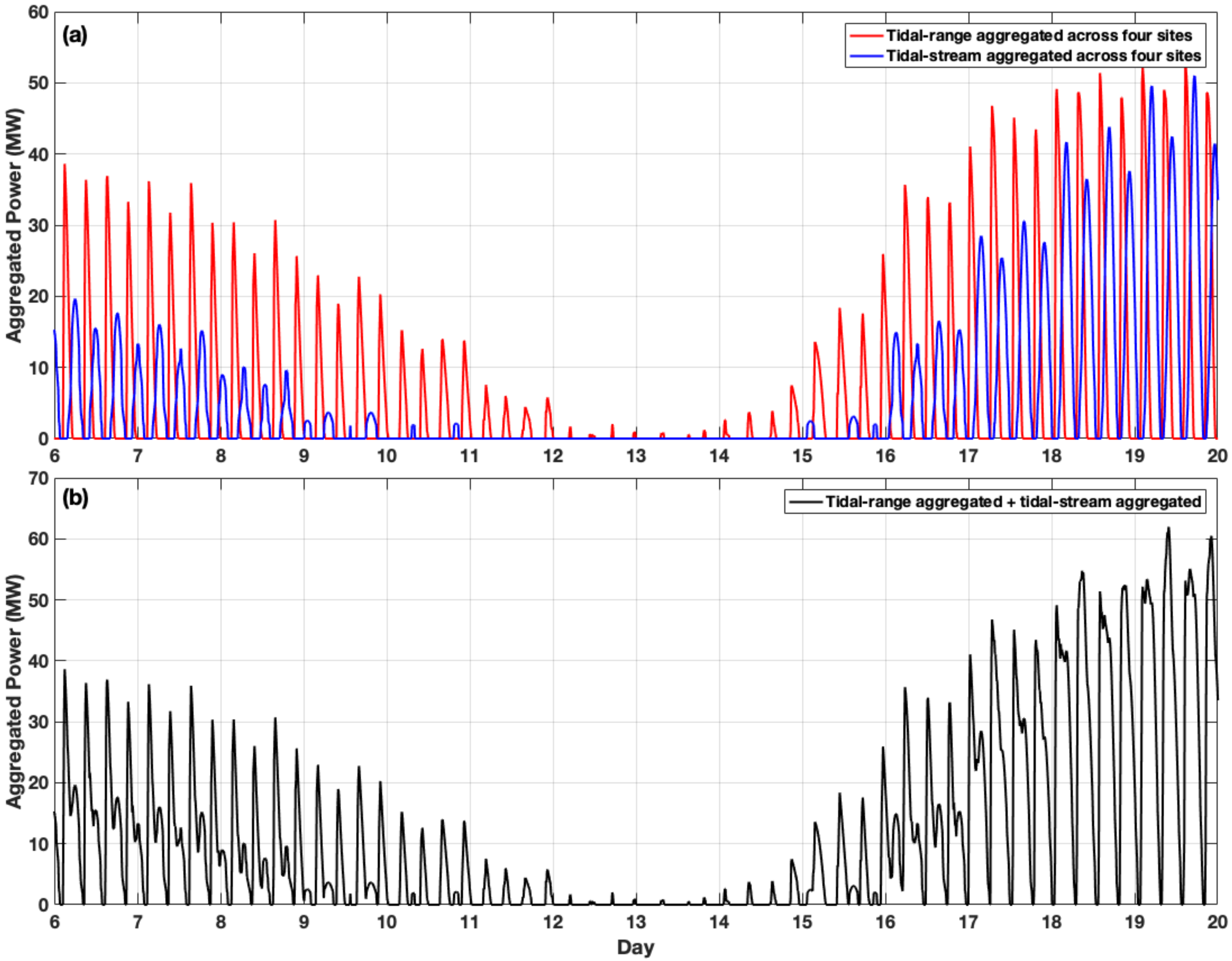

Figure 6.24. (a) Aggregated tidal-range power (red) across the four northern sites and aggregated (tidal-stream power (blue) across the four Midriff sites; (b) tidal-range and tidal stream aggregated power, for a 14-day spring/neap tidal cycle in March 2015.

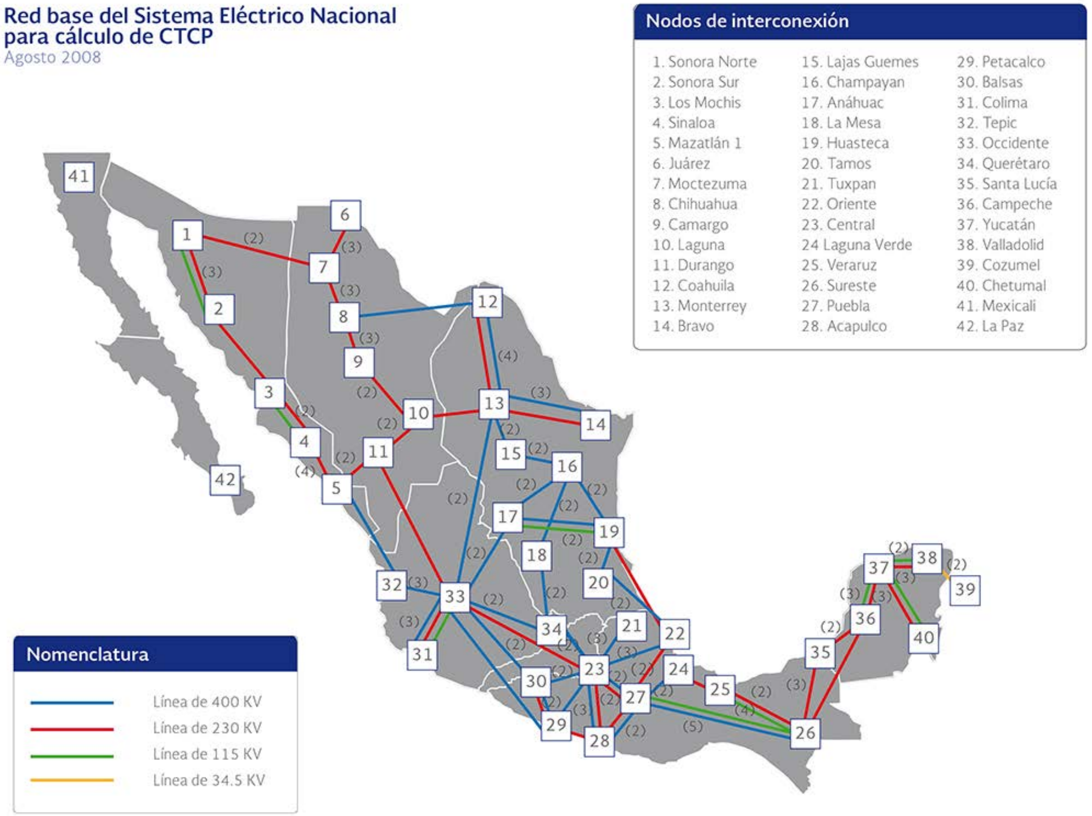

Figure 6.25. Grid connectivity Mexico. Source: https://www.cenace.gob.mx/SIM/VISTA/REPORTES/PreEnergiaSisMEM.aspx

Figure 6.26. Power generation along the country. Source: https://mapasinteractivos.didactalia.net/comunidad/mapasflashinteractivos/recurso/mapa-de-generacion-de-energia-en-mexico-inegi-de/0d08b7cd-fe7a-4801-83d8-f1e9dbb28749

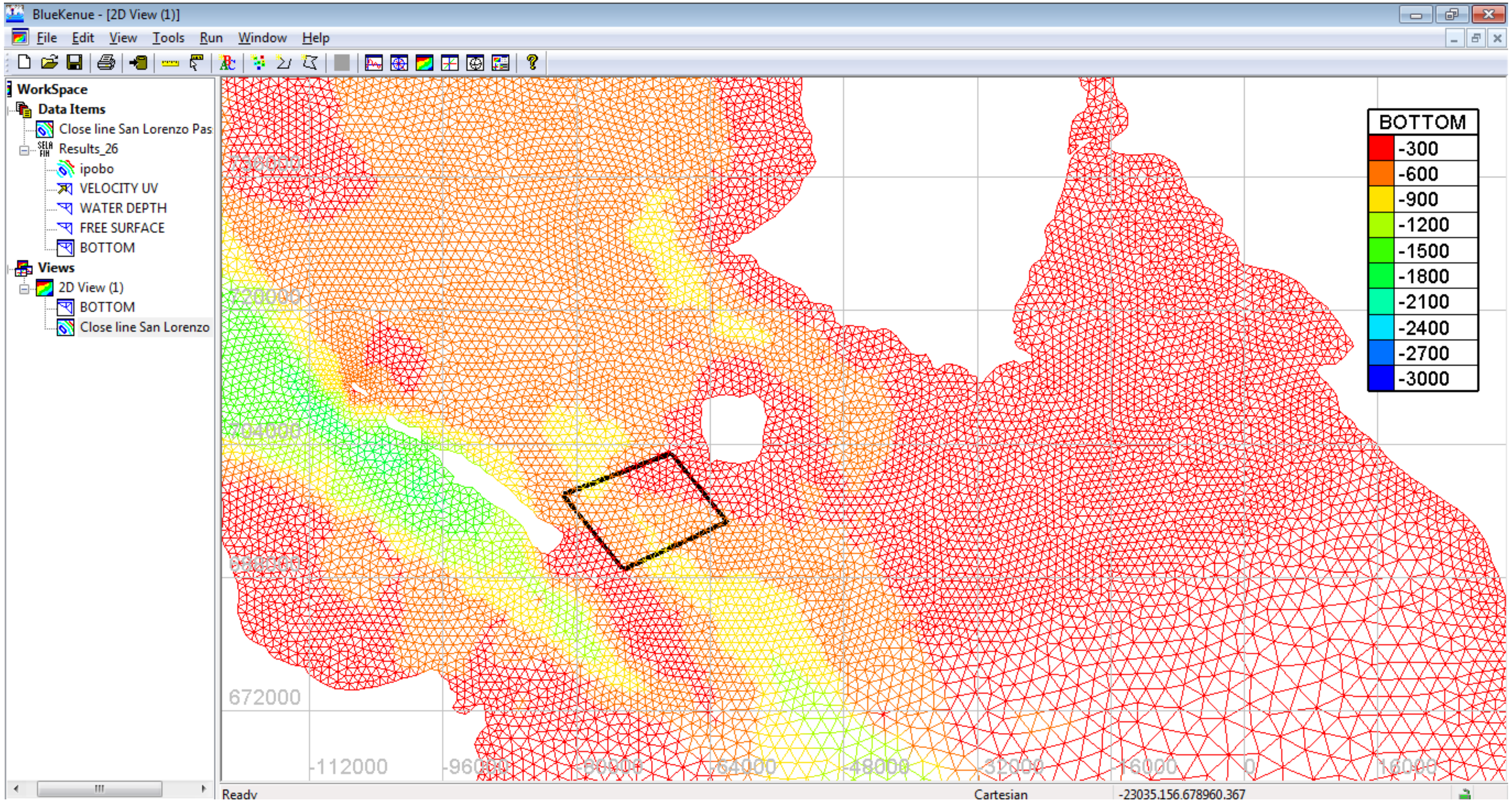

Figure 6.27. Polygon drawn in Blue Kenue within the model mesh to simulate the presence of a turbine array

Chapter 7: Conclusions

The overall aim of this thesis has been to evaluate the theoretical tidal-range and tidal-stream energy resource potentially available in the GC, Mexico. To address this aim, two study objectives were undertaken. The first quantified the present day potential theoretical tidal-range energy resource available in the GC, using tidal predictions from a validated depth-averaged numerical hydrodynamic model. The second objective, which also utilised the model predictions, determined the present day theoretical tidal-stream energy resource available in the Gulf. This chapter first summarises the model configuration and validation, then synthesizes the key findings from the two objectives, highlights novel aspects of the study, and finally draws the conclusions together to provide recommendations for future development of tidal energy extraction schemes in the study area.

To achieve objectives 1 and 2 a depth average barotropic model was configured using the TELEMAC suite of modelling tools, which have previously been used extensively in other studies to assess tidal energy resources in different parts of the world. The model domain was set up to cover the Mexican Pacific coastal region and the whole of the GC, with a resolution of ~1 km in the areas with highest potential for tidal energy extraction. The model was comprehensively validated against water level measurements from 11 tide gauge sites, with a good spatial spread across the region, and current-meter data from four sites in the Midriff area. Visual comparison of the results, along with statistical error calculations, strongly demonstrated the reliability of the model to accurately predict both tidal levels and currents in the study area, making it suitable for the energy resource assessments carried out in objectives 1 and 2. Many hundreds of model runs were undertaken to examine the sensitivity of the model to different settings and inputs, particularly bed roughness and bathymetry. Results of the later, highlighted that using free-access bathymetric data (e.g., GEBCO and ETOPO), was insufficient to accurate reproduce measured conditions, particularly in the middle and upper regions of the Gulf, which have more complex bathymetries and shallower water depths; higher resolution data was therefore included and significantly improved model performance. Sensitivity tests also showed the importance of considering a greater number of tidal constituents within the region, compared to just taking into account the main semi-diurnal (e.g., M_2 and S_2) tidal constituents.

The first objective was to quantify the present day potential theoretical tidal-range energy resource available in the GC, Mexico. Results showed that the potential annual energy yield varies between 20 to 50 kWh/m^2, in the northern reaches of the GC. The most suitable sites for tidal-range energy extraction are located in the northern most region of the GC, in the vicinity of the Gulf of Santa Clara where the tidal-range is largest. Here the theoretical annual yield is between 45 and 50 kWh/m^2. A 0-D modelling approach was used to estimate the energy that can be technically converted at four sites in the northern GC, considered a range of operational strategies and certain tidal-range power plant technical specifications. The site with the highest energy potential is in the Gulf of Santa Clara, which host the highest average tidal-range (4.59 m, approx. 2 m less than the average of Swansea Bay, UK). The results indicate that the annual energy yield ranges from 20 to 50 kWh/m^2 while the maximum values are between 45 and 50 kWh/m^2 in the vicinity of the Gulf of Santa Clara. This site was the best performing in regard to tidal-range energy potential, delivering a technical annual energy output of 125 GWh (ebb-only), 159 GWh (two-way) and 174 GWh (two-way with pumping), assuming an impound area of 10 km^2.

The second objective was to determine the present day theoretical tidal-stream energy resource available in the GC, Mexico. Results showed that there are four main locations in the central Gulf where the tidal current speeds exceeded 1.0 m/s: (1) in San Lorenzo Passage; (2) in the channel between the Baja California Peninsula and San Lorenzo Island; (3) in the Channel between San Esteban and Tiburon Island; and (4) in the northern part of the Ballenas Channel between the Baja California Peninsula and Angel de la Guarda Island. Current speeds are highest (~2.5 m/s) at the first location. The annual mean KPD across these sites was estimated to be 0.1 to 0.65 kW/m^2, which is lower than the 2.5 kW/m^2 threshold, often considered for being economically feasible for tidal energy extraction. However, as the four sites with high tidal current speeds typically exceed 100 m in water depth, the tidal energy resource in this region is potentially large (100 to 200 MW of annual mean power) if devices could utilise the full water depth and cross-sectional area of the channels. Technical power was estimated for four device types, first assuming just an array of devices near the surface, and second an array of devices down through the water depth. The estimated total annual mean technical power varied between 251 and 460 MW, considering just a near surface area, and between 304 and 1030 MW if the full water column was utilised. For the near surface array, the best majority of the energy was generated at just one site (Site A). Therefore, it was found that currently commercially available turbines are not suitable for this region. However, in the future if new turbine technologies (e.g., ‘second generation’) were developed that could extract the energy over these larger water depths, these sites would be economically feasible. Similar to objective 1, it was found that if only freely available bathymetric datasets are used in the model configuration, the available theoretical tidal-stream energy resource is underestimated by 75 % in the central Gulf; highlighting the importance of utilising higher resolution local bathymetric datasets. Additionally, it was found that the variability of the estimated resource can vary by 50%, if only the M_2 consistent is considered; highlighting the importance of considering additional tidal constituents for this region.

An assessment was made of the 3D nature of tidal currents in the central region of the GC, using a previous published 3D HAMSOM model. This analysis showed that current velocities varying considerably with depth, and the vertical profile varies depending on site. Hence, if any of these sites are chosen for tidal-stream extraction a more detailed analysis of the 3D nature of the current speeds needs to be undertaken. A novel analysis assessing was also undertaken to determine whether knowledge of the phase relationship between tidal energy sites be exploited by aggregating the electricity generated by a number of geographically distributed sites, leading to firm power supply to the electricity grid. The results highlight that if one considers tidal-range and tidal stream schemes separately, it is not possible to generate a form power supply through a day from the four tidal-range and four tidal-stream sites identified in Chapters 4 and 5, respectively. This is because the phasing of the tides is similar across the four tidal-range and four tidal-steam sites. However, if one considers tidal-range and tidal-stream sites together, it is possible to generate a more consistent supply, with few periods of zero electricity generation.

This thesis has several novel elements. First, it is the most comprehensive assessment of tidal-range energy resource to date for the GC. Two assessments have been done prior to this thesis (e.g., Hiriart-Le Bert et al., 2009; Tapia et al., 2013), but these were very limited in scope. This thesis undertook a much more sophisticated approach, than had been previously completed, which estimated the theoretical and technical tidal-range energy resource in the upper Gulf, whilst considering different operational strategies and tidal power plant technical specifications. A second novel element is that this study is the first investigation of tidal-stream energy in the GC. Furthermore, it is the first study to consider regions with deeper water (all other studies to date have consider sites with water depths <80 m), and areas were diurnal tidal constituents are typically larger (previous studies have focused on strong semi-diurnal regions). Interestingly, one of the key novel results of this study is that while sites in the central Gulf are not suitable for current tidal-stream energy devices, due to slower current speeds (<2.5 m/s) and deep water (>100 m); the tidal energy resource is potentially large, but new turbine technologies would be required to exploit this resource through the use of ‘second generation’ turbines. Another novel aspect of the study, is that it highlights the importance of including high resolution bathymetric data and a greater number of tidal constituents to estimate the available resource.

In summary, this study has provided an overall first order estimate of the available theoretical and technical tidal-range energy resource and theoretical tidal-stream energy resource in the GC. As discussed in Section 1.1, the Mexico Government has set an ambitious target of generating 35 % of its total energy from renewable sources by 2027 (SENER, 2013). Presently, 19 % of Mexico’s electricity is produced through renewable sources. Tidal energy extraction in the GC would provide a potential source of renewable energy to contribute to this target. Importantly, this thesis has provided a basis for the Mexican Government and policy makers to guide selection of suitable sites for energy extraction in the region, and provides a foundation for more detailed assessment.

References

Abedini, A. & Nikkahajoei, H. (2011). Dynamic model and control of a wind-turbine generator with energy storage. IET Renewable Power Generation, 5, 67-78.

Abolghasemi, M. A., Piggott, M. D., Spinneken, J., Virí, A., Cotter, C. J. & Crammond, S. (2016). Simulating tidal turbines with multi-scale mesh optimisation techniques. Journal of Fluids and Structures, 66, 69-90.

Adcock, T. A. A., Draper, S., Houlsby, G. T., Borthwick, A. G. L. & Serhadlıoğluet, S. (2013). The available power from tidal stream turbines in the Pentland Firth. Proceedings of the Royal Society A: Mathematical, Physical and Engineering Science, 469.

Adcock, T. A. A., Draper, S., Houlsby, G. T., Borthwick, A. G. L. & Serhadlıoğluet, S. (2014). Tidal stream power in the Pentland Firth – long-term variability, multiple constituents and capacity factor. Proceedings of the Institution of Mechanical Engineers, Part A: Journal of Power and Energy, 228, 854-861.

Adcock, T. A., Draper, S. & Nishino, T. (2015). Tidal power generation – A review of hydrodynamic modelling. Proceedings of the Institution of Mechanical Engineers, Part A: Journal of Power and Energy, 229, 755-771.

Aggidis G. A, (2010). Tidal-range fluid machinery technology and opportunities, in Ocean Power Fluid Machinery. London; 2010.

Aggidis, G. A. & Benzon, D. S., (2013). Operational optimization of a tidal barrage across the Mersey estuary using 0-D modelling. Ocean Engineering, 66, 69-81.

Aggidis, G. A. & Feather, O., (2012). Tidal-range turbines and generation on the Solway Firth. Renewable Energy, 43, 9-17.

Ahmadian, R. & Falconer, R. A. (2012). Assessment of array shape of tidal stream turbines on hydro-environmental impacts and power output. Renewable Energy, 44, 318-327.

Ahmadian, R., Falconer, R. & Bockelmann-Evans, B., (2012). Far-field modelling of the hydro-environmental impact of tidal stream turbines. Renewable Energy, 38, 107-116.

Aisiks, E. G. (1993). Tidal power in Argentina. IEEE Power Eng. Rev., 13 (3)

Aisiks, E. G. and Zyngierman, I., (1984). The San Jose Gulf tidal power plant, Argentina: Proc. ECOR 84 and 1st Alt. En. Argent. Conf. II, 1-9.

Alcérreca-Huerta, J.C., Encarnacion, J.I., Ordoñez-Sánchez, S., Callejas-Jiménez, M., Gallegos Diez Barroso, G., Allmark, M., Mariño-Tapia, I., Silva Casarín, R., O'Doherty, T., Johnstone, C., Carrillo, L., (2019). Energy Yield Assessment from Ocean Currents in the Insular Shelf of Cozumel Island. Journal of Marine Science and Engineering 7, 147.

Alemán-Nava, G. S., Casiano-Flores, V. H., Cárdenas-Chávez, D. L., Díaz-Chavez, R., Scarlat, N., Mahlknecht, J., Dallemand, J.-F. & Parra, R. (2014). Renewable energy research progress in Mexico: A review. Renewable and Sustainable Energy Reviews, 32, 140-153.

Alonso, R., Jackson, M., Santoro, P., Fossati, M., Solaris, S. & Teixeira, L. (2017). Wave and tidal energy resource assessment in Uruguayan shelf seas. Renewable Energy.

Alvarez-Borrego, S., and J.R. Lara-Lara (1991). The physical environment and primary productivity of the Gulf of California. In The Gulf and Peninsular Province of the Californias, Mem. Am. Assoc. Pet. Geol., 47, 555-567.

Andre. H., (1976). Power plant and other French hydro-powered sites, IEEE Trans Power Appar Syst, PAS-95 (4), pp. 1038-1044.

Angeloudis, A., Ahmadian, R., Falconer, R. A. & Bockelmann-Evans, B. (2016b). Numerical model simulations for optimisation of tidal lagoon schemes. Applied Energy, 165, 522-536.

Angeloudis, A., Falconer, R. A., Bray, S. & Ahmadian, R. (2016a). Representation and operation of tidal energy impoundments in a coastal hydrodynamic model. Renewable Energy, 99, 1103-1115.

Angeloudis, A., Falconer, R.A., (2017). Sensitivity of tidal lagoon and barrage hydrodynamic impacts and energy outputs to operational characteristics. Renew. Energy 114, 337–351.

Annapolis Valley Vacation, Annapolis Tidal Power Plant [online]. Available: ⟨http://www.annapolis-valley-vacation.com/tidal-power-plant.html⟩;[accessed 25.09.17].

Arcement, G. J. & Schneider, V. R. 1989. Guide for selecting Manning's roughness coefficients for natural channels and flood plains. Water Supply Paper. - ed.

Argote, M. L., Amador, A., Lavin, M. F. & Hunter, J. R. (1995). Tidal dissipation and stratification in the Gulf of California. Journal of Geophysical Research: Oceans, 100, 16103-16118.

Atkins, W.S., (2004). Tidal Electric Limited Feasibility Study for a Tidal Lagoon in Swansea Bay. [Online]. Available: ⟨http://tidalelectric.com/resources-feasibility.shtml⟩.

Aurioles-Gamboa D, Zavala-Gonzalez A. (1994). Ecological factors that determine the distribution and Abundance of the California Sea Lion Zalophus californianus, in the Gulf of California. Ciencias Marinas. 20(4):535–53.

Backhaus, J.O., (1985). A three-dimensional model for simulation of shelf sea dynamics. Deutsche Hydrographische Zeitschirft 38 (H.4), 164–187.

Badan-Dangon, A., M. C. Hendershott, and M. F. Lavın (1991), Underway Doppler current profiles in the Gulf of California, Eos Trans. AGU, 72(209), 217 – 218.

Bae, Y. H., Kim, K. O. & Choi, B. H. (2010). Lake Sihwa tidal power plant project. Ocean Engineering, 37, 454-463.

Bahaj A. S. (2013). Marine current energy conversion: the dawn of a new era in electricity production. Philosophical Transactions of the Royal Society A: Mathematical, Physical and Engineering Sciences, 371.

Bahaj, A. S. & Myers, L. (2004). Analytical estimates of the energy yield potential from the Alderney Race (Channel Islands) using marine current energy converters. Renewable Energy, 29, 1931-1945.

Bahaj, A. S. (2011). Generating electricity from the oceans. Renewable and Sustainable Energy Reviews, 15, 3399-3416.

Bahaj, A. S., Molland, A. F., Chaplin, J. R. & Batten, W. M. J. (2007). Power and thrust measurements of marine current turbines under various hydrodynamic flow conditions in a cavitation tunnel and a towing tank. Renewable Energy, 32, 407-426.

Bai, L., Spence, R. R. G. & Dudziak, G. (2009) "Investigation of the Influence of Array Arrangement and Spacing on Tidal Energy Converter (TEC) Performance using a 3-

Dimensional CFD Model", 8th European wave and tidal energy conference, Uppsala, Sweden, 7 - 10 September, Glasgow: Sgurrenergy, 654 - 660.

Baker, A. C. (1991). Tidal power, United Kingdom, Peter Peregrinus Ltd.

Baker, C. (2006). Tidal Lagoon Power Generation Scheme in Swansea Bay. HM Government, London.

Batten W.M.J., Bahaj A.S., Molland A.F., Chaplin J.R. (2008). The prediction of the hydrodynamic performance of marine current turbines. Renew. Energy 33, 1085–1096.

Batten, W. M. J., Harrison, M. E. & Bahaj, A. S. (2013). Accuracy of the actuator disc-RANS approach for predicting the performance and wake of tidal turbines. Philosophical Transactions of the Royal Society A: Mathematical, Physical and Engineering Sciences, 371.

Baumgartner T. R. and N. Christensen (1985), Coupling of the Gulf of California to large-scale interannual climatic variability. J. Mar. Res., 43, 825-848.

Bay of Fundy Tidal Power review Board. (1977). Reassessment of Fundy tidal power: reports of the Bay of Fundy Tidal Power Review Board and Management Committee, November 1977, [Ottawa], Minister of Supply and Services Canada.

Beer Ferdinand P. Johnston Jr. E. Russell Mazurek David F. Cornwell Phillip J. Vector Mechanics for Engineers: Statics and Dynamics, Twelft Edition, 2018.

Beier, E. (1997). A Numerical Investigation of the Annual Variability in the Gulf of California. Journal of Physical Oceanography - J PHYS OCEANOGR. 27. 615-632.

Betz, A. Introduction to the theory of flow machines 1966 (Pergamon Press, Oxford)

Binnie & Partners (1989) The UK potential for tidal energy from small estuaries. Energy Technology Support Unit, Harwell.

Bishop, R., Tides and the Earth-Moon System, Observer's Handbook 2008, (2007), p. 173.

Black & Veatch, (2005b). Phase II UK Tidal Stream Energy Resource Assessment. London: The Carbon Trust.

Black and Veatch Consulting Ltd. UK, Europe and global tidal stream energy resource assessment. Peer review issue 107799/D/2100/05/1, Carbon Trust, London, September 2004.

Black and Veatch. (2005) Phase II. UK tidal stream energy resource assessment. Technical Report 107799/D/2200/03, to Carbon Trust. See http://www.carbontrust.com/media/174041/phaseiitidalstreamresourcereport2005.pdf.

Blackmore T., Batten W. M. J., & Bahaj A. S. (2013). Turbulence generation and its effect in LES approximations of tidal turbines. In proceedings of 10th European Wave and Tidal Energy Conference. Aalborg, Denmark.

Blackmore T., Batten W. M. J., Harrison M. E., & Bahaj A. S. (2011). The Sensitivity of Actuator-Disc RANS Simulations to Turbulence Length Scale Assumptions. In proceedings of 9th European Wave and Tidal Energy Conference. Southampton, UK.

Blackmore T., Batten W. M. J., Muller G.U., & Bahaj A. S. (2014a). Influence of turbulence on the drag of solid discs and turbine simulators in a water current. Experiments in Fluids, 55(1), 1367.

Blackmore, T., Batten, W. M. J. & Bahaj, A. S. (2014b). Influence of turbulence on the wake of a marine current turbine simulator. Proceedings. Mathematical, physical, and engineering sciences, 470, 20140331-20140331.

Blanchfield, J., Garrett, C., Rowe, A. & Wild, P. (2008). Tidal stream power resource assessment for Masset Sound, Haida Gwaii. Proceedings of the Institution of Mechanical Engineers, Part A: Journal of Power and Energy, 222, 485-492.

Blunden, L. S. & Bahaj, A. S. (2006). Initial evaluation of tidal stream energy resources at Portland Bill, UK. Renewable Energy, 31, 121-132.

Blunden, L. S., Bahaj, A. S. & Aziz, N. S. (2013). Tidal current power for Indonesia? An initial resource estimation for the Alas Strait. Renewable Energy, 49, 137-142."Tidal current power for Indonesia? An initial resource estimation for the Alas Strait." Renewable Energy 49: 137-142.

Bourban, S., Liddiard, M., Durand, N., Cheeseman S., and A. Baldock, “High Resolution Modelling Of Tidal Resources, Extraction And Interactions Around The UK,” in 1st Marine Energy Technology Symposium (METS13), 2013, p. 8.

Bray, N. A. 1988a. Thermohaline circulation in the Gulf of California, J. Geophysics. Res., 93, 4993-5020.

Bray, N. A. and J.M. Robles (1991). Physical Oceanography of the Gulf of California. In The Gulf and Peninsular Province of the Californias, Mem. Am. Assoc. Pet. Geol., 47, 511-553.

Bray, S., Ahmadian, R. & Falconer, R. A. (2016). Impact of representation of hydraulic structures in modelling a Severn barrage. Computers & Geosciences, 89, 96-106.

Brusca C. R. (1980). Common intertidal invertebrates of the Gulf of California, 2nd (revised) ed. Tucson, AZ: University of Arizona Press; 520pp.

Bryden, I. G. & Couch, S. J. (2006) "ME1--marine energy extraction: tidal resource analysis", Renewable Energy, 31(2)**,** 133-139.

Bryden, I. G., Grinsted, T. & Melville, G. T. (2004) "Assessing the potential of a simple tidal channel to deliver useful energy", Applied Ocean Research, 26(5)**,** 198-204.

Bryden, I., J Couch, S., Owen, A. & Melville, G. (2007). Tidal current resource assessment.

Buckland H, Dolerud E, Baker T. 2015. Application of Standard Tidal Performance Specification and Performance Review to a Non-Standard Tidal Energy Converter. European Wave and Tidal Energy Conference (EWTEC), Sept 2015. Nantes, France.

Burrows, R., Walkington, I. A., Yates, N. C., Hedges, T. S., Wolf, J. & Holt, J. (2009b). The tidal-range energy potential of the West Coast of the United Kingdom. Applied Ocean Research, 31, 229-238.

Burrows, R., Walkington, I., Yates, N., Hedges, T., Chen, D., LI, M., Zhou, J., Wolf, J., Proctor, R., Holt, J. & Prandle, D. (2009c). Tapping the Tidal Power Potential of the Eastern Irish Sea.

Burrows, R., Yates, N. C., Hedges, T. S., Li, M., Zhou, J. G., Chen, D. Y., Walkington, I. A., Wolf, J., Holt, J. & Proctor, R. (2009a). Tidal energy potential in UK waters. Proceedings of the Institution of Civil Engineers - Maritime Engineering, 162, 155-164.

Burton, A., Sharpe, D., Jenkins, N., and Bossanyi, E. Wind energy handbook, (2001) (John Wiley & Sons, Chichester).

Bustos-Serrano, H. & Castro-Valdez, R. (2006). Flux of nutrients in the Gulf of California: Geostrophic approach. Marine Chemistry, 99, 210-219.

Calero Quesada, M. C., García Lafuente, J., Sánchez Garrido, J. C., Sammartino, S. & Delgado, J. (2014). Energy of marine currents in the Strait of Gibraltar and its potential as a renewable energy resource. Renewable and Sustainable Energy Reviews, 34, 98-109.

Campbell, R., Martinex, A., Letetrel, C. & Rio, A. (2017). Methodology for estimating the French tidal current energy resource. International Journal of Marine Energy, 19, 256-271.

Campos E., Alma Rosa de Campos & Jesus Angel de León-González. (2009). "Diversity and ecological remarks of ectocommensals and ectoparasites (Annelida, Crustaceans, Mollusca) of echinoids (Echinoidea: Mellitidae) in the Sea of Cortez, Mexico". Parasitology Research 105 (2): 479–487

Carballo, R., Iglesias, G. & Castro, A. (2009). Numerical model evaluation of tidal stream energy resources in the Ría de Muros (NW Spain). Renewable Energy, 34, 1517-1524.

Cardiff University Project 2019. Design Feasibility Study for a Low Velocity Tidal Stream Turbine. Available at https://gtr.ukri.org/projects?ref=EP%2FR000875%2F1. Access [19/09/2019]

Carpman, N. & Thomas, K. (2016). Tidal resource characterization in the Folda Fjord, Norway. International Journal of Marine Energy, 13, 27-44.

Carrère, L., F. Lyard, M. Cancet, A. Guillot, and L. Roblou (2012), FES 2012: A new global tidal model taking advantage of nearly 20 years of altimetry, paper presented at The Symposium 20 Years of Progress in Radar Altimetry, Venice.

Cartwright, D. E., Tayler, R.J. (1971), New Computations of the Tide-generating Potential, Geophysical Journal of the Royal Astronomical Society, 23(1), 45-73.

Cartwright, N (1999), The Dappled World: A Study of the Boundaries of Science, Cambridge University Press, Cambridge.

Castro R., M. F. Lavın and P. Ripa (1994). Seasonal heat balance in the Gulf of California, J. Geophys. Res., 99, 3249-3261.

CEE (2013). Bureau of Economic Geology, Jackson School of Geosciences, the University of Texas at Austin. Avalable at http://www.jsg.utexas.edu/lacp/files/2013-e1.pdf

Chapman, R., (1938). Tides of Australia. In: Year Book Australia, 1938, Australian Bureau of Statistics Catalogue Number 1301.0. ABS, Canberra.

Charlier, R. H. (2007). Forty candles for the Rance River TPP tides provide renewable and sustainable power generation. Renewable and Sustainable Energy Reviews, 11, 2032-2057.

Chen, W.-B., Liu, W.-C. & Hsu, M.-H. (2013). Modelling assessment of tidal current energy at Kinmen Island, Taiwan. Renewable Energy, 50, 1073-1082.

Chong, H.-Y. & Lam, W.-H. 2013. Ocean renewable energy in Malaysia: The potential of the Straits of Malacca. Renewable and Sustainable Energy Reviews, 23, 169-178.

Cisneros-Montemayor, A. & Vincent, A. (2016). Science, society, and flagship species: social and political history as keys to conservation outcomes in the Gulf of California. Ecology and Society, 21.

Clarke, A. J. & Battisti, D. S. (1981). The effect of continental shelves on tides. Deep Sea Research Part A. Oceanographic Research Papers, 28, 665-682.

Coles, D. S., Blunden, L. S. & Bahaj, A. S. (2017). Assessment of the energy extraction potential at tidal sites around the Channel Islands. Energy, 124, 171-186.

CONANP (Comisión Nacional de Áreas Naturales Protegidas). 2007. Programa de conservación y manejo Reserva de la Biosfera Alto Golfo de California y Delta del Río Colorado, México. Secretaría de Medio Ambiente y Recursos Naturales, CONANP, Mexico City, Mexico. [online] URL: http://www.conanp.gob.mx/

Cornett A, Noemie Durand, Martin Serrer (2010). 3-D Modelling and Assessment of Tidal Current Resources in the Bay of Fundy, Canada 3rd International Conference on Ocean Energy, 6 October, Bilbao

Cornett A. (2006), Inventory of Canada's Marine renewable energy resources. Canadian Hydraulics centre. CHC-TR-041. April 2006

Cornett, A., Cousineau, J. & Nistor, I. (2011). Hydrodynamic Impacts due to Tidal Power Lagoons in the Upper Bay of Fundy, Canada.

Cornett, A., Cousineau, J. & Nistor, I. (2013). Assessment of hydrodynamic impacts from tidal power lagoons in the Bay of Fundy. International Journal of Marine Energy, 1, 33-54.

De Dominicis, M., O'Hara Murray, R. & Wolf, J. 2017. Multi-scale ocean response to a large tidal stream turbine array. Renewable Energy, 114, 1160-1179.

De Dominicis, M., Wolf, J. & O'Hara Murray, R. 2018. Comparative Effects of Climate Change and Tidal Stream Energy Extraction in a Shelf Sea. Journal of Geophysical Research: Oceans, 123, 5041-5067.

DECC, Review of Tidal Lagoons, Department of Energy and Climate Change, 2010b. https://www.gov.uk/government/publications/1-severn-tidal-power-feasibility-study-conclusions-and-summary-report.

DECC. Severn power tidal power feasibility study conclusions and summary report; 2010a.

Defne, Z., Haas, K. A. & Fritz, H. M. (2011). Numerical modeling of tidal currents and the effects of power extraction on estuarine hydrodynamics along the Georgia coast, USA. Renewable Energy, 36**,** 3461-3471.

Delta Marine Consultants (2007). Tidal Power Plant: Bay of Fundy, Technical Feasibility Study. 2007.

Department of Energy (DoEn). Central Electricity Generating Board, Severn Tidal Power Group. Severn barrage project: detailed report. Harwell, UK: Energy Technology Support Unit; 1989. Report No. TID 4060.

Department of Energy (DoEn). The potential for tidal energy from small Estuaries. ETSU TID 4048-P1; 1989.

Department of Energy (DoEn). The potential for tidal energy from small Estuaries. ETSU TID 4048-P1; 1989.

Doodson, A.T. (1921). The Harmonic Development of the Tide-Generating Potential, Proceedings of the Royal Society of London. Series A, 100(704), 305-329

Draper, S., Adcock, T. A. A., Borthwick, A. G. L. & Houlsby, G. T. (2014). Estimate of the tidal stream power resource of the Pentland Firth. Renewable Energy, 63**,** 650-657.

Easton, M. C., Woolf, D. K. & Bowyer, P. A. (2012). The dynamics of an energetic tidal channel, the Pentland Firth, Scotland. Continental Shelf Research, 48, 50-60.

Egbert, G. D. and S. Y. Erofeeva (2002). "Efficient Inverse Modeling of Barotropic Ocean Tides." Journal of Atmospheric and Oceanic Technology 19(2): 183-204.

Egbert, G. D., A. F. Bennet, and M. G. G. Foreman (1994), Topex/Poseidon tides estimated using a global inverse model, Journal of Geophysical Research, 99, 24,821 24,852.

Egbert, G. D., B. G. Bills, and R. D. Ray (2004), Numerical modelling of the global semidiurnal tide in the present day and in the last glacial maximum, Journal of Geophysical Research, 109, C03,003.

El Tawil, T., Charpentier, J. F. & Benbouzid, M. (2017). Tidal energy site characterization for marine turbine optimal installation: Case of the Ouessant Island in France. International Journal of Marine Energy, 18, 57-64.

Electric power research Institute (EPRI) (2006). North America Tidal in-stream energy conversion technology feasibility study. Roger Bedard, Ocean energy leader. Award Number: DE-EE0002661.

ETSU. Tidal stream energy review. Technical report ETSU-T-05/00155/REP, Harwell Laboratory, EnergyTechnology Support Unit, DTI, 1993.

European Commission (1996). The exploitation of tidal and marine currents. Wave energy. Project results. Technical report EUR 16683 EN, Commission of the European Communities. Directorate-General for Science Research and Development.

Fairley, I., Ahmadian, R., Falconer, R. A., Willis, M. R. & Masters, I. (2014). The effects of a Severn Barrage on wave conditions in the Bristol Channel. Renewable Energy, 68, 428-442.

Fairley, I., Masters, I. & Karunarathna, H. (2015). The cumulative impact of tidal stream turbine arrays on sediment transport in the Pentland Firth. Renewable Energy, 80, 755-769.

Falconer, R., Xia, J., Lin, B. & Ahmadian, R. (2009). The Severn Barrage and other tidal energy options: Hydrodynamic and power output modelling.

Fallon, D., Hartnett, M., Olbert, A. & Nash, S. (2014). The effects of array configuration on the hydro-environmental impacts of tidal turbines. Renewable Energy, 64, 10-25.

Ferreira, R. M. & Estefen, S. F. (2009). Alternative concept for tidal power plant with reservoir restrictions. Renewable Energy, 34, 1151-1157.

Filloux, J.H. (1973). Tidal patterns and energy balance in the Gulf of California. Nature, 217-221.

Filonov, A. E. & Lavin, M. F. (2003). Internal tides in the Northern Gulf of California. Journal of Geophysical Research: Oceans, 108.

Findley LT, Torre JM, Nava A, van der Heiden M, Hastings PA., (1996). Preliminary ictiofauna analysis from a macro faunal database of the Gulf of California, Mexico. Abstracts of 76th the American society of lchtiologists and herpetologists, New Orleans, USA.

Fok, H. S. (2012), Ocean tides modeling using satellite altimetry, Geodetic Science Rep. No. 501, Ohio State Univ., Columbus.

Fong, S. and Heaps, N. S. (1978). “Note on quarter-wave tidal resonance in the Bristol Channel”.

Foreman, M.G.G (1977). Manual for tidal heights analysis and prediction. Pacific Marine Science Report No. 77-10, Institute of Ocean Sciences, Patricia Bay, Sidney, B.C., 66pp. http://www.omg.unb.ca/GGE/5013_LABS/heights.pdf.

Fraenkel, P. L. and Musgrove, P. J., (1979). Tidal and river current energy systems. International Conference on Future energy concepts, London, 30 January–1 February 1979, pp. 114–117 (IEE, London).

Fraenkel, P., (1999). Tidal currents: a major new source of energy for the millennium. London: ICG Publishing Ltd.

Fraenkel, P., (2006). Tidal Marine current turbines: Pioneering the development of marine kinetic energy converters. Proceedings of the Institution of Mechanical Engineers Part A Journal of Power and Energy (P I MECH ENG A-J POW).

Friends of the Earth Cymru (2004). Briefing-A Severn Barrage or tidal lagoons?

Funke, S. W., Kramer, S. C., & Piggott, M. D. (2016). Design optimisation and resource assessment for tidal-stream renewable energy farms using a new continuous turbine approach. Renewable Energy, 99, 1046-1061.

Gao, C. & Adcock, T. A. A. (2016). Numerical Investigation of Resonance in the Bristol Channel. The 26th International Ocean and Polar Engineering Conference. Rhodes, Greece: International Society of Offshore and Polar Engineers.

Gao, P., Zheng, J., Zhang, J. & Zhang, T. (2015). Potential Assessment of Tidal Stream Energy Around Hulu Island, China. Procedia Engineering, 116, 871-879.

Garrett, C. & Cummins, P. (2004). Generating Power from Tidal Currents. Journal of Waterway, Port, Coastal, and Ocean Engineering, 130, 114-118.

Garrett, C. & Cummins, P. (2005). The power potential of tidal currents in channels. Proceedings of the Royal Society A: Mathematical, Physical and Engineering Science, 461, 2563-2572.

Garrett, C. (1972). Tidal Resonance in the Bay of Fundy and Gulf of Maine. Nature, 238, 441.

Garrett, C., & P. Cummins (2008). Limits to tidal current power. Renewable Energy, 33, pp. 2485-2490.

Genco, M. L., Lyard, F. & Provost, C. L. (1994). The oceanic tides in the South Atlantic Ocean. Annales Geophysicae, 12, 868-886.

Georgia Tech Research Corporation, (2011). Assessment of Energy Production Potential from Tidal Streams in the United States. Final Project Report June 29, 2011. Award Number: DE-FG36-08GO18174

Georgia Tech Research Corporation, (2013). Assessment of Energy Production Potential from Ocean Currents along the United States Coastline. Final Project Report September 15, 2013. Award Number: DE-EE0002661.

Getches D.H. (2003) Impacts in Mexico of Colorado River Management in the United States. In: Diaz H.F., Morehouse B.J. (eds) Climate and Water. Advances in Global Change Research, vol 16. Springer, Dordrecht

Glorioso, P. D. & Flather, R. A. (1997). The Patagonian Shelf tides. Progress in Oceanography, 40, 263-283.

Godin, G. (1988). The resonant period of the Bay of Fundy. Continental Shelf Research, 8, 1005-1010.

Godin, G. (1993). On tidal resonance. Continental Shelf Research, 13, 89-107.

Godwin, G., (1972). The Analysis of Tides, Univ. of Toronto Press, Toronto, Canada.

González-Caballíin, J. M., Alvarez, E., Gutierréz-Trashorras, A. J., Navarro-Manso, A., Fernández, J. & Blanco, E. (2016). Tidal current energy potential assessment by a two dimensional computational fluid dynamics model: The case of Avilés port (Spain). Energy Conversion and Management, 119, 239-245.

González-Gorbeña, E., Rosman, P. C. C. & Qassim, R. Y. (2015). Assessment of the tidal current energy resource in São Marcos Bay, Brazil. Journal of Ocean Engineering and Marine Energy, 1, 421-433.

Goward Brown, A. J., Neill, S. P. & Lewis, M. J. (2017). Tidal energy extraction in three-dimensional ocean models. Renewable Energy.

Greenberg, D. A. (1979). A numerical model investigation of tidal phenomena in the Bay of Fundy and Gulf of Maine. Marine Geodesy, 2, 161-187.

Griffiths, S. D., and W. R. Peltier (2009), Modelling of polar ocean tides at the Last Glacial Maximum: amplification, sensitivity, and climatological implications, Journal of Climate, 22, 2905_2924.

Guillou, N., Neill, S. P. & Robins, P. E. (2018). Characterising the tidal stream power resource around France using a high-resolution harmonic database. Renewable Energy, 123, 706-718.

Hagerman, G., B. Polagye, R. Bedard, and M. Previsic (2006). Methodology for Estimating Tidal Current Energy Resources and Power Production by Tidal In-Stream Energy Conversion (TISEC) Devices. Electric Power Research Institute, Palo Alto, CA, USA.

Haigh, I.D. (2017). Tides and Water Levels. Encyclopaedia of Maritime and Offshore Engineering.1–13. http://onlinelibrary.wiley.com/doi/10.1002/9781118476406.emoe122/abstract

Haigh, I.D., Eliot, M., and Pattiaratchi, C. (2011) Modeling global influences of the 18.6-year nodal cycle and quasi-4.4 year cycle on high tidal levels. Journal of Geophysical Research—Oceans, 116, C06025.

Hallberg, R. W., & P. B. Rhines (1996), Buoyancy-driven circulation in an ocean basin with isopycnals intersecting the sloping boundary, Journal of Physical Oceanography, 26, 913_940.

Hammons T. J. Tidal power. Proc IEEE 1993; 3(7):421–32.

Hansson H. G., Development of the Kaplan turbine [online]. Available: ⟨⟨http:// www.actuationtestequipment.com/Reference_Materials/1977_Hannson_Kaplan_Development.pdf⟩⟩; [accessed 07.03.18].

Harrison M. E. (2011). The accuracy of the actuator disc-RANS model for predicting the performance and far wake of a horizontal axis tidal stream turbine. PhD dissertation, Faculty of Engineering and the Environment, University of Southampton, UK.

Harrison M. E., Batten W. M. J, Blunden LS, Myers LE, Bahaj AS. (2008). Comparisons of a large tidal turbine array using the boundary layer and field wake interaction models. In Proc. 2nd Int. Conf. on Ocean Energy (ICOE 2008), Brest, France, October 2008.

Harrison M. E., Batten W. M. J, Myers LE, Bahaj AS. (2009). A comparison between CFD simulations and experiments for predicting the far wake of horizontal axis tidal turbines. In Proc. 8th European Wave and Tidal Energy Conf., Uppsala, Sweden, September 2009

Hashemi Aslani, Z., Niksokhan, M. H. & Montazeri Namin, M. (2017). Assessment of the Potential of Harnessing Tidal Energy in the Khowr-e Musa Estuary in the Persian Gulf. Environmental Energy and Economic Research, 1, 15-22.

Hastie, G. D., Russell, D. J. F., Lepper, P., Elliott, J., Wilson, B., Benjamins, S. & Thompson, D. 2018. Harbour seals avoid tidal turbine noise: Implications for collision risk. Journal of Applied Ecology, 55, 684-693.

Hazim, S., Ouatouati, A. E., Janan, M. T. & Ghennioui, A. (2019). Marine Currents Energy Resource Characterization for Morocco. Energy Procedia, 157, 1037-1049.

Hendry, C. (2017). The Role of Tidal Lagoons - Final Report, 2017.

Herrera, R., Vásquez, J., Cienfuegos, R., Olivares, M., (2010). Análisis de Factibilidad Técnico-Económico del Recurso Energético Asociado a las Corrientes de Marea en el Canal del Chacao.

Hiriart-Le Bert G. and Silva-Casarin R., Tidal Power plan energy estimation. Engineering Institute, Autonomous National University of Mexico. Mexico. 11 (2) 233-245, 2009

HM Government, (2010). Department of energy and climate change, “Severn Tidal Power – Supply chain Survey Report,”.

Holbrook, J. R., J. R. Apel, and J. J. Tsai, (1980). The Sulu Sea internal soliton experiment, 2 ,Observations of large-amplitude nonlinear waves (abstract), Eos Trans. AGU, 61, 1009, 1980.

Hooper, T. & Austen, M. 2013. Tidal barrages in the UK: Ecological and social impacts, potential mitigation, and tools to support barrage planning. Renewable and Sustainable Energy Reviews, 23, 289-298.

Houlsby G., Draper S., Oldfield M. (2008) Application of linear momentum actuator disc theory to open channel flow. Technical report 2296-08, Oxford University Engineering Laboratory, UK.

House of Commons, (2013). Energy and climate change committee, “A Severn Barrage?”. Second Report of Session 2013–14 Volume II. Published on 10 June 2013. London.

Howard, D. C., Aggidis, G.; Smith, V.; Robinson, D.; Catterson, N. (2007). Tidal power from the Solway Firth; barriers, impacts and capacity. In: BHA Annual Conference Proceedings - "Delivering the Next Generation", Birnam, Perthshire, 10 - 11 October 2007.

Inger, R., Attrill, M. J., Bearhop, S., Broderick, A. C., James Grecian, W., Hodgson, D. J., Mills, C., Sheehan, E., Votier, S. C., Witt, M. J. & Godley, B. J. 2009. Marine renewable energy: potential benefits to biodiversity? An urgent call for research. Journal of Applied Ecology, 46, 1145-1153.

International Energy Agency, Key world energy statistics, (2016).World energy council 2010. 2010 survey of energy resources. [online]. Available: https://www.worldenergy.org/wp-content/uploads/2012/09/ser_2010_report_1.pdf. [Accessed 02.03.18].

IPCC, (2014). Climate Change 2014: Synthesis Report. Contribution of Working Groups I, II and III to the Fifth Assessment Report of the Intergovernmental Panel on Climate Change [Core Writing Team, R.K. Pachauri and L.A. Meyer (eds.)]. IPCC, Geneva, Switzerland, 151 pp.

Iyer, A. S., Couch, S. J., Harrison, G. P. & Wallace, A. R. (2013). Variability and phasing of tidal current energy around the United Kingdom. Renewable Energy, 51, 343-357.

Jean-Michel Hervouet, “Hydrodynamics of Free Surface Flows: Modelling with the Finite Element Method”, Wiley Blackwell, April 2007, 360p, ISBN-13: 978-0470035580.

Jia-Shiuan, T. & Chen, F. (2014). The Conceptual Design of a Tidal Power Plant in Taiwan.

Jimenez Lopez, M. E., Palacios, D. M., Jaramillo Legorreta, A., Urban R, J. & Mate, B. R. 2019. Fin whale movements in the Gulf of California, Mexico, from satellite telemetry. PLOS ONE, 14, e0209324.

Kapoor, D.C., (1981). General bathymetric chart of the oceans (GEBCO). Marine Geodesy, 5(1), pp.73–80.

Karsten, R. H., Mcmillan, J. M., Lickeley, M. J. & Haynes, R. D. (2008). Assessment of tidal current energy in the Minas Passage, Bay of Fundy. Proceedings of the Institution of Mechanical Engineers, Part A: Journal of Power and Energy, 222, 493-507.

Karsten, R., Swan, A. & Culina, J. (2013). Assessment of arrays of in-stream tidal turbines in the Bay of Fundy. Philosophical Transactions of the Royal Society A: Mathematical, Physical and Engineering Sciences, 371.

Knauss. J. A. and Garfield N. (1979) Introduction to physical oceanography. Waveland press inc. Third Edition.

Laboratorio de nivel del mar CICESE [online] Estaciones Mareográficas y Meteorológicas Costeras. Available from: http://redmar.cicese.mx/.[Accessed July 2016].

Lavın M. F. and S. Organista. (1988), Surface heat flux in the northern Gulf of California. J. Geophysics. Res., 93, 14033-14038.

Lavin M.F. and S.G. Marinone. (2003), an overview of the Physical Oceanography of the Gulf of California, Department of Physical Oceanography, CICESE, Ensenada Baja California, Mexico.

Leite Neto, P. B., Saavedra, O. R. & Souza Ribero, L. A. (2015). Optimization of electricity generation of a tidal power plant with reservoir constraints. Renewable Energy, 81, 11-20.

Lepper, P. A. & Robinson, S. P. Measurement of Underwater Operational Noise Emitted by Wave and Tidal Stream Energy Devices. 2016 New York, NY. Springer New York, 615-622.

Lewis Matt Lewis, Goward-Brown, Alice Goward-Brown, Ridgill Mike, and Neill Simon (2019). Global resource-led optimisation of tidal-stream energy power curve. EGU conference 2019

Lewis, M. J., Angeloudis, A., Robins, P. E., Evans, P. S. & Neill, S. P. (2017). Influence of storm surge on tidal-range energy. Energy, 122, 25-36.

Lewis, M., Neill, S. P., Robins, P. E. & Hachemi, M. R. (2015). Resource assessment for future generations of tidal-stream energy arrays. Energy, 83, 403-415.

Liang, D, Xia, J, Falconer, RA, and Zhang, J (2014). “Study on tidal resonance in Severn Estuary and Bristol Channel, ”Coastal Engineering Journal, 56(01),1450002.

Lim, Y. S. & Koh, S. L. (2010). Analytical assessments on the potential of harnessing tidal currents for electricity generation in Malaysia. Renewable Energy, 35, 1024-1032.

Lisboa, A. C., Vieira, T. L., Guedes, L. S. M., Vieira, D. A. G. & Saldanha, R. R. (2017). Optimal analytic dispatch for tidal energy generation. Renewable Energy, 108, 371-379.

Lloyd, T., Humphrey, V. & Turnock, S. (2014). Noise modelling of tidal turbine arrays for environmental impact assessment.

Lo Brutto. A., Nguyen, V. T., Guillou, S. S., Thiébaut J. & Gualous, H. (2016). Tidal farm analysis using an analytical model for the flow velocity prediction in the wake of a tidal turbine with small diameter to depth ratio. Renewable Energy, 99, 347-359.

Lopez, M., Candela, J. & Garcia, J. (2008). Two overflows in the Northern Gulf of California. Journal of Geophysical Research: Oceans, 113, n/a-n/a.

Lopez, M., Candela, J. & L. Argote, M. (2006). Why does the Ballenas Channel have the coldest SST in the Gulf of California?

Maganga, F., Germain, G., King, J., Pinon, G. & Rivoalen, E. (2010). Experimental characterisation of flow effects on marine current turbine behaviour and on its wake properties. IET Renewable Power Generation [Online], 4. Available: http://digital-library.theiet.org/content/journals/10.1049/iet-rpg.2009.0205.

Marine energy (2016). World energy resources. World energy council [online].Available: https://www.worldenergy.org/wp-content/uploads/2017/03/WEResources_Marine_2016.pdf. [Accessed 27.11.17].

Marinone, S. G, González, I. and Figueroa, J.M. Prediction of sea surface elevation and currents in the Gulf of California: scales from tides to seasonal. Environmental Modelling & Software, (2009), 24:140-143.

Marinone, S. G. (1997). Tidal residual currents in the Gulf of California: Is the M_2 tidal constituent sufficient to induce them? Journal of Geophysical Research: Oceans, 102, 8611-8623.

Marinone, S. G. (2006). A numerical simulation of the two- and three-dimensional Lagrangian circulation in the northern Gulf of California. Estuarine, Coastal and Shelf Science, 68, 93-100.

Marinone, S. G. (2007). A note on “Why does the Ballenas Channel have the coldest SST in the Gulf of California?”. Geophysical Research Letters, 34.

Marinone, S. G. (2008). On the three-dimensional numerical modeling of the deep circulation around Ángel de la Guarda Island in the Gulf of California. Estuarine, Coastal and Shelf Science, 80, 430-434.

Marinone, S. G., Gonzalez, J. I. & Figueroa, J. M. (2009). Prediction of currents and sea surface elevation in the Gulf of California from tidal to seasonal scales. Environmental Modelling & Software, 24, 140-143.

Marinone, S.G. (2000). Tidal Currents in the Gulf of California: Intercomparison among two and three-dimensional models with observations. Cienc. Mar., 26, 275-301.

Marinone, S.G., (2003). A three-dimensional model of the mean and seasonal circulation of the Gulf of California. Journal of Geophysical Research 108 (C10), 3325.

Marinone, S.G., Lavın, M.F., (2005). Tidal current ellipses in a 3D baroclinic numerical model of the Gulf of California. Estuarine Coastal and Shelf Sciences 64, 519–530

Marta-Almeida, M., Cirano, M., Guedes Soares, C. & Lessa, G. C. (2017). A numerical tidal stream energy assessment study for Baía de Todos os Santos, Brazil. Renewable Energy, 107, 271-287.

Martin-Short, R., Hill, J., Kramer, S. C., Avdis, A., Aallison, P. A. & Piggott, M. D. (2015). Tidal resource extraction in the Pentland Firth, UK: Potential impacts on flow regime and sediment transport in the Inner Sound of Stroma. Renewable Energy, 76, 596-607.

McMillian J, Lickley M. (2008). The potential of tidal power from the Bay of Fundy. Society of Industrial and Applied Mathematics Google Scholar.

Mejia-Olivares, C. J., Haigh, I. D., Wells, N. C., Coles, D. S., Lewis, M. J. & Neill, S. P. (2018). Tidal-stream energy resource characterization for the Gulf of California, México. Energy, 156, 481-491.

Mejia-Olivares, C.J., Haigh. I.D., Angeloudis A., Lewis, M. and Neill, S.P, (2019). Tidal range energy resource assessment of the Gulf of California, Mexico. In review with Renewable Energy (Under review).

Mejia-Olivares, C.J., Haigh. I.D., Lewis, M. and Neill, S.P, (2019). Sensitivity assessment of bathymetry and choice of tidal constituents on tidal-stream energy resource characterisation in the Gulf of California, Mexico

Mejia-Olivares, C.J., Haigh. I.D., Lewis, M. and Neill, S.P, (2019). Sensitivity of bathymetry and choice of tidal constituents on tidal-stream energy resource characterisation in the Gulf of California, Mexico.

Moore, T. & Boyle, C. (2014). The tidal energy potential of the Manukau Harbour, New Zealand. Sustainable Energy Technologies and Assessments, 8, 66-73.

Mott, R. L. (2006). Applied fluid dynamics, Sixth Edition. Edit. Pearson

Munk, W.H. & Cartwright, D.E. (1966). Tidal spectroscopy and prediction. Phil. Trans. R. Soc., Ser., vol. 259, no. 1105, p. 533-581.

Mycek, P., Gaurier, B., Germain, G., Pinon, G. & Rivoalen, E. (2014). Experimental study of the turbulence intensity effects on marine current turbines behaviour. Part I: One single turbine. Renewable Energy, 66, 729-746.

Myers L. E. & Bahaj, A. S. (2005). Simulated electrical power potential harnessed by marine current turbine arrays in the Alderney Race. Renewable Energy, 30, 1713-1731.

Myers L. E. (2003). Internal Report, Department of Civil and Environmental Engineering, University of Southampton.

Myers L. E., Bahaj AS. (2009). Near wake properties of horizontal axis marine current turbines. In Proc. 8th European Wave and Tidal Energy Conf., Uppsala, Sweden, September 2009

Myers L.E. , Bahaj A.S., (2008a). Scale reproduction of the flow field for tidal energy converters. In: Proceedings of the World Renewable Energy Congress (WRECX), Glasgow, UK, 19–25 July 2008.

Myers L.E., Bahaj A.S., Germain G. and Giles J. (2008b). Flow boundary inter-action effects for marine current energy conversion devices. In: Proceedings of the World Renewable Energy Congress (WREC X), Glasgow, UK, 19–25 July 2008.

Myers, L. E. & Bahaj, A. S. (2010). Experimental analysis of the flow field around horizontal axis tidal turbines by use of scale mesh disk rotor simulators. Ocean Engineering, 37, 218-227.

Neill S. P., Cooper M. M., Lewis M. J. (2016b). Global tidal phasing potential. New Orleans: 2016 Ocean Sciences Meeting; 2016b. p. 21e6. February 2016.

Neill, S. P., and Hashemi M. R. (2018) Fundamentals of Ocean Renewable Energy: Generating Electricity from the Sea (E-Business Solutions).

Neill, S. P., Angeloudis, A., Robins, P.E., Walkington, I., Ward, S.L., Masters, I., Lewis, M.J., Piano, M., Avdis, A., Piggott, M.D., Aggidis, G., Evans, P., Adcock, T.A.A., Židonis, A., Ahmadian, R., Falconer, R., (2018). Tidal-range energy resource and optimization – Past perspectives and future challenges. Renew. Energy 127.

Neill, S. P., Hashemi, M. R. & Lewis, M. J. (2014). The role of tidal asymmetry in characterizing the tidal energy resource of Orkney. Renewable Energy, 68, 337-350.

Neill, S. P., Hashemi, M. R. & Lewis, M. J. (2014a). Optimal phasing of the European tidal stream resource using the greedy algorithm with penalty function. Energy, 73, 997-1006.

Neill, S. P., Jordan, J. R. & Couch, S. J. (2012), Impact of tidal energy converter (TEC) arrays on the dynamics of headland sand banks. Renewable Energy, 37, 387-397.

Neill, S. P., Litt, E. J., Couch, S. J. & Davies, A. G. (2009). The impact of tidal stream turbines on large-scale sediment dynamics. Renewable Energy, 34, 2803-2812.

Neill, S. P., Vögler, A., Goward-Brown, A. J., Baston, S., Lewis, M. J., Gillibrand, P. A., Waldman, S. & Woolf, D. K. (2017). The wave and tidal resource of Scotland. Renewable Energy.

NOAA (2017). ETOPO1 Global Relief Model [online] United States of America. Available from https://www.ngdc.noaa.gov/mgg/global/. [Accessed March 2017].

Nova Scotia Power (2018). Annapolis Tidal Station [online]. Available: ⟨http://www.nspower.ca/en/home/about-us/how-we-make-electricity/renewable-electricity/annapolis-tidal-station.aspx⟩; [accessed 25.09.18].

O'Donncha, F., Hartnett, M. & Nash, S. (2013), Physical and numerical investigation of the hydrodynamic implications of aquaculture farms. Aquacultural Engineering, 52, 14-26.

O'Rourke, F., Boyle, F. & Reynolds, A. (2010). Tidal current energy resource assessment in Ireland: Current status and future update. Renewable and Sustainable Energy Reviews, 14, 3206-3212.

O'Rourke, F., Boyle, F. & Reynolds, A. (2014). Ireland's tidal energy resource; An assessment of a site in the Bulls Mouth and the Shannon Estuary using measured data. Energy Conversion and Management, 87, 726-734.

Ocean Energy Systems (2016). 2016 Annual Report, The Executive Committee of Ocean Energy Systems.

Ocean Energy Systems (2016). What is ocean energy? Available at https://www.ocean-energy-systems.org/about-oes/what-is-ocean-energy/. [Accessed March 3th 2018].

OERA (2018). Offshore Energy Research Association. Available at http://www.oera.ca/marine-renewable-energy/tidal-research-projects/. [Accessed March 22th 2019].

ORE Catapult, Tidal Stream and Wave Energy Cost Reduction and Industrial Benefit Report. ORE Catapult, May 2018

Orhan, K., Mayerle, R. & Pandoe, W. W. (2015). Assessment of Energy Production Potential from Tidal Stream Currents in Indonesia. Energy Procedia, 76, 7-16.

Osorio, A. F., Ortega, S. & Arango-Aramburo, S. (2016). Assessment of the marine power potential in Colombia. Renewable and Sustainable Energy Reviews, 53, 966-977.

Palacios-Hernandez, E., Beier, E., Lavin, M. F. & Ripa, P. (2002). The Effect of the Seasonal Variation of Stratification on the Circulation of the Northern Gulf of California. Journal of Physical Oceanography, 32, 705-728.

Park, Y. H. (2017). Analysis of characteristics of Dynamic Tidal Power on the west coast of Korea. Renewable and Sustainable Energy Reviews, 68, 461-474.

Parke, M. E., and M. C. Hendershott (1980), M2, S2, K1 models of the global ocean tide on an elastic earth, Marine Geodesy, 3, 379_408.

Parsons Brinckerhoff Ltd. Severn Tidal Power – Sea Theme Paper. London: DECC; 2010.

Pawlowicz R, Beardsley B, Lentz S (2002). Classical tidal harmonic analysis including error estimates in MATLAB using T_TIDE. Comput Geosci. 28(8):929–37.

Pekeris, C. L. and Accad, Y (1969), Solution of Laplace's equations for M2 tide in the world oceans, Phil. Trans. R. Soc. Lond., 265, 413436.

Petley, S. & Aggidis, G. (2016). Swansea Bay tidal lagoon annual energy estimation. Ocean Engineering, 111, 348-357.

Plew, D. R. and C. L. Stevens (2013). "Numerical modelling of the effect of turbines on currents in a tidal channel – Tory Channel, New Zealand." Renewable Energy 57: 269-282.

Polagye B, Copping A, Kirkendall K, Boehlert G,Walker S,Wainstein M, Cleve BV (2010) Environmental effects of tidal energy development: a scientific workshop. University ofWashington, Seattle, Workshop Briefing Paper

Prandle, D. (1984). Simple theory for designing tidal power schemes. Advances in Water Resources, 7, 21-27.

PRODESEN, 2016. National Electric System Development Program. Energy Alert - National Electric System Development Program (PRODESEN) 2016 -2030. Available from https://www.ey.com/Publication/vwLUAssets/ey-energy-alert-prodesen-2016-2030/%24FILE/ey-energy-alert-prodesen-2016-2030.pdf. [Accessed November 2018].

Pugh, D. T. (1996), Tides, Surges and Mean Sea-Level. Natural Environment Research Council Swindon, UK. Edit. John Wiley and Sons.

Pugh, D. T., and Woodworth, P. (2014). Sea-level Science: Understanding tides, surges, tsunamis and mean sea level changes, Cambridge University Press, Cambridge, United Kingdom, 395pp.

que_hacemos/pdf/programas_manejo/Final_AltoGolfo.pdf

Ripa, P. & Marinone, S. (1989). Seasonal variability of temperature, salinity, velocity, vorticity and sea level in the central Gulf of California, as inferred from historical data.

Ripa, P. (1990). Seasonal circulation in the Gulf of California, Ann. Geophysics.

Ripa, P. (1997). Toward a Physical Explanation of the Seasonal Dynamics and Thermodynamicsof the Gulf of California.

Ripa, P. and G. Velazquez, (1993). Modelo unidimensional de la marea en el Golfo de California. Geofis. Intl., 32, 41-56.

Roberts, A., Thomas, B., Sewell, P., Khan, Z., Balmain, S. & Gillman, J. 2016. Current tidal power technologies and their suitability for applications in coastal and marine areas. Journal of Ocean Engineering and Marine Energy, 2, 227-245.

Robins, P. E., Neill, S. P. & Lewis, M. J. (2014). Impact of tidal-stream arrays in relation to the natural variability of sedimentary processes. Renewable Energy, 72**,** 311-321.

Robins, P. E., Neill, S. P., Lewis, M. J. & Ward, S. L. (2015). Characterising the spatial and temporal variability of the tidal-stream energy resource over the northwest European shelf seas. Applied Energy, 147, 510-522.

Robinson, S.P and Lepper, P.A. “Scoping study: Review of current knowledge of underwater noise emissions from wave and tidal stream energy devices”. The Crown Estate, 2013

Rosario, J., Serrano, J., Carlos Mendoza Sánchez, J. & Vidal, J. (2006). Exploitation of tidal power in the Bay of Cadiz: Ancient tidal mills.

Ross, D. A. (1995). Introduction to Oceanography. New York, NY: HarperCollins. pp. 236-242.

Rourke, F. O., Boyle, F. & Reynolds, A. (2010). Marine current energy devices: Current status and possible future applications in Ireland. Renewable and Sustainable Energy Reviews, 14, 1026-1036.

Savcenko R., and W. Bosch. (2012). EOT11a - Empirical Ocean Tide Model from Multi-Mission Satellite Altimetry, DGFI Report No. 89.

Schwiderski, E. W. (1980). On charting global ocean tides, Reviews in Geophysics, 18 (1), 243_268.

Sen, S., Ganguly, S., Das, A., Sen, J. & Dey, S. (2015). Renewable Energy Scenario in India: Opportunities and Challenges.

SENER, Secretaria de Energia. (2013). Estrategia Nacional 2013-2027, Available at http://www.sener.gob.mx/res/PE_y_DT/pub/2013/ENE_2013-2027.pdf [Accessed 10 December 2014].

SENER, Secretaria de Energia. (2015). Inventario Nacional de energias renovables, Available at http://inere.energia.gob.mx/publica/version3.2/ [Accessed 10 December 2014].

Serhadlıoğluet, S., Adcock, T. A. A., Houlsby, G. T., Draper, S. & Borthwick, A. G. L. (2013). Tidal stream energy resource assessment of the Anglesey Skerries. International Journal of Marine Energy, 3–4, e98-e111.

Severn Barrage Committee (SBC) (1981). Tidal power from the Severn Estuary, vol. II. Her Majesty’s Stationery Office, Energy paper number 46, London.

Severn Tidal Power Group (STPG) (1989). The Severn barrage project: general report, energy paper No. 57. London: Her Majesty’s Stationery Office (HMSO).

Shi, W. Y., Wang, C. K., and Shen, J. F. (2011). Utilisation and prospect of ocean energy resource in China. Acta Energiae Solaris Sinica, 32(6), 913-923.

Shum, C. K., P. L.Woodworth, O. B. Andersen, G. D. Egbert, O. Francis, C. King, S. M. Klosko, C. Le Provost, X. Li, J.-M. Molines, M. E. Parke, R. D. Ray, M. G. Schlax, D.

Stammer, C. C.Tierney, P. Vincent, and C. I. Wunsch (1997), Accuracy assessment of recent ocean tide models, Journal of Geophysical Research, 102, 25,173_25,194.

Sikder, A. K., Rahman, M. T., Islam, M., Khan, N. A. & Hoque, A. Possibility of a tidal power plant in Sandwip Island of Bangladesh. (2014) 3rd International Conference on the Developments in Renewable Energy Technology (ICDRET), 29-31 May 2014 2014. 1-5.

Simpson, J., Souza A., Lavin M. (1994) Tidal Mixing in the Gulf of California. In: Beven, K.C.; Chatwin, P.C.; Millbank, J, (eds.) Mixing and Transport in the Environment. London, John Wiley and Sons, 170-182.

Sucsy, P. V., Pearce, B. R. & Panchang, V. G. (1993). Comparison of Two- and Three-Dimensional Model Simulation of the Effect of a Tidal Barrier on the Gulf of Maine Tides. Journal of Physical Oceanography, 23, 1231-1248.

Sustainable Development Commission (2007). Turning the tide – tidal power in the UK. Sustainable Development Commission.

Sutherland, G., Foreman, M. & Garrett, C. (2007). Tidal current energy assessment for Johnstone Strait, Vancouver Island. Proceedings of the Institution of Mechanical Engineers, Part A: Journal of Power and Energy, 221, 147-157.

Taguchi, E., W. Zahel, and D. Stammer. (2014). Inferring deep ocean tidal energy dissipation from the global high-resolution data-assimilative HAMTIDE model, Journal of Geophysical Research: Oceans, 119, 4573_4592.

Tang, H. S., Qu, K., Chen, G. Q., Kraatz, S., Aboobaker, N. & Jiang, C. B. (2014). Potential sites for tidal power generation: A thorough search at coast of New Jersey, USA. Renewable and Sustainable Energy Reviews, 39, 412-425.

Tapia Olivas, J. C., Ramirez Campbell, H. E. & Gil Samaniego Ramos, M. (2013). Feasibility Analysis for a Tidal Energy Pilot Site in the Gulf of California. V06BT07A087.

Tarbotton, M. & Larson, M. (2006). Canada ocean energy atlas (phase 1) potential tidal current energy resources analysis background. Report to Canadian Hydraulics Centre.

Thiébaut, M. & Sentchev, A. (2015). Estimation of Tidal Stream Potential in the Iroise Sea from Velocity Observations by High Frequency Radars. Energy Procedia, 76, 17-26.

Thiébaut, M. & Sentchev, A. (2017). Asymmetry of tidal currents off the W. Brittany coast and assessment of tidal energy resource around the Ushant Island. Renewable Energy, 105, 735-747.

Thiringer, T., Macenri, J. & Reed, M. (2011). Flicker Evaluation of the SeaGen Tidal Power Plant. IEEE Transactions on Sustainable Energy, 2, 414-422.

Tidal energy Fact sheet 10. Tidal power in Australia. Available at http://www.aie.org.au/AIE/Documents/FS10_TIDAL_ENERGY.pdf [accessed 25.09.17].

Tidal Lagoon Cardiff (2014). Welcome to Tidal Lagoon Cardiff’s website, [Online]. Available: ⟨⟨http://www.tidallagooncardiff.com/⟩⟩ [accessed 11.12.2018].

Tidal Lagoon power (2018). Harnessing power of our tides. Available at http://www.tidallagoonpower.com/projects/swansea-bay/. [Accessed May, 2018].

Tidal stream projects Meygen, 2019, Status. Available at https://simecatlantis.com/projects/meygen/ [accessed 05.06.2019]

Tiwari N.W., Mishra R.K., (2011). Advances Renewable Energy Source, RSC Publishing, 586 pp.

Triton Consultants Ltd. (2006). Canada Ocean Energy Atlas (Phase 1). Potential Tidal Current Energy Resources. Analysis Background. See www.marinerenewables.ca/wp-content/uploads/2012/11/Canada-Ocean-Energy-Atlas-Phase-1-Potential-Tidal-Current-Energy-Resources-Analysis-Background.pdf.

Triton Consultants Ltd., (2002). Green energy study for British Columbia. Phase 2: Mainland.

UK Marine energy 2019. Available at https://www.scottishrenewables.com/publications/uk-marine-energy-2019-new-industry/

UNESCO, 2018. Islands and Protected Areas of the Gulf of California. Available at https://whc.unesco.org/en/list/1182/multiple=1&unique_number=1873.[Accessed October, 2018].

Velarde E, and Anderson D.W. Conservation and management of seabird islands in the Gulf of California. Setbacks and successes. In: Nettleship DN, Burger J, Gachfeld M, editors. Seabirds on islands: threats, case studies and action plans. Bird Life Conservation Series, vol. 1, 1998. p. 229–43.

Vennell, R., Funke, S., Draper, S., Stevens, C. & Divett, T. (2015). Designing Large Arrays of Tidal Turbines: a synthesis and review.

Walkington I, Burrows R. (2009). Modelling tidal stream power potential. Appl Ocean Res 31:239–45.

Walters, R. A., Tarbotton, M. R. & Hiles, C. E. (2013). Estimation of tidal power potential. Renewable Energy, 51, 255-262.

Wang, T. & Yang, Z. (2017). A modeling study of tidal energy extraction and the associated impact on tidal circulation in a multi-inlet bay system of Puget Sound. Renewable Energy.

Ward, S. L., Robins, P. E., Lewis, M. J., Iglesias, G., Hashemi, M. R. & Neill, S. P. (2018). Tidal stream resource characterisation in progressive versus standing wave systems. Applied Energy, 220, 274-285.

Waters, S. & Aggidis, G. (2016). Tidal-range technologies and state of the art in review. Renewable and Sustainable Energy Reviews, 59, 514-529.

Waters, S. & Aggidis, G. (2016b). A World First: Swansea Bay Tidal lagoon in review. Renewable and Sustainable Energy Reviews, 56, 916-921.

Watson, M. J. & Shaw, T. L. (2007). Energy generation from a Severn Barrage prior to full commissioning. Proceedings of the Institution of Civil Engineers - Engineering Sustainability, 160, 35-39.

Webb, D. J. (1976). A model of continental-shelf resonances. Deep Sea Research and Oceanographic Abstracts, 23, 1-15.

Wilmes (2016). The impact of large-scale sea-level changes on tides in the past, present and future, PhD thesis, Bangor University.

Work, P. A., Haas, K. A., Defne, Z. & Gay, T. (2013). Tidal stream energy site assessment via three-dimensional model and measurements. Applied Energy, 102**,** 510-519.

World bank 2018. Electric power consumption (kWh per capita), Mexico. [online].Available https://data.worldbank.org/indicator/EG.USE.ELEC.KH.PC?locations=MX [accessed 06.03.18].

World Energy Council (2007). Survey of resources. London: World Energy Council. [online]. Available http://citeseerx.ist.psu.edu/viewdoc/download?doi=10.1.1.478.9340&rep=rep1&type=pd [Accessed 14.10.2018]

Wyman, P. R. and Peachey, C. J. (1979). Tidal current energy conversion. International Conference on Future energy concepts, London, 30 January–1 February 1979, pp. 164–160 (IEE, London).

Wyrtki, K (1966). Oceanography of the Eastern Ecuatorial Pacific Ocean. Oceanogr. Mar. Biol.Ann. Rev., 4, 33-68, 1966.

Wyrtki, K. (1967). Circulation and water masses in the Eastern Equatorial Pacific Ocean. Intl. J. Oceanology. & Limnol. 1, 117-147.

Xia, J., Falconer, R. A. & Lin, B. (2010). Impact of different operating modes for a Severn Barrage on the tidal power and flood inundation in the Severn Estuary, UK. Applied Energy, 87, 2374-2391.

Xia, J., Falconer, R. A., Lin, B. & Tan, G. (2012). Estimation of annual energy output from a tidal barrage using two different methods. Applied Energy, 93, 327-336.

Yates, N., Burrows, R., Walkington, I. & Hedges, T. (2010). Studies on tidal power from the estuaries of North-West England.

Yates, N., Walkington, I., Burrows, R. & Wolf, J. (2013). Appraising the extractable tidal energy resource of the UK's western coastal waters. Philosophical Transactions of the Royal Society A: Mathematical, Physical and Engineering Sciences, 371.

Zamudio, L., Metzger, E. J. & Hogan, P. (2011). Modeling the seasonal and interannual variability of the northern Gulf of California salinity. Journal of Geophysical Research: Oceans, 116.

Zhang, Y.-L., Lin, Z. & Liu, Q.-L. (2014). Marine renewable energy in China: Current status and perspectives. Water Science and Engineering, 7**,** 288-305.Zhou, Z., Scuiller, F., Charpentier, J. F., Benbouzid, M. E. H. & Tang, T. 2013. Power Smoothing Control in a Grid-Connected Marine Current Turbine System for Compensating Swell Effect. IEEE Transactions on Sustainable Energy, 4, 816-826.

Appendix A TELEMAC steering file

Example of the steering file used in the model simulation within the Gulf of California created in TELEMAC 2D. A brief explanation of the purpose of the variables is provided, in brackets, for each line.

```
/                    INFORMATION ENVIRONMENT             /
/----------------------------------------------------------------------/
BOUNDARY CONDITIONS FILE          = 'BC_BATHY_CICESE.cli' (Formatted boundary
conditions file)
GEOMETRY FILE                  = 'Selafin_BCF_with_Bathy_CICESE.slf' (Binary mesh file
containing mesh coordinates)
BINARY DATABASE 1 FOR TIDE          = './tpxo/h_tpxo7.2' (forcing file elevation)
BINARY DATABASE 2 FOR TIDE          = './tpxo/u_tpxo7.2' (forcing file tidal velocities)
MINOR CONSTITUENTS INFERENCE      = YES (For TPXO tidal data base only. Inference of minor
constituents from the one read in input files linked to keywords BINARY DATABASE 1 FOR TIDE and BINARY DATABASE
2 FOR TIDE.)
RESULTS FILE                  = 'Results_33days_BCF_CICESE.slf' (Binary results file)
/----------------------------------------------------------------------/
/                    GENERAL OPTIONS
/----------------------------------------------------------------------/
VARIABLES FOR GRAPHIC PRINTOUTS    = U,V,S,H,B (U,V=Flow speeds, H=Depth, S =Free
surface,  B= Bottom friction)
TIME STEP                                    = 10 (Seconds)
NUMBER OF TIME STEPS                         = 285120 / 33 days every 10 seconds (Total
duration of simulation)
NUMBER OF FIRST TIME STEP FOR GRAPHIC PRINTOUTS = 1 (Period between output to
results file (time steps))
GRAPHIC PRINTOUT PERIOD                       = 60 (Period between output to results file (time steps))
LISTING PRINTOUT PERIOD                      = 10 (Period between listing file output (time steps))
MASS-BALANCE                                 = YES (Determines whether or not the mass-balance over
the entire domain is checked. For each time step)
/----------------------------------------------------------------------/
/                    INITIAL CONDITIONS
/----------------------------------------------------------------------/
ORIGINAL DATE OF TIME                 = 2015;11;28 (initial simulation date)
ORIGINAL HOUR OF TIME                 = 0;0;0 (Initial simulation time)
INITIAL CONDITIONS                     = 'TPXO SATELLITE ALTIMETRY' (This is used to
define initial water depth conditions.)
/----------------------------------------------------------------------/
/                    BOUNDARY CONDITIONS
/----------------------------------------------------------------------/
OPTION FOR LIQUID BOUNDARIES                 = 2;2  (Thompson method to find unknown boundary
velocities)
/                    TIDE CONDITIONS                     /
/----------------------------------------------------------------------/
OPTION FOR TIDAL BOUNDARY CONDITIONS          = 1 (Option for tidal boundary conditions.
For real tides, option 1 is recommended.)
```

```
TIDAL DATA BASE                                    = 2 (Number 2 corresponds to TPXO
forcing file)
SPHERICAL COORDINATES                              = YES (Spherical Mercator coordinates
for simulations
/over large domains)
LATITUDE OF ORIGIN POINT                           = 23.107399 (Used to determine tide-
generating potential)
LONGITUDE OF ORIGIN POINT                          = -111.902617 (For spherical
coordinates)

SPATIAL PROJECTION TYPE                           = 2
GEOGRAPHIC SYSTEM                                 = 5 (Mercator for TELEMAC)

CORIOLIS                                           = YES (Includes the effect of the Coriolis
force)
/---------------------------------------------------------------------/
/                    HYDRODYNAMICS-PHYSICAL SETUP
/---------------------------------------------------------------------/
LAW OF BOTTOM FRICTION                  = 4 (Number 4 correspond to manning law that was used to
model bed friction over the whole domain )
FRICTION COEFFICIENT                   = 0.030 (Friction coefficient relating to Manning law friction
applied uniformly over the domain)
TURBULENCE MODEL                       = 4 (Constant turbulent viscosity throughout the
/domain, Smagorinski model.)
DIFFUSION OF VELOCITY                  = YES
VELOCITY DIFFUSIVITY                    = 1.E-6 (for option 4, the keyword VELOCITY DIFFUSIVITY
must be the value of molecular viscosity (10-6 m2/s) because it is used as such in the turbulence model.)
/--------------------------------------------------
/          ADVECTION-DIFFUSION
/--------------------------------------------------
TYPE OF ADVECTION                            = 1;5 (these numbers specifying the variables and method
are used to solve the advection step, the first number indicates the variable U and V (velocity components and the number 5
indicated the method that is PSI distributive scheme, mass-conservative (mandatory for H),

SUPG OPTION                                        = 0;0 (Upwind scheme, no upwinding)
MATRIX STORAGE                                     = 3 (keyword configures the type of
matrix storage. It is strongly recommended to use the default value as 3)
FREE SURFACE GRADIENT COMPATIBILITY                 = 0.6
TREATMENT OF THE LINEAR SYSTEM                     = 2 (Uses velocity from momentum
equation rather than continuity equation to improve computational efficiency)
TREATMENT OF FLUXES AT THE BOUNDARIES             = 1;1
INFORMATION ABOUT SOLVER                           = YES
MAXIMUM NUMBER OF ITERATIONS FOR SOLVER   = 100
SOLVER                                              = 3 (Conjugate gradient method for the
/hydrodynamic propagation step)
SOLVER ACCURACY                                     = 1.E-6 (Accuracy during propagation
step)
/---------------------------------------------------------------------/
/                    NUMERICAL OPTIONS
/---------------------------------------------------------------------/
ZERO                                                = 1.E-10
```

TIDAL FLATS = YES (*Enables wetting and drying in shallow regions*)

OPTION FOR THE TREATMENT OF TIDAL FLATS = 1 (*Enables wetting and drying in shallow regions*)

TREATMENT OF NEGATIVE DEPTHS = 2 (*specifies the type of treatment of the negative depths, there are three options: 0 : no treatment, 1 : smoothing of negative depth, 2 : Flux control).*

CONTINUITY CORRECTION = YES (*corrects velocity particularly in the boundary points)*

DISCRETIZATIONS IN SPACE = 11;11 (*binary triangle (4 node triangle) velocity and linear depth)*

/--

/ PROPAGATION /

/--

IMPLICITATION FOR DEPTH = 1. (*To account for semi-implicit discretization of time*)

IMPLICITATION FOR VELOCITY = 1. (*To account for semi-implicit discretization of time*)

IMPLICITATION FOR DIFFUSION OF VELOCITY = 1.(*recommend as default where the wave equation is not applied)*

MASS-LUMPING ON H = 1. (*this number refers to the method to accelerate the computational simulation as well as consider the setting values of H within the model)*

&FIN (*end of the steering file)*

Appendix B Model sensitivity test

Table B1. List of selection of runs, using a variety of model settings and model domains

Simulation number	Law of bottom friction	Bottom coefficient factor	Number of time steps	Model instability	Comments within the simulation	Figures domain area (on the left) and model instabilities (on the right)
001	Nikuradse formula,	0.01	60	unstable	Friction coefficient applied uniformly	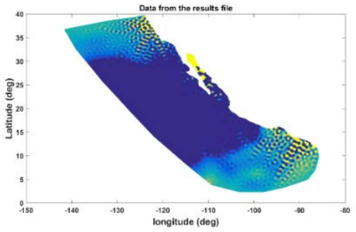 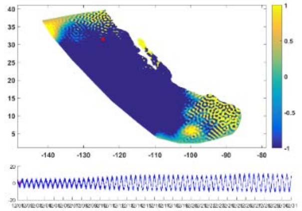
002	Nikuradse formula,	0.1	10	unstable	Since this simulation I changes the boundary conditions, then I selected only one opean boundary condition in the souhthern, northern and Pacific ocean open sea	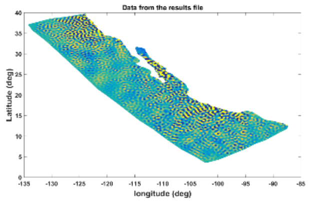 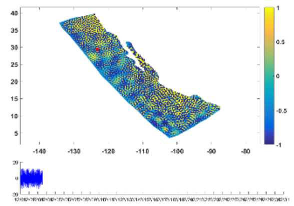
003	Nikuradse formula,	0.02	60	unstable		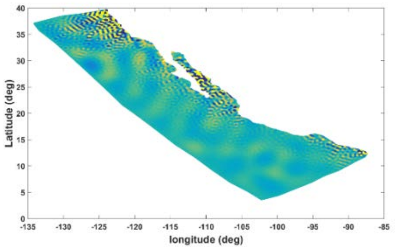

Simulation number	Law of bottom friction	Bottom coefficient factor	Number of time steps	Model instability	Comments within the simulation	Figures domain area (on the left) and model instabilities (on the right)
004	Nikuradse formula,	0.003	60	unstable		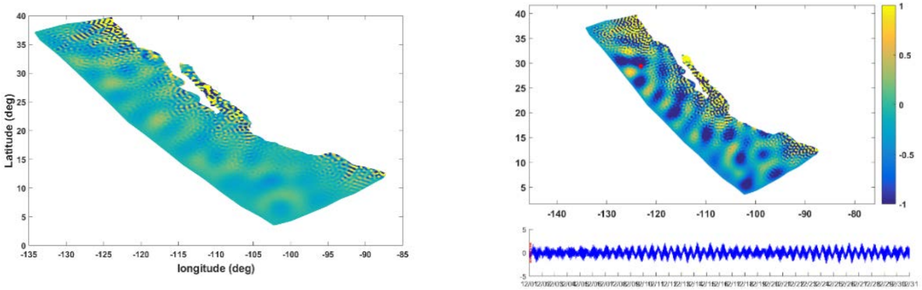
005	Nikuradse formula,	0.015	60	YES	UBOR (10) VBOR (20) AUBOR(.010). I just changed the boundary parameters based on the manual's comments page 19 Blue Kenue mesh	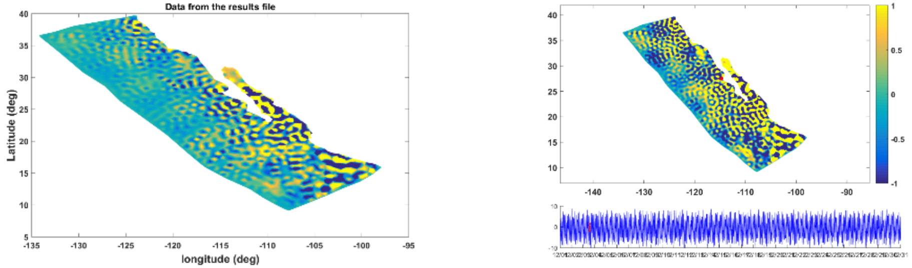
006	Nikuradse formula,	0.015	60	YES	Same as the previous one. Additionally I have changed the boundary conditions seeting up as open boundary with prescriber Q and H and tracer code as Opean boundary with prescribed tracer	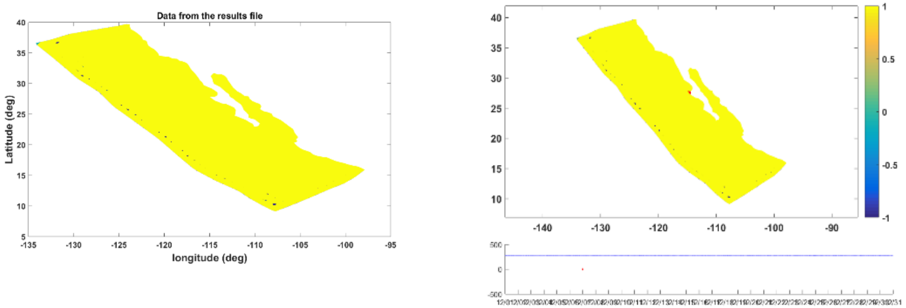

Simulation number	Law of bottom friction	Bottom coefficient factor	Number of time steps	Model instability	Comments within the simulation	Figures domain area (on the left) and model instabilities (on the right)
007	Nikuradse formula,	0.015	60	YES	Same as the previous one but I changed the boundary conditions setting up as open boundary with prescriber UV and H and tracer code as Opean boundary with free tracer.	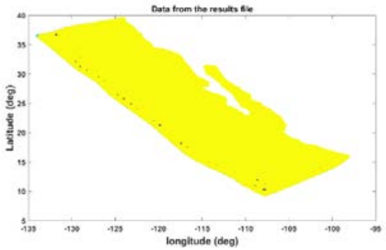 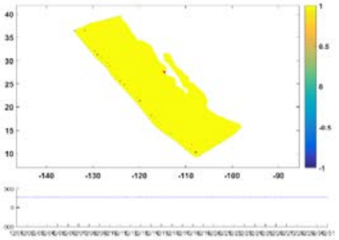
008	Manning formula,	0.001	60	YES	I included the mass balance with the model settings. Therefore the model still present instabilities.	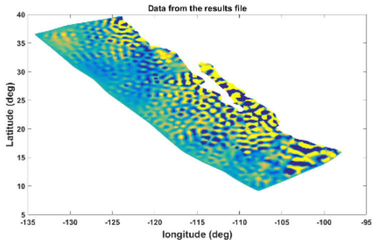 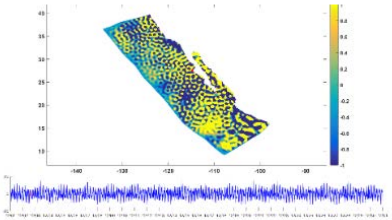
009	Chézy formula,	80	60	YES	I changed the law bottom coefficient to confirm whether the law friction was affecting the results.	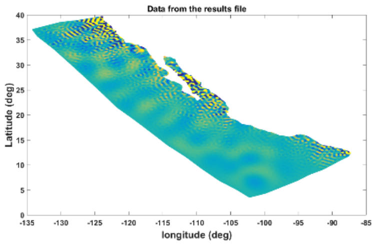 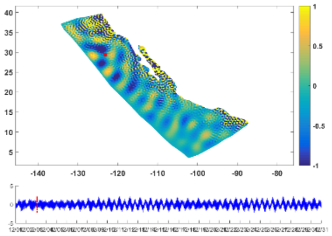

Simulation number	Law of bottom friction	Bottom coefficient factor	Number of time steps	Model instability	Comments within the simulation	Figures domain area (on the left) and model instabilities (on the right)
0010	Chézy formula,	100	60	YES	In this simulation I increased the bottom friction number however the results were still unstable.	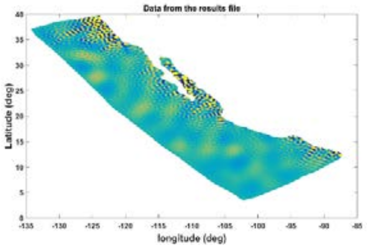 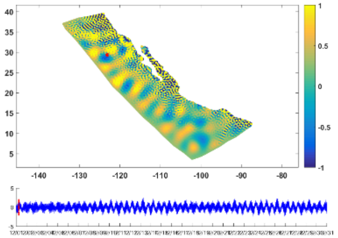
0011	Chézy formula,	10	60	YES	The simulation slightly improved however there are still instabilities within the Gulf	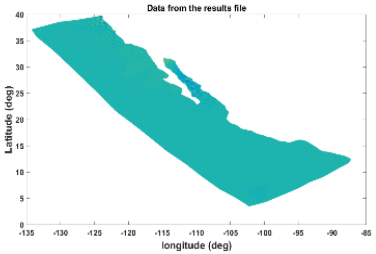 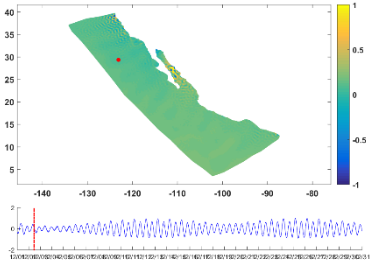
0012	Chézy formula,	30	60	YES	I increased the bottom coefficient but the instabilities returned	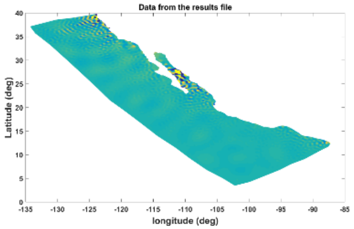 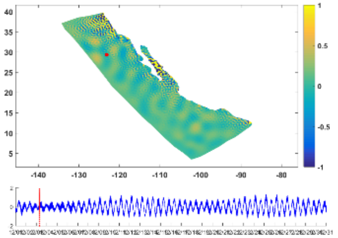

Simulation number	Law of bottom friction	Bottom coefficient factor	Number of time steps	Model instability	Comments within the simulation	Figures domain area (on the left) and model instabilities (on the right)
0013	Chézy formula,	90	60	YES		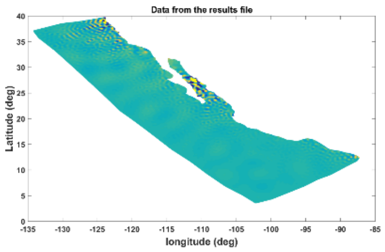 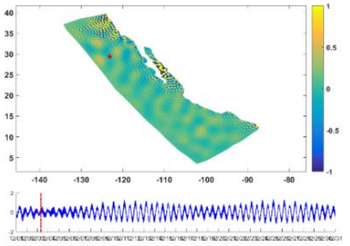
0014	Chézy formula,	5	60	YES	I started to obtain some model instabilities as a result of small values of bottom coefficient using Chezy formula. Also, I created a multiple poligons and linked them within the variable bottom coefficient so that It seems like they are linked with the variable within the selafin file, however, the simulation in TELEMAC does not work	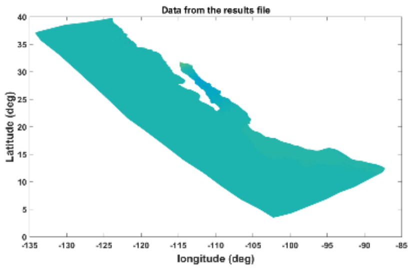 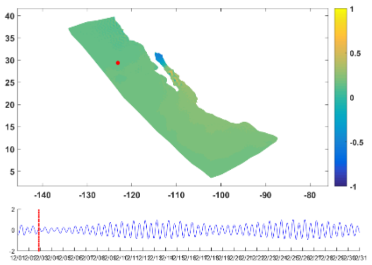
0015	Manning formula,	0.025	60	YES	I returned to the original model settings using manning law	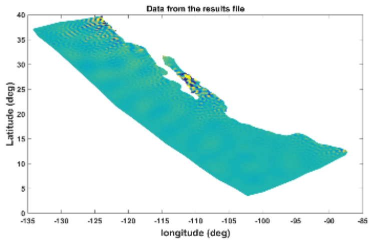 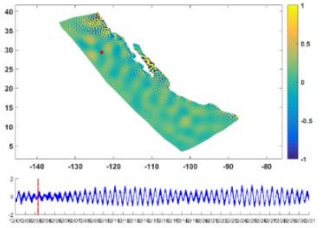

Simulation number	Law of bottom friction	Bottom coefficient factor	Number of time steps	Model instability	Comments within the simulation	Figures domain area (on the left) and model instabilities (on the right)
0016	Manning formula,	0.030	60	YES	I started to extend the model domain.	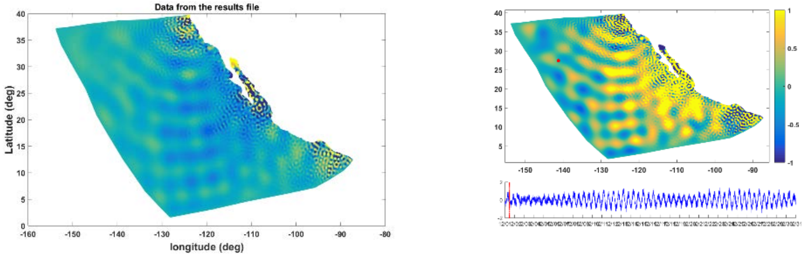
0017	Manning formula,	0.05	60	YES	The model started to be slightly stable at the pacific ocean west boundary conditions however there are significant instabilities in the east boundary condition along the pacific coast wall.	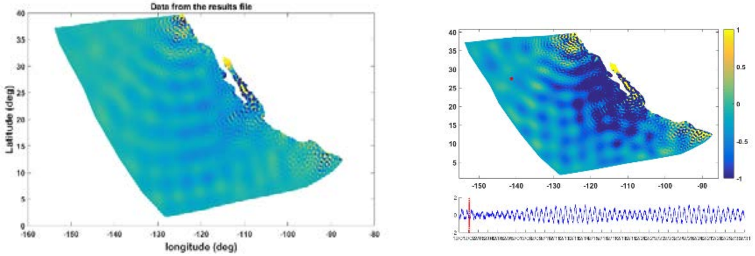
0018	Manning formula,	0.1	60	YES		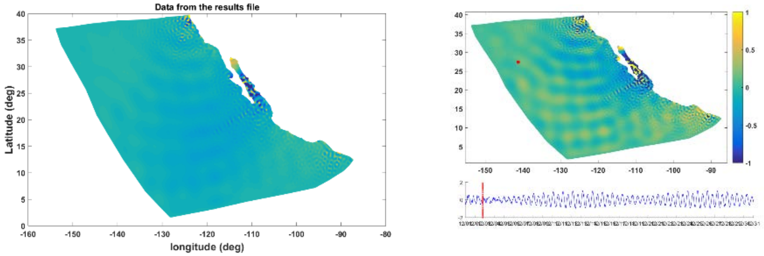

Simulation number	Law of bottom friction	Bottom coefficient factor	Number of time steps	Model instability	Comments within the simulation	Figures domain area (on the left) and model instabilities (on the right)
0019	Manning formula,	0.4	60	YES		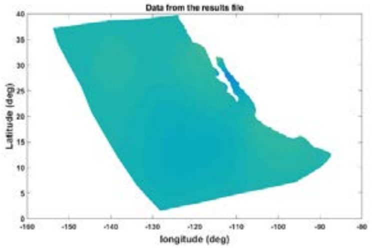 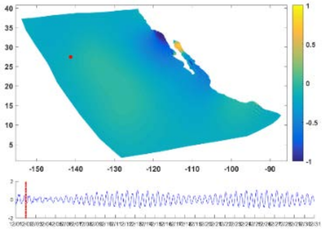
0020	Manning formula,	0.6	60	YES	The model started to present stability.	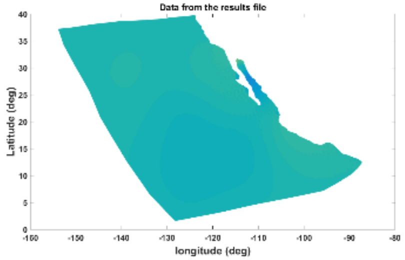 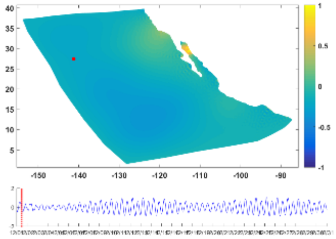
0021	Manning formula,	0.8	60	YES	The model was slightly better than the previous one.	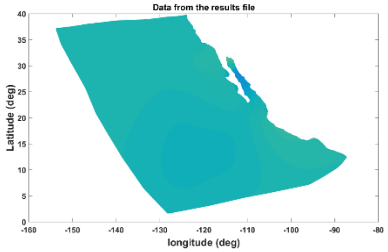 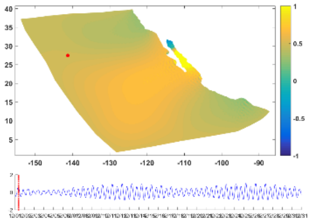

Simulation number	Law of bottom friction	Bottom coefficient factor	Number of time steps	Model instability	Comments within the simulation	Figures domain area (on the left) and model instabilities (on the right)
0022	Manning formula,	1.0	60	YES	This simulation seems to be very stable then from now onwards I consider higher coefficient factors	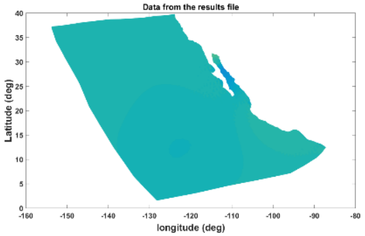 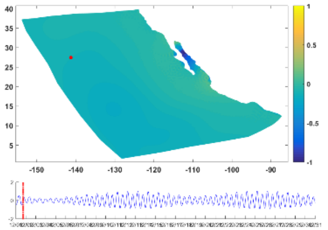
0023	Nikuradse formula,	0.003	60	YES	I ran the next three simulation to compare the Nikuradse law and Manning law. Also I started to include the turbulent model number 2 related to Elder model	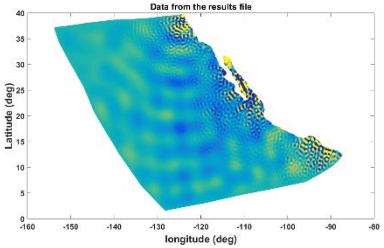 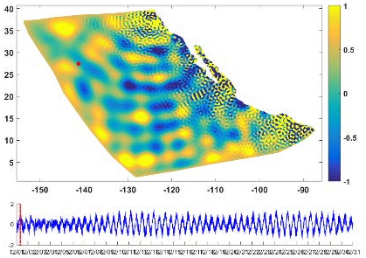
0024	Nikuradse formula,	0.004	60	YES		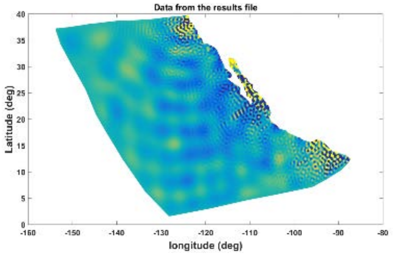 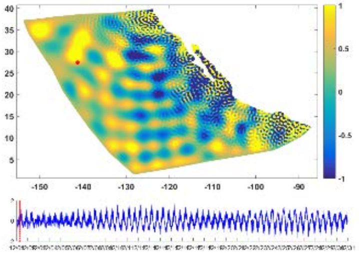

Simulation number	Law of bottom friction	Bottom coefficient factor	Number of time steps	Model instability	Comments within the simulation	Figures domain area (on the left) and model instabilities (on the right)	
0025	Nikuradse formula,	0.03	60	YES	The stabilities reduce significantly as a comparison of the previous two simulations.	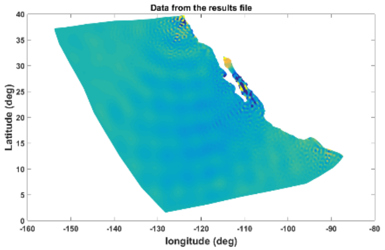	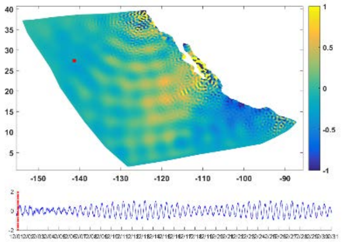
0026	Manning formula,	0.6	60	NO		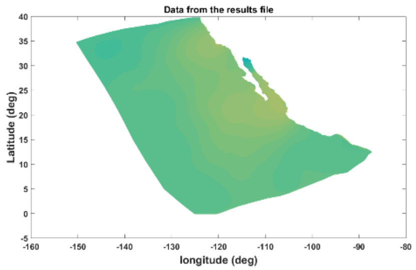	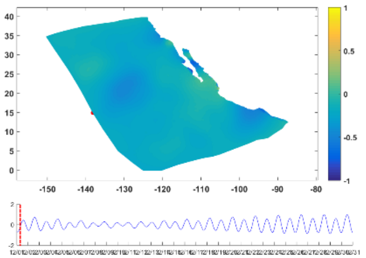
0027	Manning formula,	0.03	30	NO	At this time I started to used rounded boundaries, reduce the time step and I ran the simulation for a short period of time for sensitivity test simulations. Moreover, I added the converted coordinates system as Dr. Christos recommend me.	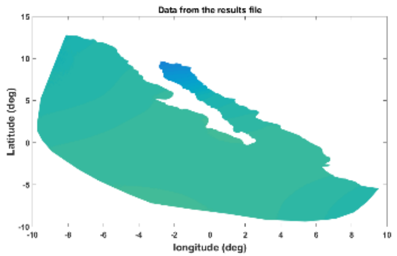	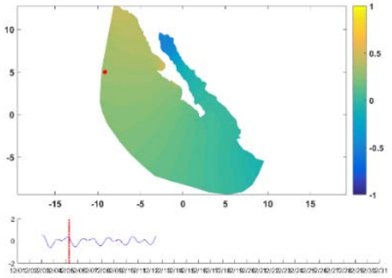

Simulation number	Law of bottom friction	Bottom coefficient factor	Number of time steps	Model instability	Comments within the simulation	Figures domain area (on the left) and model instabilities (on the right)
0028	Manning formula,	0.03	30	NO	"I added the MASS-LUMPING ON VELOCITY AND THE PARAMETER COMPATIBILITY OF FREE SURFACE GRADIENT = 0.5 Based on the TELEMAC forum recommendations. "FREE SURFACE COMPATIBILITY GRADIENT 0.1 and I added also MASS-LUMPING ON VELOCITY = 1	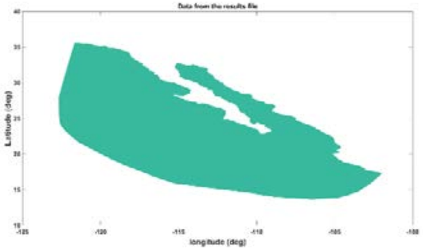 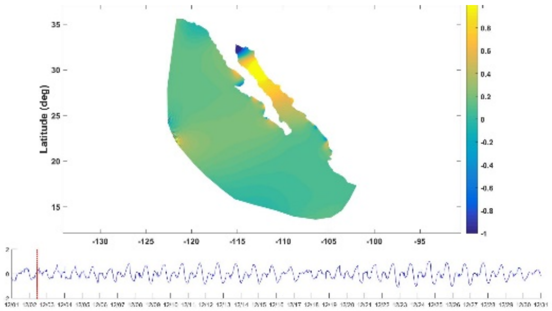

Appendix C Example of the validation simulations which use a variety of model settings and model domains.

Table C1: Examples of model validation, Water level, statistic results and tidal constituents (amplitude and phase) comparisons

Simulation domain Fig. 3.22a	Grid and model mesh	Water level results
Simulation number: 001 Law bottom coefficient: Manning formula, Friction coefficient value= 0.03	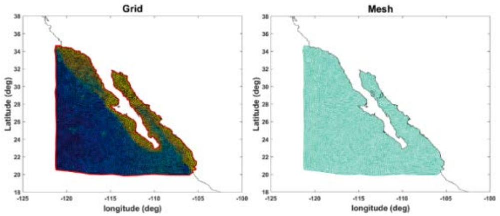 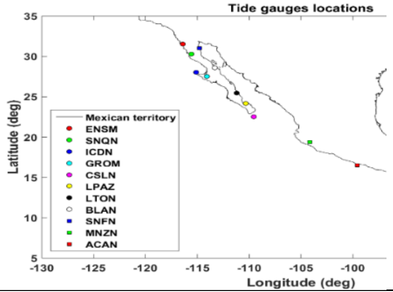 	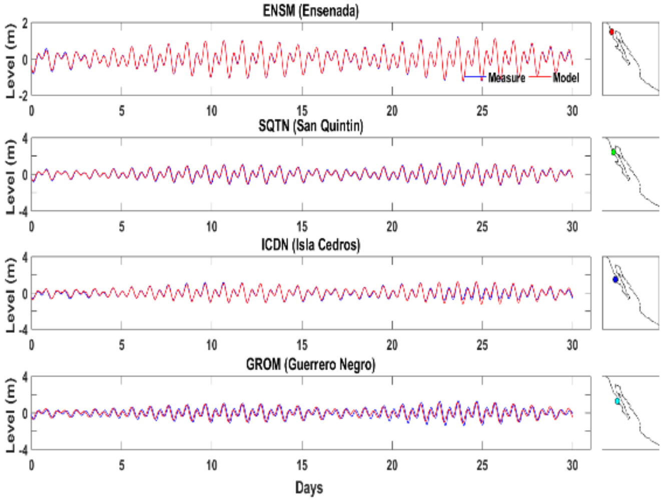
	Statistics results using Taylor diagram 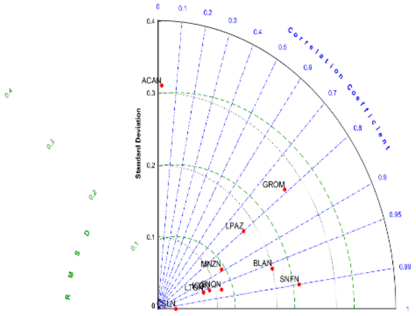 	**Comparison model results vs observations** 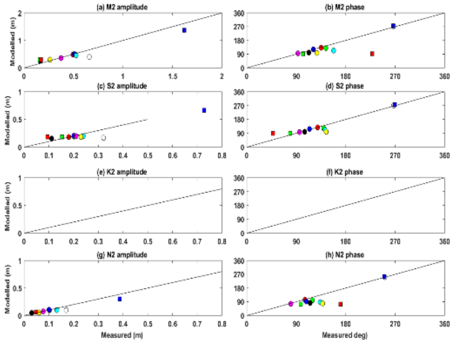

Simulation domain Fig. 3.22a	Grid and model mesh	Water level results
Simularion number: 002 Law bottom coefficient: Manning formula, Friction coefficient value= 0.04	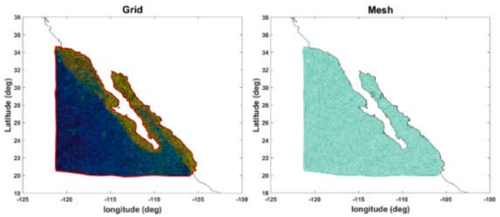 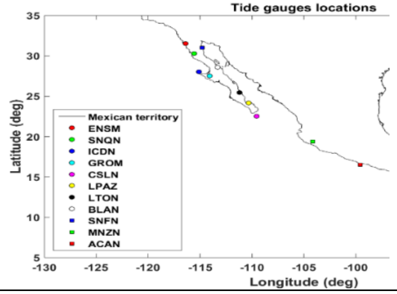	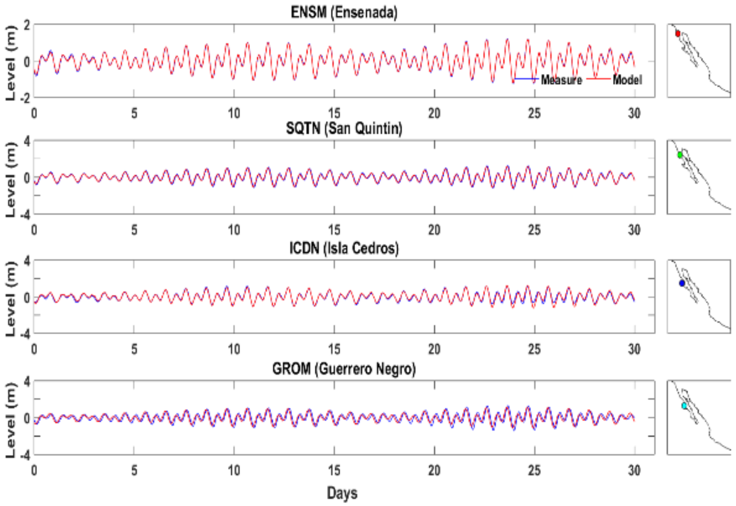
	Statistics results using Taylor diagram 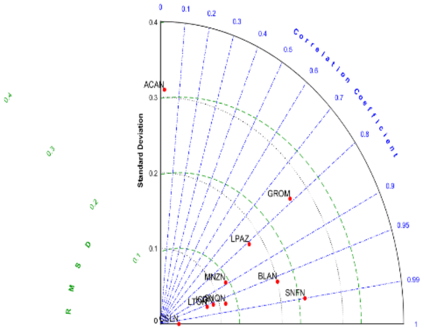	Comparison model results vs observations 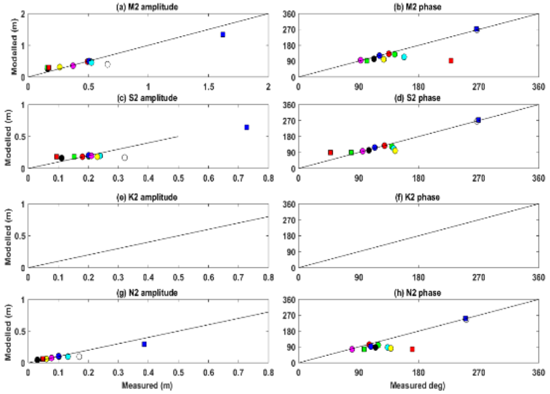

Simulation domain Fig. 3.22a	Grid and model mesh	Water level results
Simularion number: 003 Law bottom coefficient: Manning formula, Friction coefficient value= 0.05	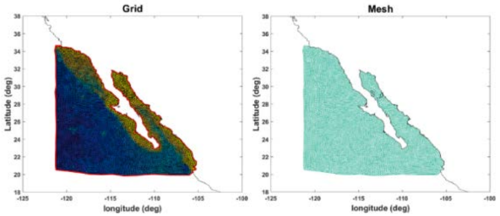 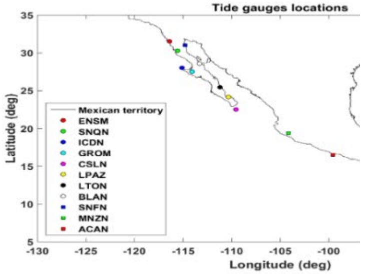	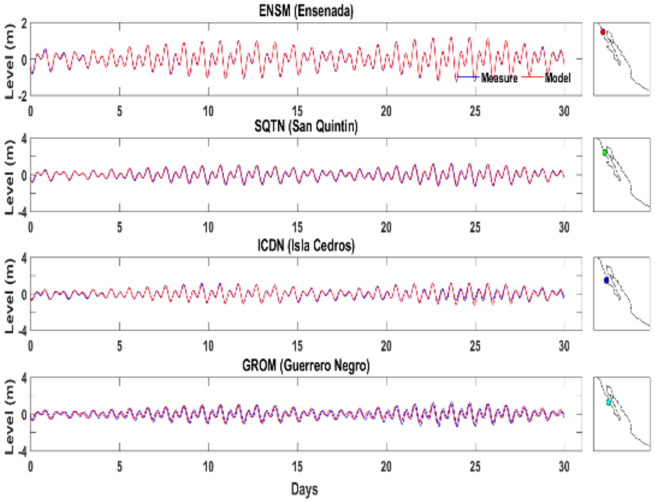
	Statistics results using Taylor diagram 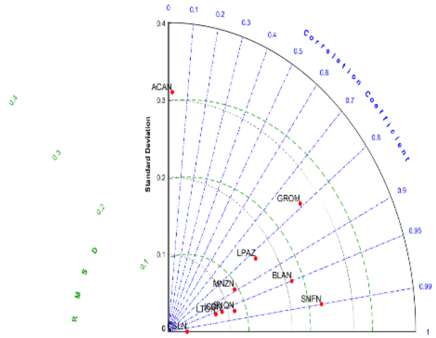	**Comparison model results vs observations** 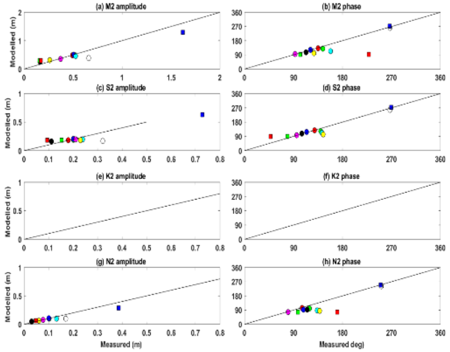

<table>
<tr><th>Simulation domain Fig. 3.22a</th><th>Grid and model mesh</th><th>Water level results</th></tr>
<tr><td>Simularion number: 004
Law bottom coefficient:
Manning formula,
Friction coefficient value= 0.06</td><td>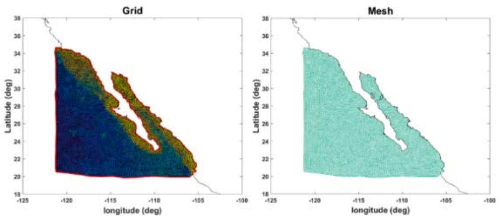

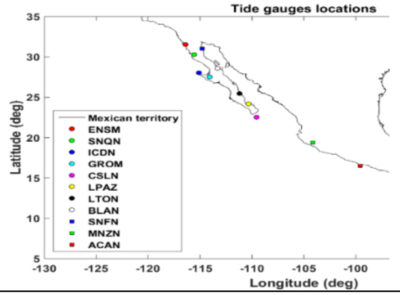
</td><td>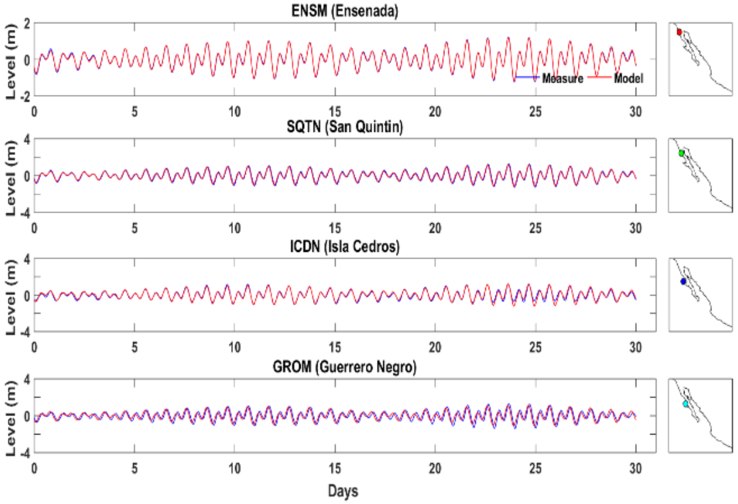
</td></tr>
<tr><td></td><td>Statistics results using Taylor diagram
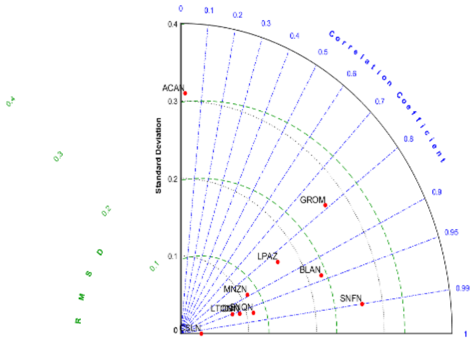
</td><td>Comparison model results vs observations
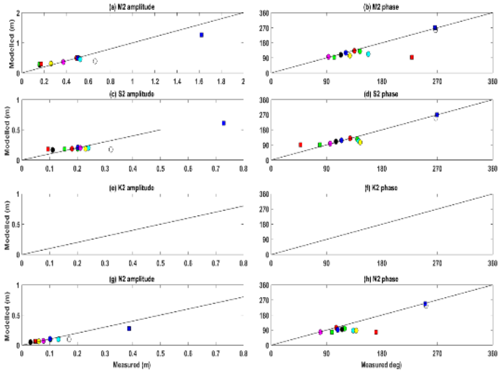
</td></tr>
</table>

Simulation domain Fig. 3.22a	**Grid and model mesh**	**Water level results**
Simularion number: 005 Law bottom coefficient: Manning formula, Friction coefficient value= 0.07	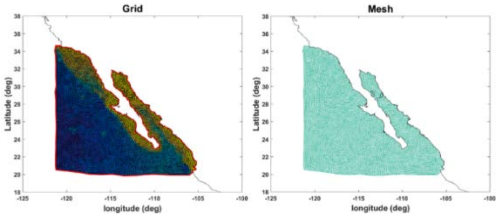 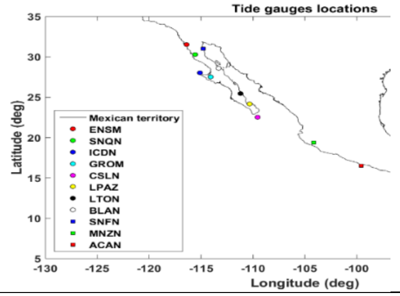	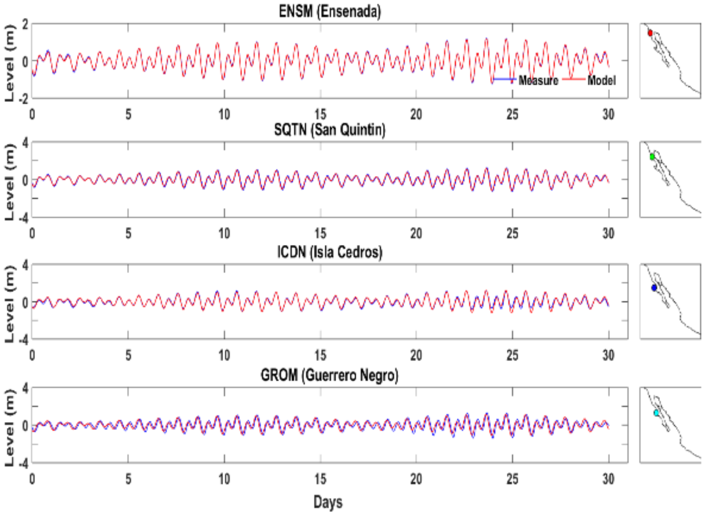
	Statistics results using Taylor diagram 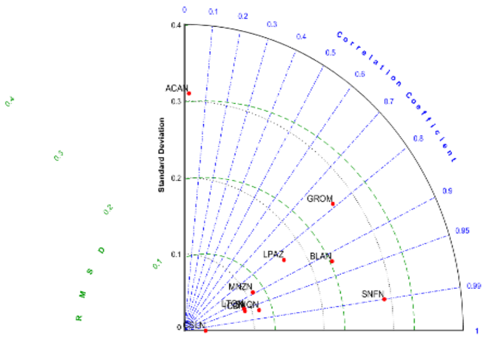	**Comparison model results vs observations** 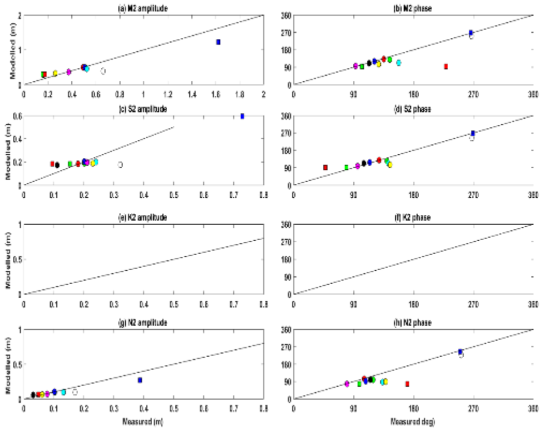

Simulation domain Fig. 3.22a	Grid and model mesh	Water level results
Simularion number: 006 Law bottom coefficient: Manning formula, Friction coefficient value= 0.08	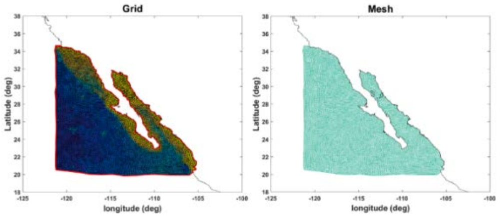 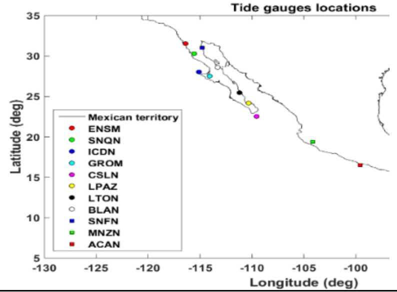	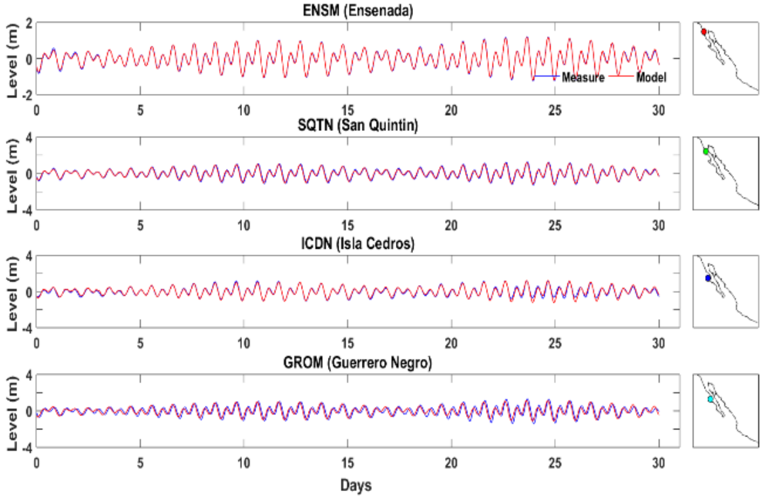
	Statistics results using Taylor diagram 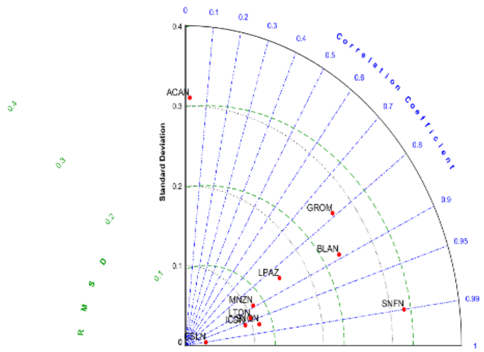	Comparison model results vs observations 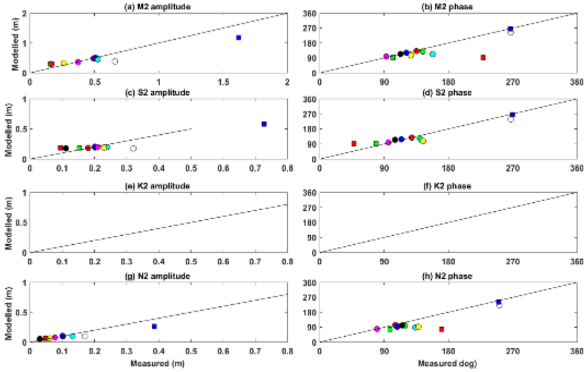

Appendix D Subroutine to increase the bottom coefficient to simulate the turbines

```
                  *****************
                   SUBROUTINE DRAGFO
!                  *****************
!
    &(FUDRAG,FVDRAG)
!
!***********************************************************************
! TELEMAC2D   V6P2                              21/08/2010
!***********************************************************************
!
!brief    ADDS THE DRAG FORCE OF VERTICAL STRUCTURES IN THE
!+                MOMENTUM EQUATION.
!code
!+  FU IS THEN USED IN THE EQUATION AS FOLLOWS :
!+
!+  DU/DT + U GRAD(U) = - G * GRAD(FREE SURFACE) +..... + FU_IMP * U
!+
!+  AND THE TERM FU_IMP * U IS TREATED IMPLICITLY.
!
!warning  USER SUBROUTINE
!
!history  J-M HERVOUET
!+        01/03/1990
!+        V5P2
!+
!
!history  N.DURAND (HRW), S.E.BOURBAN (HRW)
!+        13/07/2010
!+        V6P0
!+   Translation of French comments within the FORTRAN sources into
!+   English comments
!
!history  N.DURAND (HRW), S.E.BOURBAN (HRW)
!+        21/08/2010
!+        V6P0
!+   Creation of DOXYGEN tags for automated documentation and
!+   cross-referencing of the FORTRAN sources
!
!~~~~~~~~~~~~~~~~~~~~~~~~~~~~~~~~~~~~~~~~~~~~~~~~~~~~~~~~~~~~~~~~~~~~~~
~~~
!| FUDRAG         |<--| DRAG FORCE ALONG X
!| FVDRAG         |<--| DRAG FORCE ALONG Y
!~~~~~~~~~~~~~~~~~~~~~~~~~~~~~~~~~~~~~~~~~~~~~~~~~~~~~~~~~~~~~~~~~~~~~~
~~~
!
```

```
      USE BIEF
      USE DECLARATIONS_TELEMAC2D
!
      USE DECLARATIONS_SPECIAL
      IMPLICIT NONE
!
!+-+-+-+-+-+-+-+-+-+-+-+-+-+-+-+-+-+-+-+-+-+-+-+-+-+-+-+-+-+-+-+-+-+-+-+-+-+-+
!
      TYPE(BIEF_OBJ), INTENT(INOUT) :: FUDRAG,FVDRAG
!
!+-+-+-+-+-+-+-+-+-+-+-+-+-+-+-+-+-+-+-+-+-+-+-+-+-+-+-+-+-+-+-+-+-+-+-+-+-+-+
!
      INTEGER IELEM,I,I4,NSOM,DISCLIN
      DOUBLE PRECISION UNORM,AIRE,SOM,XSOM(4),YSOM(4),X4,Y4
!     DOUBLE PRECISION, PARAMETER :: CD=1.56D0,DIAM=2.D0
      DOUBLE PRECISION, PARAMETER :: CD=1.34D0,DIAM=2.D0
      INTEGER, PARAMETER :: N=1
!
      DOUBLE PRECISION P_DSUM
      EXTERNAL         P_DSUM
!
!-----------------------------------------------------------------------
!
!     COMPUTES THE MASSE INTEGRALS
!
      CALL VECTOR (T1,'=','MASBAS          ',UN%ELM,1.D0,
     &             S,S,S,S,S,S,MESH,.FALSE.,S)
!
      CALL CPSTVC(UN,FUDRAG)
      CALL CPSTVC(VN,FVDRAG)
      CALL OS('X=C     ',FUDRAG,FUDRAG,FUDRAG,0.D0)
      CALL OS('X=C     ',FVDRAG,FVDRAG,FVDRAG,0.D0)
!
!-----------------------------------------------------------------------
!
!     EXAMPLE : DRAGFORCE IS SET IN A QUADRILATERAL DEFINED BY
!               4 NODES
!     SURFACE OF 20 X 40 CENTERED ON (0,0)
!
      NSOM = 4 (Set up a polygon of 4 points)
      XSOM(1) = -75259.D0 (coordinates of the polygon where the natural bottom friction
could be increased)
      XSOM(2) =  -65000.D0
      XSOM(3) =  -65000.D0
      XSOM(4) = -75259.D0
      YSOM(1) = 7.00000D5
      YSOM(2) = 7.00000D5
      YSOM(3) =  696526.D0
      YSOM(4) =  696526.D0
!
```

```
!-----------------------------------------------------------
!
!    P1 POINTS
!
     AIRE=0.D0
     DO I=1,BIEF_NBPTS(11,MESH)
!
       IF(INPOLY(X(I),Y(I),XSOM,YSOM,NSOM)) THEN
         UNORM = SQRT(UN%R(I)**2+VN%R(I)**2)
         FUDRAG%R(I) =  - 0.5D0 * N * DIAM * CD * UNORM
         FVDRAG%R(I) =  - 0.5D0 * N * DIAM * CD * UNORM
         AIRE = AIRE + T1%R(I)
       ENDIF
!
     ENDDO
!
!    QUASI-BUBBLE POINTS
!
     IF(FU%ELM.EQ.12) THEN
!
       DISCLIN=11
       CALL CHGDIS(FUDRAG,DISCLIN,12,MESH)
       CALL CHGDIS(FVDRAG,DISCLIN,12,MESH)
!
       DO IELEM = 1 , NELEM
         I4=IKLE%I(IELEM+3*NELMAX)
         X4=(X(IKLE%I(IELEM        ))+
    &        X(IKLE%I(IELEM+  NELMAX))+
    &        X(IKLE%I(IELEM+2*NELMAX)))/3.D0
         Y4=(Y(IKLE%I(IELEM        ))+
    &        Y(IKLE%I(IELEM+  NELMAX))+
    &        Y(IKLE%I(IELEM+2*NELMAX)))/3.D0
         IF(INPOLY(X4,Y4,XSOM,YSOM,NSOM)) AIRE = AIRE + T1%R(I4)
       ENDDO
!
     ENDIF
!
!    IN PARALLEL THE AREA MAY BE SPLIT INTO SEVERAL SUB-DOMAINS
!
     IF(NCSIZE.GT.0) AIRE=P_DSUM(AIRE)
!
!    NOW PREPARING THE DIVISION
!
     IF(AIRE.GT.1.D-6) THEN
       SOM = 1.D0 / AIRE
     ELSE
       IF(LNG.EQ.1) WRITE(LU,*) 'DRAGFO : AIRE DE LA ZONE NULLE'
       IF(LNG.EQ.2) WRITE(LU,*) 'DRAGFO: AREA OF ZONE EQUAL TO ZERO'
       CALL PLANTE(1)
       STOP
```

```
      ENDIF
!
!      DIVIDING BY THE AREA
!
      CALL OS('X=CX    ',X=FUDRAG,C=SOM)
      CALL OS('X=CX    ',X=FVDRAG,C=SOM)
!
!-----------------------------------------------------------------------
!
      RETURN
      END
```